A NEW ENERGY MINIMIZATION METHOD
FOR ATOMISTIC SIMULATIONS

A NEW ENERGY MINIMIZATION METHOD FOR ATOMISTIC SIMULATIONS

By

LI PAN, M.A.Sc, B.ENG

A Thesis

Submitted to the School of Graduate Studies

in Partial Fulfilment of the Requirements

for the Degree

Doctor of Philosophy

McMaster University

DOCTOR OF PHILOSOPHY (2007)   McMaster University
(Mechanical Engineering)   Hamilton, Ontario

TITLE: A new energy minimization method for atomistic simulations

AUTHOR: Li Pan, M.A.Sc (McMaster University)

SUPERVISOR: Dr. D.R. Metzger, Associate Professor
                             Department of Mechanical Engineering

                             Dr. M. Niewczas, Associate Professor
                             Department of Materials Science and Engineering

NUMBER OF PAGES: xxxiv; 239

Abstract

A novel energy minimization framework, based on the Dynamic Relaxation technique, is developed to numerically determine the equilibrium of atomic positions in a crystalline lattice containing internal defects and subjected to the external traction.

The internal force and stiffness of individual atoms are obtained as derivatives of the potential energy function. The external traction is axially applied on boundary atoms by means of a newly developed periodic symmetry technique, which allows the deformation of the model to be carried out and ensures the stability of the model during the simulation. The damping ratio adjusts the amount of artificial damping introduced into the numerical integration to dissipate the kinetic energy, so that the simulation is more efficient and accurate for various configurations.

The relaxation of the model containing a single edge or screw dislocation without the external loading is in line with the experimental observation and theoretical predictions. The external traction does not prevent the dislocation from dissociation, but changes the separation width between partial dislocations after the relaxation.

The interactions between two dislocations gliding on the same slip plane are in agreement with the theory. The increase of the height of two dislocations with the opposite Burgers vectors gliding on parallel slip planes leads to the formation of faulted dipoles or perfect stable dipoles. Two opposite screw dislocations on inclined slip planes can annihilate by the mechanism of re-combination and re-dissociation,

and the compression along the slip direction increases the critical height of the annihilation.

The present approach has created the capability to provide insight into the atomistic mechanisms and processes of the formation of particular structures in crystalline materials.

Acknowledgements

Table of Contents

List of Tables

List of Figures

Chapter 1

Introduction

1.1   Background and Motivation

Understanding the plastic deformation and working hardening of materials is critical to control the behavior of materials during manufacturing for obtaining high-quality industrial products. Nowadays, developing a material with desirable mechanical properties is a new focus aspect of the research. For example, new aluminum alloys with high strength are being developed, which could be used for environment-friendly lightweight vehicles. It is well known that the mechanical properties of a material are determined by its microstructure. While the relationships between the mechanical properties and the microstructure in materials have been examined by both theoretical and experimental approaches, the mechanisms underlying these relationships are not fully understood. Computer simulations for the investigation of the atomic structures of crystalline materials are increasingly important because they allow deeper understanding of the relationship between internal structures and properties of these materials without the necessity to carry out sophisticated and expensive experiments. With more fundamental knowledge and better computational techniques, the mechan-

ical properties of materials could be investigated by utilizing atomistic or multi-scale simulations in the future.

Dynamical approaches, e.g. Molecular Dynamics (MD) schemes, for the atomistic simulation are widely used since simulations can be performed at finite temperatures. Atoms without or with initial velocities (temperature) in a non-equilibrium state are allowed to re-arrange themselves according to classical Newton's laws, and eventually vibrate around their new equilibrium positions. Though simulations based on dynamical methods can model equilibrium and thermodynamical properties, the thermal energy available in the system can generate new processes in the material system, which do not occur at the temperature of absolute zero. For example, the external applied stress and thermal activation both can trigger the cross-slip mechanism of a screw dislocation, which is suppressed at low temperatures. Thus, the static or steady-state approaches are needed, in which the temperature is set to 0K, to provide simpler interpretation of these mechanisms. In these methods, atoms move to new equilibrium positions as the total potential energy in the system is going down to the minimal value, but they are stationary or in the steady-state in the initial and final configurations.

The other limitation of dynamical methods is that the simulation time to obtain the equilibrium configuration is quite long. Supposed that the equilibrium occurs at the time of 10^{-6} second, there are at least 10^8 steps required to achieve the solution in the MD approach with the time step of 10^{-14} second that stabilizes the simulation. However, the static or steady-state methods should be efficient to locate equilibrium positions via some techniques and assumptions, e.g. the optimization of the path of minimizing the potential energy, or the increase of the masses of atoms since the inertia term $(m\ddot{u})$ disappears eventually. Therefore, static or steady-state approaches based on minimizing the potential energy can play a crucial role in the

atomistic modeling for investigating the change of local atomic structures of materials.

The computers available today allow one to solve atomic systems with tens of millions degrees of freedom. However, currently available numerical platforms to locate a configuration with minimum potential energy at 0K are subjected to various limitations and sometimes do not converge to correct solutions. There are two examples: (i) In order to obtain the static configuration in MD simulations (quenched dynamics), some criteria are introduced to apply the artificial damping to atoms when atoms vibrate around their equilibrium positions. The simulation time is actually the same as pure dynamical approaches, and the criteria themselves usually are not accurate enough, which could yield static solutions with errors; (ii) Conjugate gradient method efficiently locates the minimum potential energy configuration by mathematically optimizing the total potential energy function. However, the result is often the local minimum that is close to the initial configuration and in fact other local minima or even the global minimum, which could be the correct solution, may be missed.

In short, developing a new efficient and accurate numerical algorithm of the potential energy minimization, which would allow the calculation of stable configurations of atoms in crystalline materials with or without external loading conditions, is necessary and important. From the fundamental and academic point of view, the new numerical framework can help to gain better knowledge of mechanisms underlying structure-property relationships and to independently verify results from other methods in particular when there are no experimental observations available. From the practical point of view, the new framework may be used to solve complex problems in real material systems.

1.2   Objectives

The objectives of the present research are:

(1) To develop a new theoretical framework of the potential energy minimization based on the Dynamic Relaxation technique for the simulations of the atomic structures of crystalline materials containing internal defects and subjected to the axial external traction. The new approach allows (a) locating multi-minimal potential energy positions by adjusting the damping ratio; (b) revealing the intermediate process path of the relaxation, and (c) applying the external traction directly on boundary atoms of the model via a novel periodic symmetry technique.

(2) To better understand the processes leading to the formation of some complex defects in crystalline lattices and their stable configurations. The basic mechanisms of the formation of defects, which include the processes of the annihilation of edge and screw dislocation dipoles, the formation and structures of faulted dipoles in Z or S configurations, and the process of annihilation of screw dislocation dipoles on inclined slip planes, are investigated by the new approach.

1.3   Outline of the thesis

The thesis consists of six chapters. In chapter 2, the literature review is conducted with regard to potential energy functions, current available numerical approaches and the periodic symmetry. The previous research work is summarized as well. The development of the new framework including the numerical algorithm and post-process techniques are explained in chapter 3. The numerical responses simulated by the new approach are demonstrated in chapter 4, which includes models containing one single dislocation free of the external traction, and subjected to the uni-axial or bi-

axial external traction along the dislocation line direction and/or the slip direction. In chapter 5, the interactions between two dislocations are studied. They include modeling of the interactions of two edge dislocations on the same slip plane, edge and screw dislocation dipoles on parallel slip planes and screw dislocation dipoles on inclined slip planes. Finally, the conclusions and recommendations for the future research are provided in chapter 6.

Chapter 2

Literature Review

There are three major components in the theoretical framework of the potential energy minimization. Potential energy functions control the way by which two or more atoms interact with each other in the assembly, and determine the total energy of the system and ultimately the minimum point at which the simulation is terminated. The periodic symmetry allows a relatively small number of atoms in the model to accurately represent a larger system that would otherwise be difficult or impossible to be handled by the computer. Numerical methods, used in simulations, allow converging the system to the configuration where the potential energy is minimum. This chapter summarizes the previous research work on these topics available in the literature, with the emphasis on the Dynamic Relaxation technique.

2.1 Potential energy functions

The success of all atomistic simulations depends on how accurately the potential energy function reproduces interatomic interactions in the real crystal lattice. Though there are many types of potential energy functions available, the most commonly used

functions in atomistic simulations are: pair potentials and Embedded Atom Method (EAM) potentials.

2.1.1 Pair potential functions

The common pair potentials used in atomistic simulations are the following [7]:

(i) Born-Mayer potential

$$V(r_{ij}) = A \exp[-\rho(r_{ij} - r_0)/r_0] \tag{2.1}$$

where A and ρ are arbitrary constants, r_0 is a reference value as the nearest neighbor distance in the perfect lattice, and r_{ij} is the distance separated by one pair of atoms i and j.

(ii) Morse potential

$$V(r_{ij}) = A \exp[-2\rho(r_{ij} - r_0)] - 2A \exp[-\rho(r_{ij} - r_0)] \tag{2.2}$$

(iii) 12-6 Lennard-Jones potential

$$V(r_{ij}) = 4\epsilon \left[\left(\frac{\sigma}{r_{ij}} \right)^{12} - \left(\frac{\sigma}{r_{ij}} \right)^{6} \right] \tag{2.3}$$

where parameters σ and ϵ are chosen to fit the physical properties of different materials. In the real simulation, it is usual to set $\sigma = \epsilon = 1$ with the adjustment of units in the system.

The 12-6 Lennard-Jones (LJ) pair potential function has often been used in investigating the behavior of systems consisting of atoms or more complex molecules. The balance distance, in which the repulsive force is equal to the attractive force, is

around 1.122σ. The term $\sim 1/r^{12}$ dominates for the repulsion at a short distance while $\sim 1/r^6$ represents the attraction with a large separation between atoms. Thus, in LJ potential, the repulsion is stronger than the attraction, and the corresponding repulsive force increases very strongly when two atoms move closer.

The potential energy of individual atoms is determined by adding all of its interactions with other atoms in the system together. Considering the size of a model, the number of neighboring atoms could be limited when the cut-off radius is introduced. Then, the total potential energy of the system is half of the summation of the energy of individual atoms.

$$U_{tot} = \frac{1}{2} \sum_i \sum_j V(r_{ij}) \qquad (2.4)$$

The advantage of LJ potential is that the calculation of its value or its derivatives is simple and fast, which is especially important in modeling very large atomic assembles. LJ potential is usually used to investigate fundamental issues, rather than studying the properties of a specific material [14]. However, there are some drawbacks in using LJ potential in molecular simulations. First of all, the scheme of pair potentials is not convenient to model ionic systems. The elastic constants in metals are not properly reproduced. Finally, the formation energy for different internal defects is overestimated [14][16]. Thus, it is necessary to develop a new potential energy function specific for a given material, which accurately reproduces the properties of a material and can be used efficiently in numerical computations.

2.1.2   EAM potential functions

Embedded Atom Method (EAM) has been developed for two decades. The basic idea behind EAM potentials is to include the electron density function to the pair

potential. This new approach was proposed by Daw and Baskes [36] and the scheme of the potential energy of an atom i in the system is written as:

$$U_i = -f(\rho_i) + \frac{1}{2} \sum_j V(r_{ij})$$

(2.5)

The total potential energy of the model U_{tot} is given by:

$$U_{tot} = \sum_i U_i$$

(2.6)

Here $V(r_{ij})$ is a pair potential and $f(\rho_i)$ is an embedded function (electron density function). The distance r is the solo variable in pair potential functions. It is convenient to calculate EAM functions when the same variable is adopted in the embedded part. Thus ρ is constructed as:

$$\rho_i = \sum_j \phi(r_{ij})$$

(2.7)

where $\phi(r_{ij})$ is a different pairwise interaction between two atoms compared to $V(r_{ij})$.

The calculation of ϕ and V is within the limited number of neighboring atoms in the range introduced by the cut-off radius. The interaction disappears when the distance is larger than the critical value of the cut-off radius. Generally, the cut-off radius is equal to the distance that extends from one to four nearest neighbors in the perfect lattice.

The computational procedure for calculating the EAM potential energy is similar to that for a pair potential. For atom i, both $\phi(r_{ij})$ and $V(r_{ij})$ are summed over neighbors j within the cut-off radius, and then a single evaluation of $f(\rho_i)$ is performed [58]. Therefore, the nonlinear embedded function $f(\rho_i)$ plays a critical role

in the form of EAM potentials and there is a lot of research work that focused on the generation of accurate f for various materials. There are two basic approaches to determine the function f. One methodology is the direct curve-fitting such as the early work performed by Foiles *et al.* [18] and the recent work done by Mishin *et al.* [35]. They used a series of experimental data, including the sublimation energy, equilibrium lattice constant, elastic constants, vacancy-formation energies and other lattice properties, to fit Equation(2.5) providing that V and ρ are determined. A table or a curve of f with respect to the values of ρ_i for a specific material is provided for the simulation. Another scheme is to construct an empirical equation of f first, then to build equations for ρ and V with unknown coefficients, and finally to fit these coefficients according to experimental data. The most famous one in the later group was presented by Finnis and Sinclair (to be referred to as FS) [16]. They used a square-root function to mimic the result of the tight-binding theory, in which $\phi(r_{ij})$ could be interpreted as a sum of squares of overlap integrals [33].

$$f(\rho_i) = \sqrt{\rho_i} \qquad (2.8)$$

There are some other formats of the function f, such as the one developed by Kogure *et al.* [30].

$$f(\rho_i) = D\rho_i \ln \rho_i \qquad (2.9)$$

where D is determined by fitting the function to the experimental values of the cohesive energy E_c , the lattice parameter a, the material stiffness (C_{11},C_{12},C_{44}), and the vacancy formation energy E_v. However, these formats are not as simple and widely used as FS type.

Ackland *et al.* [2][3] gave the formula and corresponding parameters for N-

body potential of the FS type for face-centred-cubic (f.c.c) metals and alloys.

$$V(r_{ij}) = \sum_{k=1}^{6} a_k (r_k - r_{ij})^3 H(r_k - r_{ij}) \qquad (2.10)$$

$$\phi(r_{ij}) = \sum_{k=1}^{2} A_k (R_k - r_{ij})^3 H(R_k - r_{ij}) \qquad (2.11)$$

where r_k and R_k are chosen as knot points such that $r_1 > r_2 > r_3 > r_4 > r_5 > r_6$ and $R_1 > R_2$. Hence, r_1 and R_1 represent the cut-off radius of functions $V(r_{ij})$ and $\phi(r_{ij})$, respectively. In the case of copper, the radius is set to cover three nearest neighboring atoms in the perfect lattice. r_6 is set to equal the nearest-neighbor spacing r_{nn} in all cases, so that this term multiplied by a_6 contributes only for $r < r_{nn}$, where the pair potential part shows strong repulsion. The coefficient a_1, ..., a_5, A_1 and A_2 are determined by fitting exactly to a series of parameters, which include the equilibrium lattice parameter a, the cohesive energy E_c, the material stiffness (C_{11}, C_{12}, C_{44}), a lower bound of the unrelaxed vacancy formation energy E_v^f and the stacking fault energy. The coefficient a_6 cannot be found by fitting to any harmonic property of the lattice, so it is adjusted for metals, such as copper, to fit the pressure-volume relation calculated by Christensen et al. [9]. Since the copper is used throughout the thesis as the model material, the parameters of Ackland are summarized in Table(2.1).

In conclusion, EAM potential energy functions provide more accuracy and offer more reasonable interpretation for results in the simulation than pair potentials. EAM potentials need more computational time. However, with the continuous increase of the computer speed, the time to calculate the value of the potential energy in EAM methodology is acceptable even for a large size of the model.

Table 2.1: The coefficients of the Ackland *et al.* [3] potential for the copper.

Coefficient	Copper
a_1	29.059214
a_2	-140.05681
a_3	130.07331
a_4	-17.48135
a_5	31.82546
a_6	71.58749
R_1	1.2247449
R_2	1.0000000
A_1	9.806694
A_2	16.774638
r_1	1.2247449
r_2	1.1547054
r_3	1.1180065
r_4	1.0000000
r_5	0.8660254
r_{61}	0.7071068

(The coefficients for V and ϕ are in the unit of eV, and r_k and R_k are in the unit of the lattice parameter $0.3615nm$.)

2.1.3   Other potential functions

Besides popular pair potentials and EAM potentials, there are other types of potentials available for specific metals or alloys. Erkoc [13] summarized 38 different formats of potential energy functions under three groups. In many atomistic simulations, other two types of potential energy functions are used in recent years.

Rosato *et al.* [48] proposed a potential energy scheme for f.c.c. transition metals, such as copper and nickel, based on the tight-binding theory. The potential energy of an atom i is expressed as:

$$
\begin{aligned}
U_i &= E_b^i + E_r^i \\
&= -\left\{ \sum_j \xi^2 \exp\left[-2q\left(\frac{r_{ij}}{r_0} - 1 \right) \right] \right\}^{1/2} + \sum_j A \exp\left[-p\left(\frac{r_{ij}}{r_0} - 1 \right) \right]
\end{aligned} \quad (2.12)
$$

where E_b is the band energy modeling the attraction while E_r adopts the Born-Mayer pair potential to represent the repulsion. The parameters A, p, ξ, and q are determined by fitting experimental values for various metals.

Jacobsen *et at.* [27][28] suggested an approximate total energy method, which is called the effective-medium theory (EMT). The basic idea of EMT is to calculate the energy of an atom i in a suitable reference system, i.e. the effective medium, and then estimate the energy difference between the real and reference systems.

$$
\begin{aligned}
U_i &= E_c(n_i) + E_{AS}(i) \\
&= E_c(n_i) + \left[\sum_j V(r_{ij}) - \sum_j^{ref} V(r_{ij}) \right]
\end{aligned} \quad (2.13)
$$

Here, $E_c(n_i)$ is the cohesive energy of an atom with respect to the electronic density n_i from its neighboring atoms in the reference system, e.g. the perfect f.c.c lattice.

$E_{AS}(i)$ is the atomic-sphere correction. In the current approach, the correction represents the difference of pair potential values in real systems (models with defects) and reference systems (perfect lattices). The coefficients used in Equation(2.13) are determined by fitting experimental data for a specific material.

2.2   Periodic symmetry

In order to eliminate the surface effect dominated in the model, the periodic symmetry (or the periodic boundary condition) is applied to mimic the presence of an infinite bulk in an N-atom system. The model containing N atoms is treated as the primitive cell of an infinite periodic lattice of identical cells [19].

In Figure(2.1) as a two-dimensional domain, any atom i interacts with all other atoms including the atoms in the primitive cell and in all its image cells within the cut-off radius. When applying the periodic symmetry to the model, the resultant internal force on a certain atom and on all of its corresponding images should be identical. Therefore, the atom and all its images should have the same acceleration (motion). A method, herein called the traditional method [19][22], has been developed to form the appropriate resultant force required to assume that the motion is compatible with the symmetry.

Followings are some key points of the traditional method for the calculation of the periodic symmetry:

(1) For three-dimensional models, applying a periodic symmetry to one coordinate direction is widely used. For example, in dislocation simulations, it is usual to apply the periodic symmetry in the direction that is coincident with the dislocation line, which assumes that the dislocation line is infinitely long. Thus, for a given atom i, there are two images in one direction, which is shown in Figure(2.2).
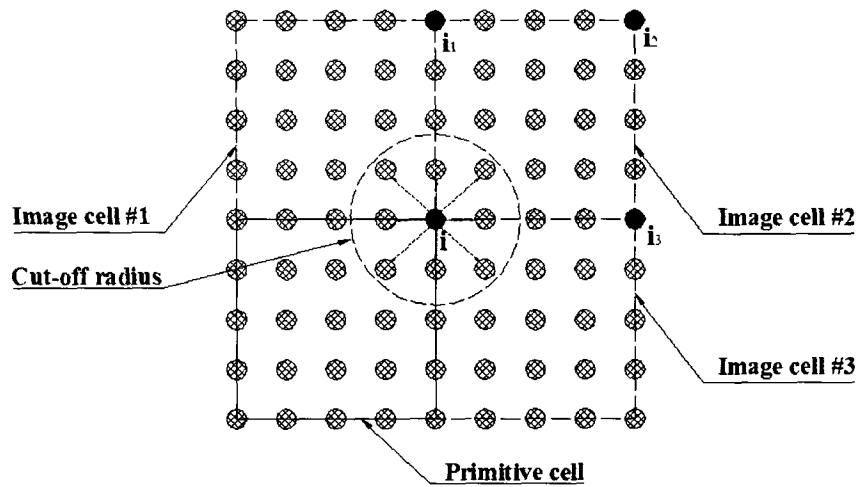
Figure 2.1: The scheme of the periodic symmetry in atomistic simulations.
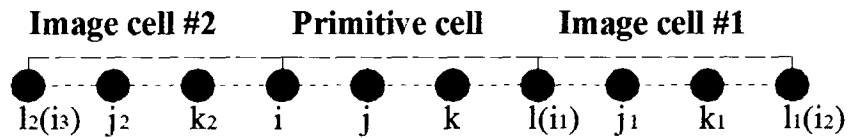
Figure 2.2: The periodic symmetry along one coordinate direction.

(2) Generally, the cut-off radius r_c must be less than half of the length of the primitive cell r_L (periodic length) in the designated direction. Otherwise, some image atoms could be missed or double counted.

(3) The distance r_{ij} between atoms i and j now is determined by atom $i(x_i, y_i, z_i)$, atom $j(x_j, y_j, z_j)$ and all j's images by fixing the position of atom i. For the periodic symmetry in one coordinate direction, one need first evaluate the distance r_{ij}. If $r_{ij} > r_c$, then it is necessary to evaluate the distance between atom i and two images of atom j: $j_1(x_j + r_L, y_j, z_j)$ and $j_2(x_j - r_L, y_j, z_j)$. Three possible cases are:

(a) If neither r_{ij1} nor r_{ij2} is within the cut-off radius r_c, atom j is skipped;

(b) If either r_{ij1} or r_{ij2} is within the cut-off radius r_c, this value is taken as the distance between i and j;

(c) if both r_{ij1} and r_{ij2} are within the cut-off radius r_c, the minimum value of r_{ij1} and r_{ij2} is the distance r_{ij}.

In the traditional method of applying the periodic symmetry to the model, in order to preserve the periodicity, the periodic length r_L must be kept constant during the simulation. Otherwise, atoms and their images lose uniform motion. Therefore, in the usual treatment, the periodic length could not be stretched or compressed but the corresponding periodic boundaries are allowed to move and deform, but at a constant spacing. Consequently, the periodic symmetry generates a kind of restrictive 'kinematic constraint' between the periodic boundaries. The relaxation under the periodic symmetry in the traditional method takes place only within these boundaries until even spacing between adjacent atoms is achieved.

One technique called 'tied nodes' [49], which is used in Finite Element Methods

16

(FEMs) [10][53], could be used in the atomistic simulation. This technique forces

two nodes (or atoms, in this case) to follow identical motions during the simulation.

Though the technique of 'tied nodes' provides another way to obtain the motion of

corresponding pair of an atom and its image, it can only apply to the pair of physical

boundary atoms while inner atoms in the model still need use the traditional method

to calculate their movements. In the 'tied node' method, forces on the boundary

atoms, $\mathbf{F}_i$, are first obtained without any regard for symmetry (no images considered).

Then the resultant force $\mathbf{F}_i^R$ on each boundary node (atom) i is calculated by adding

(assembling) the force from its image node i',

$$\mathbf{F}_i^R = \mathbf{F}_i + \mathbf{F}_{i'} = \mathbf{F}_{i'}^R \tag{2.14}$$

This ensures that the resultant forces on a boundary node and its image are the same.

Therefore, this method is equivalent to the traditional method. Since this method

need extra efforts to search for the pairs of boundary atoms, the computational burden

is higher than the traditional method.

The traditional treatments are acceptable when the change of atomic struc-

tures is only dependent on internal forces. If external forces are involved into the simu-

lation, e.g. the axial traction, the unit length between adjacent atoms is changed. The

periodic length should follow the same trend and be the identical parameter through-

out the model. However, the periodic length of the corresponding periodic boundary

under traditional treatments is fixed. On the one hand, the traditional method itself

enforces over-restrictive kinematic constraints between periodic boundaries since it

requires any pair of boundary atoms be in the same motion. In fact, boundary atoms

don't have to be in the same motion as long as all pairs of boundary atoms in the

model could maintain a unique periodic length at any time during the simulation.

On the other hand, randomly distributing external traction acting directly on atoms at most of cases causes the model to easily lose its unique periodic length, so that the periodicity of the model is subverted. Hence, a new method is needed to ensure that the periodicity is upheld, while avoiding unnecessary constraints of the repeating cell boundaries.

2.3 Numerical methods

Generally, there are two approaches to minimize the total potential energy of the atomic system. In one group of techniques called gradient methods, the focus is on mathematically optimizing the function of total potential energy E_{tot}, such as Equation(2.6), with the gradient $dE_{tot} = 0$. Since the distance r_{ij} is the function of the space coordinates of atoms i and j, the potential energy is the function of coordinates. Once the total potential energy function is minimized, the new equilibrium positions of atoms are determined. Another treatments called dynamical methods rely on numerical solutions of the differential equation of motion for individual atoms in the system. In the equilibrium state, the minimum total potential energy is obtained when the overall kinetic energy is maximum due to the energy conservation in the system.

2.3.1 Gradient methods

The gradient methods include the steepest descents method [8][46], the conjugate gradient method [8][17][31][46], Newtom-Raphson method and Quasi-Newton method [8][31]. Newton-Raphson method and Quasi-Newton method, which use the second derivative of the potential energy function, cause the storage problem due to the Hessian matrix and its inverse if large number of atoms is simulated. Therefore these

methods are seldom used for the atomistic simulation except for models containing small number of degrees of freedom.

In the method of steepest descent, the positions of atoms are updated along the direction of the steepest descent iteratively with the total potential energy going down. The descent direction $\mathbf{S}$ is the opposite direction of E'_{tot}, which causes E_{tot} to decrease more quickly.

$$\mathbf{S} = -\nabla E_{tot} \tag{2.15}$$

If there are N atoms in the model, the total degrees of freedom are $3N$ in the three-dimensional space so that the target potential energy function has $3N$ variables. Supposed that the vector $\mathbf{X}$ has $3N$ components,

$$E_{tot}(\mathbf{X}) = \sum_{j} V(r_{ij}) = E_{tot}(\mathbf{X_1}, ..., \mathbf{X_n}) = E_{tot}(x_1, ..., x_{3n}) \tag{2.16}$$

Combined with Equations(2.15) and (2.16), the vector $\mathbf{S}$ is calculated as:

$$\mathbf{S} = -\nabla E_{tot} = \begin{Bmatrix} \frac{\partial E_{tot}}{\partial x_1} \\ \frac{\partial E_{tot}}{\partial x_2} \\ \vdots \\ \frac{\partial E_{tot}}{\partial x_{3n-1}} \\ \frac{\partial E_{tot}}{\partial x_{3n}} \end{Bmatrix} \tag{2.17}$$

In any iterative step i, the updated positions of atoms for the step $(i + 1)$ are based on the current positions and gradients.

$$\mathbf{X}_{i+1} = \mathbf{X}_i + h\mathbf{S}_i = \mathbf{X}_i - h\nabla E_{tot,i} \tag{2.18}$$

Here, h is the step length, which shows how far atoms move in the gradient direction $\mathbf{S}$. The h could be an arbitrary value or be optimized as h^*. The arbitrary step length could be determined before the start of the simulation and be adjusted during the simulation by certain criteria. The optimal step length h^* is selected where the total potential energy is minimum along the line $\mathbf{S}$. After $\mathbf{S}_i$ is obtained, based on Equations(2.16) and (2.18), the updated total potential energy with respect to h_i along the gradient direction, i.e. $E_{tot}(\mathbf{X}_i + h_i\mathbf{S}_i)$ is obtained. With $dE_{tot}/dh_i = 0$, h_i^* is evaluated at the current step. Obviously, the arbitrary step length approach may need more steps to converge to the minimum value but with fewer function evaluations. Thus, it may require less computational time than more rigorous line search approach.

The convergence criteria can be established based on: (i) the change of the total potential energy in two consecutive iterations, or (ii) the difference of the positions of atoms in two consecutive iterations, or (iii) the value of the first derivative of the total potential energy, is within the tolerance value. The trajectory to the minimal value by the steepest descent method is in the form of a 'zigzag' as shown in Figure[2.3(a)]. Since the new gradient is always perpendicular to the previous direction, the convergence rate is quite slow if the path to the minimal value is long and narrow. The convergence characteristics of the steepest descent method could be improved by the conjugate gradient method, which optimizes the direction of the gradient to make the convergence as quickly as possible. As depicted in Figure[2.3(b)], the conjugate gradient method does not require the directions of the gradient be orthogonal. Fletcher and Reeves [17] developed the scheme to obtain the search direction considering current and previous gradients. In its iterative procedure, after

the first step, the descent direction is modified from Equation(2.15),

$$\mathbf{S}_i = -\nabla E_{tot,i} + \frac{|\nabla E_{tot,i}|^2}{|\nabla E_{tot,i-1}|^2} \mathbf{S}_{i-1} \tag{2.19}$$

The conjugate gradient method provides better convergence, and thus is used in many applications in atomistic simulations. It has been proven that there may be a number of minima on the potential energy surface for a specific molecular model [23]. However, the minimum potential energy of the system obtained by the conjugate gradient method is often the local one and in fact other local minima or even the global minimum, which could be important in some disciplines, may not be obtained. Moreover, the process of the potential energy minimization simulated by the conjugate gradient method is a mathematical iteration, in which the attention is more on quickly achieving the relaxed configuration. Therefore, the intermediate configurations calculated by the conjugate gradient method may not be controlled by the physical law. In many cases, the physical path of atoms approaching the equilibrium is useful to investigate the formation of certain atomic structures.

2.3.2 Dynamical methods

Rather than studying total potential energy functions, the target of dynamical methods is individual atoms in the system. If the net force acting on every atom is rebalanced, i.e. $\sum \mathbf{F} = 0$, the potential energy is minimum because the first derivative of the potential energy as the internal force is zero. In dynamical methods, atoms are regarded as mass points and modeled using the classical mechanics. Thus, the general equation of motion for a single atom at any time t is

$$M\ddot{\mathbf{u}}^t + K\mathbf{u}^t = \mathbf{F}_{ext}^t \tag{2.20}$$
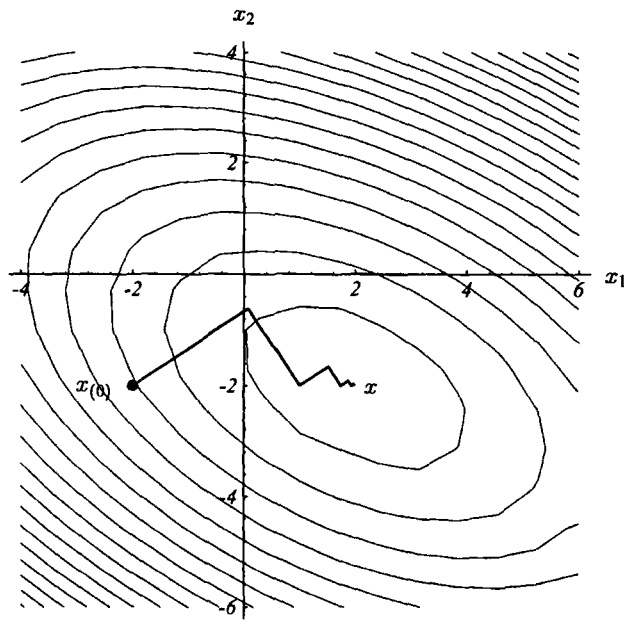
(a)
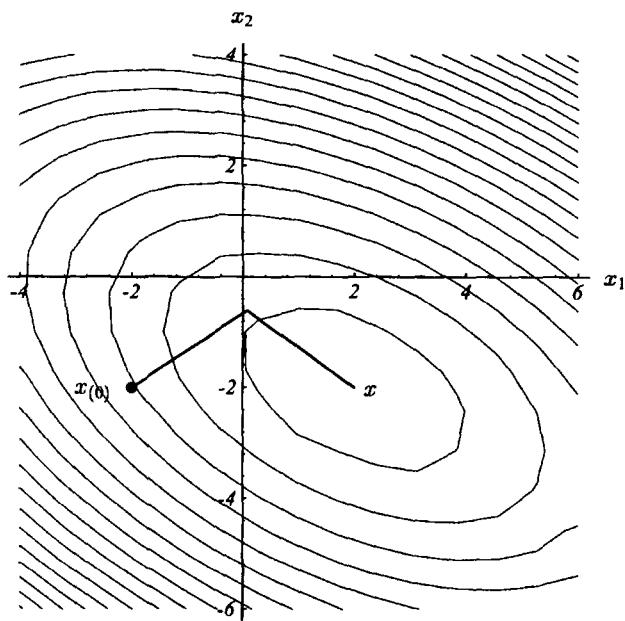
(b)

Figure 2.3: The depiction of gradient methods. (a) The steepest descent method; (b) The conjugate gradient method [52].

Here, M is the mass of an atom; K is the stiffness and u is the displacement. F_{ext} is the external force. If the source for the change of the atomic structure is internal defects, then $F_{ext} = 0$. For nonlinear problems, the internal force F_{int}, calculated by the first derivative of the potential energy of an atom, is used in place of Ku so that the whole system is decoupled.

Thus, dynamical methods integrate the motion of atoms iteratively. Supposed that the acceleration of an atom in any time step t is expressed as:

$$\ddot{\mathbf{u}}^t = \frac{\mathbf{F}^t_{ext} - \mathbf{F}^t_{int}}{M} \tag{2.21}$$

Beeler $et\ al.$ [20] summarized four different integration schemes. The central difference method [8][21] and Verlet algorithm [19] are widely used in the simulation. In the central difference method, in order to obtain the new position of an atom at time step $t + \Delta t$, the new velocity $\dot{u}$ is calculated as

$$\dot{\mathbf{u}}^{t+\Delta t/2} = \dot{\mathbf{u}}^{t-\Delta t/2} + \ddot{\mathbf{u}}^t \Delta t \tag{2.22}$$

Then, the corresponding displacement u and position x are obtained by

$$\mathbf{u}^{t+\Delta t} = \mathbf{u}^t + \Delta t \dot{\mathbf{u}}^{t+\Delta t/2} \tag{2.23}$$

$$\mathbf{x}^{t+\Delta t} = \mathbf{x}^t + \Delta t \dot{\mathbf{u}}^{t+\Delta t/2} \tag{2.24}$$

In the Verlet algorithm, the new position and velocity at time step $t + \Delta t$ are obtained by two sub-steps to reduce the truncation error.

$$\mathbf{x}^{t+\Delta t} = \mathbf{x}^t + \Delta t \dot{\mathbf{u}}^t + (1/2)\ddot{\mathbf{u}}^t \Delta t^2 \tag{2.25}$$

$$\dot{\mathbf{u}}^{t+\Delta t/2} = \dot{\mathbf{u}}^t + (1/2)\ddot{\mathbf{u}}^t \Delta t \tag{2.26}$$

$$\ddot{\mathbf{u}}^{t+\Delta t} = \frac{\mathbf{F}_{ext}^{t+\Delta t} - \mathbf{F}_{int}^{t+\Delta t}}{M} \tag{2.27}$$

$$\dot{\mathbf{u}}^{t+\Delta t} = \dot{\mathbf{u}}^{t+\Delta t/2} + (1/2)\ddot{\mathbf{u}}^{t+\Delta t}\Delta t \tag{2.28}$$

Both methods above use the explicit operation, in which the information of an advanced time step is all based on current quantities. With the explicit method, the algorithm is very simple and the computer memory is sufficient to handle for a large atomic model. However, in order to stabilize the simulation, the time step should be chosen below some critical values. There are no clear criteria to obtain such critical values so that the time step is normally $10^{-14} - 10^{-15}$ second according to the experience to ensure the convergence. Thus, the total simulation time could be quite long to achieve the equilibrium.

It is known that the time integration for Equation(2.20) would not bring the static solution for atoms. In the equilibrium, atoms oscillate around balanced positions by the harmonic motion. If there is no energy added or removed from the system, the total energy in the system is conserved. Therefore, the positions of atoms with the maximum kinetic energy is the configuration where the potential energy is minimum.

Dynamical methods provide the transient approach to the equilibrium with the physical foundation. They can not only simulate mechanical properties such as the equilibrium positions of atoms, but also model thermodynamic properties of the material at finite temperatures. The desired temperature is obtained by introducing the proper velocity distribution to atoms in the initial state and rescaling velocities

of atoms during the simulation. For example, Equation(2.28) could be replaced by

$$\dot{\mathbf{u}}^{t+\Delta t} = \sqrt{\frac{T_0}{T^t}}\dot{\mathbf{u}}^{t+\Delta t/2} + (1/2)\ddot{\mathbf{u}}^{t+\Delta t}\Delta t \qquad (2.29)$$

where T_0 is the desired temperature and T^t the instantaneous temperature at time t [14].

2.4 Dynamic Relaxation technique

There were couple attempts to obtain static equilibrium configurations by applying the artificial damping to atoms. Gibson *et al.* [21] introduced the method to set zero velocity of atoms each time when the total kinetic energy reaches a maximum value. Evans *et al.* [20] developed an advanced criterion that the velocity of atoms are overwritten to zero whenever the velocity-force dot product becomes negative. Both techniques above dissipate the kinetic energy after atoms enter the equilibrium state with a simple harmonic motion so that the simulation time is in the same level as pure dynamical approaches.

In order to combine the advantages of gradient methods and dynamical methods, which is to quickly obtain the relaxed configuration by the iterative process controlled by classical Newton's laws, the Dynamic Relaxation (DR) technique is selected as a new approach to supply the quasi-static (steady-state) solutions. DR introduces the damping into Equation(2.20) to fast track the new equilibrium positions of atoms. Due to the highly non-linear nature of potential energy functions, e.g. EAM potential, DR with the explicit operator becomes a very good method for the energy minimization because (i) large-scale models involving tens of thousands of degrees of freedom are possible and (ii) the DR method has good records to han-

dle highly non-linear applications (geometry and material) when being coupled with Finite Element Methods (FEMs).

The Dynamic Relaxation technique was first proposed by Day [12] for the solution of partial differential equations by finite difference methods. DR can be efficiently implemented into the FEMs to obtain quasi-static solutions. However, in early applications, e.g. Brew *et al.* [6] or Pica *et al.* [44], the overshoot was a problem in DR methodology because it is not acceptable in nonlinear problems such as elasto-plastic deformation whose responses are path-dependent. Kant *et al.* [29] tried to solve nonlinear structure problems by DR but the overshoot caused its suitability only to small deformation or the linear behavior of materials under loading. Underwood [56] suggested the derivation of the adaptive damping, mass and time step, which leads to the steady-state solution presumably without overshoot. Following his ideas, Sauvé *et al.* [50] derived an algorithm for DR which is applicable to highly nonlinear problems without overshoot and is fully compatible with the explicit Finite Element analysis.

Pan *et al.* [41][42] proposed the modified DR algorithm, which is based on Sauvé *et al.*'s approach, in the energy minimization for atomistic simulations without any external traction. In this approach the motion of atoms is governed by the equation of motion of a regular mechanical system for time t:

$$M\ddot{\mathbf{u}}^t + C\dot{\mathbf{u}}^t + \mathbf{F}_{int}(\mathbf{u}^t) = \mathbf{F}_{ext}^t = 0 \qquad (2.30)$$

Here M is the lumped mass matrix of atoms, C is a damping matrix. In the DR technique, time t usually does not represent the real time but is referred to an iteration (cycle) counter. The revised algorithm is summarized as follows:

(1) The internal forces cannot be obtained by a regular routine from elements. How-

ever, the FS type EAM potential function, i.e. Equation(2.5), is defined for separate atoms. It is a cubic function, so that non-local internal forces at atoms can be easily obtained by the first derivative of the potential energy function. Therefore, internal forces in three coordinate directions ($\alpha = \mathbf{x}, \mathbf{y}, \mathbf{z}$) acting on atom i can be calculated as:

$$
\begin{aligned}
\mathbf{F}^\alpha_{int,i} &= -\left(\frac{\partial U(r_{ij})}{\partial \alpha_i}\right) = -\left[\mathbf{F}^\alpha_{EAM,i} + \mathbf{F}^\alpha_{Pair,i}\right] \\
&= -\frac{1}{2}\left(\sum_j \phi(r_{ij})\right)^{-\frac{1}{2}} \cdot \sum_j \frac{\partial \phi(r_{ij})}{\partial \alpha_i} + \frac{1}{2}\sum_j \frac{\partial V(r_{ij})}{\partial \alpha_i}
\end{aligned}
\tag{2.31}
$$

(2) Since the acceleration and velocity of the system are dissipated to zero at the end by the damping, $\{M\ddot{u}+C\dot{u}\}$ are arbitrary dynamic terms. The masses of atoms could be artificially scaled to make the simulation as fast as possible. The specification of mass M is related to the stiffness K of the system under the DR framework. The previous estimation of the stiffness, which directly derives the second derivative of the potential energy, does not work in the atomistic simulation because there are repulsive and attractive forces existing between atoms. When the attractive force is dominant at one atom, the stiffness could exhibit the negative value, which behaves like a 'negative spring'. In order to get a positive mass, the absolute function is applied to the stiffness value and the mass is calculated as a summation of the absolute values of the stiffness, which is based on *Gerschgorin*'s circle theorem [39]. Under this theorem, the mass of atoms i is approximated by:

$$
m_i \geq \frac{1}{2}\Delta t_{cr}^2 \sum_{j\neq i} |K_{ij}|
\tag{2.32}
$$

where Δt_{cr} is the critical time step and K_{ij} is the stiffness between atoms i and j within

the cut-off radius. In order to save computational efforts, a one-dimensional approach with ignoring the orientation is used to find the stiffness between any pair of atoms. Then the atomistic system is analogous to a structure problem, i.e. like spring-mass or truss. The stiffness of any atom can be obtained by the second derivative of its potential energy. For instance,

$$K_i = \sum_{j \neq i} |K_{ij}| = \sum_{j \neq i} \left| -\frac{d^2 V(r_{ij})}{dr_{ij}^2} \right| \tag{2.33}$$

It is noted that the complicated EAM part calculation is omitted in the stiffness estimation. The stiffness from the EAM part is small and always opposite to the value from the pair part so that the stiffness is enlarged less than 5%, which is safe for the stability in the calculation. The value of mass is customary to be the quarter of the stiffness, that is

$$m_i = \frac{1}{4} \sum_{j \neq i} |K_{ij}| \tag{2.34}$$

And the critical time step Δt_{cr} should be correspondingly scaled back to $\sqrt{2}/2$ to satisfy the inequality(2.32).

(3) Damping is used to control the manner in which the system approaches the equilibrium. Mass proportional critical damping is applied to dissipate the kinetic energy in the system.

$$C = 2\xi \omega M \tag{2.35}$$

Here ξ is the damping ratio and ω is the natural frequency corresponding to the participating mode of loading. Since the mass matrix is lumped and the corresponding damping matrix is diagonal as well, the system is not necessary to factor a full matrix.

In the regular Finite Element analysis, ξ is usually set to 1.0 to apply the critical damping into the system. In the atomistic simulation, the damping ratio

ξ is more than an indicator of the convergence rate. Because damping dissipates the kinetic energy of the system, the results of the relaxation are always obtained at the temperature of absolute zero (0K) when no kinetic energy exists. As shown in Figure(2.4), when applying a lower damping ratio, the system can experience higher kinetic energy prior to reaching the equilibrium so atoms oscillate around point C and have highly opportunity to overpass the point E to move into a new configuration. Finally, atoms could stop at lower minimum energy positions F if existing. This in turn may require more steps to get the convergence. Contrarily, applying a higher damping ratio affects the maximum kinetic energy of the system so that atoms oscillate less between points B and D. Thus, atoms are less likely to jump over point E and could stop at local equilibrium positions C, which is the closest relaxed configuration from the starting configuration A. However, this may converge in a shorter time. By adjusting the damping ratio, different relaxed configurations can be obtained.

The Rayleigh quotient is used to estimate the frequency at cycle t,

$$\omega^t = \left[\frac{(\mathbf{u}^t)^T K \mathbf{u}^t}{(\mathbf{u}^t)^T M \mathbf{u}^t} \right]^{1/2} \tag{2.36}$$

where $\mathbf{u}$, K and M are current displacement vector, tangent stiffness matrix and mass matrix, respectively.

To avoid possible instability during nonlinear calculations, only positive ω is allowable, i.e. $\omega^t = \max(\omega^t, 0)$. The velocity $\dot{u}$ replaces the displacement u as the mode shape in Equation(2.36) to keep non-zero values in the denominator. Thus, ω
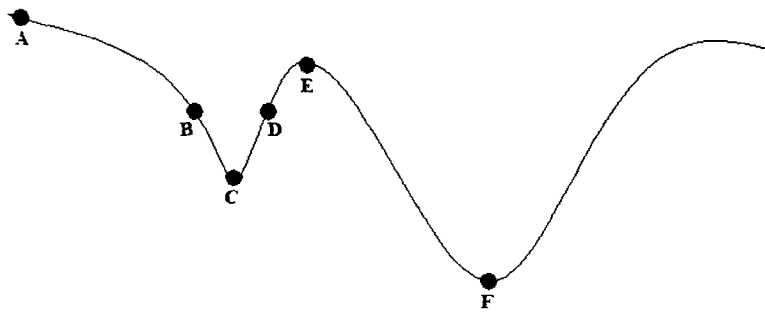
Figure 2.4: The scheme of the energy minimization path by the Dynamic Relaxation technique.

can be written as

$$\omega^t = \left[\frac{(\dot{\mathbf{u}}^{t-\Delta t/2})^T K \dot{\mathbf{u}}^{t-\Delta t/2}}{(\dot{\mathbf{u}}^{t-\Delta t/2})^T M \dot{\mathbf{u}}^{t-\Delta t/2}}\right]^{1/2} = \left[\frac{(\dot{\mathbf{u}}^{t-\Delta t/2})^T K(\mathbf{u}^t - \mathbf{u}^{t-\Delta t/2})/\Delta t}{(\dot{\mathbf{u}}^{t-\Delta t/2})^T M \dot{\mathbf{u}}^{t-\Delta t/2}}\right]^{1/2}$$

$$= \left[\frac{\sum_{i=1}^{3n}(\dot{u}_i^{t-\Delta t/2})[F_{int,i}^t - F_{int,i}^{t-\Delta t}]/\Delta t}{\sum_{i=1}^{3n}(\dot{u}_i^{t-\Delta t/2})^2 m_{ii}}\right]^{1/2} \tag{2.37}$$

With above prediction of the participating frequency ω, in the typical situation of the mass proportional damping as shown in Figure(2.5), the critical damping is applied to the participating frequency ω that tends to begin at a high end of the system. Thus, the lowest participating frequency of the system is overdamped at the current time. With more iterations, the participating frequency ω goes lower as high frequencies gradually damp out. When the lowest participating frequency is critically damped, high frequencies are underdamped but they are already damped out at this moment. Therefore, the solution is below the true response so that the overshoot does not appear.

(4) Combined with Equation(2.22), the governing equation, Equation(2.30), is approximated by [5]

$$M\frac{\dot{\mathbf{x}}^{t+\Delta t/2} - \dot{\mathbf{x}}^{t-\Delta t/2}}{\Delta t} + C\frac{\dot{\mathbf{x}}^{t+\Delta t/2} + \dot{\mathbf{x}}^{t-\Delta t/2}}{2} + \mathbf{F}_{int}^t = 0 \tag{2.38}$$

With Equation(2.35), Equation(2.38) can be written as:

$$\dot{\mathbf{u}}^{t+\Delta t/2} = \frac{1 - \xi\omega\Delta t}{1 + \xi\omega\Delta t}\dot{\mathbf{u}}^{t-\Delta t/2} + \frac{-\Delta t\mathbf{F}_{int}^t}{M(1 + \xi\omega\Delta t)}$$

$$= \frac{1 - \xi\omega\Delta t}{1 + \xi\omega\Delta t}\dot{\mathbf{u}}^{t-\Delta t/2} + \frac{\Delta t}{1 + \xi\omega\Delta t}\ddot{\mathbf{u}}^t \tag{2.39}$$
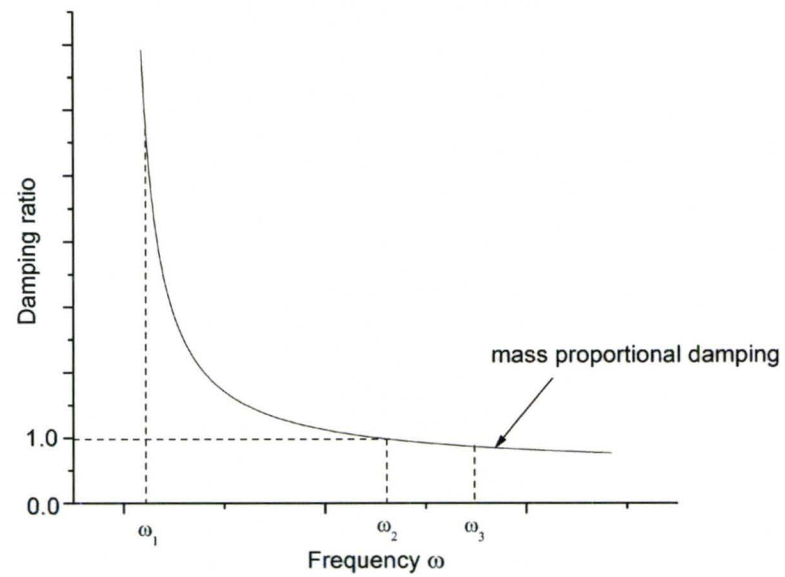
Figure 2.5: Damping ratio versus frequency for the mass proportional damping via Rayleigh quotient. $\omega_3 > \omega_2 > \omega_1$, and ω_1 is the lowest participating frequency for a given system. The participating frequency is dissipated from the high end.

(**5**) Dynamic Relaxation is based on viewing the solution of a static problem as the steady-state solution of a damped dynamic problem. Since external forces have not been applied to the system yet, the structural change is the result from internal forces. Therefore, the steady-state solution for the system implies that

$$\mathbf{F}_{int}^{t} = \mathbf{F}_{ext}^{t} = 0 \tag{2.40}$$

which is achieved when the simulation is finished. Therefore, the dimensionless convergence criterion based on Euclidean norm $\| \ \|_2$ is:

$$\frac{\|\mathbf{F}_{int}^{t}\|_2}{\max\left(\|\mathbf{F}_{int}\|_2\right)} < f_{tol} \tag{2.41}$$

Euclidean norm is a most commonly used function to assign a positive value to all vectors, such as internal forces in this case, in a vector space. Compared to other norms, e.g. uniform norm, Euclidean norm integrates all elements in the vector space so that the value comprehensively represents the size of the space. f_{tol} in inequality(2.41) is the tolerance value, which is set before the simulation.

Chapter 3

Further development of potential energy minimization framework

The further development of the framework lies on (i) the new periodic symmetry method and the corresponding revision of the Dynamic Relaxation algorithm and (ii) the pre-process of the model and the post-process of results from the simulation.

3.1 New periodic symmetry method

The periodic symmetry method is used for the simulation of lattice models with dislocation(s) in the present research in order to reduce overall computational efforts. Current available periodic symmetry technique over-restricts the repeating cell boundaries, and the corresponding periodic length is fixed as a constant value. The new periodic symmetry method is developed to solve the drawbacks of the traditional method and gives more flexible treatments to boundary atoms.

The new method is based on the view of the equilibrium of objects with balanced loadings in the static mechanics. As shown in Figure(3.1), for example, there

is a rod with opposite forces F applied on both ends. If the rod is randomly divided into three portions, the corresponding internal traction, whose magnitude is F as well, balance themselves or external applied forces on every portion. Thus, three portions could be analyzed independently to obtain the same results compared to the bulk calculation if the stress on the intersection plane is evenly distributed. Such an idea can be extended to more general periodic or repeating structures with proper kinematic constraints on repeating boundaries to save considerable computational time and efforts in the simulation.

The primitive cell in the atomistic simulation, which is surrounded by an infinite number of image cells with exactly the same structure and defects, is assumed to be a minimum unit to represent the feature of the material model. For example, as shown in Figure(3.2), there is an atomic model with the pattern of vacancies and applied forces at each end. Then the minimum unit as the primitive cell is 6×6 atoms with two holes. In terms of the equilibrium, internal traction F' is equal to the external force F. However, due to the nature of the atomic structure and defects in the model, the stress is not evenly distributed on the boundaries of the unit cell so that certain kinematic constraints need be applied to boundary atoms in the primitive cell to ensure the compatible deformation at the boundaries, which is under the assumption that the model maintains its periodicity after the relaxation.

Based on the scheme proposed by Metzger [34], the model of one line of atoms is used to explain the scheme of the new method of the periodic symmetry. In Figure(3.3), the primitive cell is from boundary atom i to boundary atom i' and the corresponding periodic length is c. The cut-off radius is supposed to extend to the one nearest neighbor in this case. Therefore, in the traditional method, atom i (or atom i') should interact with two atoms, one of which is the image atom (white circle in Figure[3.3(a)]). In the new method as shown in Figure[3.3(b)], forces on boundary
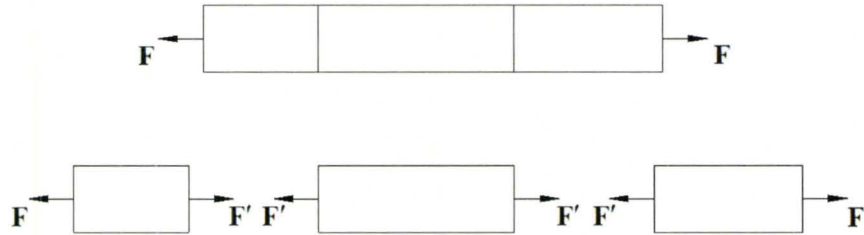
Figure 3.1: The scheme of the equilibrium according to the static mechanics.
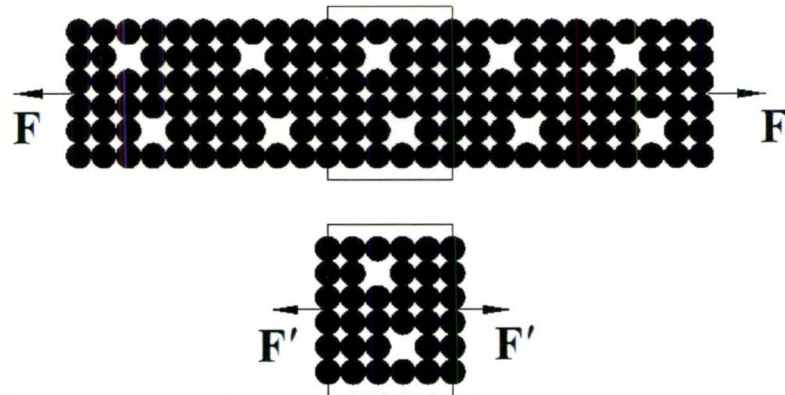
Figure 3.2: The scheme of the equilibrium in the atomic model.
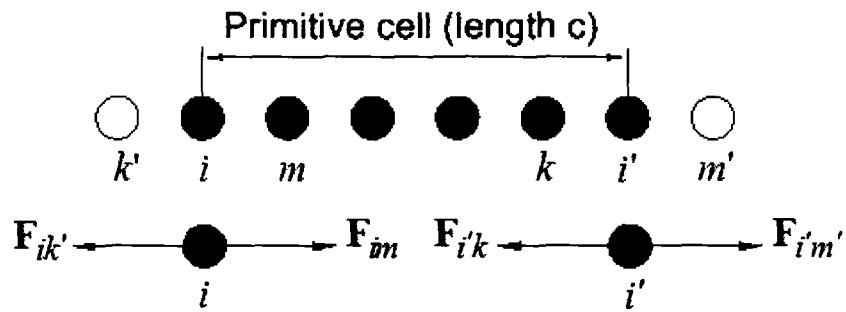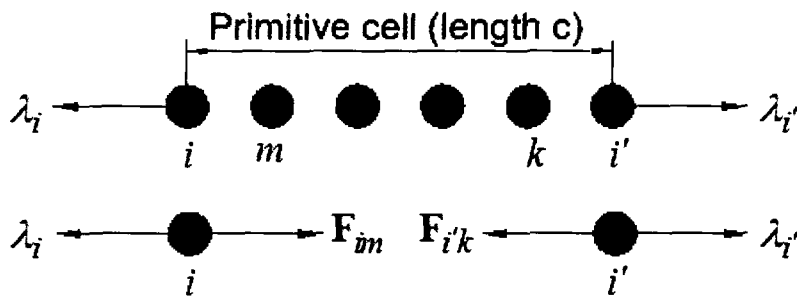
Figure 3.3: The scheme of the force equilibrium on boundary atoms. (a) The traditional method; (b) The new approach.

node i and its image i' are found without regard for any symmetry, which is the same as 'tied nodes' method. However, the boundary force or external traction λ_i is used in place of the interaction between boundary atoms and image atoms, which gives resultant forces $\mathbf{F}^R$ on atoms i and i',

$$\mathbf{F}_i^R = \mathbf{F}_i + \lambda_i \tag{3.1}$$

$$\mathbf{F}_{i'}^R = \mathbf{F}_{i'} + \lambda_{i'} \tag{3.2}$$

where $\mathbf{F}_i$ and $\mathbf{F}_{i'}$ are the net internal force within the primitive cell. Since the new method does not require (i) the periodic length to be a constant value during the simulation, and (ii) the physical pair of boundary atoms i and i' has identical motion, the acceleration of these two boundary atoms are related by:

$$\ddot{\mathbf{u}}_i - \ddot{\mathbf{u}}_{i'} = \ddot{c} \tag{3.3}$$

Therefore, according to the equation $F = ma$, combined with Equations(3.1) and (3.2), Equation(3.3) is re-written as:

$$\frac{\mathbf{F}_i^R}{m_i} - \frac{\mathbf{F}_{i'}^R}{m_i} = \frac{\mathbf{F}_i + \lambda_i}{m_i} - \frac{\mathbf{F}_{i'} + \lambda_{i'}}{m_{i'}} = \ddot{c} \tag{3.4}$$

And, the boundary forces have the same magnitude but opposite directions in order to be compatible between the periodic boundaries, i.e.

$$\lambda_i = -\lambda_{i'} \tag{3.5}$$

By inserting Equation(3.5) into Equation(3.4), the external traction λ_i could be ob-

tained as follows:

$$\lambda_i = -\lambda_{i'} = \left(\frac{m_i m_{i'}}{m_i + m_{i'}}\right)\left[\ddot{c} - \left(\frac{\mathbf{F}_i m_{i'} - \mathbf{F}_{i'} m_i}{m_i m_{i'}}\right)\right] \qquad (3.6)$$

When the acceleration of the periodic length c is set to zero, Equation(3.6) becomes

$$\lambda_i = -\lambda_{i'} = -\frac{\mathbf{F}_i m_{i'} - \mathbf{F}_{i'} m_i}{m_i + m_{i'}} \qquad (3.7)$$

Equation(3.7) reveals how much external traction is needed in every cycle to be applied on boundary atoms to keep the periodic length constant during the simulation. Therefore, results of the relaxation based on Equation(3.7) should be in agreement with results from the traditional method and 'tied nodes' method.

Supposed that the mass of individual atoms in the system is a unique value, Equation(3.7) could be further simplified as:

$$\lambda_i = -\lambda_{i'} = -\frac{\mathbf{F}_i - \mathbf{F}_{i'}}{2} \qquad (3.8)$$

Then, combined with Equation(3.8) and Equation(3.4),

$$\frac{\mathbf{F}_i^R}{m_i} - \frac{\mathbf{F}_{i'}^R}{m_i} = \frac{\mathbf{F}_i + \mathbf{F}_{i'}}{2m_i} - \frac{\mathbf{F}_{i'} + \mathbf{F}_i}{2m_{i'}} = \ddot{c} \qquad (3.9)$$

Apparently, the acceleration of boundary atoms in the new method is half of it in the traditional method. Though the change would not affect the final result, it is customary to cut the masses of boundary atoms into half value in order to obtain the same path of the relaxation as the traditional method when $\ddot{c} = 0$ is used in the new method.

In order to prove the suitability of the new method, a model with 7 atoms in a

row with randomly different spacing is examined so that the relaxation proceeds under the periodic symmetry. The initial positions and spacing between adjacent atoms are shown in Figure[3.4(a)] and Table(3.1). The movements of atoms are restricted to the horizontal direction. Two methods, the traditional method and the new method with $\ddot{c} = 0$, are both applied to the model. The potential energy function is chosen as simple Lenard-Jones pair potential, and the tolerance to terminate the simulation is that the total net force value is less than 0.001. The results are demonstrated in Figures[3.4(b)], [3.4(c)] and Table(3.1). It is noted that the external traction is only applied to the boundary atoms in the new method. Displacements of other atoms within the primitive cell are calculated in the same way as in the traditional method.

From Figure(3.4) and Table(3.1), the new method is proved to be effective for applying the periodic symmetry to the atomic model because both methods converge to the state that the distances between adjacent atoms are equal. The periodic length is not changed as it in the case with the traditional method. The system momentum is balanced by both methods since the external traction (reactions) is in the equilibrium state. The position of Center of Gravity (CG) R of the model is calculated as a discretized particle system, which is

$$R = \frac{1}{M} \sum_{i=1}^{7} m_i r_i \tag{3.10}$$

where M is the sum of particle masses, m_i is the mass of individual atoms, and r_i is the distance to the reference point as zero in this case. With the same mass of inner atoms and half mass of two boundary atoms in the initial model, the position of CG is 2.15. As the positions of atoms after the relaxation, the position of CG is unchanged from both methods. Thus, the apparent rigid motion is due to the relative motion of the boundaries not the movement of the Center of Gravity in the model.
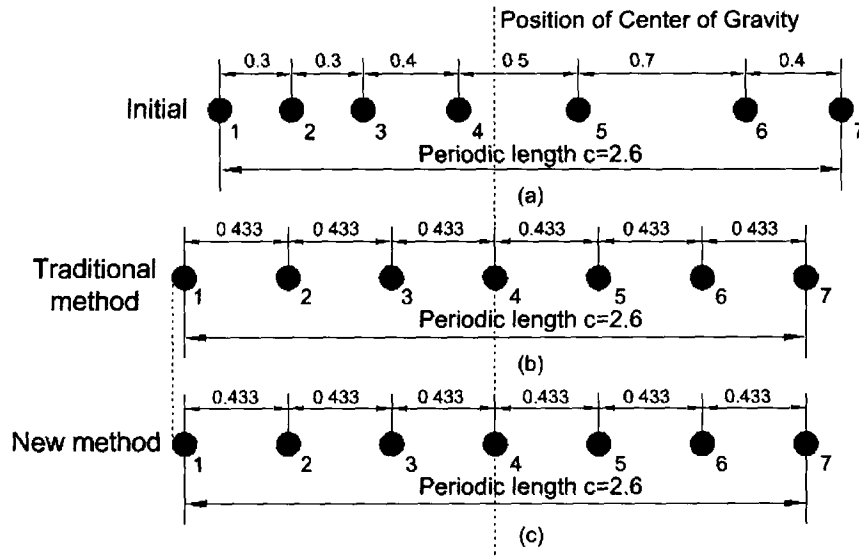
Figure 3.4: The model of one line of atoms. (a) The initial configuration; (b) The new equilibrium configuration after the relaxation by the traditional periodic symmetry method; (c) The new equilibrium configuration after the relaxation by the new periodic symmetry method.

Table 3.1: The positions of atoms in one-dimensional model before and after the relaxation by the traditional periodic symmetry method and the new method.

Atoms	Initial positions	Final positions- the traditional method	Final positions- the new method
x(1)	1.0	0.85	0.85
x(2)	1.3	1.283	1.283
x(3)	1.6	1.717	1.717
x(4)	2.0	2.15	2.15
x(5)	2.5	2.583	2.583
x(6)	3.2	3.017	3.017
x(7)	3.6	3.45	3.45

41

Therefore, the new method not only includes the features of the traditional method, but also provides a way of applying the external traction to the model when $\ddot{c}$ is not equal to zero.

Rather than the model of one row atoms, with more layers of atoms, the external traction need be decomposed into a series of forces applied on every pair of boundary atoms to maintain the periodicity. A two-dimensional model is used to demonstrate the details of external traction distributions, as shown in Figure(3.5), in which a pair of tensile forces $\mathbf{T}$ with the corresponding periodic symmetry is applied in the X direction of the model while free boundary condition is used in the Y direction. In the X direction, the shape of the boundary is random but the periodic length of every row of atoms is unique. For every pair of boundary atoms, the external traction is distributed as different λ values. However, the sum of λs should be equal to $\mathbf{T}$, which is

$$\sum_{i=1}^{n}(-\lambda_i) = \sum_{i=1}^{n}\lambda_{i'} = \mathbf{T} \qquad (3.11)$$

where the positive sign of $\mathbf{T}$ is customary to point to the right. Based on Equation(3.6), after substituting Equation(3.11), it is obtained

$$\sum_{\substack{i=1 \\ i=i'}}^{n}\left\{\left(\frac{m_i m_{i'}}{m_i + m_{i'}}\right)\left[\ddot{c} - \frac{\mathbf{F}_i m_{i'} - \mathbf{F}_{i'} m_i}{m_i m_{i'}}\right]\right\} = \mathbf{T} \qquad (3.12)$$

There are two unknowns in Equation(3.12), $\mathbf{T}$ and $\ddot{c}$. One of these must be specified before the simulation starts so that the other unknown could be calculated. $\mathbf{T}$ or $\ddot{c}$ could change every cycle step to adapt to the change of internal forces until convergence.

Two examples using a two-dimensional cubic configuration of atoms are used to illustrate the application of the new method for the periodic symmetry. The first
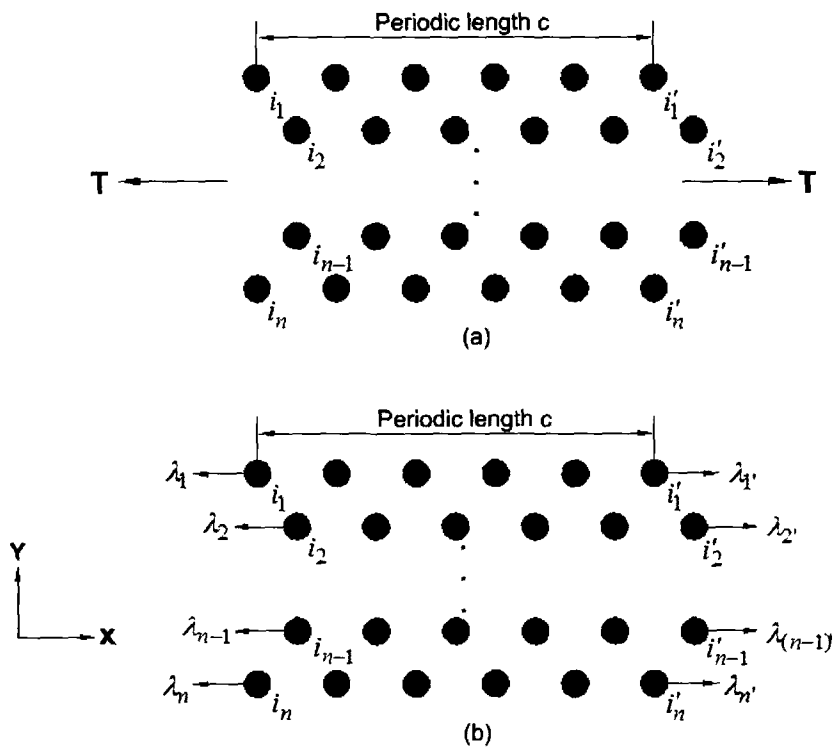
Figure 3.5: A two-dimensional model with the external traction applied in the X direction. (a) Total force; (b) Force components.

example applies the periodic symmetry to the rectangular atomic model with even spacing in the columns as shown in Figure(3.6). The numerical parameters are set as follows:

(a) The periodic length is initially set to 4.0-arbitrary-units.

(b) Simple Lennard-Jones pair potential is used.

(c) A pair of tensile traction, which is 0.0-arbitrary-units, 4.0-arbitrary-units and −4.0-arbitrary-units respectively, is applied to the boundary in the X direction of the model with the new periodic symmetry while free boundary condition is used in the Y direction.

(d) Cut-off radius is 1.6, which is set to cover one nearest neighbor.

(e) Damping ratio is 1.0

(f) Tolerance value as the total net force is 0.001

The new equilibrium configurations calculated by the new method are shown from Figure[3.6(b)] to Figure[3.6(d)]. Since atoms are not under the equilibrium in the initial configuration, when zero external traction is applied, atoms have opportunity to adjust their positions until net resultant forces are zero so that the periodic length is extended to 4.437-arbitrary-units. According to this value as a reference length, when tension or compression is applied on the boundary atoms, the periodic length in all rows becomes 4.531-arbitrary-units and 4.372-arbitrary-units, respectively. Because the repulsive force is stronger than the attractive force derived from the potential energy function, the deviation from the reference periodic length is not the same as the same amount of tension or compression is applied. Thus, all the numerical responses are in agreement with expectations.
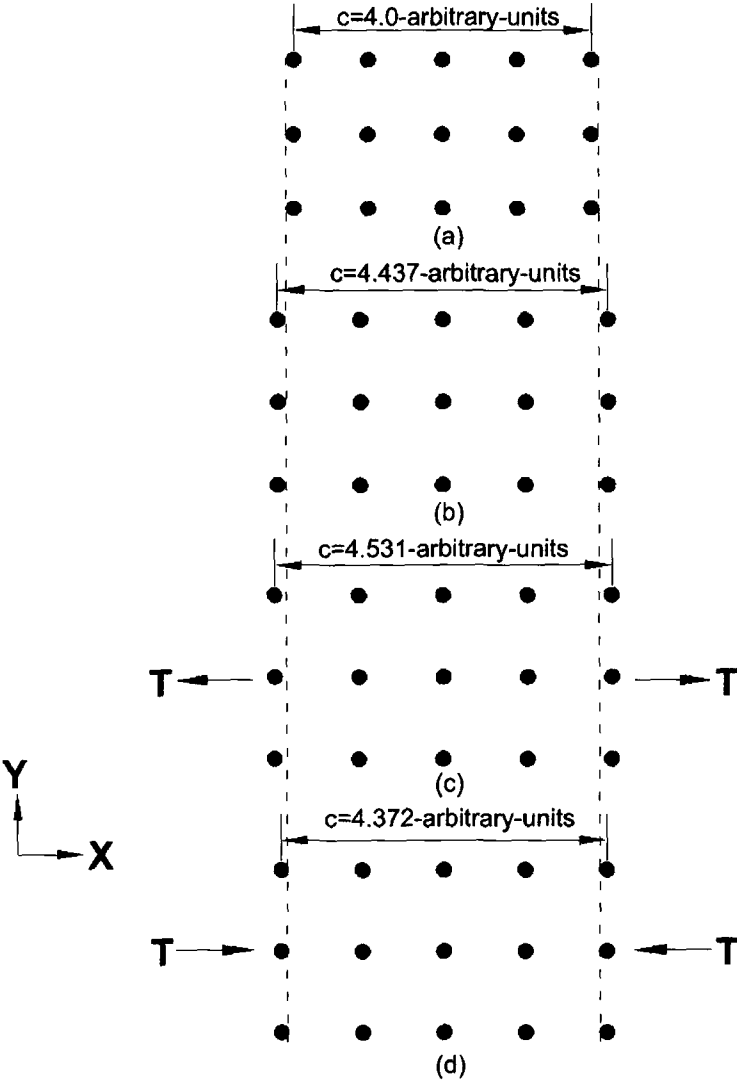
Figure 3.6: A two-dimensional rectangular model with the new periodic symmetry applied in the X direction. (a) The initial configuration; (b) The equilibrium configuration after applying zero external traction; (c) The equilibrium configuration after applying 4.0-arbitrary-units external tension; (d) The equilibrium configuration after applying −4.0-arbitrary-units external compression.

As discussed in the previous work [41], a rectangular or cubic assembly of atoms in a two-dimensional model is a local minimum potential energy configuration with certain spacing. Therefore, after applying the new periodic symmetry with corresponding external traction in the X direction, the spacing between atoms is equally increased and the unique periodic length is maintained during the simulation. However, the configuration with lower minimum potential energy (i.e. closed-packed configuration) is not achieved.

Another example is that the periodic symmetry is applied to the parallelogram atomic model with even distance between adjacent atoms in X and Y directions shown in Figure[3.7(a)]. The periodic length and the numerical parameters for the simulation are the same as in the previous example. Two approaches of the periodic symmetry are applied in the X direction. Figures[3.7(b)], [3.7(c)] and [3.7(d)] show the results of respective equilibrium configurations by applying $\ddot{c} = 0$ as the traditional method, 4.0-arbitrary-units tension, and -4.0-arbitrary-units compression based on Equation(3.12).

The parallelogram model is another kind of minimum potential energy configuration since it could generate closed-packed arrangements of atoms. It was proved that the minimum potential energy value of the model is dependent on the angle θ and spacing r between atoms [41]. With four-atom parallelogram model, the angle θ is 29.7°. If the traditional method as $\ddot{c} = 0$ is used, the relaxation in the X direction would not happen since the even spacing is already achieved between atoms, which is shown in Figure[3.7(b)]. In the Figure[3.7(c)], when the tension is applied in the X direction, it is found that the angle θ of the parallelogram model is changed from original 45.0° to 30.7° while the periodic length is stretched to 4.614-arbitrary-units. In the Figure[3.7(d)], when the compression is applied in the X direction, the angle θ of the model is shrunken to 29.4° while the periodic length is changed to 4.412-
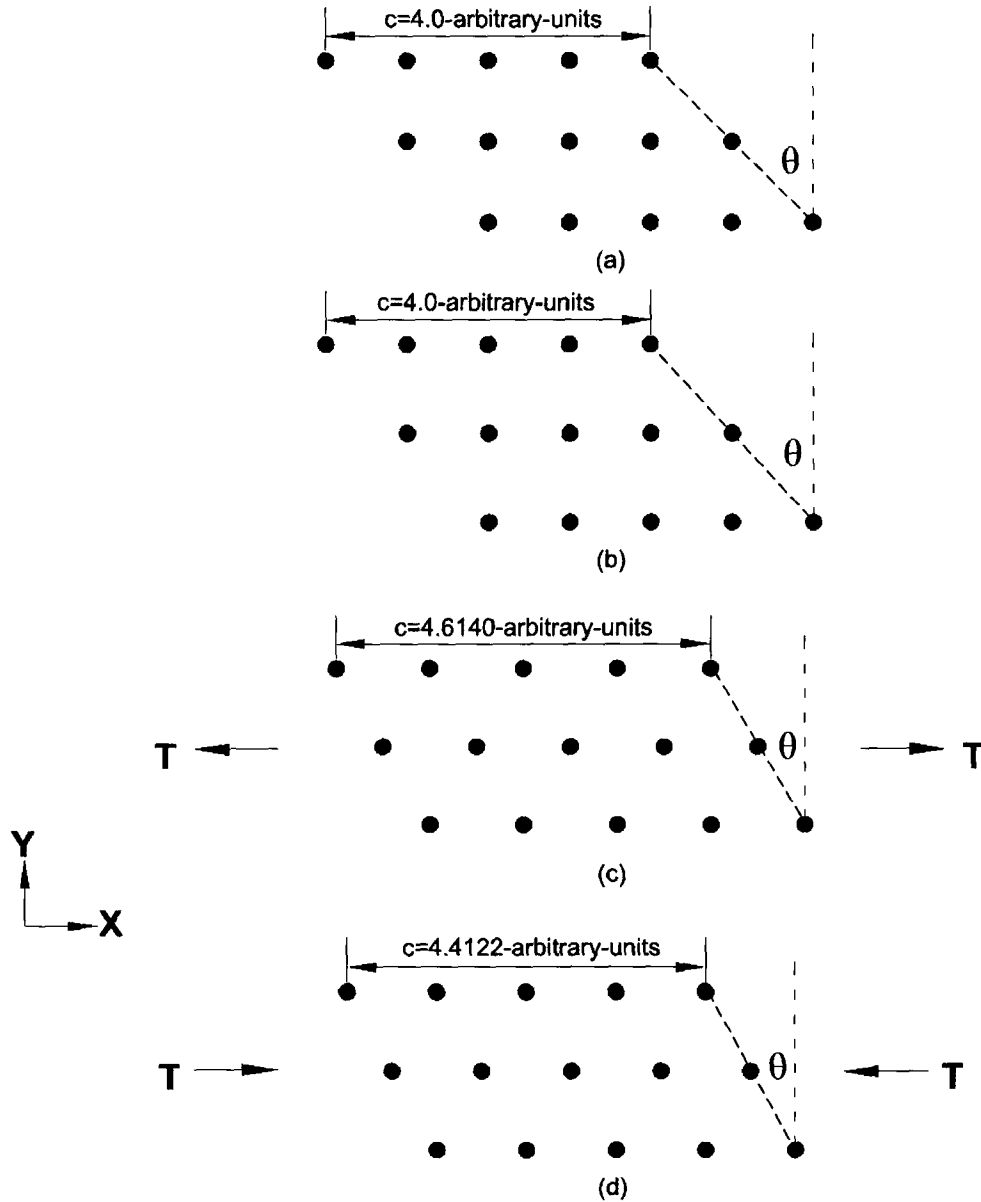
Figure 3.7: A two-dimensional parallelogram model with the periodic symmetry applied in the X direction. (a) The initial configuration; (b) The equilibrium configuration after applying $\ddot{c}_x = 0$; (c) The equilibrium configuration after applying 4.0-arbitrary-units external tension; (d) The equilibrium configuration after applying -4.0-arbitrary-units external compression.

arbitrary-units. The angle θ in the latter two cases both converges to approximate 30°, which means that the new method allowing for applying the external traction does not prevent the model from relaxing to the configuration with lower potential energy compared to the traditional method. However, just like other boundary conditions, the new method causes the relaxation to be in the restrictive way, i.e. the relaxation must be compatible to boundary conditions.

Compared with the traditional method, the new method overcomes the over-restrictive constraint within the repeating cell boundaries and in the meantime keeps the periodicity of the model so that it supplies a flexible treatment for the periodic symmetry and is suitable for broad cases in atomistic simulations especially when the external traction is applied. The new method could be used fully in place of the traditional method when $\ddot{c} = 0$. However, the traditional method, with advantages of being straightforward and easily implemented, could still be the choice for cases that the change of atomic structures is dominated by internal forces. The new method needs computational efforts to search for the pairs of boundary atoms, but this could be offset by the need to calculate fewer pairs of internal forces for the boundary atoms. Therefore, the computational burden of the new method is about the same level as the traditional method in the simulation.

3.2 Force evaluation

In the previous work [41], the motion of atoms is mainly driven by internal forces from internal defects and the traditional periodic symmetry. When the new method of the periodic symmetry is implemented to a real dislocation model such as the face-centered-cubic (f.c.c.) lattice, the external traction is actually applied on boundary atoms with a 'zig-zag' boundary shape. When the equilibrium state is reached,

the forces acting along one coordinate direction α, e.g. dislocation line, should be balanced such that

$$\mathbf{F}_{int}^{EAM,\alpha} + \mathbf{F}_{int}^{pair,\alpha} + \lambda = 0 \qquad (3.13)$$

where λ is the net external traction. According to Equation(2.31), here:

$$\mathbf{F}_{int}^{EAM,\alpha} = -\frac{1}{2}\left[\sum_{j}\phi(r_{ij})\right]^{-\frac{1}{2}} \cdot \sum_{j}\frac{\partial\phi(r_{ij})}{\partial\alpha} \qquad (3.14)$$

and

$$\mathbf{F}_{int}^{pair,\alpha} = \frac{1}{2}\sum_{j}\frac{\partial V(r_{ij})}{\partial\alpha} \qquad (3.15)$$

Since the dislocation is a two-dimensional defect, the lattice is always perfect along the third dimension, i.e. dislocation line. Therefore, as shown in Figure[3.8(a)], if the periodic length is kept constant, there is no relative displacement within rows, such as $j - j'$ or $i - i'$ but the displacement between rows is allowed. If the external traction is applied, the spacing between atoms in one row is equally increased or decreased. However, in the current perfect configuration as the periodic length is fixed, for example, boundary atom i interacts with more neighboring atoms than its image i' so that the value of coefficient $[\sum_{j}\phi(r_{ij})]^{-1/2}$ in Equation(3.14) is not identical for the pair of boundary atoms. This in turn generates the problem that the resultant internal forces in the perfect lattice, which could be calculated by assembling internal forces from the atom and its image, are not equal to zero so that the ideal perfect f.c.c configuration is not maintained. As a result due to the large error, the relaxation of a dislocation would not equilibrate at correct positions under above assumptions. In order to make $[\sum_{j}\phi(r_{ij})]^{-1/2}$ a common coefficient in the force calculation, the traditional method of applying the periodic symmetry is used to determine $\phi(r_{ij})$ in EAM part. The remaining terms in Equations(3.14) and (3.15) follow the new

approach of the periodic symmetry.

Based on Equation(3.12), the new method of the periodic symmetry exchanges the internal forces of the pair of boundary atoms to determine the external traction, which is in place of the interaction between the primitive cell and image cells. As shown in Figures[3.8(a)] and [3.8(b)], for a boundary atom i in the perfect f.c.c. lattice, there should be six neighboring atoms around it, one of which is an image atom. When atoms i and i' exchange their internal forces, atom i' brings three interactions to atom i, however, two of which are already counted by atom i such as links between i and j, and its image i' and j'. Double calculation of the interaction between two boundary atoms causes incorrect determination of the external traction. The current solution is to record the information of the interaction between boundary atoms. If one link has been generated, the corresponding image link would be excluded.

When the new periodic symmetry is applied to the dislocation model along the dislocation line and slip directions, it is more challenging to collect correct internal forces of boundary atoms. As shown in Figure[3.9(a)], atoms A, B, C and D are the boundary atoms at the corner of the model in the XZ plane. According to atom A, atom B is its image atom in the Z direction and atom C is its image atom in the X direction as well. When the periodic symmetry is applied in the X or Z direction, atom D has no relationship with atom A. However, if the periodic symmetry is applied in the XZ plane, atom D becomes one of atom A's images. In the case that the periodic length is not allowed to change, i.e. $\ddot{c} = 0$ in both X and Z directions, the forces applied to atom A and all of its images B, C and D should be identical so that the motion of these atoms are the same providing that the mass of atom is unique.

The general external traction in the 2D plane, such as XZ plane shown in Figure[3.9(a)], is normally decomposed into two components along X and Z directions so that corresponding internal forces should have two components. In any direction,
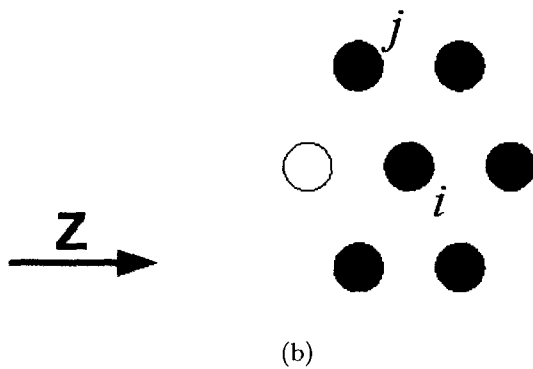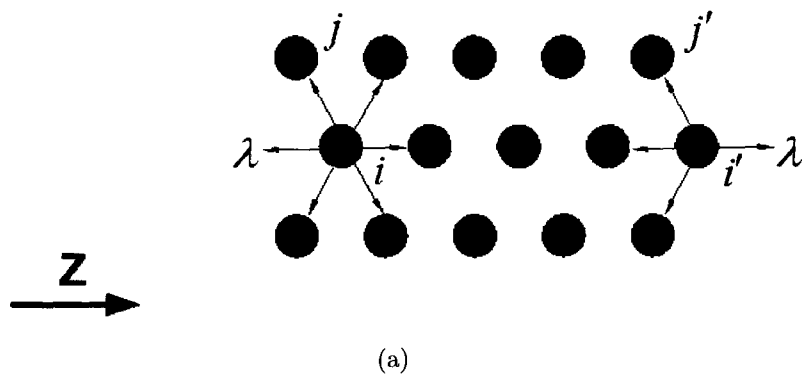
Figure 3.8: The scheme of the perfect configuration in one direction in the face-centered-cubic lattice. (a) The full geometry; (b) The detail of one boundary atom (white cycle is an image atom).
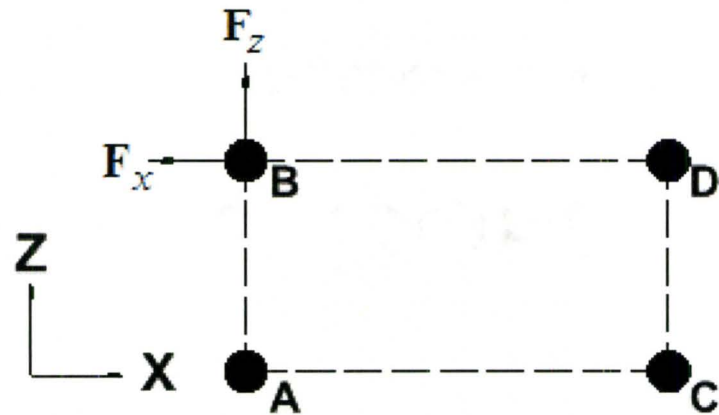
(a)
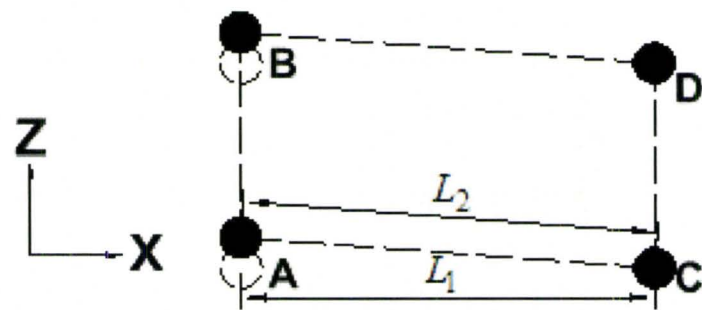
(b)

Figure 3.9: The scheme of atoms at the corner of the XZ plane (a) in the perfect lattice; (b) in the lattice with a screw dislocation.

the new method of the periodic symmetry is implemented by Equation(3.12).

In order to apply the external traction on boundary atoms in the model, the initial periodic length is used to search for the pairs of boundary atoms, which is under the assumption that the periodic length is equal to the direct distance between one boundary atom and its corresponding image (the pair). The periodic length along the direction of the dislocation line is not changed after a dislocation is introduced into the model so that the search algorithm of the pairs of boundary atoms is successful in simple cases that the periodic symmetry is applied along the dislocation line. However, such assumption is not valid in the direction other than the dislocation line. As shown in Figure[3.9(b)], the known periodic length L_1 is not equal to the distance L_2 between atoms A and C when a screw dislocation is initially generated in the model (A, B, C and D represent atoms at the corner of any XZ plane). Therefore, the old search algorithm generates unacceptable errors in finding the incorrect positions of boundary atoms, which results in errors of internal forces. The current solution is to build a boundary-atom list from a perfect lattice under the original search algorithm. Then the external traction is applied to the pairs of boundary atoms based on the list rather than their present positions. Thus, the lattice creator software used in the current framework need supply the perfect lattice and the corresponding defective lattice with the same number of atoms.

3.3   Mass scaling

From the original DR algorithm as stated in Section(2.4), mass is proportional to the stiffness of an atom. On the one side, due to the highly non-linear nature of potential energy functions, the stiffness and the corresponding mass changes faster than general structural problems; On the other side, the stiffness and mass from

the EAM potential is related to the number of neighboring atoms. For example, boundary atoms have less mass than inner atoms because of the lack of neighboring atoms. Though the non-identical mass can be handled under the framework of the new method of applying the periodic symmetry and the external traction, it may adversely affect the progress of solutions in certain circumstances.

Therefore, an alternative approach is to use fixed mass value for every atom in the system during the simulation. The mass for every atom is obtained by inequality(2.32), and then this value is kept constant throughout the simulation. Such an idea could be further extended to the unique mass scheme. Considering the complexity of the dislocation model, the mass is chosen as a possible largest value in the system and determined as follows:

(i) The new periodic symmetry is usually applied to one or two coordinate direction(s). In order to make an identical mass in three directions, the value is obtained based on inequality(2.32) and the traditional periodic symmetry approach;

(ii) The maximum mass value is chosen in the first cycle as the unique mass;

(iii) The mass of every atom in three directions is set to the unique mass and kept constant during the simulation.

With the system approaching the equilibrium, the trend of the stiffness and mass is going down. Therefore, the above unique mass scheme ensures that the responded natural frequency must be lower than the maximum frequency so that the whole process of the simulation is stable.

When the unique mass is used, the critical time step is changed by every time

step.

$$\Delta t_{cr} = \delta \frac{2}{\omega_{max}} \tag{3.16}$$

Here,

$$\omega_{max} = \max\left(\sqrt{\frac{K_i}{m_i}}\right), i = 1, \cdots, n \tag{3.17}$$

where K_i and m_i is the stiffness and mass in every degree of freedom and δ is a coefficient to scale back the critical time step to satisfy inequality(2.32). Normally, $\delta = 0.5 \sim 0.7$ is safe enough to stabilize the simulation.

3.4 Convergence criterion

After the external constant traction is applied to boundary atoms, all changes in the structure of the model are the result of the integration of internal forces and externally applied traction. According to Equation(3.13), the steady-state solution for any boundary atom becomes

$$\mathbf{F}_{int,i}^{net} = \mathbf{F}_{ext,i} = \lambda_i \tag{3.18}$$

This is achieved when the simulation is finished.

When atoms find equilibrium positions, the summation of net force vectors equals zero. Therefore, the convergence criterion is extended to include the external traction from inequality(2.41):

$$\frac{\left\|\mathbf{F}_{int,i}^t - \lambda_i\right\|_2}{\max\left(\left\|\mathbf{F}_{int,i} - \lambda_i\right\|_2\right)} < f_{tol} \tag{3.19}$$

Generally, when damping is applied to the system, the unbalanced force in the first cycle is the largest one. Therefore, the maximum value $\left\|\mathbf{F}_{int,i} - \lambda_i\right\|_2$ in inequality(3.19)

is normally obtained after the first iterative step. For non-boundary atoms and in directions without the periodic symmetry, λ_i is set to zero.

For the general case, in order to balance the efficiency and the accuracy of the simulation, f_{tol} is set up as 0.001, which means the simulation would be terminated when the total net force acting on atoms is below 0.1% of its maximum value. However, in some cases, if the maximum net force in the system is already very small, the tolerance threshold could be properly increased.

3.5 Some pre-process and post-process techniques

3.5.1 Verlet list

Due to the existence of the cut-off radius in potential energy functions, every single atom has its own neighboring atoms to interact with. Such neighboring-atom list for individual atoms needs to be updated every cycle or several cycles because of the movements of atoms during the relaxation. The computational time for searching neighboring atoms is increased, which is proportional to the square of the total number of atoms in the system N^2. The speed is acceptable when the system consists of several hundreds of atoms. However, the relaxation process becomes very slow when the model with hundreds of thousand atoms is used, in which above 90% CPU time is for updating the neighboring-atom list.

During the relaxation, atoms would not move far from their initial positions so that the Verlet circle or Verlet sphere [19] in a three dimensional model is introduced to reduce the computational burden. As shown in Figure(3.10), beyond the cut-off radius r_c, a new Verlet radius r_v is setup for individual atoms. In the simulation, the neighboring-atom list is generated based on the Verlet radius in the first iterative
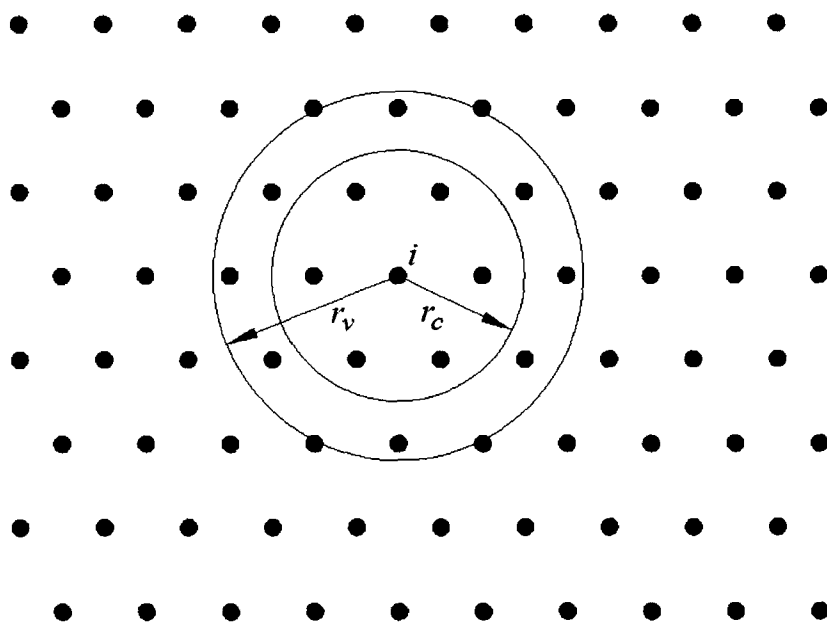
Figure 3.10: An atom i in a two dimensional face-centered-cubic model interacts with neighboring atoms within the cut-off radius r_c while the Verlet list contains all atoms within the radius r_v.

cycle. Starting from the second cycle, atoms search for their interactions within the cut-off radius from neighboring-atom list so that the computational time increases linearly as total number of atoms increases. If the displacement of an atom at any iterative cycle from its reference position is larger than the difference between the cut-off radius and the Verlet radius, such as

$$\left|\mathbf{x}_i^t - \mathbf{x}_{i,ref}\right| > \left|r_v - r_c\right|, \tag{3.20}$$

the neighboring-atom list need be updated and the reference atomic positions are changed to the current configuration.

There is no specific criterion to determine the value of the Verlet radius. If the radius is too small, updating neighboring-atom list becomes frequent so that the technique is not effective. If the radius is too large, the computational time is wasted to exclude the atoms between r_c and r_v in every cycle. Therefore, according to the experience, the Verlet radius r_v is chosen as $1.5v_c$. In the most of cases demonstrated in later chapters, the neighboring-atom list is generated in the first cycle and not updated any more during the simulation.

3.5.2   Stress of atoms

Unlike nodes in the Finite Element analysis, the stresses of atoms could not be obtained by interpolating the continuum stress field in elements, or by a specific constitutive stress-strain relationship. Currently, as developed by Machová [32], the stress components of individual atoms are calculated as the local volume stress assuming that an unstressed atom has the shape of a sphere. Based on the FS type EAM

potential scheme, i.e. Equations(2.5) and (2.7).

$$\sigma_{\alpha\beta}(i) = \frac{F_i \sum_j \varphi_\alpha(i,j) r_\beta(i,j) + \frac{1}{2} \sum_j v_\alpha(i,j) r_\beta(i,j)}{w(i)} \tag{3.21}$$

where

$$F_i = \frac{df}{d\rho_i}, \ as \ f = -\sqrt{\rho_i} \tag{3.22}$$

$$\varphi_\alpha = \frac{d\phi}{dr_\alpha} \tag{3.23}$$

$$v_\alpha = \frac{dV}{dr_\alpha} \tag{3.24}$$

$$w(i) = \frac{4}{3}\pi R^3, \ as \ R = \frac{\sqrt{2}a_0}{4} \ in \ f.c.c \ lattices. \tag{3.25}$$

Here a_0 is the lattice constant, and α and β are indices representing coordinate directions **x**, **y** and **z** respectively so that nine-components stress tensor is obtained by different combinations of α and β.

Rather than checking the maximum stress value, the interest in the atomistic simulation of the stress field is focused on the area of tension or compression when defects are introduced into the model. Therefore, the raw stress data are sorted, ranked and normalized into ten groups from minimum 1.0 to maximum 10.0. The rule of distributing stress is shown in Table(3.2). The 3% highest stress from the top is assigned to number 10.0 while the 3% lowest stress from the bottom is given value 1.0. The stress values of boundary atoms are expected to be inaccurate due to boundary conditions. Thus, their original stress components are overwritten to zero in the ranking process. Such manipulation does not alter the stress distribution in the dislocation core since boundary atoms are far from the positions of dislocations.

The normalized stress values are then imported into the visualization software

Rasmol [51]. In the software, red color represents the highest stress group while blue color is for lowest stress values. For example, for a single edge dislocation model, due to the existence of an extra half plane in the upper half of the model, there is the compression in the upper half of the model and the tension correspondingly is in the lower half of the model along the X direction. The contour of σ_{xx}, which is plotted in Figure[3.11(a)] [24], demonstrates the compression and tension are symmetrical. As shown in Figure[3.11(b)], the local volume stress and the normalized technique reproduce the same shape of the contour of σ_{xx}, where red color is the highest stress area (tension) and blue color represents lowest stressed atoms (compression) based on their values. It is noted that blue color in this case represents negative stress values, and the green color is for atoms with approximately zero stress (stress free).

3.5.3   Position of defects (dislocations)

It is very difficult to determine the exact positions of the dislocation(s) or other types of defects during the process of the relaxation. However, locating the positions of dislocations is crucial to understand the mechanism of the formation or organization of certain defective configurations. In current simulations, the potential energy is used to approximately indicate where dislocations are, since the potential energy increases abruptly where the lattice distorts most.

Unlike the treatment of stress components, the raw potential energy value for individual atoms need not be normalized in order to obtain the point of the highest potential energy. To reduce the adverse effect of boundary atoms with fewer neighboring atoms, the potential energy values of boundary atoms are overwritten to the lowest value in the system.

The series of potential energy values is introduced into Rasmol [51]. Red and

Table 3.2: The rule of the normalization of stress values and the corresponding ranges of the distribution.

Distribution range (from the bottom)	Normalized value
[0%,3%]	1.0
(3%,13%]	2.0
(13%,23%]	3.0
(23%,33%]	4.0
(33%,43%]	5.0
(43%,53%]	6.0
(53%,77%]	7.0
(77%,87%]	8.0
(87%,97%]	9.0
(97%,100%]	10.0

(a)

(b)
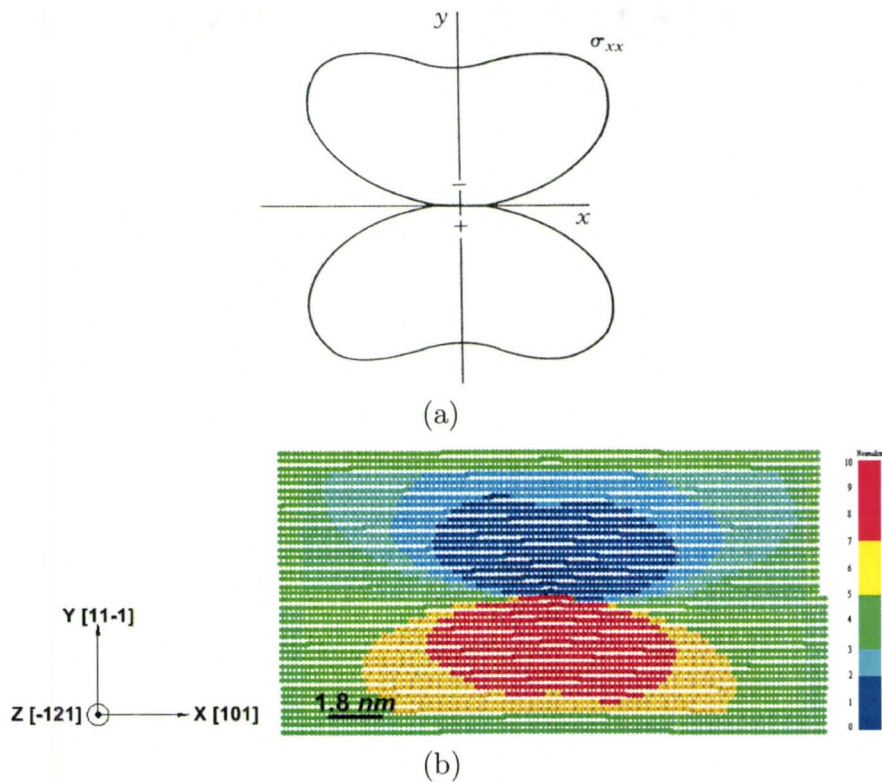
Figure 3.11: The contours of stress component σ_{xx} around an edge dislocation introduced into the center of the model. (a) The theoretical analysis [24]; (b) The normalized local volume stress.

61

blue colors represent the highest and lowest values, respectively. Figure(3.12) shows an example of demonstrating the positions of dislocations by the potential energy. There is a single edge dislocation in the center of model as shown in Figure[3.12(a)]. The pure edge dislocation is well known to be not stable and it splits into two Shockley partial dislocations with a distance as the stacking fault, which is shown in Figure[3.12(b)].

3.5.4 Disregistry

Disregistry is a scheme proposed by Hoagland [25] to calculate the displacement of a series of pair atoms above and below the slip plane in the dislocation model. By the analysis of the displacement field, the evolution of the Burgers vector of a dislocation during the simulation could be obtained quantitatively.

As shown in Figure(3.13), in one dimension, atoms i and i' is a pair above and below the slip plane. When a dislocation is introduced, the displacement u^+ of atom i and u^- of i' are calculated as

$$u^+ = U(i_u) - U(i_{0,u}) \tag{3.26}$$

$$u^- = U(i'_l) - U(i'_{0,l}) \tag{3.27}$$

Thus, the disregistry Δ is obtained by

$$\Delta = u^+ - u^- \tag{3.28}$$

If the above scheme is expanded to a three-dimensional model, the X component of Δ is the edge component of the Burgers vector of a dislocation and the Z component of Δ represents the screw component.
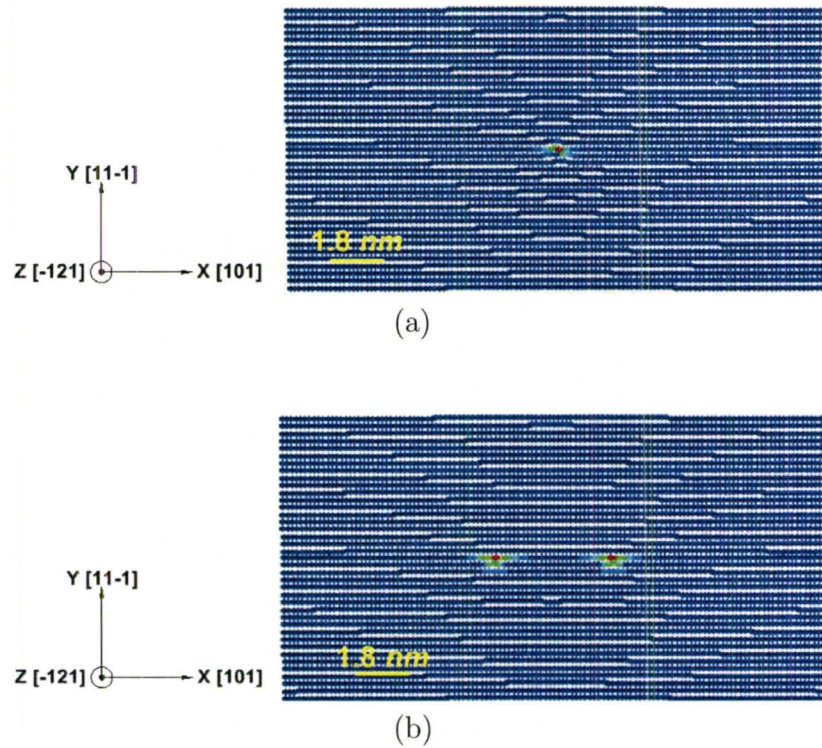
Figure 3.12: The positions of dislocations shown by the contour of the potential energy around an edge dislocation, in which red and blue colors represent the highest and lowest values respectively. (a) The initial configuration; (b) The relaxed configuration showing two Shockley partial dislocations.

Figure(3.14) demonstrates the change of the edge component of the Burgers vector of the models shown in Figure(3.12). For the creation of a dislocation in the lattice, the corresponding displacement field is introduced to a half plane from the edge to the center of the model so that the structure of another half is perfect at the initial state. During the relaxation, the atoms within the boundary are free to move so the positions of two Shockley partial dislocations are approximately at the symmetry about the central plane.

The implementation of Disregistry to the slip plane could be extended to any designated planes in the model. In these cases, the relative displacements of atoms above and below the designated plane are calculated following Equations(3.26) and (3.27). Throughout this thesis, the X and Z components of the displacement field of the dislocation are called edge and screw components, respectively, as used in the literature of the subject.

3.6 Summary of the framework

The new theoretical energy minimization method based on the Dynamic Relaxation technique as a solver is developed to calculate the change of atomic structures at zero temperature. This framework needs to import three-dimensional atomic coordinates generated by the lattice creator software. Then, the simulation is performed for the model with internal defects only or the combination of internal defects and the external traction through the new periodic symmetry method. Finally, a series of data, which include new positions of atoms, the potential energy, the stress components of atoms and other properties, could be exported to other software for further post-processing. Table(3.3) summarizes the algorithm and flow of the new framework.
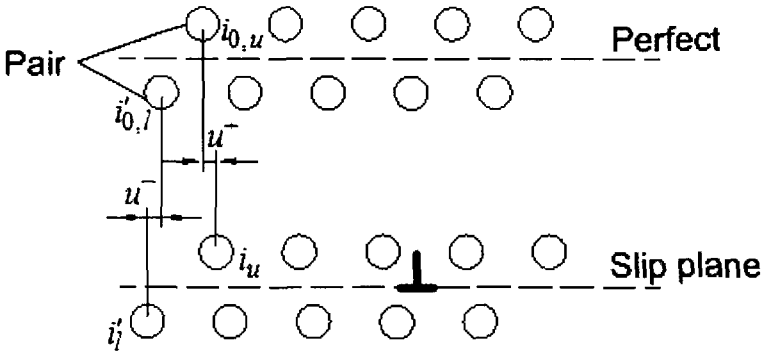
Figure 3.13: The scheme of Disregistry to calculate the displacement of a pair of atoms above and below the slip plane [25].
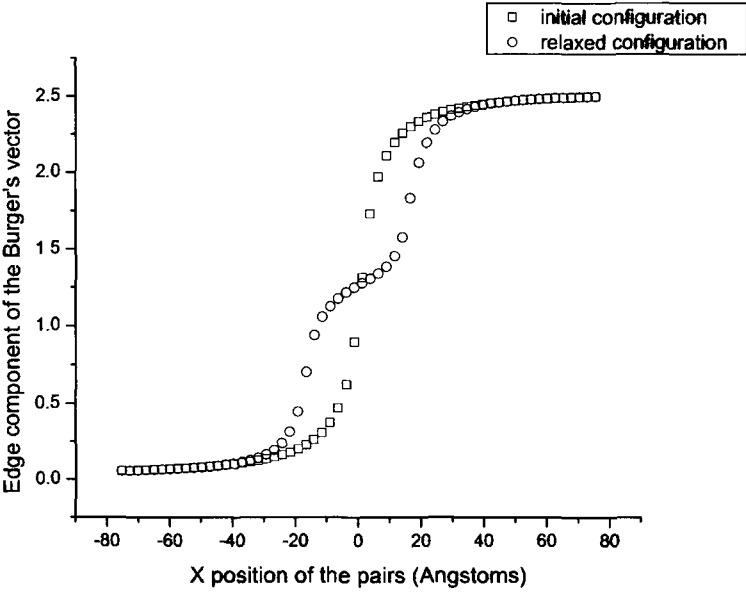
Figure 3.14: The edge components of the Burgers vector about a single edge dislocation, and its corresponding two Shockley partial dislocations after the relaxation.

Table 3.3: New energy minimization method based on the Dynamic Relaxation technique (fixed mass scheme).

I.	Get coordinates of atoms both from defective and perfect configurations; Determine immobile atoms according to the boundary conditions.
II.	Sort the pairs of boundary atoms in one or two directions from the prefect model.

III.	(i) Set Verlet Radius r_v, update Verlet list for every atom.
	 (ii) Get internal force $\mathbf{F}_{int,i} = \frac{\partial U_i}{\partial \mathbf{x}_j}$ from initial defective positions and mass m_i
	 (iii) Scaling mass:
	      if $\ddot{c} = 0$, mass of boundary atoms $m_i' = \frac{1}{2}m_i$
	      otherwise $m_i' = m_{max}$
	 (iv) Get external traction λ, and $\mathbf{F}_{sum,i} = \mathbf{F}_{int,i} + \lambda_i$
	 (v) $\Delta t = 0.5 \sim 0.7$

IV.	At any cycle n, time t, (i)$\ddot{\mathbf{u}}_i^t = m_i^{-1}\mathbf{F}_{sum,i}$ (ii)$\dot{\mathbf{u}}_i^{t+\Delta t/2} = \frac{1-\xi\omega\Delta t}{1+\xi\omega\Delta t}\dot{\mathbf{u}}_i^{t-\Delta t/2} + \frac{\Delta t}{1+\xi\omega\Delta t}\ddot{\mathbf{u}}_i^t$ (iii)$\mathbf{u}_i^{t+\Delta t/2} = \mathbf{u}_i^t + \Delta t\dot{\mathbf{u}}_i^{t+\Delta t/2}$, $\mathbf{x}_i^{t+\Delta t/2} = \mathbf{x}_i^t + \Delta t\dot{\mathbf{u}}_i^{t+\Delta t/2}$ (iv)Check if $|\mathbf{x}_i^t - \mathbf{x}_{i,ori}| > |r_v - r_c|$, update Verlet list. (v)Check error if $\frac{\left\| \mathbf{F}_{int,i}^t - \lambda_i \right\|_2}{\max\left(\|\mathbf{F}_{int,i} - \lambda_i\|_2\right)} < f_{tol}$, terminated. Otherwise, go to next step. (vi)Record current positions of atoms if indicated for intermediate images. (vii)Obtain $\mathbf{F}_{int,i}^{t+\Delta t}$ and ω_i (viii)Obtain $\mathbf{F}_{sum,i}^{t+\Delta t} = \mathbf{F}_{int,i}^{t+\Delta t} + \lambda_i$ (ix)$\Delta t_{cr} = \frac{2}{\omega_{max}}$ and $\Delta t_{n+1} = 0.5 \sim 0.7\Delta t_{cr}$ (x)estimate ω $K_{ii}^t = \dot{\mathbf{u}}_i^{t+\Delta t/2}(\mathbf{F}_{int,i}^{t+\Delta t} - \mathbf{F}_{int,i}^t)/\Delta t_{n+1}$ $K_{ii}^t = \max(K_{ii}^t, 0.0)$ $\omega = \left[\frac{\sum K_{ii}^t}{\sum m_{ii}(\dot{u}_i^{t+\Delta t/2})^2} \right]^{1/2}$ (xi) Go to (i) and repeat
V.	Output positions of atoms, stress components of atoms, potential energy of atoms.

Chapter 4

Numerical responses of single dislocation models

The chapter discusses the numerical responses of models containing one dislocation simulated by the new energy minimization framework. Some results obtained from dislocation models without applied external traction are compared with experimental observations and the other theoretical analysis in order to validate the new approach. Then, the investigation is focused on the responses of models subjected to the external traction, which includes cases of (i) external traction applied along the direction of the dislocation line and (ii) external traction applied along the direction of the dislocation line and the slip direction.

4.1 Validation and benchmark results

4.1.1 Single perfect edge dislocation models

Based on the dislocation theory [26][59], one perfect edge dislocation ($\mathbf{b}$) is not stable in the f.c.c. crystal and it dissociates into two Shockley partial dislocations ($\mathbf{b}_1$, $\mathbf{b}_2$)

to lower the total potential energy in the system. For example, the perfect edge dislocation could dissociate as:

$$\mathbf{b} = \mathbf{b_1} + \mathbf{b_2} \Rightarrow \frac{a}{2}[1\ 0\ 1] = \frac{a}{6}[2\ 1\ 1] + \frac{a}{6}[1\ \bar{1}\ 2] \tag{4.1}$$

According to the Frank's rule, the energy of the dislocation(s) before and after the splitting is

$$E_{single} = \alpha\mu b^2 = \alpha\mu\frac{a^2}{4}(1^2 + 0 + 1^2) = \frac{\alpha\mu a^2}{2} \tag{4.2}$$

$$E_{splitting} = \alpha\mu b_1^2 + \alpha\mu b_2^2 = \alpha\mu\frac{a^2}{36}(2^2 + 1^2 + 1^2) + \alpha\mu\frac{a^2}{36}[1^2 + (-1)^2 + 1^2] = \frac{\alpha\mu a^2}{3} \tag{4.3}$$

where b, b_1 and b_2 are the Burgers vectors of respective dislocations, α is the coefficient, μ and a are the shear modules and the lattice parameter of the material.

Osetsky *et al.* [40] indicated that the model with a constant periodic length along the dislocation line and fixed boundary conditions in the other two directions would give the approximately correct core structure as long as the length along the slip direction is larger than 100b while the proper potential energy function is used. Though the model may not be generated so large to obtain the correct solution for the relaxation of a single perfect edge dislocation, the result from a large size model could be used as the benchmark. A perfect edge dislocation from the solution of the anisotropic elastic theory is introduced into the center of the model with 114,950 atoms, whose geometry and the boundary condition in X and Y directions are shown in Figure(4.1). According to the dislocation theory, excluding the small area around the position of the perfect edge dislocation (less than 5b), the stress field is continuous for the rest of the model and could be calculated as:

$$\sigma_{xx} = \frac{\mu b}{2\pi(1 - \nu)} \frac{y(3x^2 + y^2)}{(x^2 + y^2)^2} \tag{4.4}$$
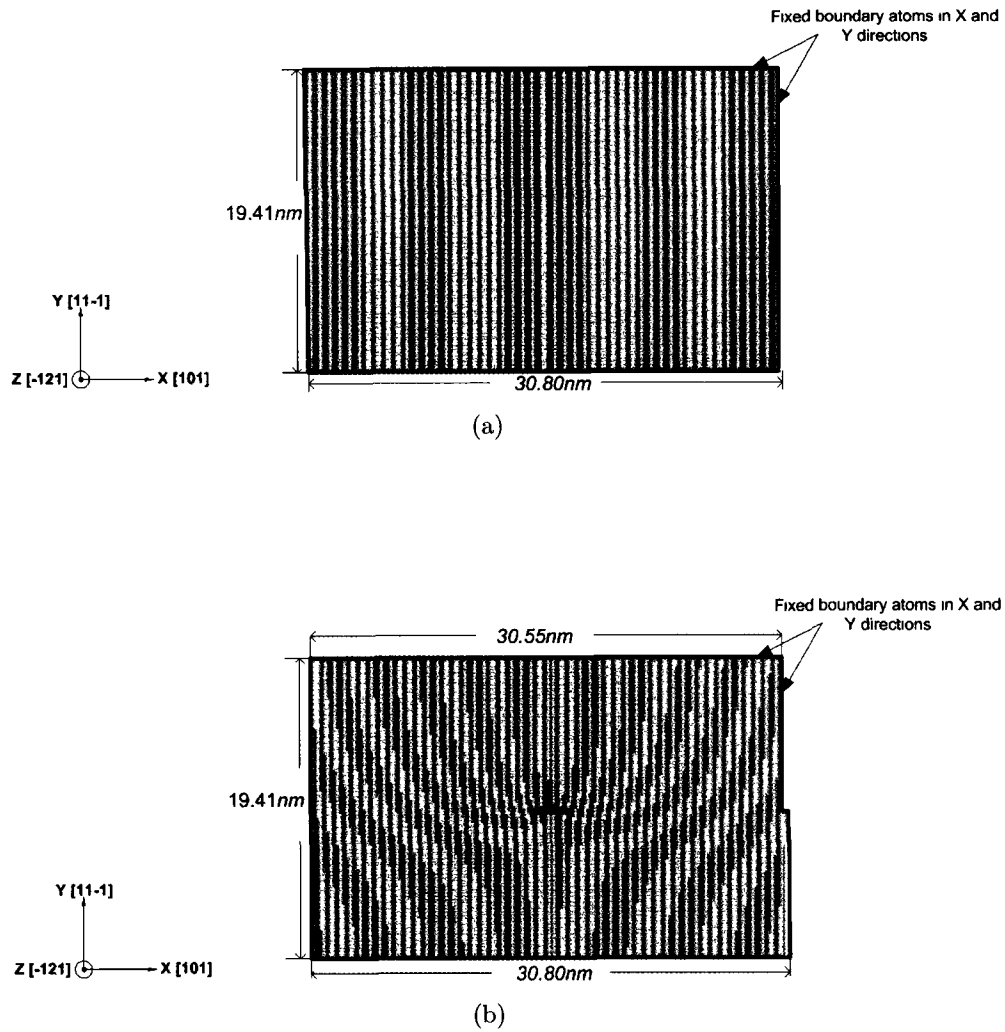
Figure 4.1: The geometry of a copper lattice with physical boundary atoms fixed in X and Y directions. (a) The perfect model; (b) The model containing a perfect edge dislocation with the dislocation line along the Z direction.

$$\sigma_{yy} = -\frac{\mu b}{2\pi(1-\nu)}\frac{y(x^2-y^2)}{(x^2+y^2)^2} \tag{4.5}$$

$$\sigma_{xy} = -\frac{\mu b}{2\pi(1-\nu)}\frac{x(x^2-y^2)}{(x^2+y^2)^2} \tag{4.6}$$

where x and y are coordinates according to the dislocation (origin). Therefore, the contour of stress components can be plotted from Equations(4.4), (4.5) and (4.6) [24]. From the atomistic simulation, stress components of atoms are calculated discretely. However, their profiles should be compatible to the theoretical analysis. Figure(4.2) compares stress contours from the continuum approach and the atomistic simulation for a perfect edge dislocation. The contour from the simulation does not perfectly match the theoretical contour. The pattern of two contours, however, is exactly the same. This is because the distribution of stress values, which are calculated from the discrete approach, into groups is difficult to be fully compatible with results from the theoretical analysis. The definition of the positive direction of the shear stress σ_{xy} in the theoretical analysis and the discrete calculation is opposite, so that this pair of contours is inverse mutually.

Thus, it proves that the lattice creator generates a correct configuration of a perfect edge dislocation. After the relaxation, all stress components imply that there are two dislocations in the model as shown in Figure(4.3).

More clear evidence to validate the relaxation is obtained by measuring the distance between two partial dislocations, i.e. the length of the stacking fault in the slip direction. From the experimental observation [54], the equilibrium width scatters from $3.2nm$ to $4.2nm$ and the average is $3.8nm$. The result from the simulation approximately stands for $4.0nm$ as shown in Figure(4.4), which indicates that the new approach works well.

Another validation procedure compares the results of the new approach to
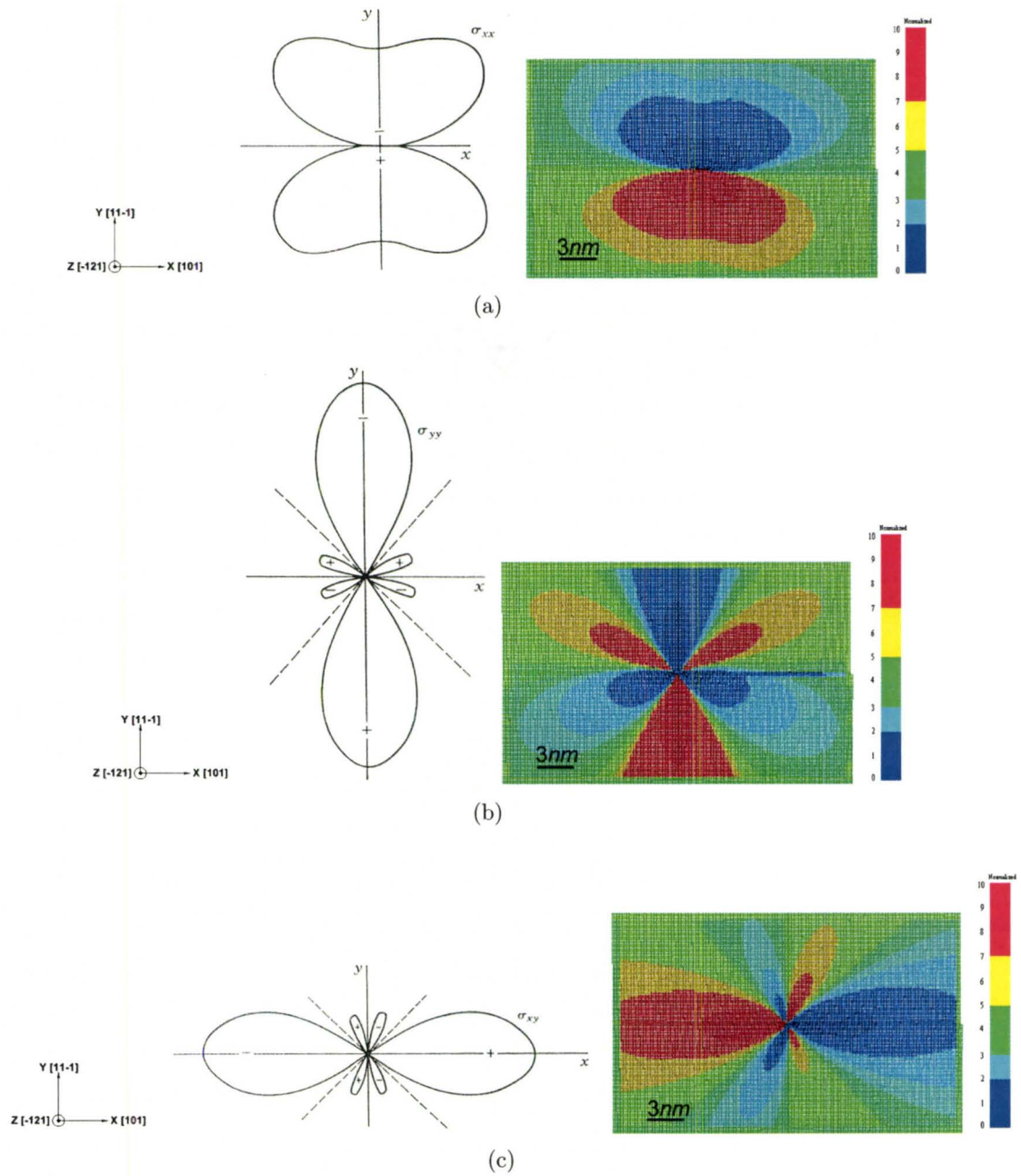
Figure 4.2: The comparison of the stress components of a perfect edge dislocation calculated by the theoretical analysis and the atomistic simulation. (a) σ_{xx}; (b)σ_{yy}; (c)σ_{xy}.
[Note: red color represents atoms with the highest stress (positive values) and blue color represents atoms with the lowest stress (negative values).]
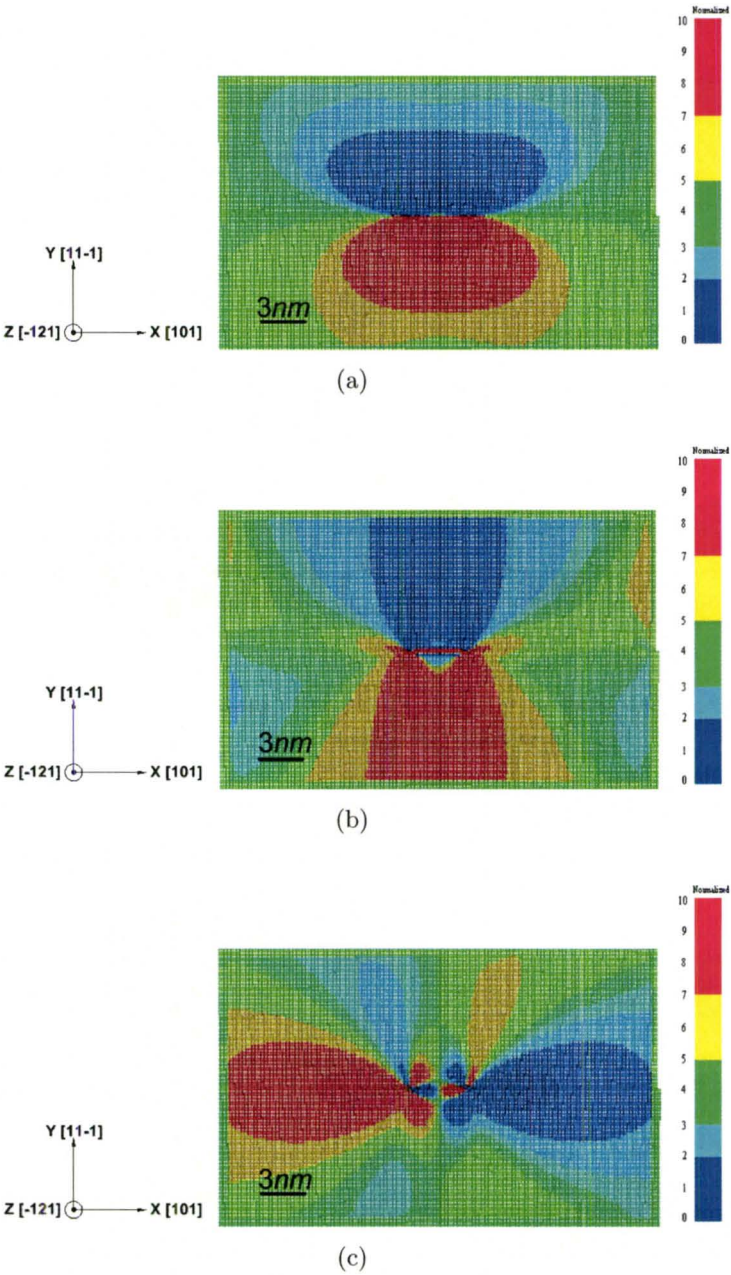
Figure 4.3: The stress components of two Shockley partial dislocations from the relaxation of a perfect edge dislocation calculated by the atomistic simulation. (a) σ_{xx}; (b)σ_{yy}; (c)σ_{xy}.
[Note: red color represents atoms with the highest stress (positive values) and blue color represents atoms with the lowest stress (negative values).]

(a)
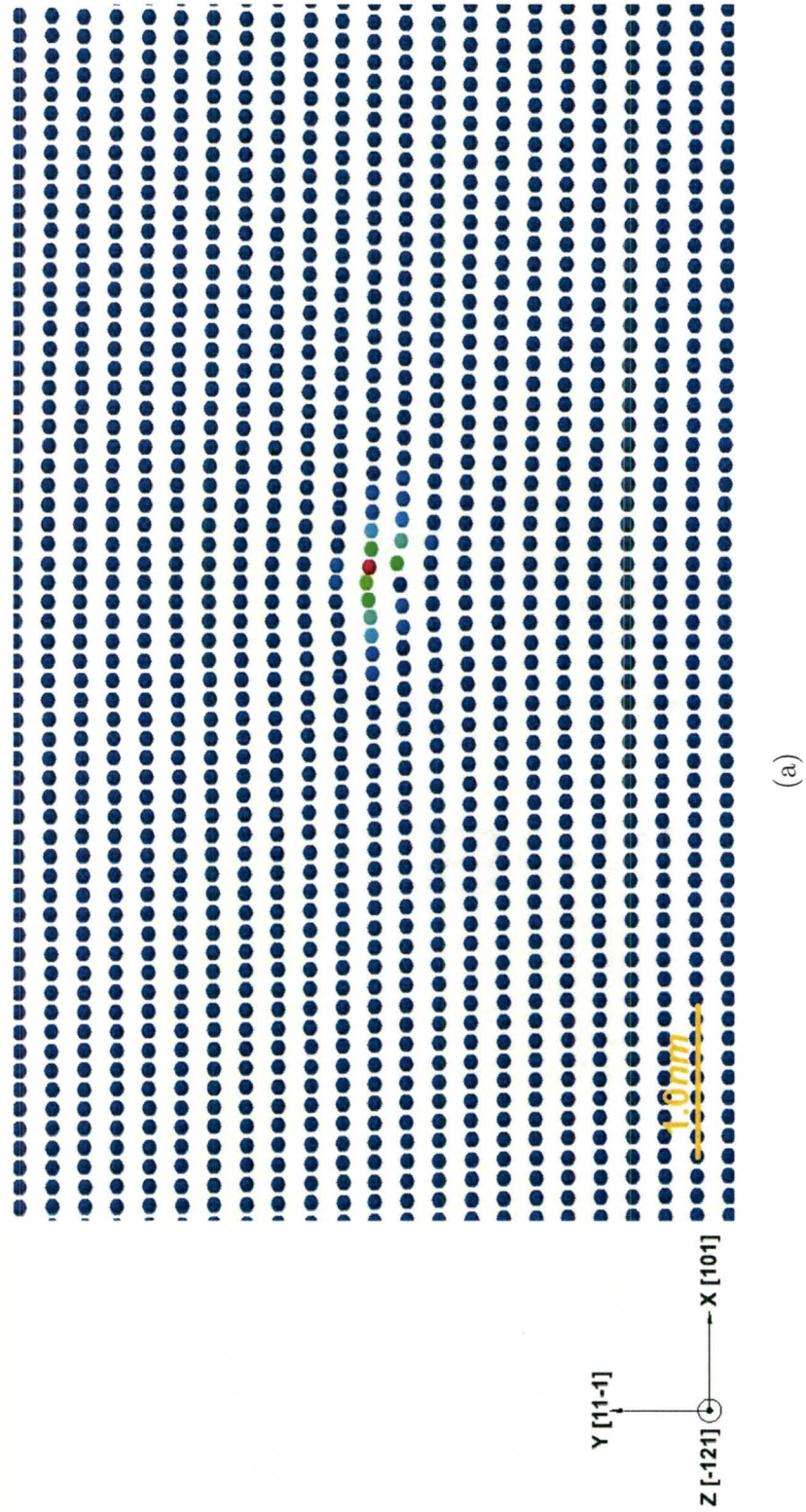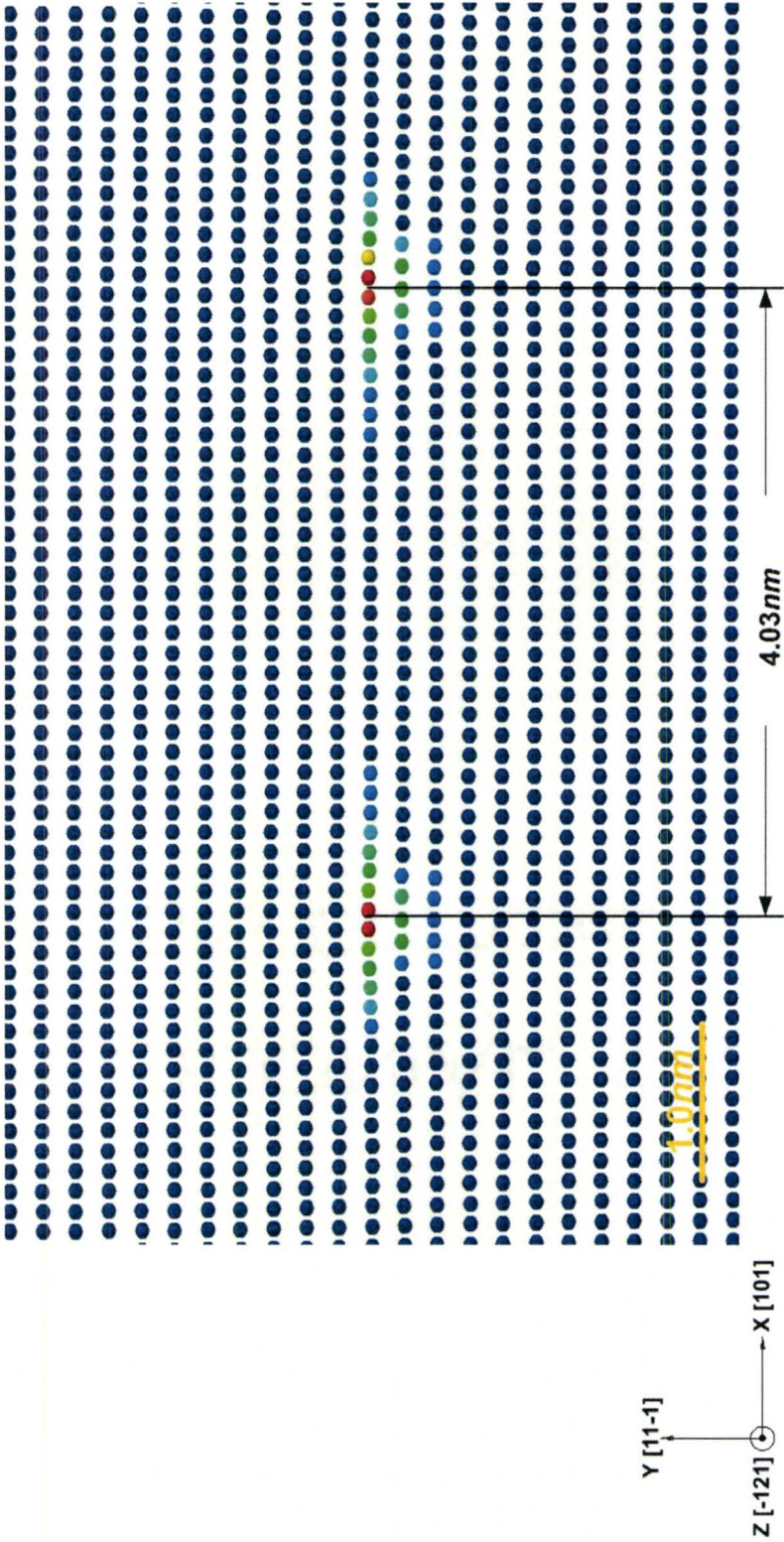
(b)
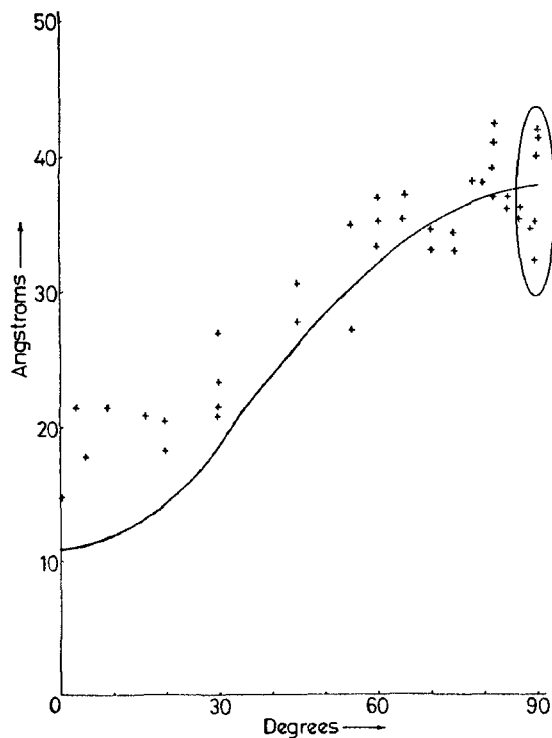
(c)

Figure 4.4: The positions of dislocations determined by the highest potential energy (red color) in the model with a constant periodic length in the direction of the dislocation line (Z). (a) A perfect edge dislocation; (b) Two Shockley partial dislocations; (c) The experimental observation of the separations of partial dislocations as a function of dislocation line orientation [54].

Note: The origin of a dislocation is normally not located on any atom. The atom with the highest potential energy value is most close to the origin of a dislocation. Therefore, the distance between dislocations determined from the positions of the highest potential energy atoms is subjected to some errors.

results obtained by the existing atomistic simulation method. The available code is based on the classical Molecular Dynamics (MD) with the time step 10^{-15} second. The model under consideration is a cylindrical model with 14,901 atoms, in which a perfect edge dislocation is introduced in the center and the dislocation line is along the Z direction. The corresponding orientation, geometry and boundary conditions are illustrated in Figure(4.5). By relaxing the model from both methods, results show some differences as shown in Figures(4.6) and (4.7). The new DR-based method captures the upper limit of the separation as determined by the experiment [54], while the result from MD simulation is around the lower limit.

The following work is to investigate the reason of the discrepancy from two methods. Figure(4.8) shows the path of the edge component of the Burgers vector from the initial configuration to the final equilibrium state by the new DR-based framework. It is found that the path crosses the final configuration calculated from the MD method, which may imply that the result simulated by the MD method is regarded as an intermediate stage but not the final equilibrium determined by the new DR-based method. Thus, from the view of the new DR-based method, the MD method does not fully relax the structure of a perfect edge dislocation.

Of course, another scenario is possible that the DR-based method misses the correct equilibrium configuration but converges to the wrong limit. Therefore, the simulated result from the DR-based method is re-calculated by the MD method. If the configuration calculated from the DR-based method deviates from the correct relaxed lattice, the potential energy is higher and the MD method should fix it to the correct one. After the relaxation, the configuration is not changed as shown in Figure(4.9), which proves that the relaxed configuration simulated from the DR-method is an equilibrium state. It is expected that there would be slight difference between two configurations in Figure(4.9) due to not exactly the same format of the

(a)

(b)
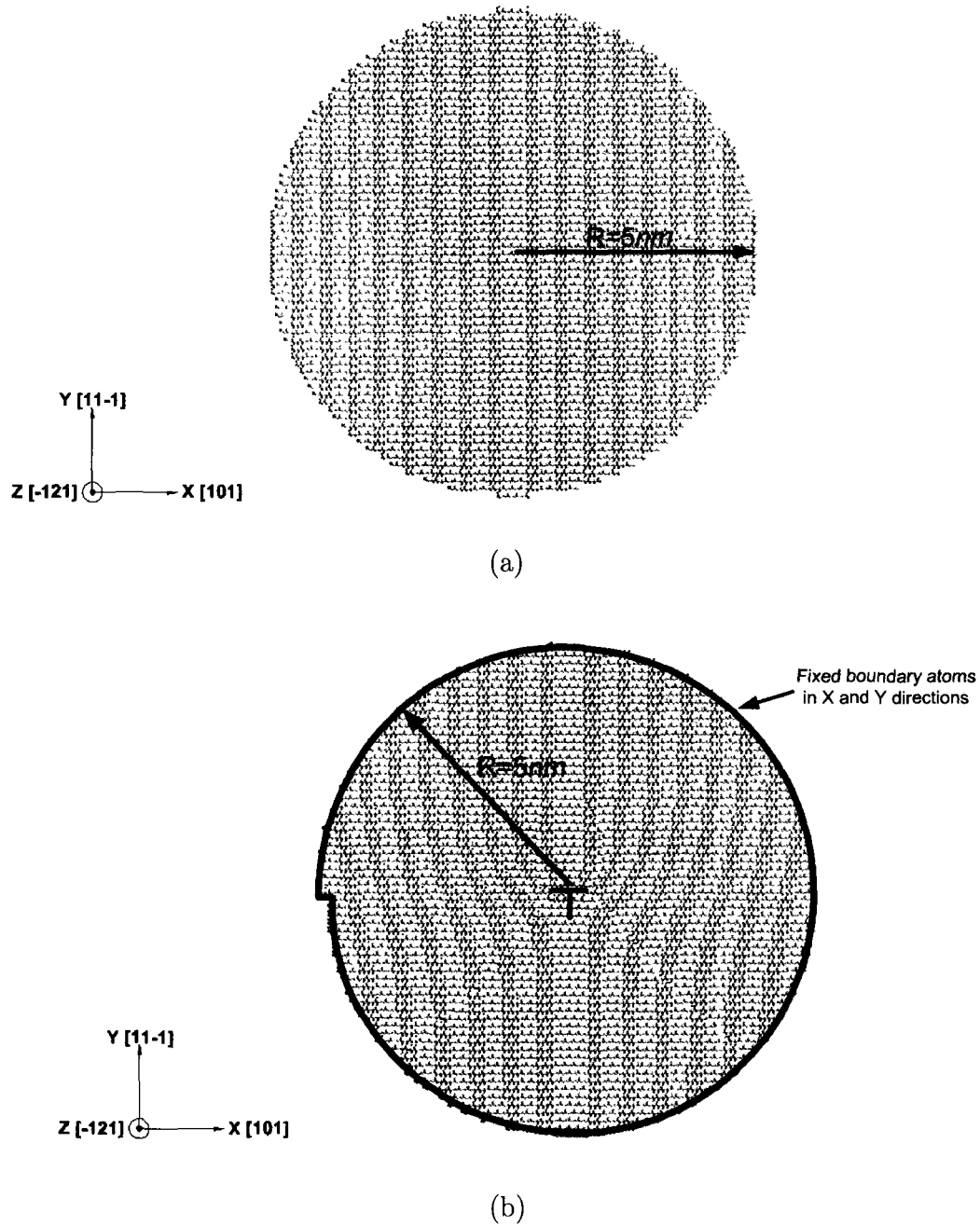
Figure 4.5: The cylindrical geometry of a copper lattice with physical boundary atoms fixed in X and Y directions. (a) The perfect model; (b) The model containing one perfect edge dislocation with the dislocation line along the Z direction.
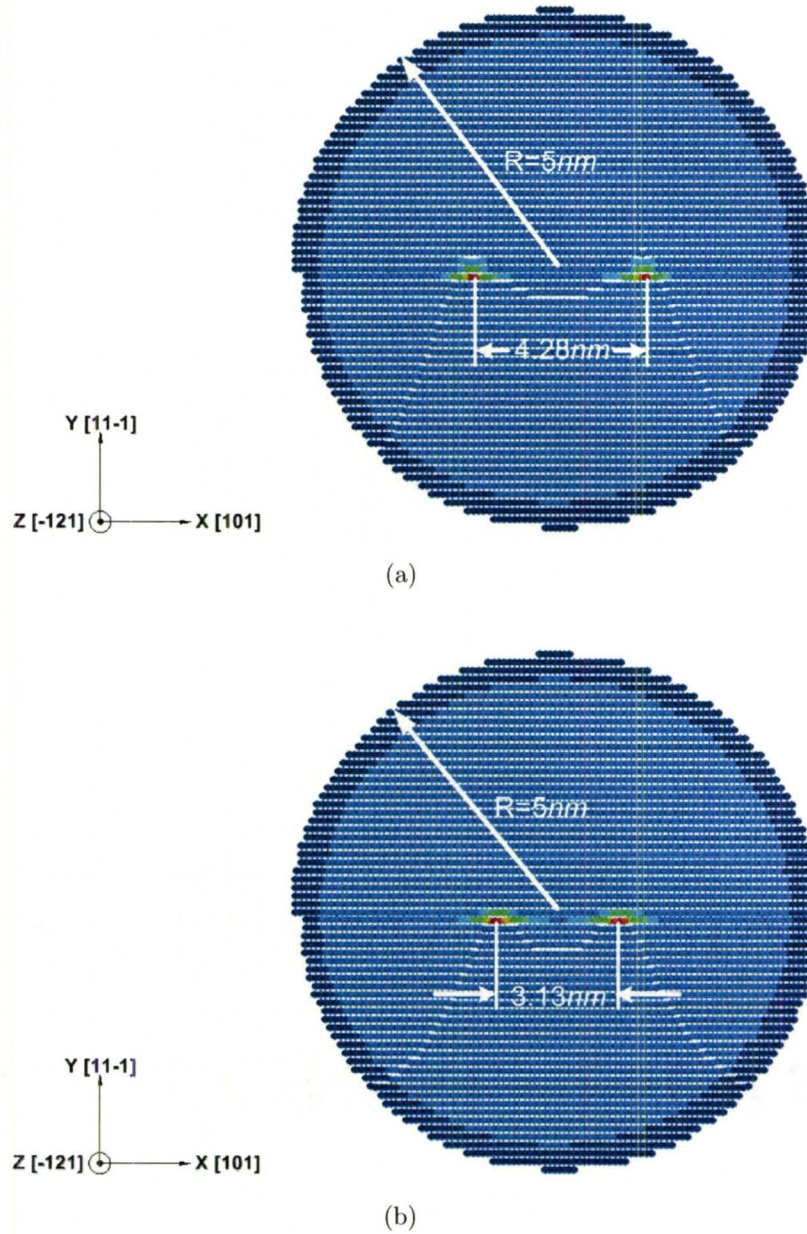
Figure 4.6: The separation of partial dislocations from the relaxation of a perfect edge dislocation. (a) The result from the DR-based method; (b) The result from the classical MD method.
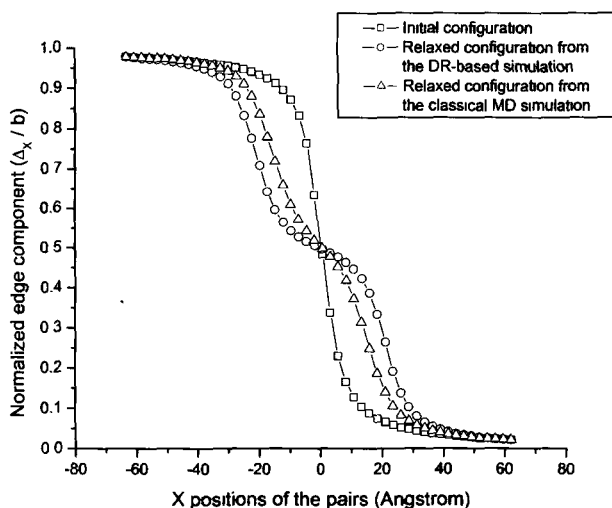
Figure 4.7: The comparison of the edge components of the Burgers vector in relaxed configurations simulated by two theoretical methods from an initial model containing a perfect edge dislocation. The edge component is determined by Disregistry.
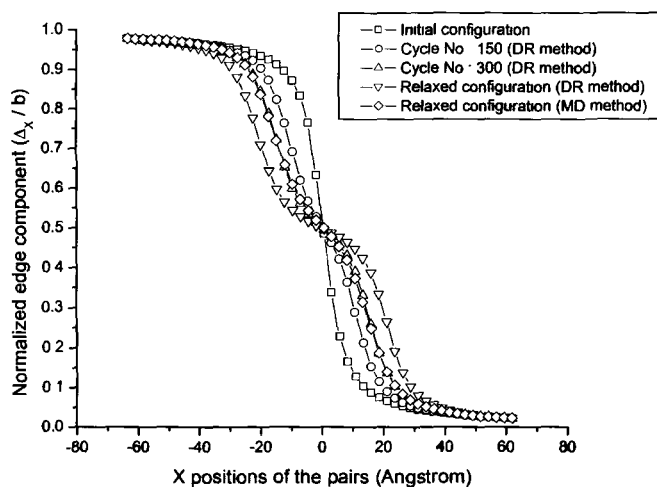
Figure 4.8: The comparison of edge components of the Burgers vector of configurations calculated by the DR-based method in relaxing a perfect edge dislocation, and the edge components of the Burgers vector in the relaxed configuration calculated by the classical MD method from an initial model containing a perfect edge dislocation. The edge component is determined by Disregistry.

potential energy function and the boundary condition.

Finally, the relaxed configuration from the MD method is put into the DR-based method for further relaxation. After the calculation, the original relaxed positions from MD simulation exactly move to the final configuration previously calculated by the DR-based method, which is illustrated in Figure(4.10). Therefore, the conclusion could be drawn that both methods could correctly relax a model containing a perfect edge dislocation. However, the internal threshold of terminating the simulation in the MD method is assumed to be set too high so that the relaxation is stopped on the way to the equilibrium. Another possibility is the criterion of choosing the configuration with the lowest potential energy is not optimized in the current MD code. Since atoms vibrate around the equilibrium positions after the relaxation in the MD simulation, the final equilibrium configuration depends on how to stop the motion of atoms. If the second conjecture happens, the results from two methods would be close providing that the advanced optimized criterion is available to obtain a relaxed stationary configuration.

In short, the new DR-based energy minimization framework works well for the relaxation of a perfect edge dislocation, and the result of the relaxation in the model with 114,950 atoms is regarded as the benchmark for later simulation cases considered in this work.

4.1.2 Single perfect screw dislocation models

Unlike the edge dislocation, in which the directions of the Burgers vector and the dislocation line are perpendicular, the Burgers vector and the dislocation line are parallel in the screw dislocation. Thus, there is no determined slip plane for a screw dislocation so that a perfect screw dislocation could dissociate on different $\{1\ 1\ 1\}$
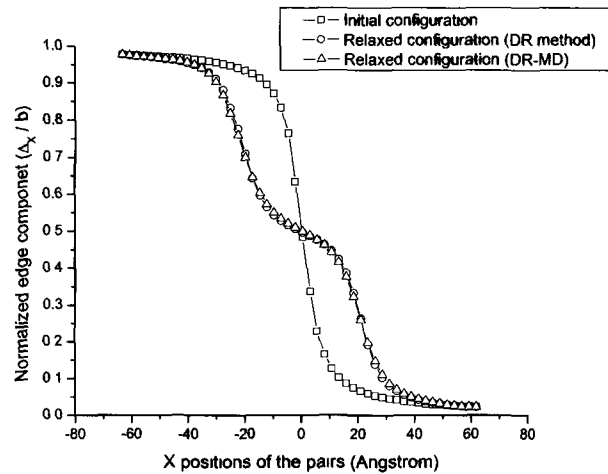
Figure 4.9: The comparison of the edge components of the Burgers vector in two relaxed configurations, i.e. the original simulation result by the DR-based method, and the new simulation result by the MD method from the original relaxed configuration calculated by the DR-based method. The edge component is determined by Disregistry.
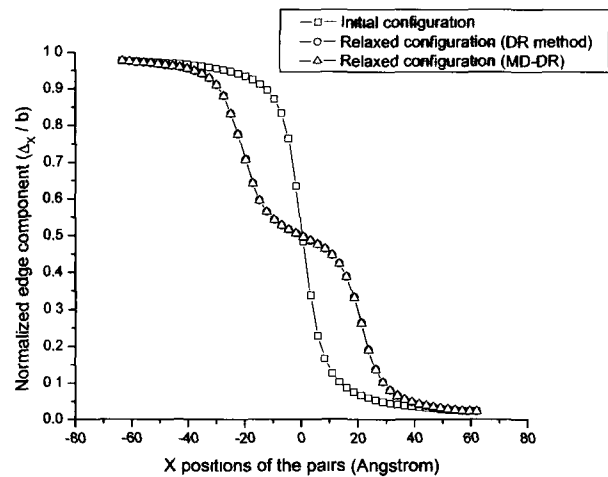
Figure 4.10: The comparison of the edge components of the Burgers vector in two relaxed configurations, i.e. the original simulation result by the DR-based method, and the new simulation result by the DR-based method from the original relaxed configuration calculated by the classical MD method. The edge component is determined by Disregistry.

planes. As an example, a perfect screw dislocation dissociates on the horizontal (1 1 1) plane or the inclined (1 1 -1) plane depending on the location of its origin, which is demonstrated in Figure(4.11). However, the dissociation on the horizontal plane is more convenient for the purpose to investigate the numerical responses of screw dislocations.

A perfect screw dislocation is generated in the center of the model with 114,000 atoms. The model coordinates and the corresponding geometry are shown in Figure(4.12). After the relaxation, as shown in Figures[4.13(a)] and [4.13(b)], the distance between two partial dislocations is around 1.4nm, which is in agreement with the experimental observation as indicated in Figure[4.13(c)]. Meanwhile, the screw and edge components of the Burgers vector in the initial and relaxed configurations are shown in Figure(4.14). By the comparison of the simulation and the experimental result, the relaxed configuration could be treated as the benchmark result for future screw dislocation simulations considered in this work.

4.1.3 Damping effect

As discussed in Section(2.4), the damping ratio controls the manner in which the system approaches the equilibrium. However, in the practical simulations of the relaxation of edge or screw dislocations, because the relaxed configuration of a dislocation is determined, the choice of the damping ratio to approach the correct minimum configuration is important.

For edge dislocation cases, a perfect edge dislocation could dissociate in the reasonable separation range with a higher damping ratio so that the damping ratio closer to critical 1.0 could achieve the relaxation more promptly. Lower damping ratios used in the edge dislocation simulation cause the process of the relaxation

(a)

(b)
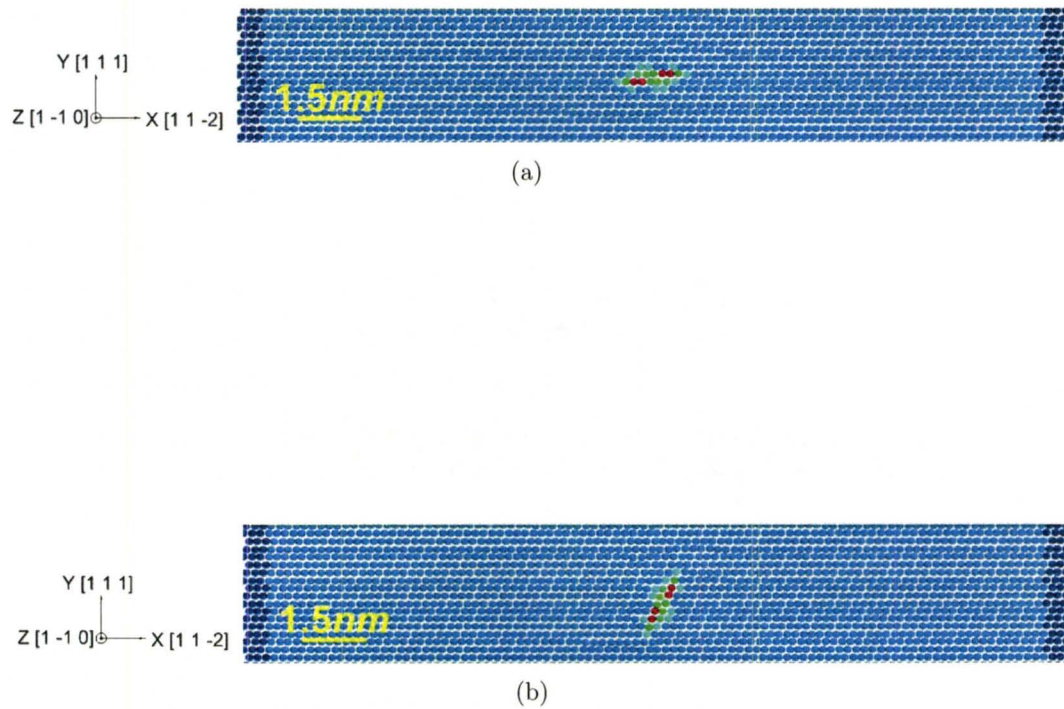
Figure 4.11: The dissociation of a perfect screw dislocation on different slip planes. (a) The horizontal (1 1 1) plane; (b) The inclined (1 1 -1) plane.
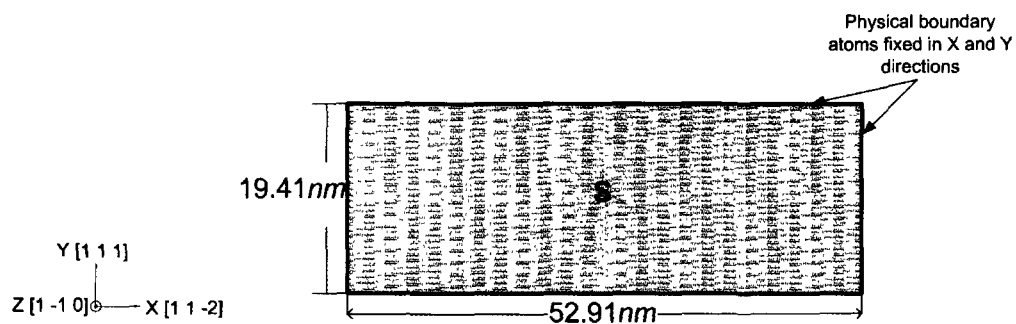
Figure 4.12: The geometry of a copper lattice containing a perfect screw dislocation with the dislocation line along the Z direction.

(a)

(b)

(c)
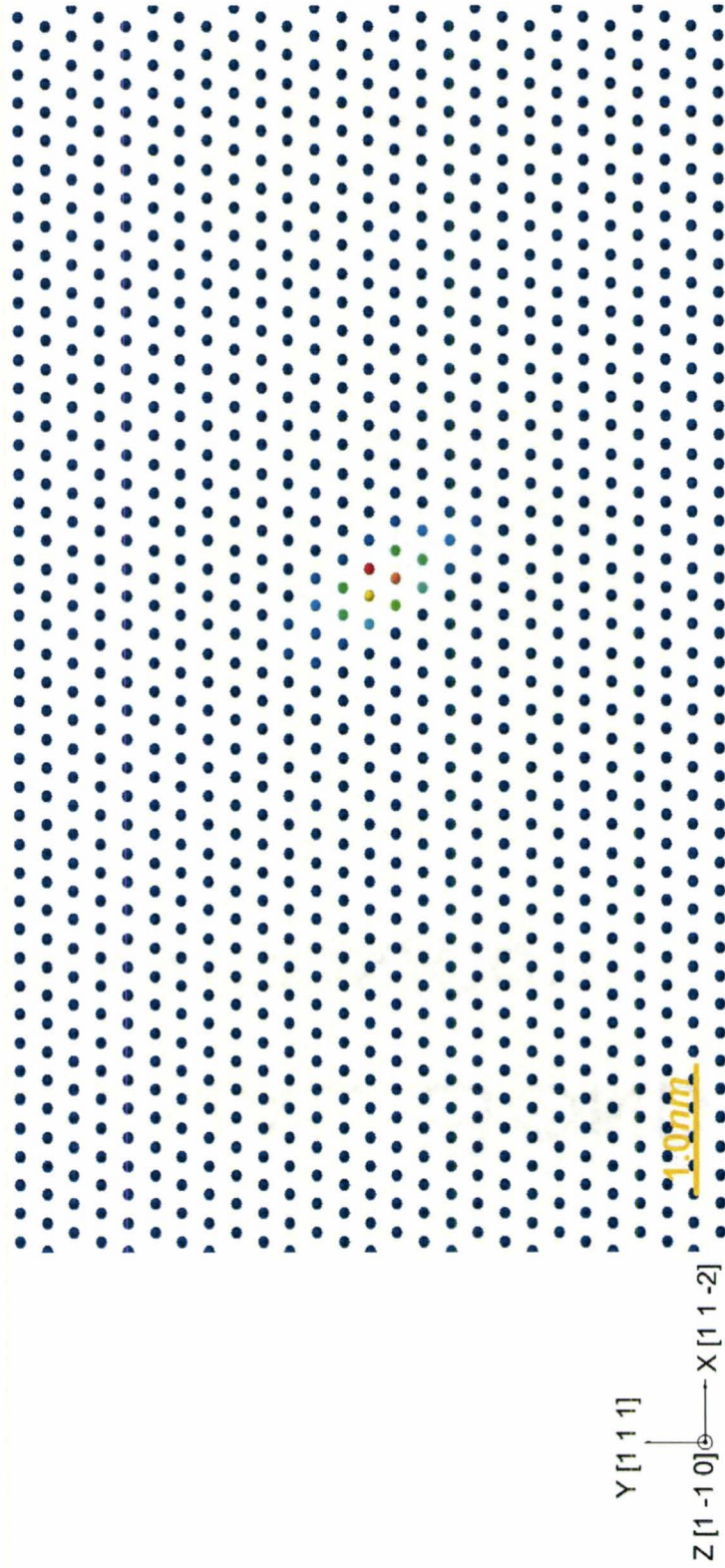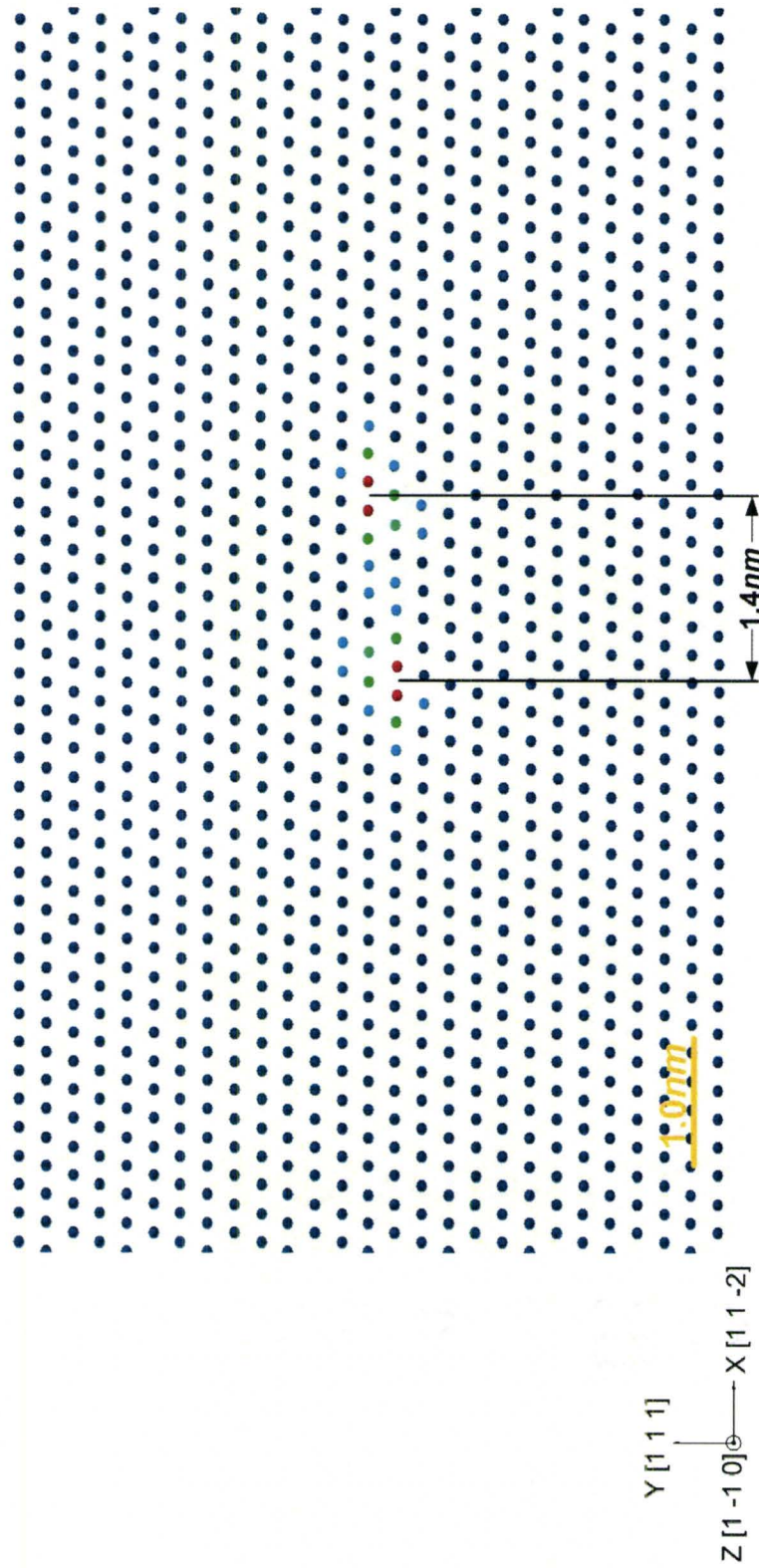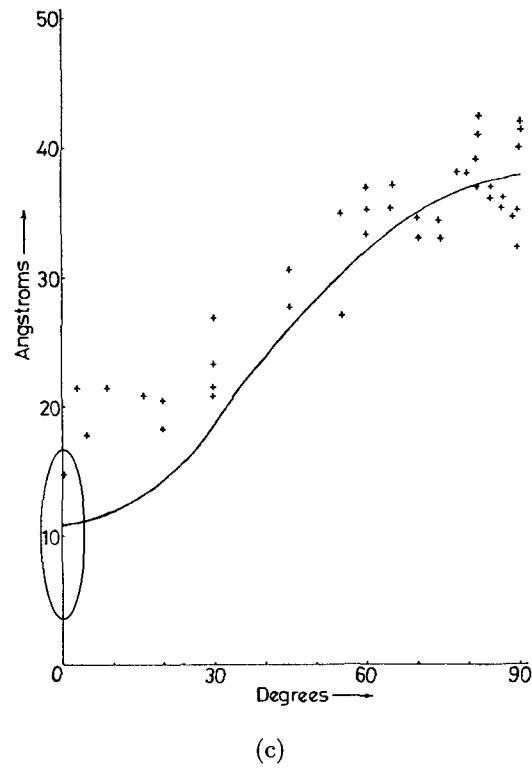
Figure 4.13: The positions of dislocations determined by the highest potential energy (red color) in the model with a constant periodic length in the Z direction. (a) A perfect screw dislocation; (b) Two Shockley partial dislocations; (c) The experimental observation of the separations of partial dislocations as a function of dislocation line orientation [54].
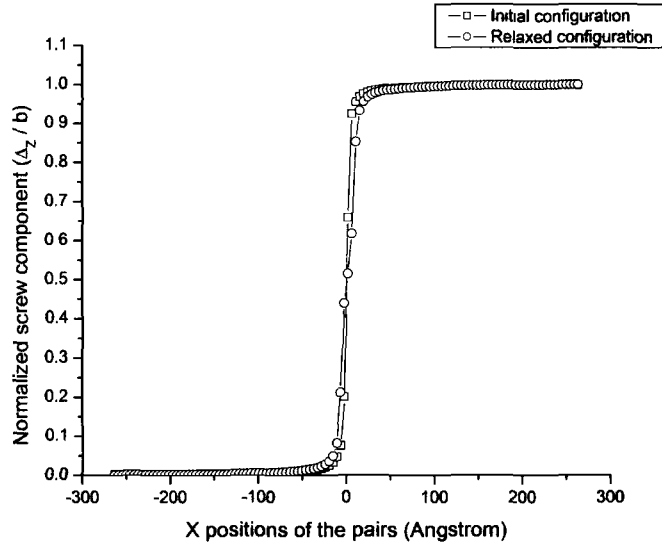
(a)
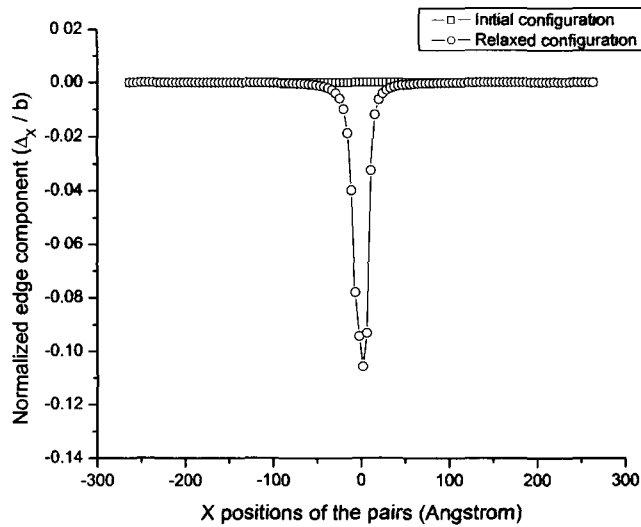
(b)

Figure 4.14: The comparison of the screw and edge components of the Burgers vector in the initial model containing a perfect screw dislocation and the relaxed configuration containing two Shockley partial dislocations. (a) The screw components; (b) The edge components. (a) and (b) are determined by Disregistry.

to take longer and alter the relaxed configuration to some extent. For example, as shown in Figure(4.15), the relaxation of the benchmark edge dislocation model with damping ratio 0.5 needs 650 computational cycles but needs 890 cycles with damping ratio 0.05. There is 0.5% difference of the total potential energy in two cases. Considering the numerical noise in the case with a lower damping ratio, the final potential energy values in these two cases are almost the same. However, the edge components of the Burgers vector in relaxed configurations in the two cases show some discrepancy as shown in Figure[4.16(b)]. The reason is that the separation between partial dislocations increases from half to one interatomic distance in the slip direction, which could be up to $4.22nm$ as shown in Figure[4.16(a)]. Therefore, under almost the same potential energy, from the numerical point of view, the equilibrium positions are not strictly fixed but are in some narrow range. In order to obtain reliable simulation results, a higher damping ratio of 0.5 is conservatively chosen for the benchmark case and future edge dislocation simulations.

For screw dislocation cases, the effect of the damping ratio is similar to edge dislocation cases. For the benchmark model, as the example, there is 0.8% difference of the total potential energy with higher damping ratio 0.5 and lower damping ratio 0.05, which is illustrated in Figure(4.17). The length of the stacking fault calculated from the lower damping ratio is more in agreement with experimental data, which is around $1.4nm$. However, a higher damping ratio makes the separation of partial dislocations around $0.8nm$. Such differences are also reflected in the analysis of the screw component of the Burgers vector, which is demonstrated in Figure(4.18). Though the result calculated from the higher damping ratio may be correct from the numerical point of view as a local minimum configuration, it could not be supported by available experimental observations. Therefore, a higher damping ratio is not suitable for relaxing dislocation models with a screw component. In the benchmark case of the
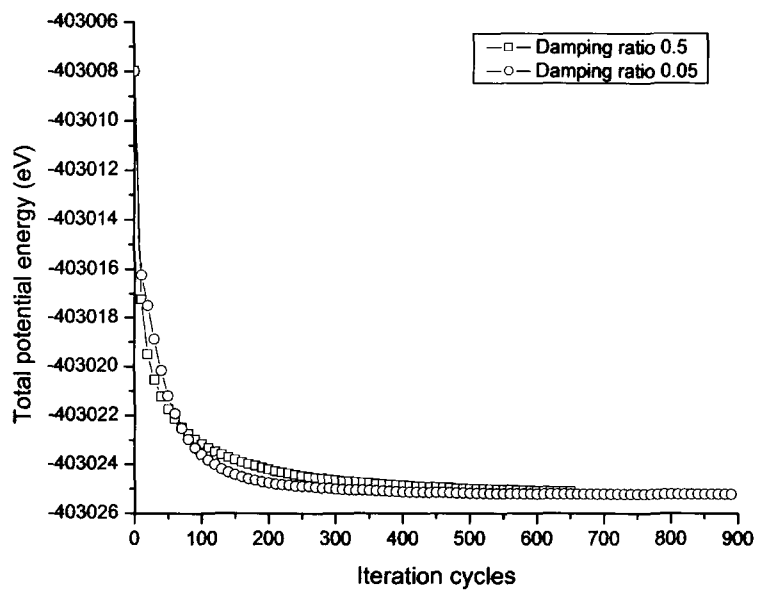
Figure 4.15: Potential energy as a function of the simulation time for the relaxation of a perfect edge dislocation with higher and lower damping ratios (stop at the same tolerance value).
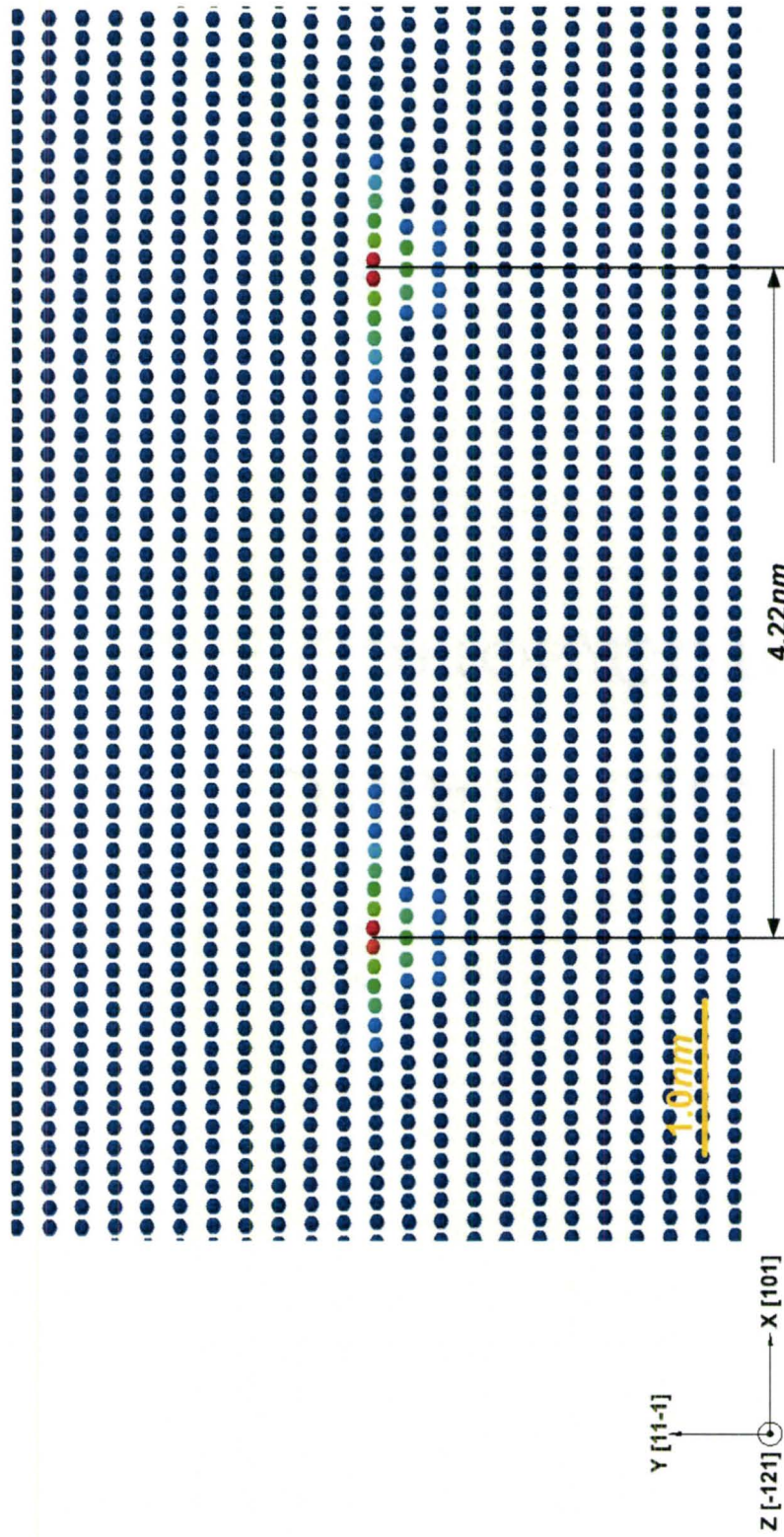
(a)
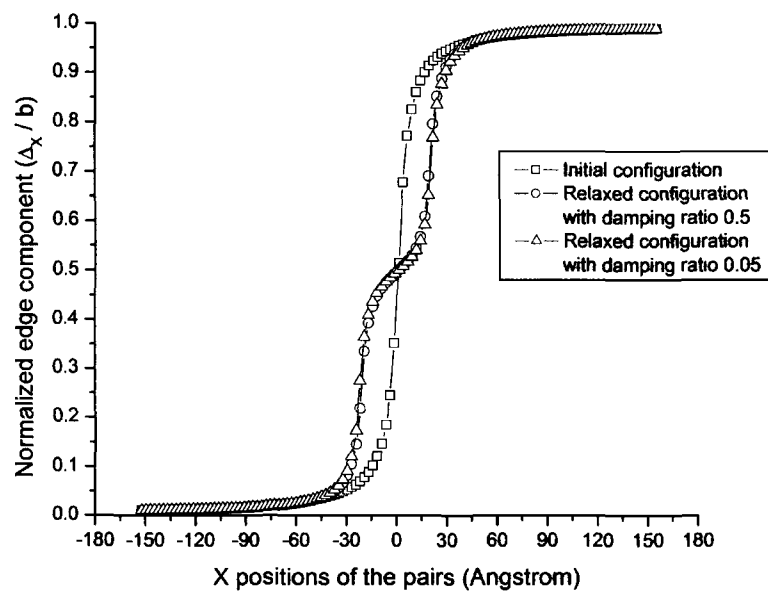
(b)

Figure 4.16: The relaxation of a perfect edge dislocation with damping ratios 0.5 and 0.05. (a) The separation of partial dislocations with damping ratio 0.05; (b) The edge components of the Burgers vector determined by Disregistry.
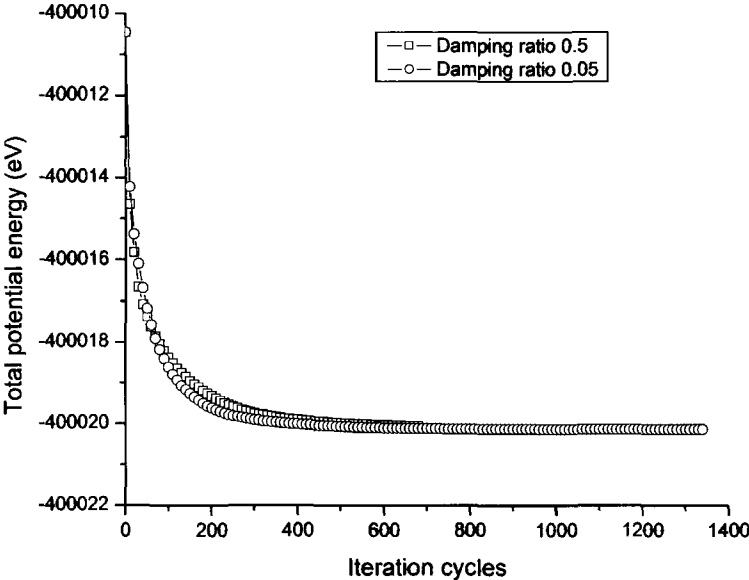
Figure 4.17: Potential energy as a function of the simulation time for the relaxation of a perfect screw dislocation with higher and lower damping ratios (stop at the same tolerance value).

(a)

Y [1 1 1]

Z [1 -1 0]⊙ ⟶ X [1 1 -2]

0.78nm

1.0nm
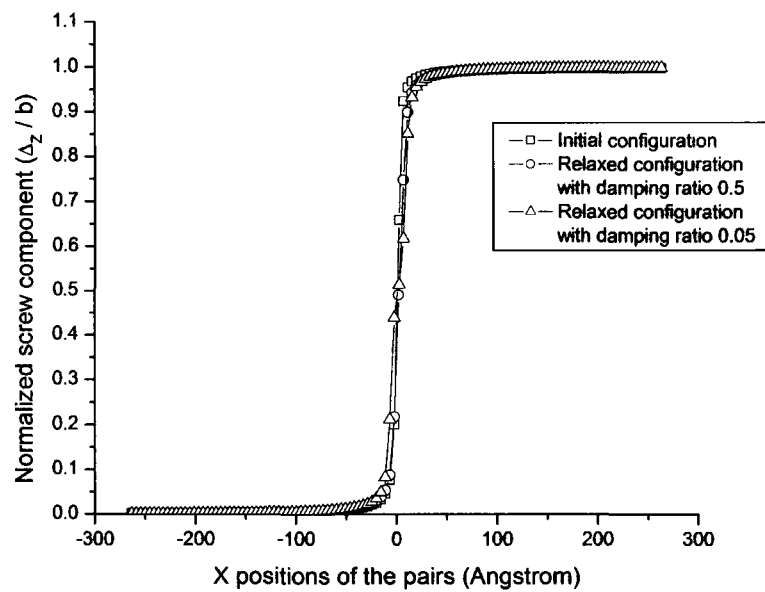
(b)

Figure 4.18: The relaxation of a perfect screw dislocation with damping ratios 0.5 and 0.05. (a) The separation of partial dislocations with damping ratio 0.5; (b) The screw components of the Burgers vector determined by Disregistry.

relaxation of a perfect screw dislocation, lower damping ratio 0.05 is used.

In summary, the damping ratio, as a flexible parameter in the new DR-based energy minimization framework, makes simulations more accurate and efficient. Although the damping ratio for dislocation simulations is settled, there is no general rule to choose damping ratios in various simulation cases. Normally, this parameter is chosen on a case-by-case basis and could be optimized from repeated tests for a specific atomic configuration.

4.2 One dimensional external traction

4.2.1 Unit length in the perfect lattice

Lattice parameter a defines the perfect length of the unit cell in the perfect crystalline lattice. The lattice parameter a is $0.3615nm$ for the copper. The atomic model with the perfect unit length should be in the stress-free state and the length of the unit cell is retained if no external traction is applied in any direction.

However, in the current simulation by the new periodic symmetry applied in the Z direction, when the external traction $\mathbf{T}$ is set to zero, the unit length deviates from the lattice parameter a, which is similar to the circumstance that there are extra external forces applied on every boundary atom in the XY plane but the net of these forces is equal to zero. This unexpected discrepancy of the unit length will exaggerate or underestimate the effect of the change of the periodic length from the real external traction, which causes the difficulty in explaining results for dislocation models. The reason for this problem arises from the fixed boundary condition applied to physical boundary atoms in X and Y directions. For example, the worst positions for boundary atoms are at the corner of the model. Although the force is balanced

along the Z direction for boundary atoms at the corner, the internal forces without considering the symmetry for these atoms are quite different to atoms within the boundary due to the reduced number of neighbors. The difference in the raw internal force values under the new periodic symmetry as Equation(3.12) exerts extra forces on the rest of atoms in the model in order to maintain the unique periodic length in the Z direction during the simulation.

As shown in Figure(4.19), this error can be reduced by increasing the number of atoms in the model. For example, when the model consists of 256 atoms, the unit length is 2.66% smaller than the lattice parameter. However, the difference between the unit length and the lattice parameter is just 0.36% when the number of atoms increases to 19,600. This is because the percentage of boundary atoms without enough neighbors in the whole model decreases with the increase in the number of atoms, so that the amount of extra external forces applied on individual atoms becomes smaller, which means more atoms within the boundary are subjected to the extra traction.

It has been determined that this error is generated due to the fixed boundary condition. The solution for the problem is to substitute the periodic symmetry for the fixed boundary condition in the other two directions during the simulation. The computational cost for three dimensional periodic symmetry is very high, and it is not necessary for many cases. Therefore, if the fixed boundary condition is used, a larger scale simulation model (10^5 or up) is needed to avoid a large error in the calculation.

4.2.2   One dimensional external traction in the perfect lattice

One dimensional external traction is first applied to the lattice without containing any defects. The copper model consists of 95,000 atoms and its dimension is $25.56nm \times 19.41nm \times 1.99nm$ as shown in Figure(4.20). The model coordinates are X[1 0 1],
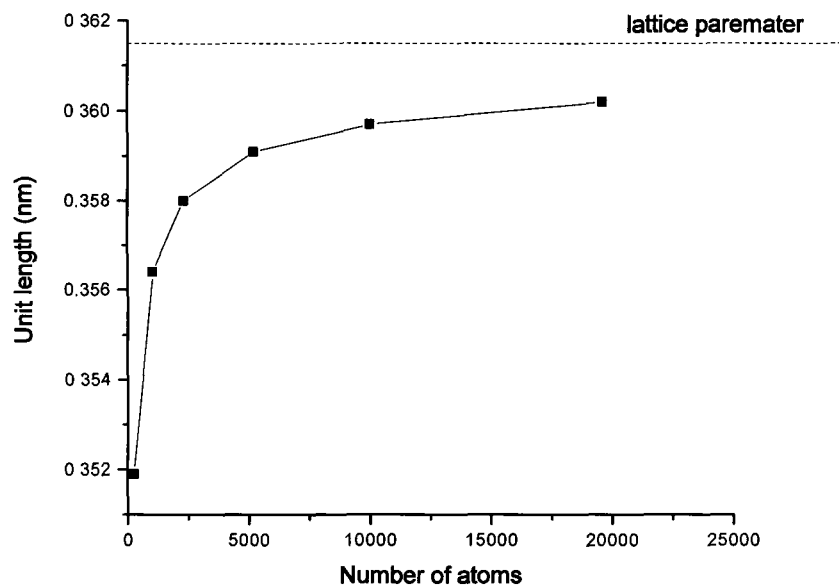
Figure 4.19: The unit length after the relaxation for various number of atoms in the perfect lattice where physical boundary atoms are fixed in X and Y directions and the periodic symmetry is applied along the Z direction as $\mathbf{T}_x = 0$. (Dash line is the lattice parameter 0.3615nm for the copper)

Y[1 1 -1] and Z[-1 2 1], and the traction is applied in the XY plane and along the Z direction. The boundary condition in X and Y directions is obtained by fixing physical boundary atoms whereas the atoms within the boundary are free to move in the XY plane. The damping ratio is 0.5 while the tolerance is 0.001 in the simulation.

In the current EAM potential energy function, the unit is electronvolts (eV) with normalized distances between atoms based on the lattice parameter in Angstrom units. Therefore, the values of calculated internal forces and applied external traction are in arbitrary units, which are not units commonly used in engineering. The coefficient is calculated to convert the force in arbitrary units to Newtons, that is

$$1 \ arbitrary \ unit \times \frac{1.602 \times 10^{-19}}{10^{-10}} = 1.602 \times 10^{-9} N. \tag{4.7}$$

The periodic length along the Z direction in the initial model is $1.770981nm$ including five atoms. When zero traction is applied, due to the error stated in Section(4.2.1), the periodic length after the relaxation shrinks to $1.7689704nm$, which is about 0.1% smaller than the original length. Thus, for later simulations, the new length is regarded as the reference quantity l_0 to calculate the strain of the periodic length with respect to the applied traction and the corresponding normal stress along the Z direction. Both tensile and compressive forces F_z are applied in the range of 5-40 arbitrary units in increments of 5 arbitrary units. The normal stress in the unit of $Pascal$ (Pa) along the Z direction is calculated as

$$\sigma_{zz} = \frac{F_z \times 1.602 \times 10^{-9}}{A_{XY}} \tag{4.8}$$

where A_{XY} is the area of the XY plane intersection. The normal strain ϵ_{zz} is obtained

by the engineering strain approach,

$$\epsilon_{zz} = \frac{l - l_0}{l_0} \tag{4.9}$$

where l is the new periodic length after the relaxation. The 16 pairs of stresses and strains are plotted in Figure(4.21), in which these values show strong linear trend. By the linear curve regression with $R = 0.9998$, the relationship is obtained by

$$\sigma_{zz} = 1.11 \times 10^{11} \epsilon_{zz} - 1.23 \times 10^6. \tag{4.10}$$

It is known that the slope in Equation(4.10) represents Young's modulus E according to Hooke's Law. The value is quite in agreement with the Young's modulus of the copper, $110 - 120GPa$. Therefore, the responses of the perfect lattice subjected to the external traction reproduced the correct elastic property.

4.2.3 One dimensional external traction in the lattice with a dislocation

The benchmark model, as shown in Figure(4.1), is chosen for the investigation. The boundary lines in the XY plane are assumed to be straight and the area is approximately $5.95 \times 10^{-16} m^2$ so that the corresponding dislocation density in the model is of the order of $10^{16} m^{-2}$. The dislocation line is along the Z direction. The damping ratio and tolerance are chosen as 0.5 and 0.001, respectively.

Since the lattice in the Z direction is still free of defects, in the ideal condition, the benchmark model with a constant periodic length ($\ddot{c} = 0$) in the Z direction and the new model with zero external traction ($T = 0$) yield the same relaxation results. After the simulation, compared to the results of the benchmark model, the model
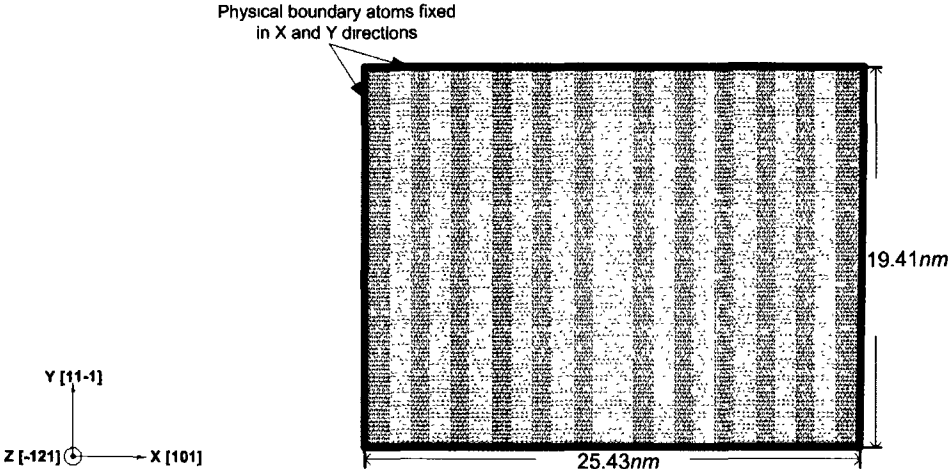
Figure 4.20: The geometry of a perfect copper lattice subjected to various external traction along the Z direction.
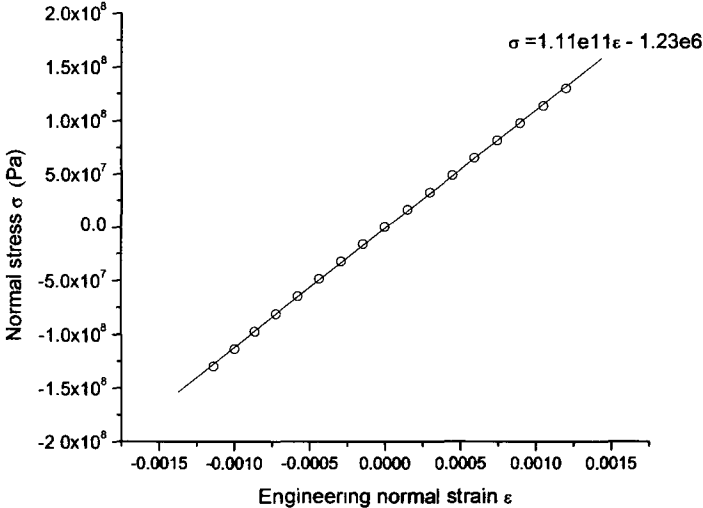
Figure 4.21: The relationship between normal stress σ_{zz} and strain ϵ_{zz} determined by a perfect copper lattice subjected to external tension or compression.

101

with zero external traction shows similar results. From the relaxation curve of the potential energy as shown in Figure(4.22), two models minimize their potential energy following the same trend at the early stage. With different boundary treatments in the Z direction, two models gradually diverge their minimization path and finally have 4.6% difference in the rate of change of the total potential energy. From the edge component of the Burgers vector analyzed by Disregistry shown in Figure(4.23), the trends of the dissociation of an edge dislocation in two models are almost the same but there are some differences in a couple of pairs of atoms in the relaxation region. This means the formation of the dissociation is the same but the distance between two partial dislocations is changed. Figure(4.24) demonstrates approximate positions of two partial dislocations distinguished by the highest potential energy in the system. The distance between two partial dislocations in the model with zero external traction is approximate half b larger than the benchmark model. The reason for above discrepancy is that two boundary treatments change the periodic length in the Z direction. As expected, the periodic length in the model with zero external traction shrinks 0.09%, which changes the configuration of the model a little bit. Fortunately, such a change does not alter the pattern of the stress distribution. The contours of σ_{xx} in two models are almost the same as shown in Figure(4.25). Since an edge dislocation glides on the horizontal $\{1\ 1\ 1\}$ plane, σ_{xx} is a stress component characterizing the behavior of the dissociation of an edge dislocation.

A series of external traction is applied along the direction of the dislocation line. The forces along the Z direction include 25.0, −25.0, 50.0, −50.0, 100.0 and −100.0 in arbitrary units, which are equivalent to the normal stresses σ_{zz} of $67.3MPa$, $−67.3MPa$, $134.6MPa$, $−134.6MPa$, $269.2MPa$ and $−269.2MPa$ applied on the XY plane. Unlike the perfect lattice, for the model containing a dislocation, the numerical responses from the external compression do not mirror themselves from
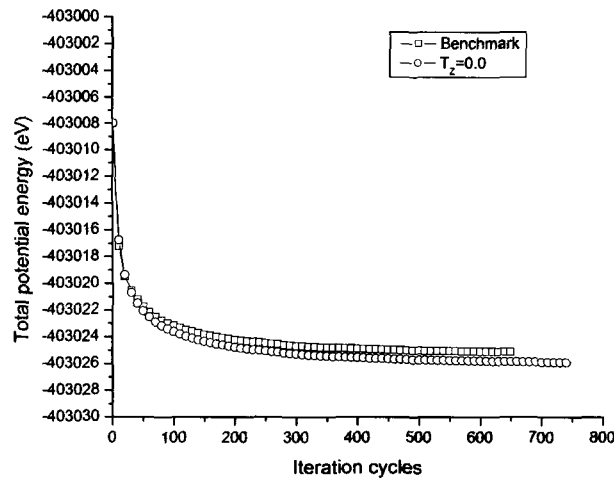
Figure 4.22: Potential energy as a function of the simulation time for the relaxation of a perfect edge dislocation under two boundary conditions in the direction of the dislocation line (Z) (stop at the same tolerance value).
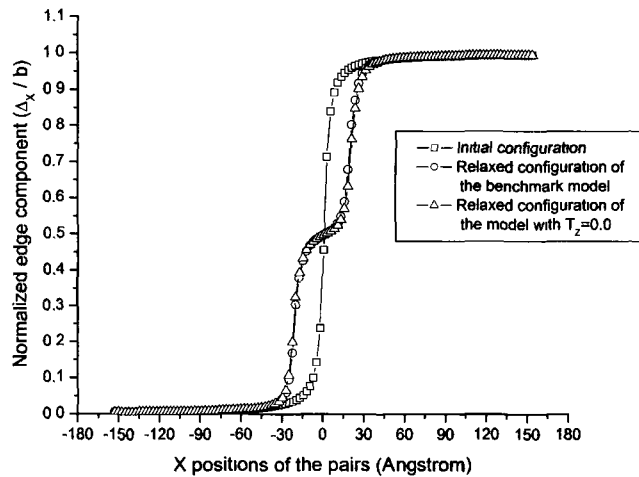
Figure 4.23: The edge components of the Burgers vector in the relaxation of a perfect edge dislocation under two boundary conditions in the direction of the dislocation line (Z). The edge component is determined by Disregistry.

(a)

(b)
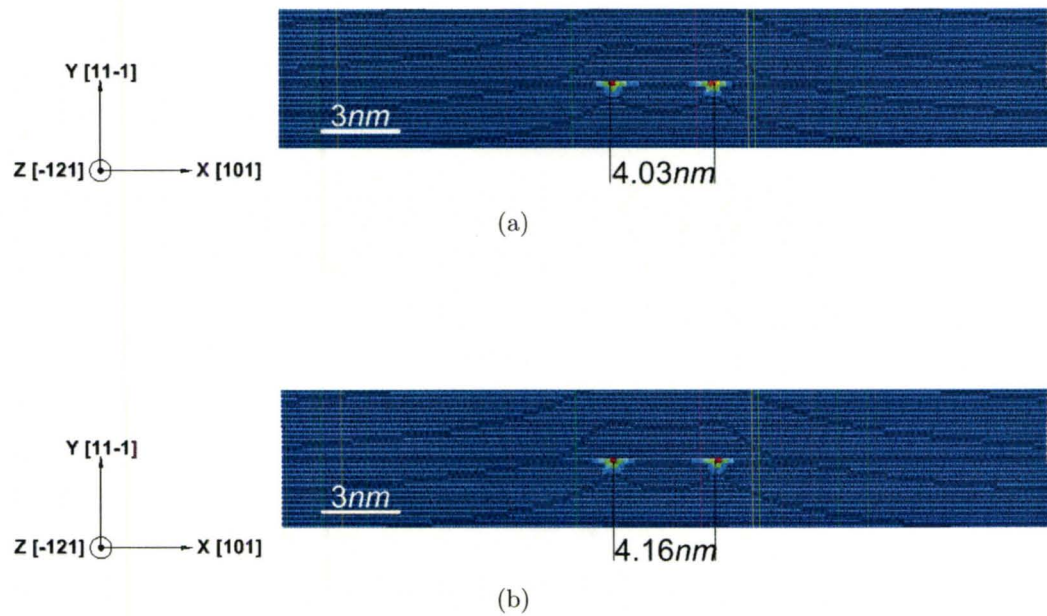
Figure 4.24: The positions of dislocations in relaxed configurations from initial models containing a perfect edge dislocation under two boundary conditions in the direction of the dislocation line (Z). (a) The benchmark result ($\ddot{c}_z = 0$); (b) The result from the model with traction $T_z = 0$.

(a)

(b)
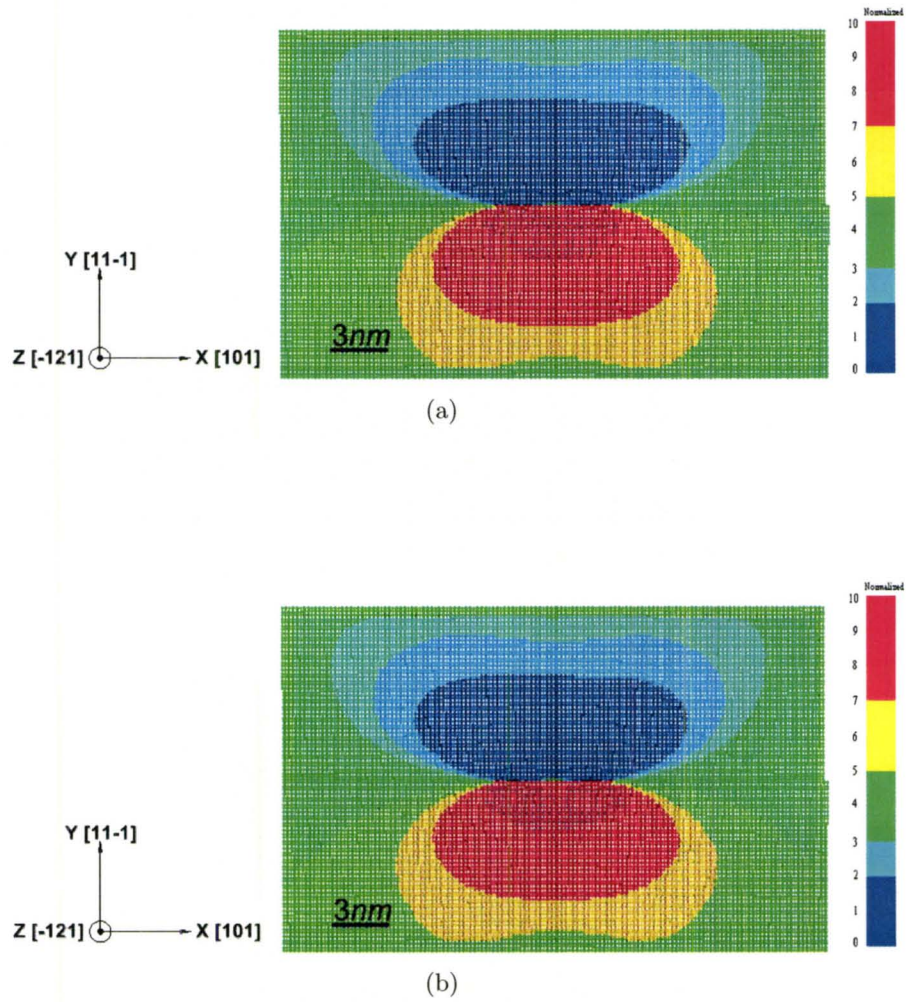
Figure 4.25: Normal stress component σ_{xx} in relaxed configurations from initial models containing a perfect edge dislocation under two boundary conditions in the direction of the dislocation line (Z). (a) The benchmark result ($\ddot{c}_z = 0$); (b) The result from the model with traction $T_z = 0$.

the external tension. The applied traction in the Z direction shrinks the lattice in X and Y directions, which is similar to the concept of the Poisson's ratio. Thus, the external compression in the Z direction generates tendency of moving outward in X and Y directions. Such effect in the X direction would push two partial dislocations to move far from their original distance of the stacking fault energy. However, the external tension in the Z direction applies the compression on the dislocations in the X direction. If two partial dislocations move closer than their original distance, the path of the relaxation is reversed, which needs high energy and is actually not favorable.

For tension cases, the strains of the periodic length in the Z direction corresponding to the length under zero traction are 6.0×10^{-4}, 1.2×10^{-3} and 2.4×10^{-3} respectively. For compression cases, strains are -5.8×10^{-4}, -1.15×10^{-3} and -2.27×10^{-3}. The slight differences of the strain from the external tension and compression are expected since the repulsive force and the attractive force derived from the potential energy are not symmetrical.

The curves of the potential energy minimization are shown in Figures(4.26) and (4.27) under the groups of the magnitude of the external traction. Figure(4.26) summarizes results from small and intermediate external traction. Due to the existence of the error explained in Section(4.2.1), the new periodic length in the Z direction is around the perfect value so that the final values of the potential energy are close to the reference value (benchmark result). Moreover, the potential energy gradually increases with the increase of the external traction because more and more extra energy is introduced into the system. Figure(4.27) shows results from large external traction. The values of the potential energy in this group have significant change from the reference value. Although the pattern of minimization curves is almost the same, the compression generates lower potential energy than the tension because partial
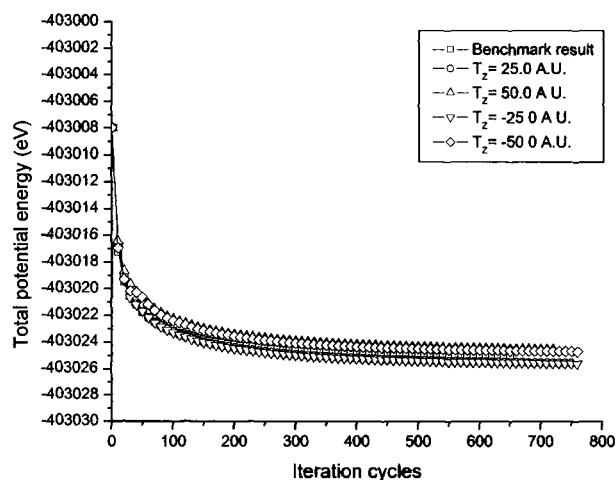
Figure 4.26: Potential energy as a function of the simulation time for the relaxation of initial models containing a perfect edge dislocation and subjected to small and intermediate external traction along the direction of the dislocation line (Z) (stop at the same tolerance value).
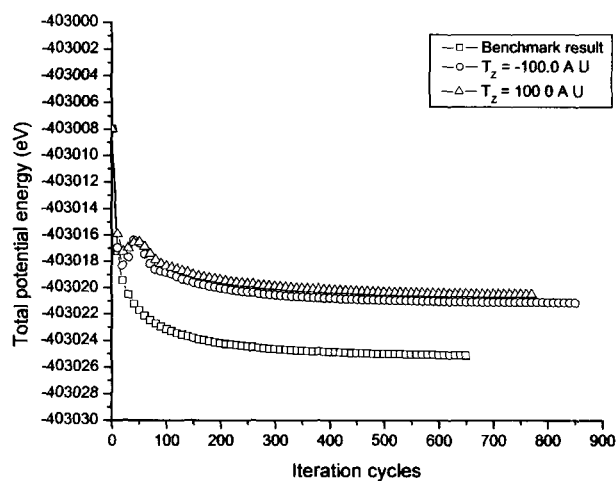
Figure 4.27: Potential energy as a function of the simulation time for the relaxation of initial models containing a perfect edge dislocation and subjected to large external traction along the direction of the dislocation line (Z) (stop at the same tolerance value).

dislocations with larger distance compensates some extra energy introduced by the external compression.

The most powerful evidence of the movement of partial dislocations is demonstrated by the disregistry of the edge component of the Burgers vector and corresponding approximate positions of partial dislocations. Figure(4.28) compares the edge components of the Burgers vector from the model with the external traction of 100.0 in arbitrary units and the benchmark model. It is obvious that there is almost no change in the calculation of the edge component of the Burgers vector in these two cases. Thus, the distance of two partial dislocations is maintained at $4.03nm$ as the reference model. However, the change becomes significant when the compression of -100.0 in arbitrary units is applied along the Z direction as shown in Figure(4.29). From the profile of the edge component of the Burgers vector, the curve from the model with the compression of -100.0 in arbitrary units shows the proportional expansion from the reference curve, which implies the distance between two partial dislocations visibly increases. Then the contour of the potential energy approximately indicates the distance becomes $4.54nm$ compared to the original $4.03nm$. The change of the distance is roughly equivalent to $2b$ in the slip (X) direction.

The contour pattern of the stress component σ_{xx} basically does not change when the traction is applied along the direction of the dislocation line. The small difference is due to the obvious shift of the origins of partial dislocations when the external compression is applied. However, the external traction adjusts the distribution of the stress component σ_{zz} significantly as shown in Figure(4.30). For the benchmark model, the profile of the stress σ_{zz} maintains the symmetrical contour of tension and compression. When the tension is applied, the area of compression decreases with the tensile stress gradually dominating the whole system as zero stress at boundary atoms becomes the lowest value. Contrarily, when the compression is
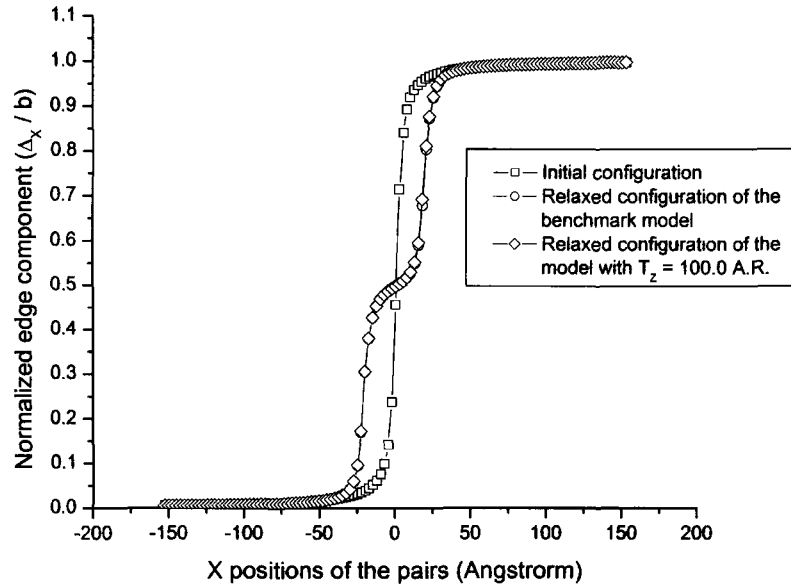
(a)

(b)

Figure 4.28: The comparison of relaxed configurations from initial models containing a perfect edge dislocation (i) with a constant periodic length in the direction of the dislocation line (Z) (benchmark), and (ii) subjected to the tension of 100.0 in arbitrary units along the direction of the dislocation line (Z). (a) The edge components of the Burgers vector determined by Disregistry; (b) The distance between two partial dislocations when the tension of 100.0 in arbitrary units is applied along the Z direction.
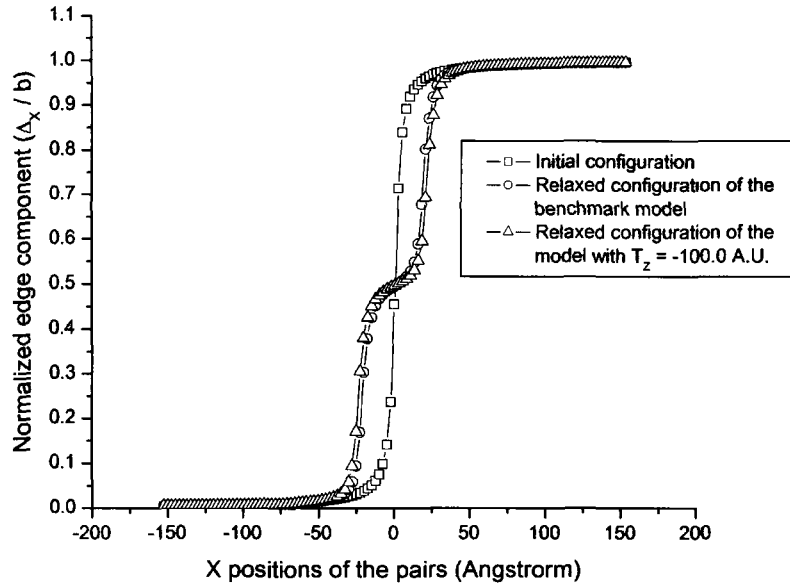
(a)

(b)

Figure 4.29: The comparison of relaxed configurations from initial models containing a perfect edge dislocation (i) with a constant periodic length in the direction of the dislocation line (Z) (benchmark), and (ii) subjected to the compression of −100.0 in arbitrary units along the direction of the dislocation line (Z). (a) The edge components of the Burgers vector determined by Disregistry; (b) The distance between two partial dislocations when the compression of −100.0 in arbitrary units is applied along the Z direction.

(a)

(b)

(c)
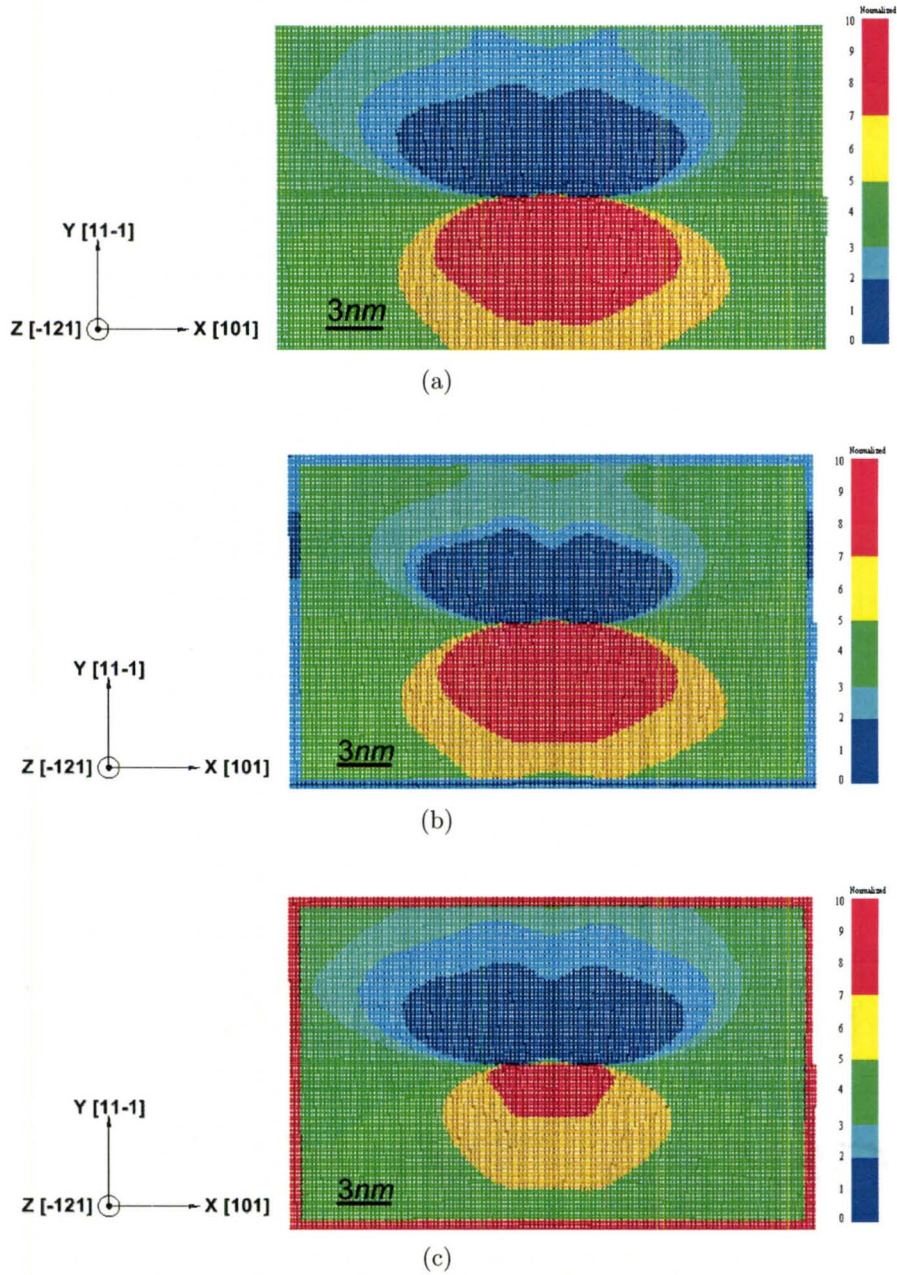
Figure 4.30: Normal stress component σ_{zz} in relaxed configurations from initial models containing a perfect edge dislocation under various boundary conditions in the direction of the dislocation line (Z). (a) The benchmark result; (b) The tension of 100.0 in arbitrary units applied along the Z direction; (c) The compression of -100.0 in arbitrary units applied along the Z direction.

applied, the area of tension reduces significantly.

For the case of the compression of -100.0 in arbitrary units applied along the Z direction, two different damping ratios 0.5 and 0.05 are used in the simulation. After the relaxation, the strains of the periodic length are -2.27×10^{-3} with damping ratio 0.5 and -2.32×10^{-3} with damping ratio 0.05. The comparison of the total potential energy and the edge component of the Burgers vector is shown in Figures(4.31) and (4.32). There is almost no change in the final values of the potential energy with two damping ratios. However, the lower damping ratio causes the oscillation of the relaxation path approaching the equilibrium so that the iteration cycle in the case using lower damping ratio is about 25% more than the case using the higher damping ratio. The edge components of the Burgers vector in two cases show the same trend but there is some discrepancy for a couple of pairs of atoms. According to previous results, the movement of partial dislocations in the model with damping ratio 0.05 is more than in the model with damping ratio 0.5 (less than half b). Considering the numerical noise introduced by a lower damping ratio, in this case, the damping ratio does not affect results very much.

In short, small external traction along the direction of the dislocation line does not alter the relaxation of the model containing a perfect edge dislocation. With large external compression along the direction of the dislocation line, there are obvious movements of the origins of Shockley partial dislocations, which increases the separation between two partial dislocations.

4.3   Two dimensional external traction

For dislocation models, two dimensional external traction is normally applied along the direction of the dislocation line (Z) and the slip direction (X). The fixed boundary
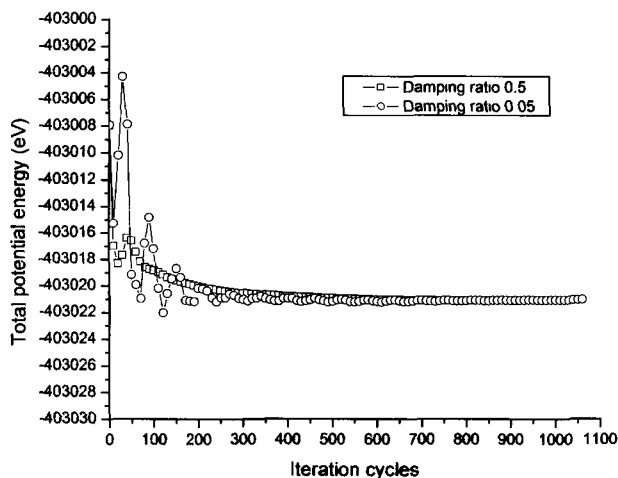
Figure 4.31: Potential energy as a function of the simulation time for the relaxation of initial models containing a perfect edge dislocation and subjected to the compression of -100.0 in arbitrary units along the direction of the dislocation line (Z) with damping ratios 0.5 and 0.05 (stop at the same tolerance value).
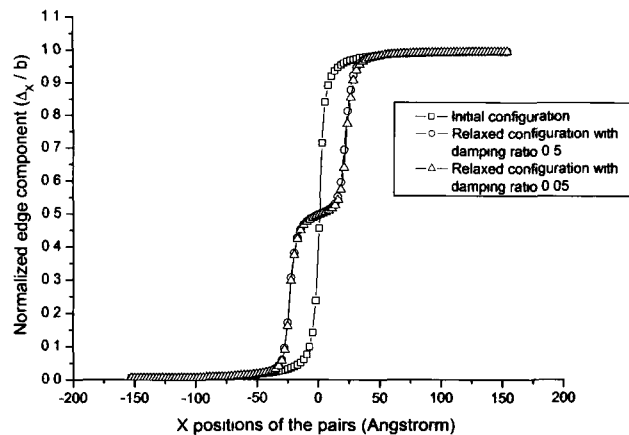
Figure 4.32: The comparison of the edge components of the Burgers vector in relaxed configurations from initial models containing a perfect edge dislocation and subjected to the compression of -100.0 in arbitrary units along the direction of the dislocation line (Z) with damping ratios 0.5 and 0.05. The edge component is determined by Disregistry.

113

condition is applied to the physical boundary atoms in the third direction (Y).

4.3.1 Two dimensional external traction in the perfect lattice

The perfect lattice is adopted from the model used for one dimensional external traction and the dimension is shown in Figure(4.20). The damping ratio is 0.5 and the tolerance is 0.001. Various boundary treatments as $T = 0$ and $\ddot{c} = 0$ in the new periodic symmetry are applied in X and Z directions, and the responses of the change of the periodic length are summarized in Table(4.1).

In cases of 1 and 2, under the approximately same condition as the fixed periodic length in the X direction, the deviation of the periodic length in the Z direction from the perfect value is reduced more than half, which supports the previous statement that applying the periodic symmetry in more than one direction would trim the error down.

Cases 3 and 4 both reveal that the periodic length in the X direction is stretched rather than shrunk as it is in the Z direction under zero external traction. The difference is due to the orientation of a model in X and Z directions, in which the interatomic distances between atoms are $0.255nm$ and $0.442nm$, respectively. Using the lattice parameter a as $0.3615nm$, one can determine that there is the repulsive force dominated in the X direction while the attractive force in the Z direction. Moreover, the decrease of the periodic length in the Z direction increases the periodic length in the X direction and vice verse because of the Poisson's effect. Therefore, the error in Case 4 is the largest one among four cases.

By comparing Case 2 and Case 3, it is found that the strain in the X direction is larger than it in the Z direction. There may be possible two reasons: (i) the total extra traction introduced by boundary atoms with fewer neighboring atoms along the

114

Table 4.1: The strains of the periodic length in X and Z directions of a perfect lattice when $T = 0$ or $\ddot{c} = 0$ is applied.

Case	Boundary	Perfect length (nm)	New length (nm)	Strain
1	X: Fixed	X: 25.306291	X: 25.306291	0.0%
	Z: $T_z = 0$	Z: 1.7709810	Z: 1.7689704	-0.11%
2	X: $\ddot{c}_x = 0$	X: 25.306291	X: 25.306291	0.0%
	Z: $T_z = 0$	Z: 1.7709810	Z: 1.7700669	-0.05%
3	X: $T_x = 0$	X: 25.306291	X: 25.324844	0.07%
	Z: $\ddot{c}_z = 0$	Z: 1.7709810	Z: 1.7709810	0.0%
4	X: $T_x = 0$	X: 25.306291	X: 25.343315	0.14%
	Z: $T_z = 0$	Z: 1.7709810	Z: 1.7686161	-0.13%

X direction is applied on the smaller YZ plane than the XY plane, which implies that the extra external traction on individual atoms in the YZ plane is larger or (ii) Young's modulus in the X direction is weaker than in the Z direction. In order to determine which reason is dominant, the elastic property along the X direction is investigated by applying a series of external traction on the YZ plane ($3.867 \times 10^{-17}m^2$). The stress-strain relationship is shown in Figure(4.33) as the new length along the X direction in Case 3 is used as the reference to calculate the strain. After performing the line regression analysis with $R = 0.997$, the Young's modulus along the X direction $< 1\ 0\ 1 >$ is estimated as $119.5GPa$, which is a little bit higher than $111GPa$ found along the Z direction $< -1\ 2\ 1 >$ but is still compatible with experimental data. Thus, the smaller area of YZ plane causes the larger strain in the X direction when zero external traction is applied.

4.3.2   Two dimensional external traction in the lattice with a dislocation

A perfect screw dislocation model shown in Figure(4.34) is used to examine the numerical responses after the two dimensional external traction is applied. The areas of XY plane and YZ plane are $1.03 \times 10^{-15}m^2$ and $2.23 \times 10^{-17}m^2$, respectively. The new periodic symmetry is applied in X and Z directions while physical boundary atoms are fixed in the Y direction. The dislocation line is along the Z direction and the dissociation occurs in the X direction. The damping ratio is chosen as 0.05, and for this lower damping ratio, a limit to the maximum number of computational cycle is introduced into the simulation to avoid unnecessary long-time small oscillation around the equilibrium. After the maximum computational cycle is reached, the corresponding tolerance is less than 0.005, which is good enough to be regarded as the equilibrium
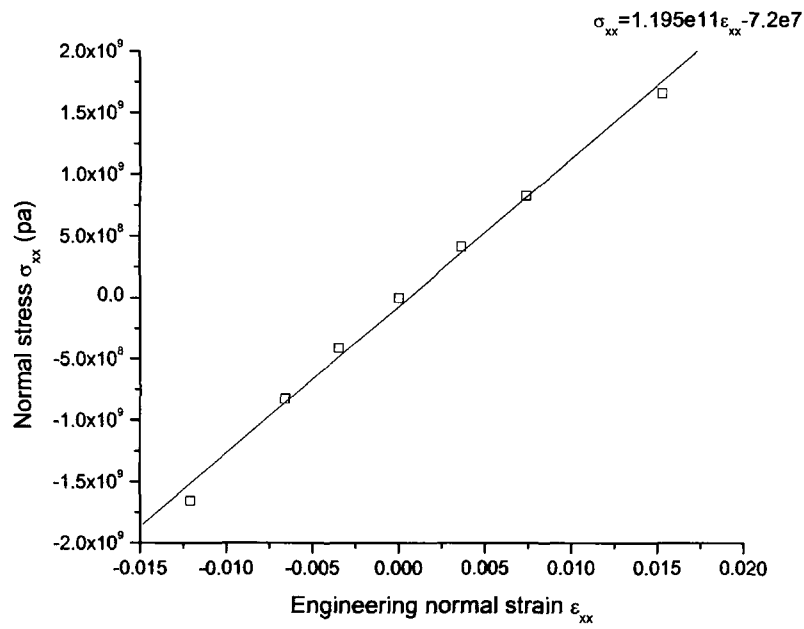
Figure 4.33: The relationship between normal stress σ_{xx} and strain ϵ_{xx} determined by a perfect copper lattice subjected to various external tension or compression.

state in the simulation.

As shown in Figure(4.35), when (i) $\ddot{c}_x = 0$ and $\ddot{c}_z = 0$, (ii) $T_x = 0$ and $\ddot{c}_z = 0$, (iii) $\ddot{c}_x = 0$ and $T_z = 0$, and (iv) $T_x = 0$ and $T_z = 0$, are applied respectively, all distances between two partial dislocations after the relaxation maintain $1.4nm$ as the benchmark. In the current configuration, the interatomic distance between adjacent atoms in the X direction is almost equal to the cut-off radius in the calculation of the potential energy and corresponding internal forces. Thus, the boundary atoms directly subjected to the external traction show some irregular motion when they are dragged out the cut-off distance from atoms in the inner lattice. However, these boundary atoms are not important to interpret the relaxed configuration in the area of the dislocation core.

At the first stage, the external traction is applied in the slip direction while the periodic symmetry with $\ddot{c} = 0$ is implemented along the direction of the dislocation line. Three tensile traction of 1.5, 3.0 and 6.0 in arbitrary units, are applied along the X direction, which are equivalent to the normal stress (σ_{xx}) $108MPa$, $216MPa$ and $432MPa$ applied on the YZ plane. The normal strains (ϵ_{xx}), according to the length in the zero external traction along the X direction, are 1.0×10^{-3}, 2.0×10^{-3} and 4.1×10^{-3} respectively. However, all the external tension does not change the relaxed configuration. As shown in Figure[4.36(a)], the screw components of the Burgers vector of two partial dislocations after the relaxation remain the same as from the zero tension despite the increase of the tensile force. The edge components of the Burgers vector of two partial dislocations are illustrated in Figure[4.36(b)], and are in the same trend from all cases. The small discrepancy between three cases is expected since the error of calculating Δ_x based on Equation(3.28) increases when the tension increases.

Similarly, external compressive forces are applied along the X direction in
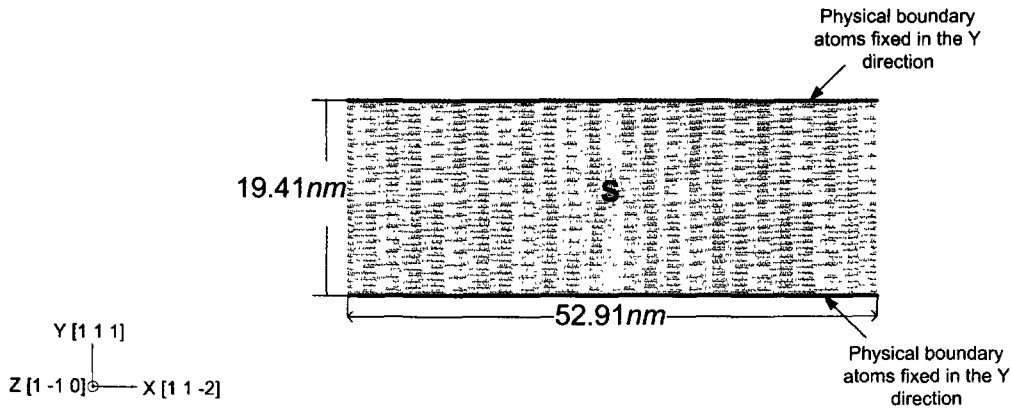
Figure 4.34: The geometry of a copper lattice containing a perfect screw dislocation subjected to the external traction along X and Z directions.
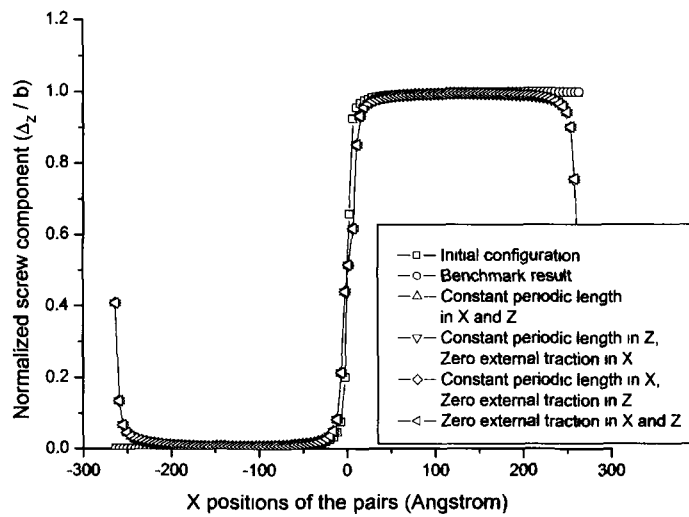
Figure 4.35: The comparison of the screw components of the Burgers vector in relaxed configurations from initial models containing a perfect screw dislocation under (i) $\ddot{c}_z = 0$ (benchmark result), (ii) $\ddot{c}_x = \ddot{c}_z = 0$, (iii) $T_x = 0$ and $\ddot{c}_z = 0$, (iv) $\ddot{c}_x = 0$ and $T_z = 0$, and (v) $T_x = T_z = 0$. The screw component is determined by Disregistry.

119
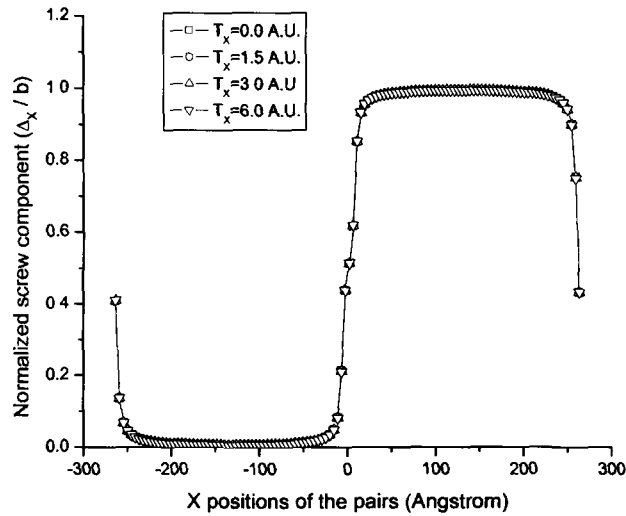
(a)
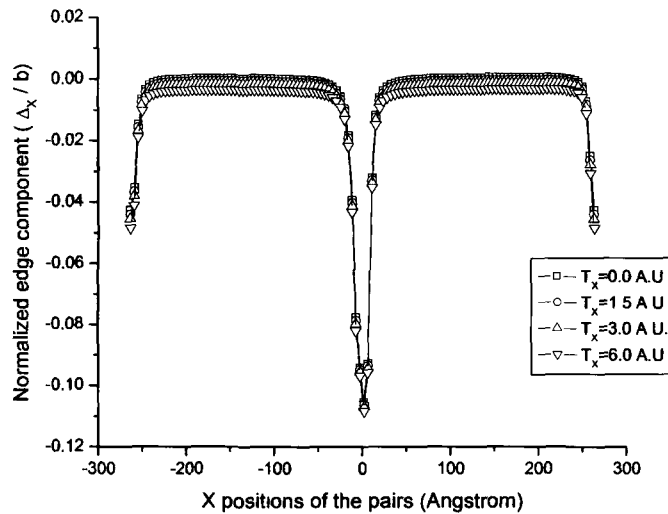
(b)

Figure 4.36: The comparison of relaxed configurations from initial models containing a perfect screw dislocation and subjected to various external tension along the slip (X) direction. (a) The screw components of the Burgers vector; (b) The edge components of the Burgers vector. (a) and (b) are determined by Disregistry.

the amount of -1.5, -3.0 and -6.0 in arbitrary units. The normal strains (ϵ_{xx}), according to the length in the zero external traction, are -0.97×10^{-4}, -1.9×10^{-3} and -3.7×10^{-3} respectively. The group of screw components and edge components of the Burgers vector in relaxed configurations are shown in Figure(4.37). Still, there are no obvious changes in all results compared to the case of zero external traction in the X direction. In short, for a perfect screw dislocation model, the external traction along the slip direction could not move two partial dislocations after the relaxation. However, the interatomic distance along the slip direction proportionally increases or decreases upon the external tension or compression.

In the second stage, the external traction is applied along the direction of the dislocation line while the periodic symmetry with $\ddot{c} = 0$ is implemented in the slip direction. In order to apply approximately the same stress on the XY plane as previous YZ plane, three external tension 70.0, 140.0, 280.0 in arbitrary units are used, which correspond to $110MPa$, $219MPa$ and $439MPa$ on the XY plane. The normal strains ϵ_{zz}, according to the new length in the zero external traction, are 1.0×10^{-3}, 2.1×10^{-3} and 4.2×10^{-3}, respectively. After the relaxation, two partial dislocations move closer in the slip direction with the increase of tensile stress in the Z direction, which is demonstrated in Figure(4.38). As discussed before, there are two relaxed configurations with minimum potential energy for the model containing a perfect screw dislocation calculated by higher or lower damping ratios. From the numerical point of view, the equilibrium distance between two partial dislocations is not stiff but in a limited range, so that it is possible that they could move closer during the relaxation. The range in the current calculation is between $b/2$ and b in the slip direction.

Contrarily, the same amount of external compression applied along the Z direction makes no change for the relaxation as shown in Figure(4.39), in which the screw
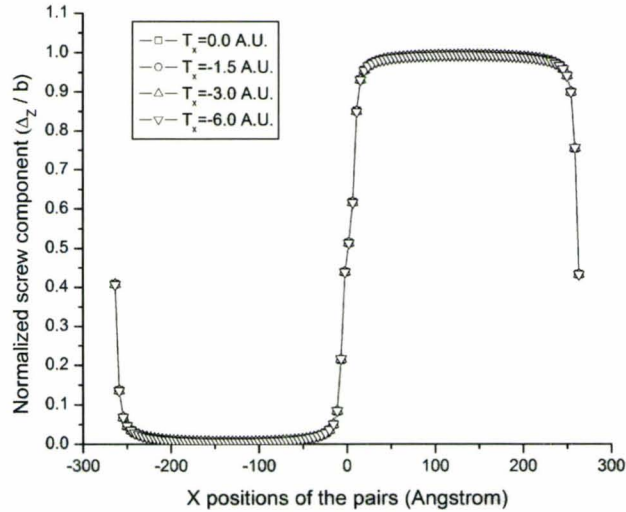
(a)
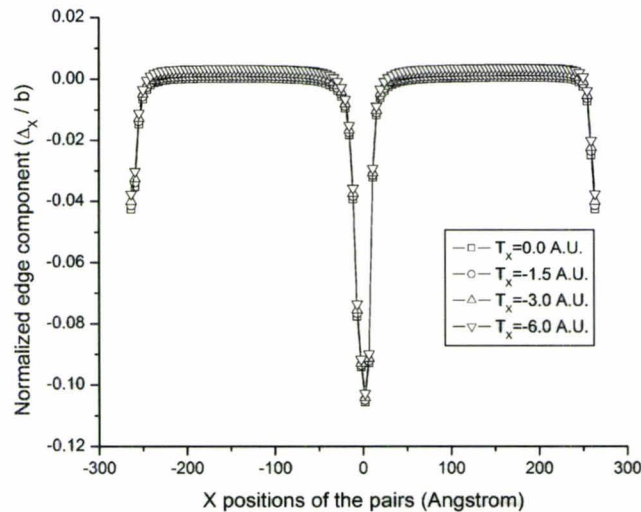
(b)

Figure 4.37: The comparison of relaxed configurations from initial models containing a perfect screw dislocation and subjected to various external compression along the slip direction (X). (a) The screw components of the Burgers vector; (b) The edge components of the Burgers vector. (a) and (b) are determined by Disregistry.
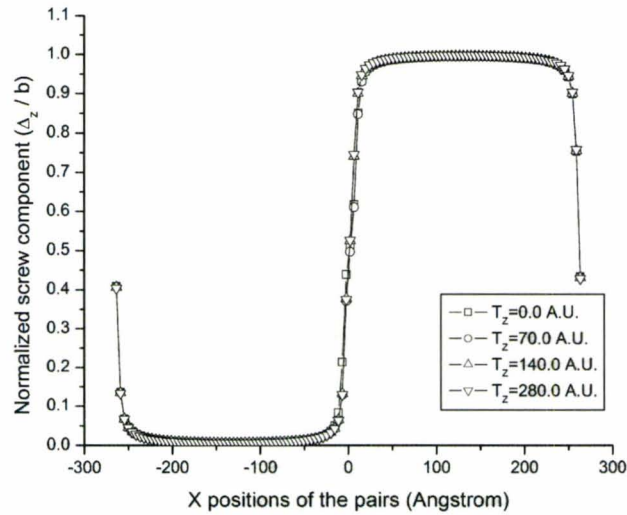
(a)

(b)

Figure 4.38: The comparison of relaxed configurations from initial models containing a perfect screw dislocation and subjected to various external tension along the direction of the dislocation line (Z). (a) The screw components of the Burgers vector determined by Disregistry; (b) The distance of two partial dislocations when the external tension of 280.0 in arbitrary units is applied.

and edge components of the Burgers vector remain the same despite the compression increases. The possible explanation could be that the distance of the stacking fault with a lower damping ratio is approaching its limit. With more distance between two partial dislocations, the basic configuration of the stacking fault would be broken, which is not energetic favorable. The corresponding normal strains ϵ_{zz} in cases are -9.9×10^{-4}, -2.0×10^{-3} and -3.8×10^{-3}, respectively.

As expected, when medium external traction is applied along the slip direction and the direction of the dislocation line, as shown in Figure(4.40), only the external tension in the direction of the dislocation line (Z) could change the relaxed configuration.

4.3.3 Discussion of the boundary treatment of an edge dislocation model subjected to two dimensional external traction

For a lattice model containing a perfect edge dislocation, although there is the same number of atoms in the defective and perfect models generated by a lattice creator code, the periodic length other than the direction of the dislocation line varies, e.g. the slip direction (X), due to the displacement field introduced by the dislocation. Different periodic lengths in one direction make it difficult to implement the new periodic symmetry. However, the new periodic symmetry should work in the slip direction theoretically. As shown in Figure(4.41), there are two image cells (dashed line) surrounding the primitive simulation cell (solid line) in the slip (X) direction. Thus, the shape of boundary layers A and A' (dash-dot line) should be the same because the effect on these layers from dislocations is identical. Due to the limitation of the lattice creator software, the model with dislocations is generated without considering
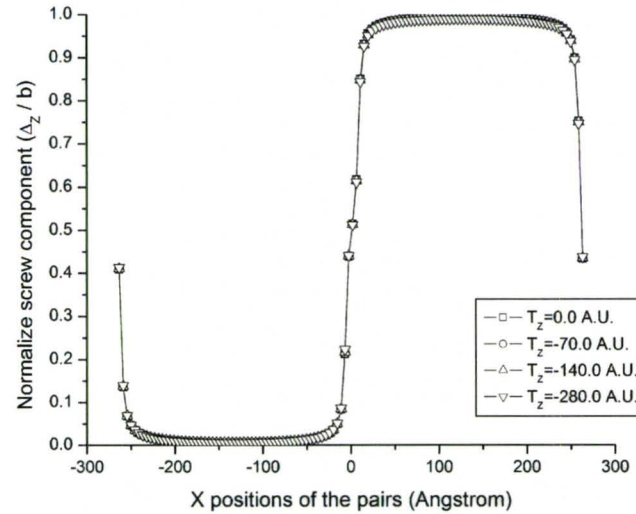
(a)
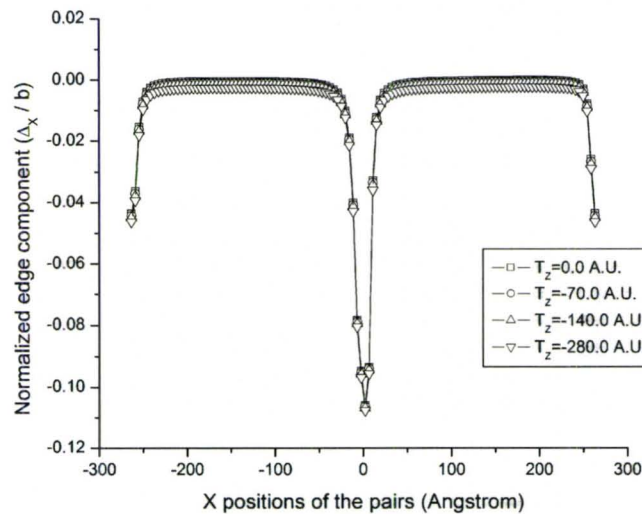
(b)

Figure 4.39: The comparison of relaxed configurations from initial models containing a perfect screw dislocation and subjected to various external compression along the direction of the dislocation line (Z). (a) The screw components of the Burgers vector; (b) The edge components of the Burgers vector. (a) and (b) are determined by Disregistry.

125
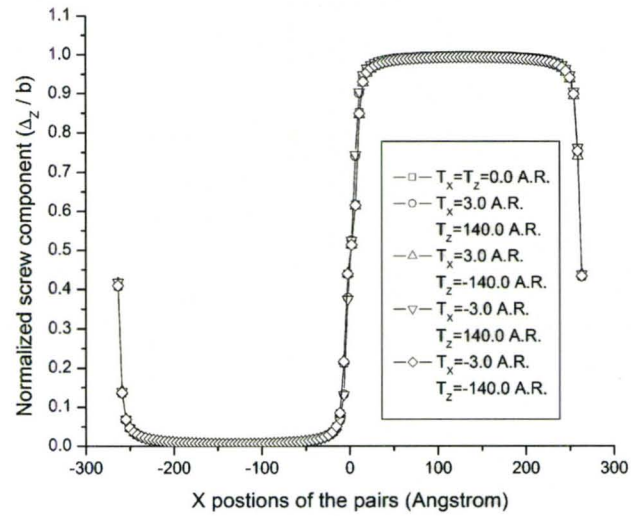
Figure 4.40: The comparison of the screw components of the Burgers vector in relaxed configurations from initial models containing a perfect screw dislocation and subjected to various external traction along the slip direction (X) and the direction of the dislocation line (Z). The screw component is determined by Disregistry.
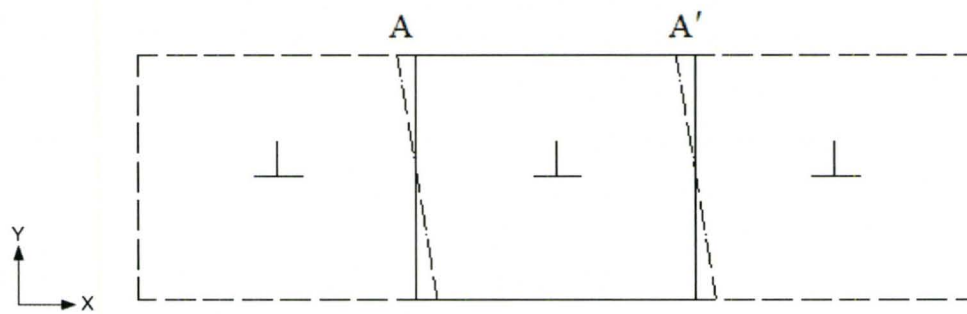
Figure 4.41: The schematic shapes of boundary layers A and A' of the perfect edge dislocation cell under the periodic symmetry in the X direction.

any periodic symmetry in any direction. In fact, any kind of the periodic symmetry applied to a single simulation cell somewhat destroys the displacement field on the boundary layer and the primitive cell is strained. Thus, the fixed boundary condition, which initially satisfies the displacement field, are widely used as long as the length in the slip direction is long enough. However, external normal or shear stresses are difficult to apply under the fixed boundary condition. In order to deploy two-dimensional periodic symmetry, there should be the pre-treatment of the boundary in the model.

Osetsky et al. [40] followed the idea by Daw et al. [11] to strain an edge dislocation model so that the periodic length in the slip direction is unique. Their dislocation models are generated by inserting an extra half plane of atoms into the center of the model, which is shown in Figure[4.42(a)]. Then the strained crystal is restored into a rectangular shape according to the value in the perfect lattice L as shown in Figure[4.42(b)]. The difference between the actual length in a row, such as $L + b/2$, and the perfect value L, is equally distributed to atoms on that row. If the number of atoms in one row is large enough, e.g. 200, the movement or the corresponding applied strain of individual atoms is small enough to be neglected. They indicated the approach is successful especially when the external shear stress is applied. However, the method is not suitable for dislocation models throughout this thesis. Current dislocation models are built up by squeezing interatomic distances between atoms in the upper or lower half of the crystal. Osetsky's treatment actually reverses the process of the generation of an edge dislocation in the current approach of the lattice creation. Therefore, the relaxation yields the perfect lattice rather than the dissociation.

Another possible treatment is to shift boundary atoms (one half at each side) to maintain the periodic length according to the length in the perfect lattice as shown in Figure(4.43) [43]. Moving pairs of atoms from their initial positions is equivalent to

(a)

(b)
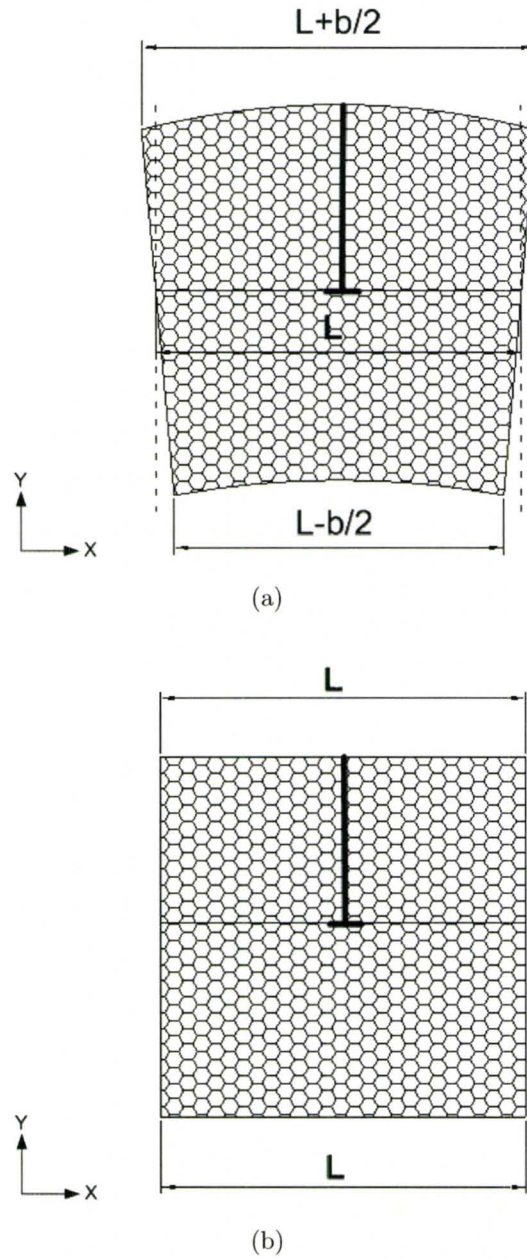
Figure 4.42: An edge dislocation in an unstrained crystal (a) and in a strained crystal after the unbending into a rectangular shape (b) [40].

applying different stresses on pairs of boundary atoms in the slip direction. Therefore, the lengths of some rows are stretched under tension while some rows are shrunken under compression. The periodic length could be chosen as its perfect value without any defects. The change of the positions of boundary atoms could result in the stress increase for atomic layers adjacent to the boundary, and the stress is assumed to be relaxed during the simulation due to no kinematic restriction in the slip direction. Although this treatment does not change any configuration in the area of the dislocation core, the relaxation of the extra stress would affect the dissociation of the perfect edge dislocation. Furthermore, it is difficult to distinguish this effect from the extra stress introduced by the boundary treatment or the applied stress. Thus, only for the quantitative study, this treatment could be used for a large model providing that the effect from the extra stress is small.

The above two treatments are feasible only for the model containing one perfect edge dislocation. Otherwise, excessive correction of atomic positions causes instability in the simulation. Therefore, at the current stage, the developed new periodic symmetry method could be applied along the direction of the dislocation line and the slip direction in all screw dislocation models and in models containing edge dislocation dipoles. The eventual solution for implementing the new periodic symmetry method to any type of dislocation models is to further develop the lattice creation framework based on the view of the periodic symmetry of the lattice, which is in line with the basic assumption of the atomistic simulation.
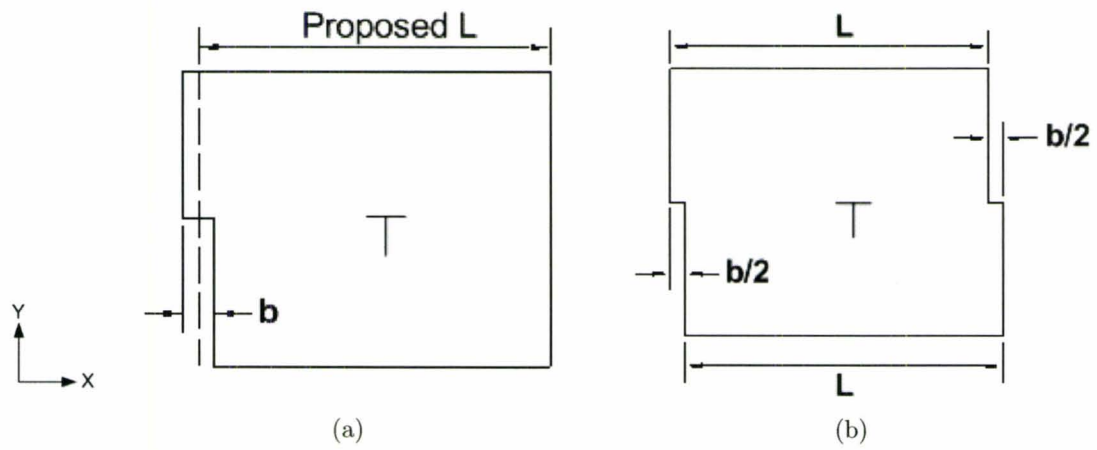
Figure 4.43: An edge dislocation in an unstrained crystal (a) and in a strained crystal after the boundary is treated to adapted to the new periodic symmetry (b).

Chapter 5

Interactions between two dislocations

The chapter discusses interactions between two dislocations simulated by the new energy minimization framework. The cases of two dislocations include a pair of edge dislocations, screw dislocations and 60-degree dislocations. Two dislocations are placed on the same slip plane, parallel slip planes and on inclined slip planes. The possible interactions between two opposite dislocations include annihilation, the formation of faulted dipoles and the formation of perfect stable dipoles. The numerical responses of applying external traction to models containing dislocation dipoles are investigated as well.

5.1 Two edge dislocations on the same slip plane

Crystal models containing two edge dislocations on the same slip plane are used to validate the DR-based new energy minimization method. These results can easily be verified against well established theory of dislocations [26]. The cases include two

edge dislocations with the same Burgers vector and opposite Burgers vectors gliding on the same slip plane.

5.1.1   Two edge dislocations with the same Burgers vector

The simulation model is the cubic copper lattice shown in Figure[4.1(a)]. Two perfect dislocations with the Burgers vector $\mathbf{b} = (a/2)[1\ 0\ 1]$ are introduced into the model using the anisotropic elasticity theory. These two dislocation lines are parallel to each other and are oriented along the Z direction. The boundary conditions for the simulation are (i) the physical boundary atoms are fixed in X and Y directions; (ii) the periodic length is constant in the Z direction ($\ddot{c}_z = 0$). The damping ratio is 0.5 and the tolerance is 0.001.

According to the theory of dislocations, when two parallel perfect dislocations with the same sign of the Burgers vector $\mathbf{b}$ lie on the same slip plane and are very close to each other, i.e. with the spacing $0.5nm$, the effective Burgers vector of such configuration could be assumed as $\mathbf{2b}$. The total potential energy is calculated from the Frank's rule:

$$E_{initial} = \alpha\mu(2b)^2 = 4\alpha\mu b^2 = 4\alpha\mu\frac{a}{4}[1^2 + 0^2 + 1^2] = 2\alpha\mu a^2 \tag{5.1}$$

where a is the lattice constant, μ is the shear modulus and α is a coefficient which is identical for the same type of dislocations. Since the lattice is not stable due to the high-energy state, the pair of dislocations tends to repel each other in order to reduce the energy, which is depicted in Figure(5.1). When the distance between two dislocations is large enough, the total potential energy becomes

$$E_{relaxed} = \alpha\mu(b)^2 + \alpha\mu(b)^2 = \alpha\mu\frac{a}{4}[1^2 + 0^2 + 1^2] + \alpha\mu\frac{a}{4}[1^2 + 0^2 + 1^2] = \alpha\mu a^2 \tag{5.2}$$

(a)

(b)
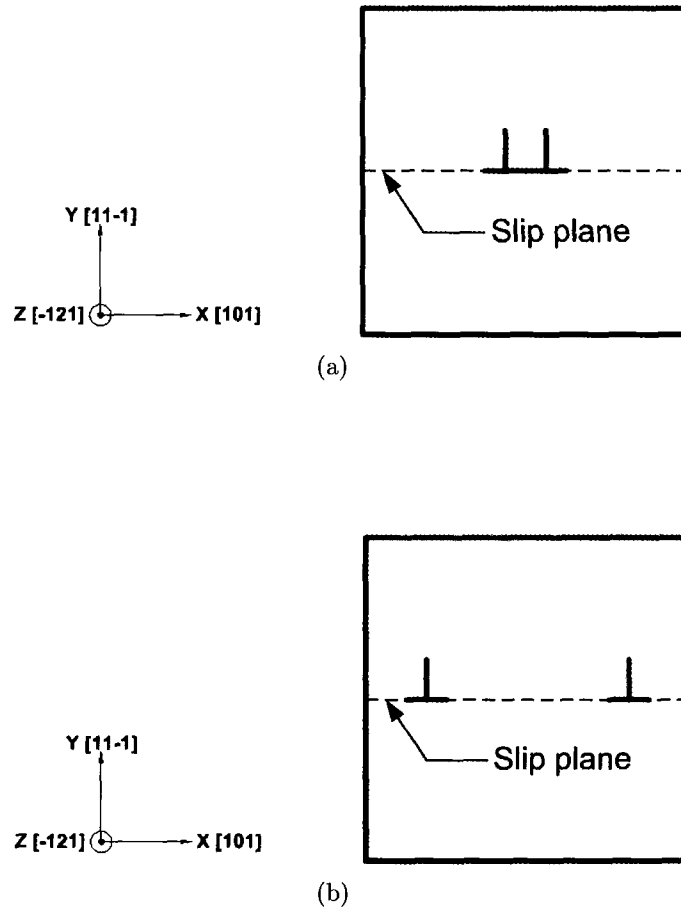
Figure 5.1: The schematic configurations of two edge dislocations with the same Burgers vector gliding on the same slip plane. (a) The initial model; (b) The relaxed model according to the theory of dislocations.

Therefore, the movement of dislocations is energetically feasible.

A perfect edge dislocation is not stable in the crystal lattice and would split into two Shockley partial dislocations to reduce the energy. The splitting and corresponding energy change is given by Equations(4.1) to (4.3). Therefore, in this case, two perfect edge dislocations dissociate into four partial dislocations in the relaxed configuration as shown in Figure(5.2). It is found that the separation of partial dislocations increases for both perfect edge dislocations compared to the benchmark result, i.e. $4.03nm$. This is because one perfect edge dislocation is subjected to the repulsive force from the other one. It is expected that such force would change the relaxed configuration to some extent. However, the increase of the separation is not symmetrical. The length of the stacking fault in the left pair is larger than the right pair within one interatomic distance b. It is not clear why the relaxation in two perfect dislocations is not identical. The possible reason could be that the system achieves a local energy minimum at this configuration.

The assumption, that two closely positioned dislocations with the same Burgers vector b could be regarded as a larger dislocation with Burgers vector $2b$, is supported by the stress profiles. In Figure(5.3), the stress contours of σ_{xx}, σ_{yy} and σ_{xy} in the initial configuration follow the same pattern as the benchmark (one perfect edge dislocation). The stress contours of the relaxed configuration also clearly illustrate the dissociation of two perfect edge dislocations into four Shockley partial dislocations. Every pair of partial dislocations is compatible to the benchmark (relaxed lattice of a perfect edge dislocation). Figure(5.4) demonstrates the intermediate process during the relaxation, which reveals that the movement and dissociation of two perfect edge dislocations occur simultaneously in the beginning, and there is no obvious sequence of actions during the rest of the simulation time.
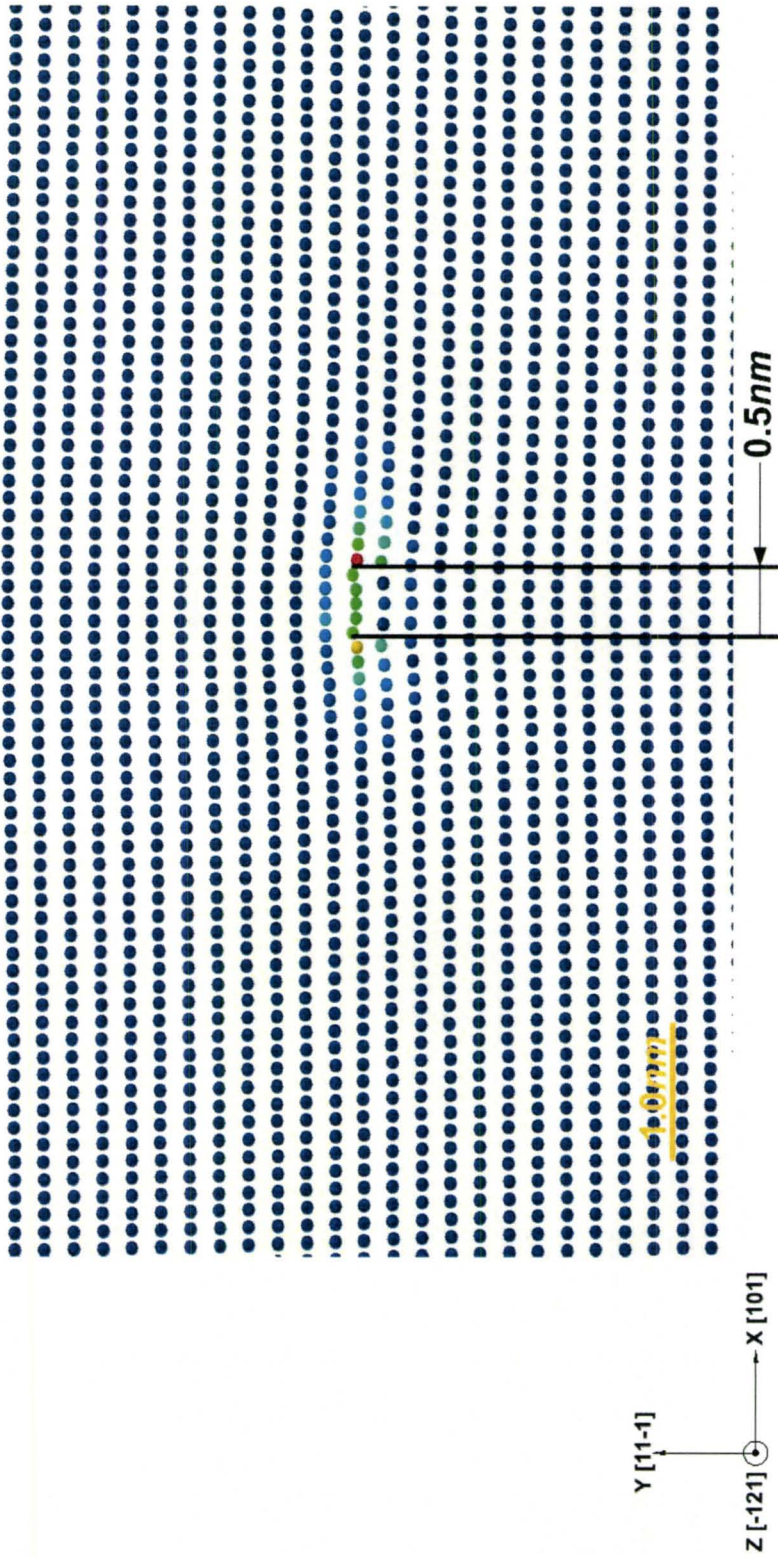
(a)
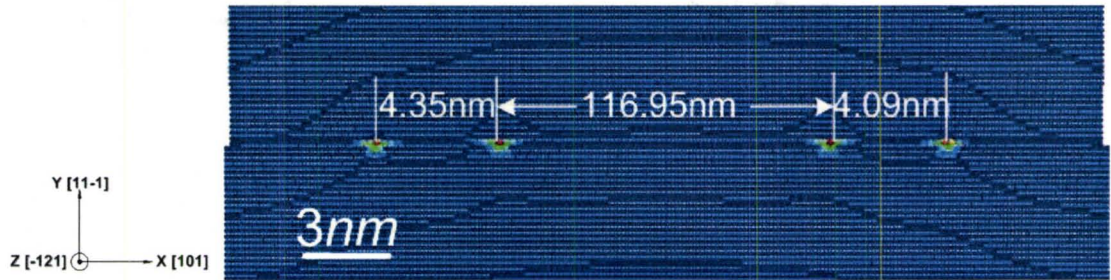
(b)
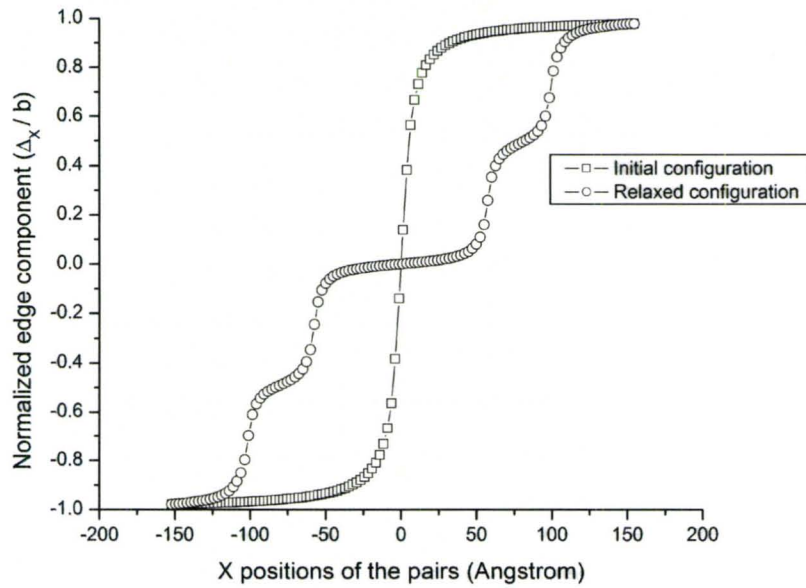
(c)

Figure 5.2: The relaxation of two prefect edge dislocations with the same Burgers vector gliding on the same slip plane. (a) The initial configuration; (b) The relaxed configuration; (c) The analysis of the edge components of the Burgers vector in (a) and (b) by Disregistry.
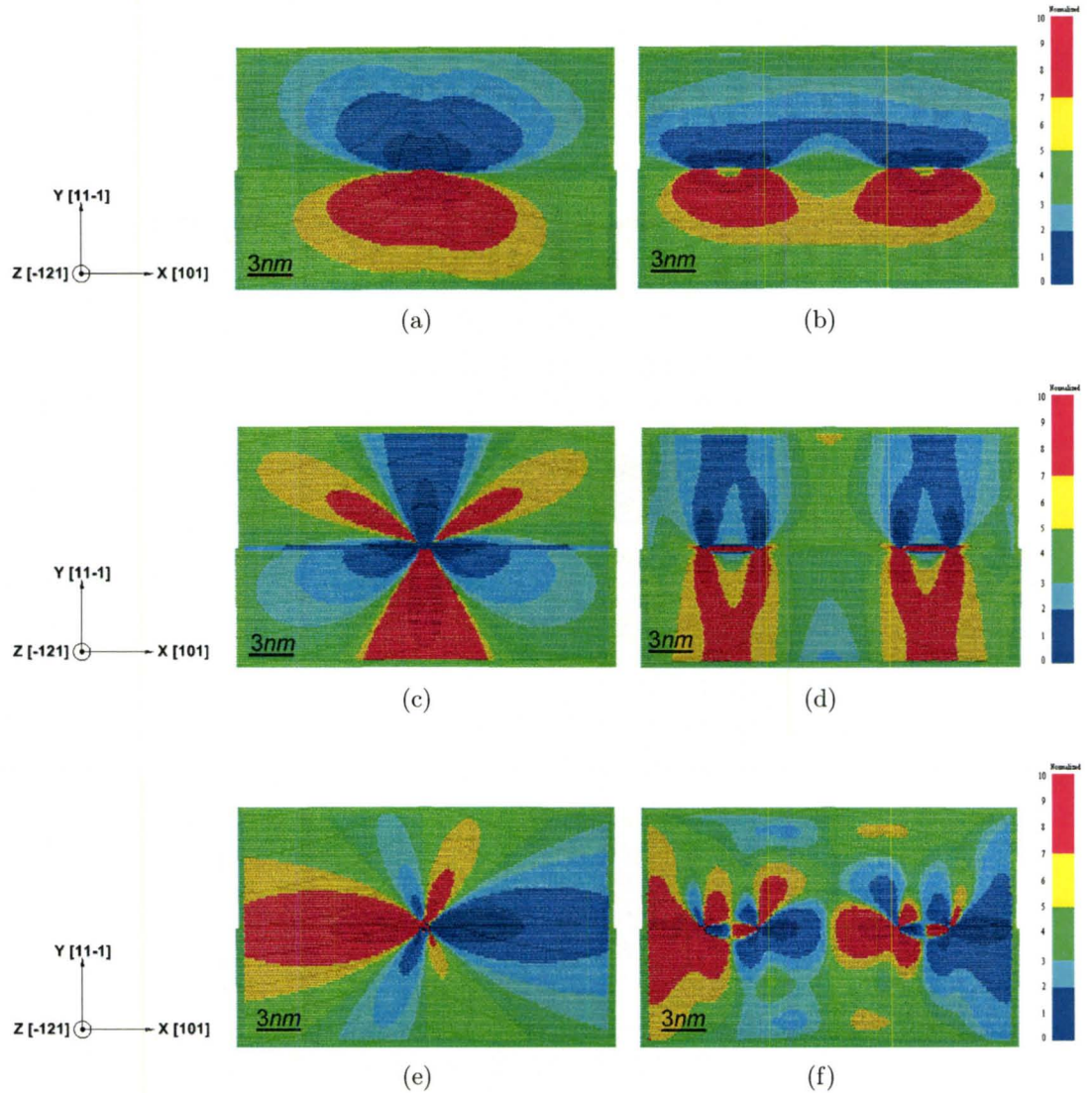
Figure 5.3: The stress components of the initial and relaxed configurations in the relaxation of two perfect edge dislocations with the same Burgers vector gliding on the same slip plane. (a) σ_{xx} in the initial configuration; (b)σ_{xx} in the relaxed configuration; (c)σ_{yy} in the initial configuration; (d) σ_{yy} in the relaxed configuration; (e)σ_{xy} in the initial configuration; (f) σ_{xy} in the relaxed configuration.
[Note: (1) red color represents atoms with highest stress (positive values) and blue color represents atoms with the lowest stress (negative values); (2) the scale of stress values in the initial and relaxed models is not the same.]
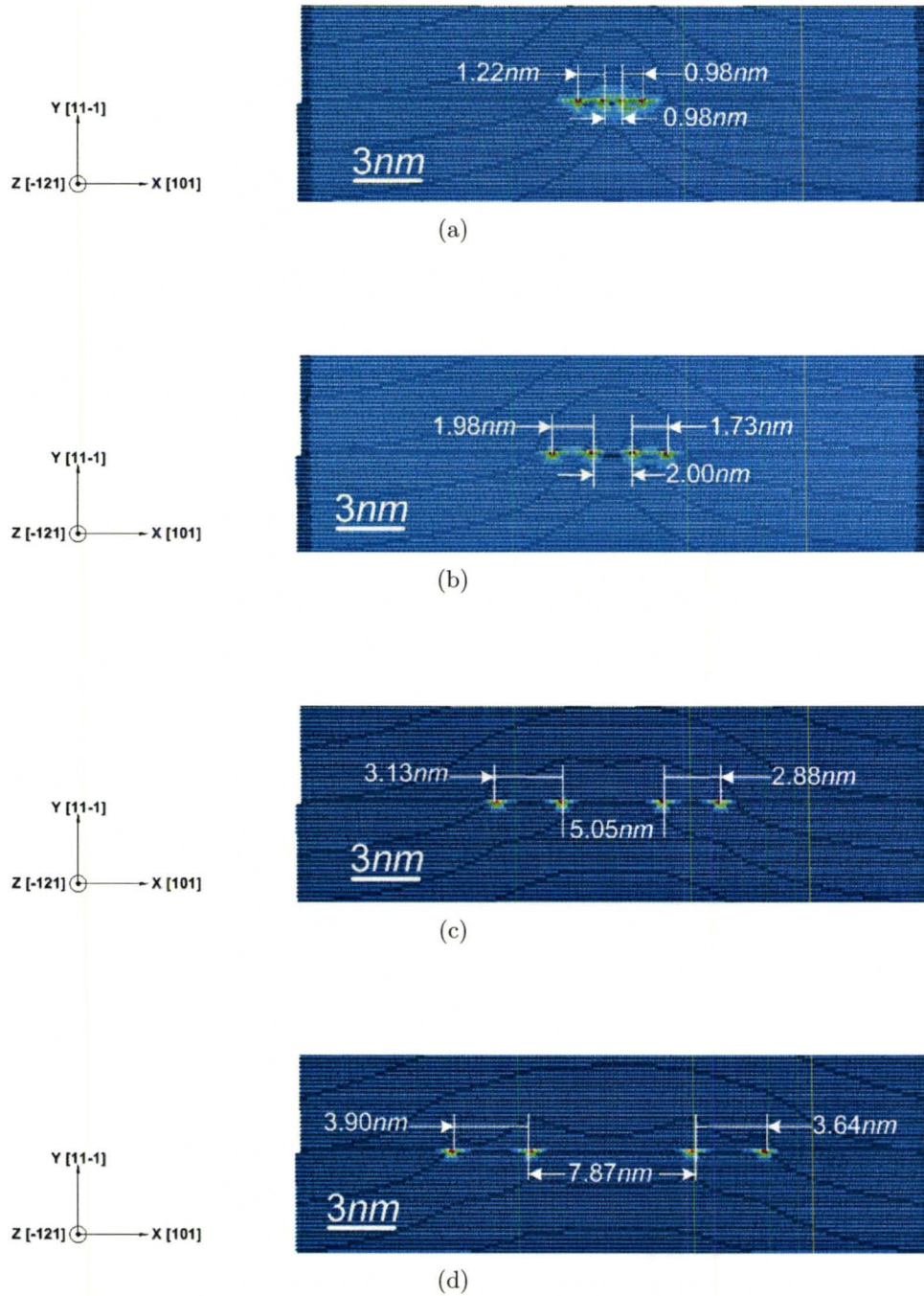
Figure 5.4: The positions of dislocations during the relaxation of two perfect edge dislocations with the same Burgers vector gliding on the same slip plane. (a) Cycle No: 50; (b) Cycle No: 100; (c) Cycle No: 300; (d) Cycle No: 600.

5.1.2   Two edge dislocations with the opposite Burgers vectors

Two dislocations with the opposite Burgers vectors are introduced on the same slip plane and the dislocation lines are parallel to each other. There are two configurations in the initial model shown in Figures[5.5(a)] and [5.5(b)]. At first, two dislocations are set in a limited distance $8nm$ apart so that the energy in the initial model is the same as given in Equation(5.2). This pair of dislocations tends to attract each other to reduce the energy. When these two dislocations move closer and closer, the effective magnitude of the Burgers vector is zero. In practice it means that such dislocations annihilate and the model inherits the perfect lattice as shown in Figure[5.5(c)], whose potential energy is apparently the global minimum, which is in agreement with the principles of the dislocation theory.

The boundary conditions are initially set to be the same as in the case of two perfect edge dislocations with the same Burgers vector. After the relaxation, the results show no difference between two initial configurations. As shown in Figure(5.6), the energy contour in the relaxed configuration does not show any color gradient, which implies there is no dislocation existing in the model and the annihilation occurs between this pair of perfect edge dislocations. The analysis of the Burgers vector shown in Figure(5.7) illustrates the edge component is zero in both relaxed configurations, which is also the evidence that these two dislocations annihilate during the relaxation.

During the simulation, as expected, the attractive force between these two dislocations does not prevent these dislocations dissociating into partial dislocations. From the total potential energy minimization curve shown in Figure[5.8(a)], there are two steep drops located at regions A and B, which implies that one pair of partial
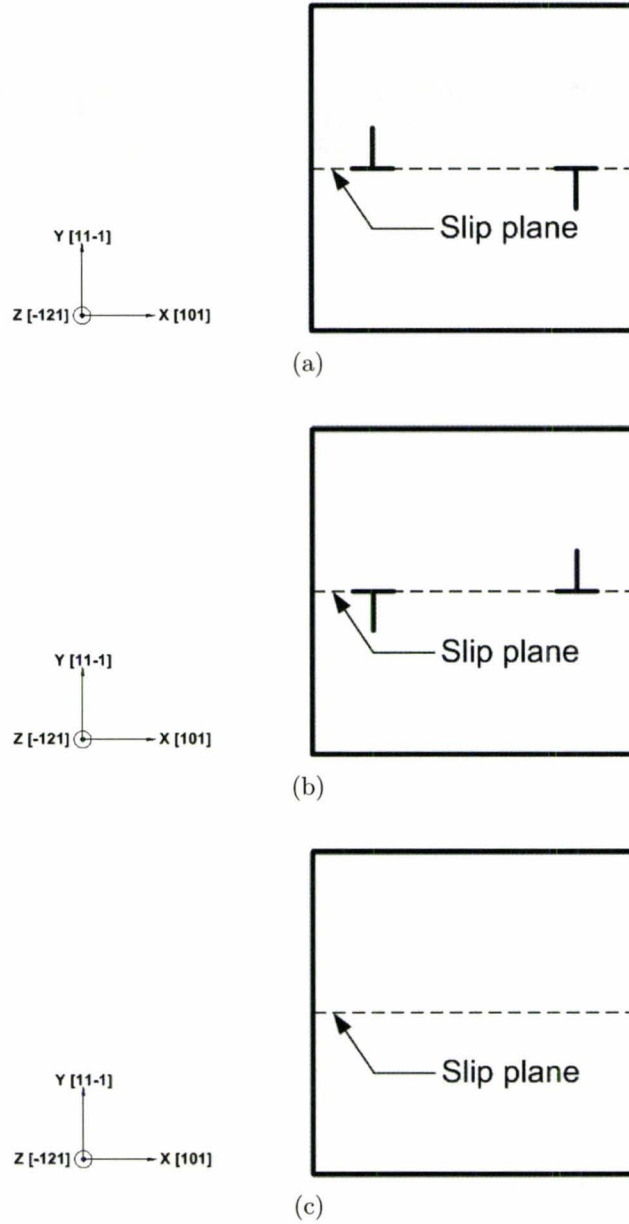
Figure 5.5: The schematic configurations of two perfect edge dislocations with the opposite Burgers vectors gliding on the same slip plane. (a) Initial configuration I; (b) Initial configuration II; (c) The relaxed dislocation-free model.
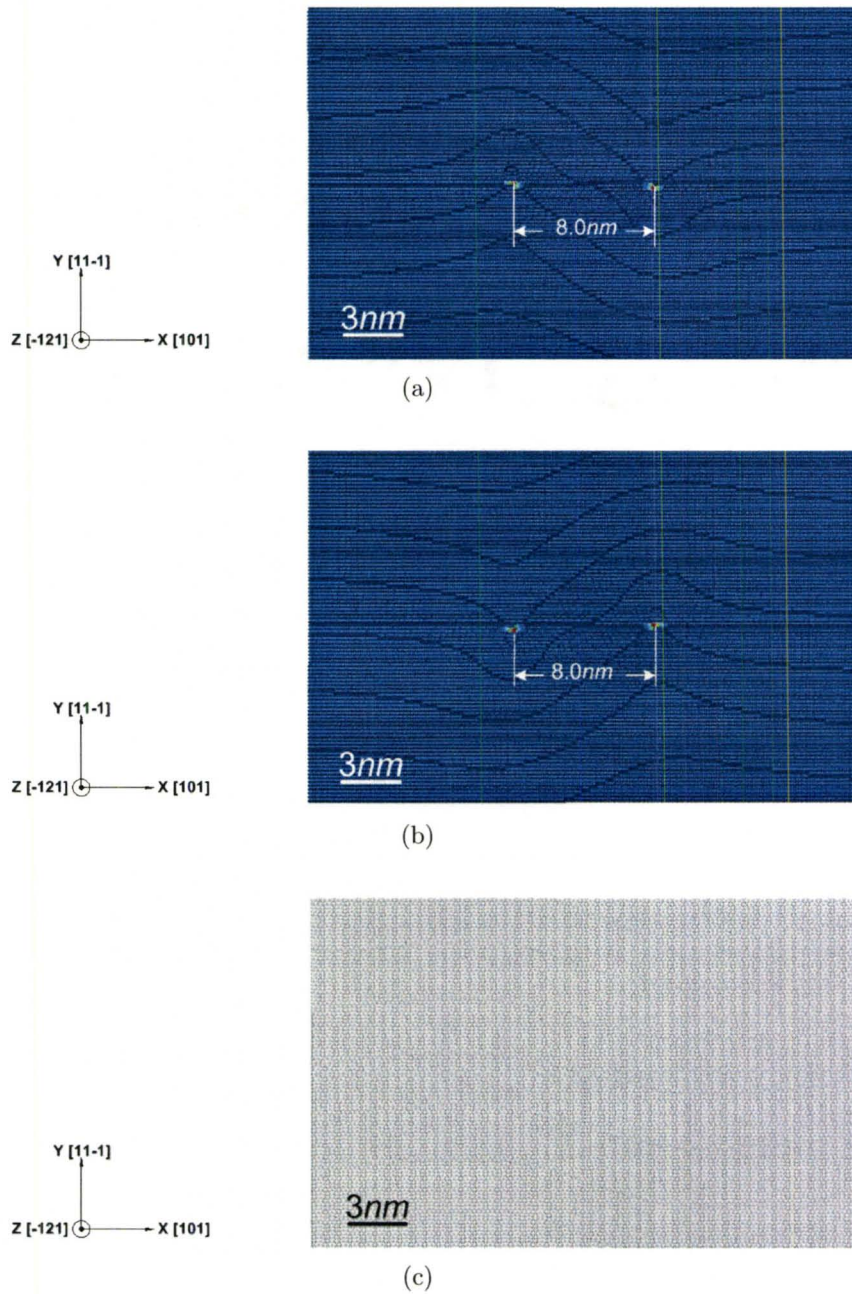
Figure 5.6: The positions of dislocations in the relaxation of two perfect edge dislocations with the opposite Burgers vectors gliding on the same slip plane. (a) The initial configuration corresponding to Figure[5.5(a)]; (b) The initial configuration corresponding to Figure[5.5(b)]; (c) The relaxed configuration.
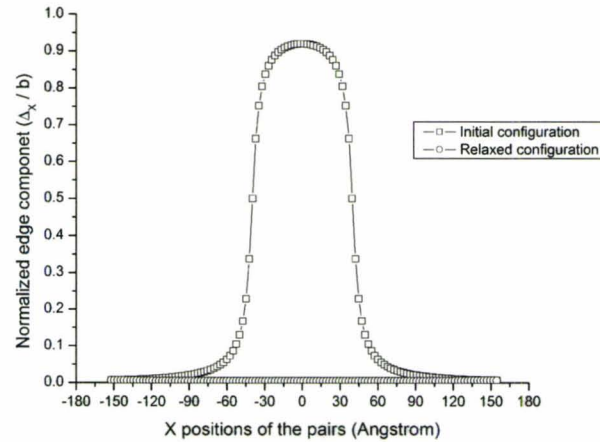
(a)
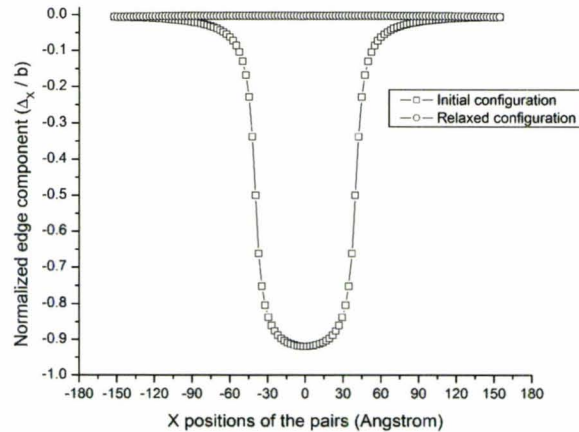
(b)

Figure 5.7: The analysis of the edge components of the Burgers vector in the initial model containing two perfect edge dislocations with the opposite Burgers vectors gliding on the same slip plane, and in the corresponding relaxed configuration. (a) Configuration I corresponding to Figure[5.5(a)]; (b) Configuration II corresponding to Figure[5.5(b)]. The edge component is determined by Disregistry.

dislocations annihilates followed by another annihilation of partial dislocations. This is supported by Figures[5.8(b)] and [5.8(c)], which show the configurations of the model entering the regions A and B.

Under current boundary conditions, though two dislocations could annihilate in the center of the model, the residual stress σ_{xx}, is built up across the boundary in X and Y directions as shown in Figure(5.9). The reason for this is the propagation of the stress wave to the fixed boundary walls. The problem could be partially solved by replacing fixed boundary condition with the periodic symmetry in the slip (X) direction. Thus, a new set of the boundary condition is to (i) apply the periodic symmetry to both X and Z directions and (ii) fix physical boundary atoms in the Y direction.

Figure(5.10) compares the stress component σ_{xx} in relaxed configurations under two conditions that $T_x = \ddot{c}_z = 0$ and $\ddot{c}_x = \ddot{c}_z = 0$, in which $\ddot{c}_x = 0$ is equivalent to the traditional periodic symmetry method applied to the X direction. It is found that no residual stress accumulates in the X direction and the residual stress only exists in the Y direction after two boundary conditions are applied. However, the stress distribution is not similar in these two cases. The lowest stress is not fully relaxed in the center of the model when $\ddot{c}_x = 0$ is applied. In the case of $T_x = 0$, the stress is relaxed and becomes flat in the center but the whole model is under the tensile stress. Such difference of the stress profile σ_{xx} in two cases is due to the change of the periodic length in the X direction. When $T_x = \ddot{c}_z = 0$, there is the trend of the expansion of the periodic length in the X direction because of the error, which is explained in Section(4.2.1). The periodic length in the X direction is correspondingly changed from $30.674nm$ to $30.694nm$ and the normal strain ϵ_{xx} is around 0.07%, which is compatible to the case shown in Table(4.1). Thus, such strain causes the small internal tensile stress in the whole model. However, in the case of $\ddot{c}_x = \ddot{c}_z = 0$,
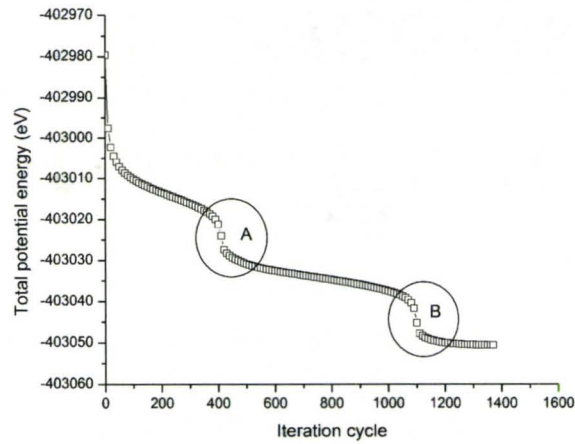
(a)
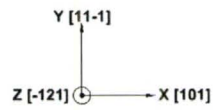
(b)
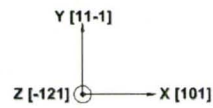
(c)

Figure 5.8: The relaxation of two perfect edge dislocations with the opposite Burgers vectors gliding on the same slip plane. (a) The total energy minimization curve; (b) The intermediate configuration of A region in (a); (c) The intermediate configuration of B region in (a).

(a)

(b)
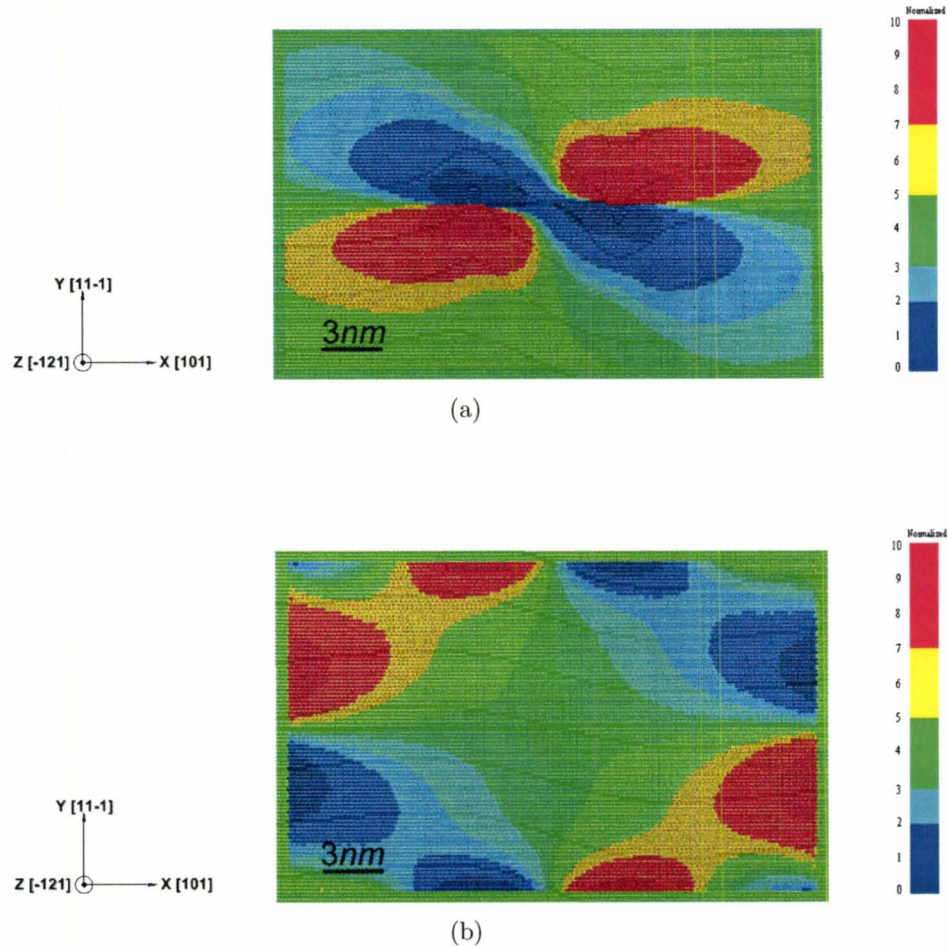
Figure 5.9: Stress component σ_{xx} in the relaxation of two perfect edge dislocations with the opposite Burgers vectors gliding on the same slip plane. (a) The initial configuration; (b) The relaxed configuration with the fixed boundary condition for physical boundary atoms in X and Y directions, and the periodic symmetry with $\ddot{c}_z = 0$ along the direction of the dislocation line (Z).
[Note: The scale of stress values in the initial and relaxed models is not the same.]

(a)

(b)
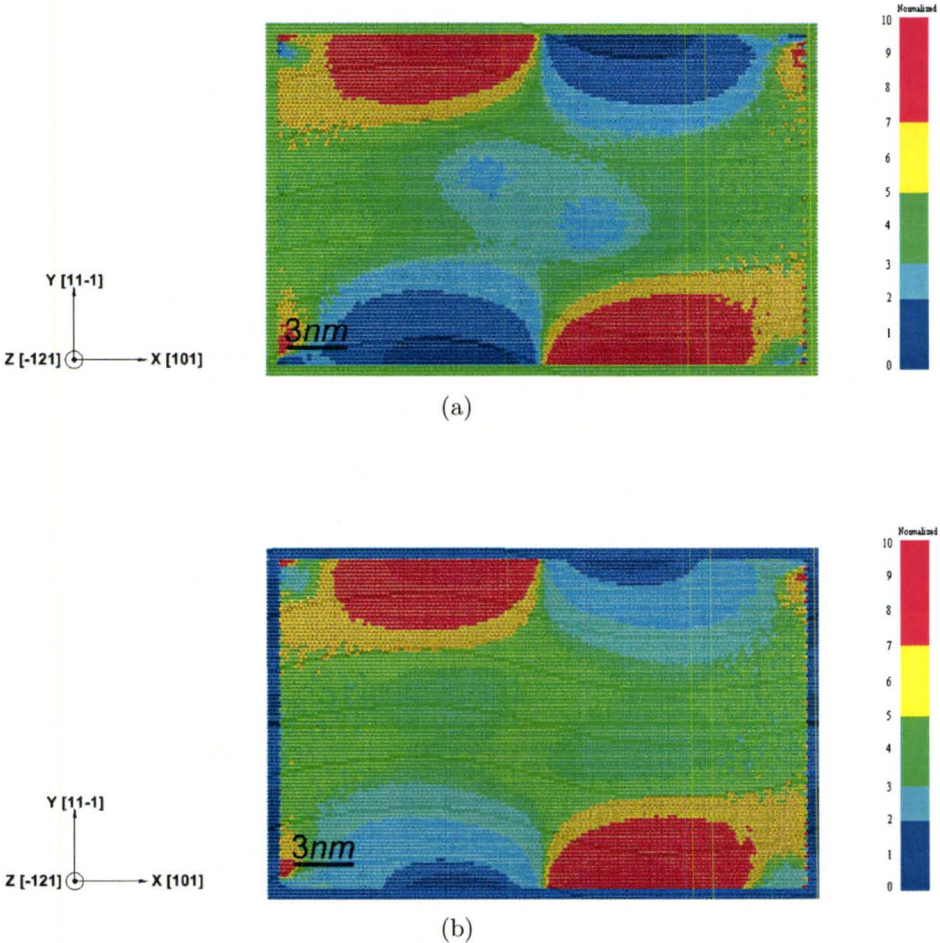
Figure 5.10: Stress component σ_{xx} in relaxed configurations from initial models containing two perfect edge dislocations with the opposite Burgers vectors gliding on the same slip plane under two boundary conditions in the slip direction (X). (a) Constant periodic length $\ddot{c}_x = \ddot{c}_z = 0$; (b) Zero traction $T_x = \ddot{c}_z = 0$.

in order to maintain the periodic length in the X direction, the compression need to be applied along the X direction. Thus, some residual compressive stress remains in the center of the model. The boundary layer in the case of $T_x = 0$ is flexible and atoms in the boundary are allowed to move so that the model could accommodate more complicated reactions during the relaxation such as the annihilation of dislocations.

In short, the periodic symmetry provides more flexible boundary treatment than the simple fixed boundary condition for the cases of interactions between defects. Moreover, the newly developed periodic symmetry approach is more flexible than the traditional one. The computational burden of the periodic symmetry, however, increases from applying it in one coordinate direction of the model to three directions eventually.

5.1.3   Two-opposite-edge-dislocation model subjected to external traction

The configuration I of two dislocations (Figure[5.5(a)]) is used to examine numerical responses when the external traction is applied. At first, the normal stress is applied on the YZ plane along the slip direction (X) while the periodic length in the Z direction is fixed ($\ddot{c}_z = 0$). In order to approximate the same level of stress values as the model subjected to external traction along the Z direction illustrated in Section(4.2), external forces 1.6, 3.2, 6.4, -1.6, -3.2 and -6.4 in arbitrary units are applied along the X direction respectively, which is equivalent to $66.4MPa$, $132.7MPa$, $265.4MPa$, $-66.4MPa$, $-132.7MPa$ and $-265.4MPa$ of σ_{xx} applied on the YZ plane, whose area is $3.8626 \times 10^{-17}m^2$. For tension cases, according to the reference length as $30.693544nm$, the normal strains ϵ_{xx} are 5.18×10^{-4}, 1.04×10^{-3} and 2.14×10^{-3}. For compression cases, the strains ϵ_{xx} become -5.13×10^{-4}, -1.03×10^{-3} and -2.08×10^{-3}.

The external traction in the slip direction does not prevent the annihilation of two edge dislocations with the opposite Burgers vectors, since the annihilation is the only way in the system to reduce the total potential energy. Figure(5.11) shows the analysis of the edge component of the Burgers vector after the relaxation when tension or compression is applied in the X direction. As in previous results, the edge component is zero in both relaxed configurations. Though the external traction in the X direction does not alter the relaxation process itself, it does change the distribution of the residual stress after the relaxation. Figure[5.12(a)] illustrates the profile of the residual stress component σ_{xx}, as an example, when the tensile force 6.4 in arbitrary units is applied. Zero stress at the boundary becomes the lowest value (the stress values of atoms at boundary layers are overwritten to zero no matter which boundary conditions are), and the highest stress appears in the adjacent area where the force is applied, and in the same tensile area as in the case that zero traction is applied as shown in Figure[5.10(b)]. The original compressive area is relaxed when the tension is applied. Contrarily, when the compressive force -6.4 in arbitrary units is applied, the stress values in the system are negative so that the zero stress of atoms at the boundary layers are the largest values numerically, as shown in Figure[5.12(b)]. The largest compressive stresses are in the adjacent area from the boundary and original compressive area in the case of zero traction as shown in Figure[5.10(b)]. The original tensile area is relaxed when the compression is applied.

In the second step, the external traction is applied on the XY plane along the direction of the dislocation line (Z) with a constant periodic length in the slip direction ($\ddot{c}_x = 0$). The external traction 25.0, 50.0, 100.0, -25.0, -50.0 and -100.0 in arbitrary units is respectively applied on the area of $5.97828 \times 10^{-16} m^2$, which generate $67.3 MPa$, $134.0 MPa$, $268.0 MPa$, $-67.3 MPa$, $-134.0 MPa$ and $-268.0 MPa$ of σ_{zz}, respectively. The tensile strains ϵ_{zz} based on the reference length $1.7701143 nm$ are
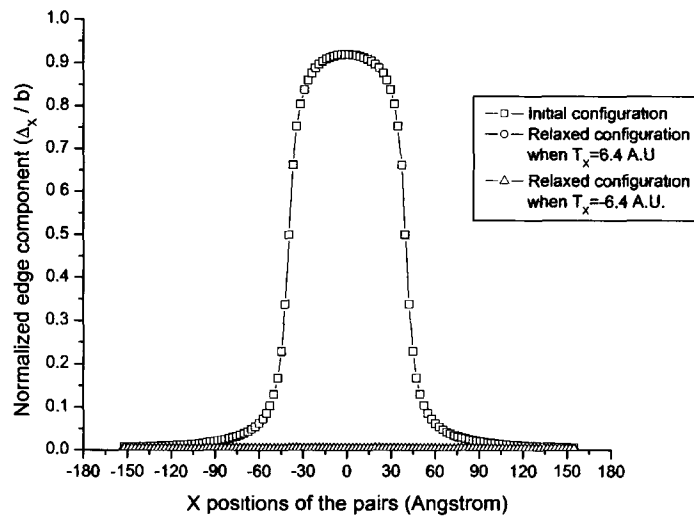
Figure 5.11: The analysis of the edge components of the Burgers vector in initial models containing two perfect edge dislocations with the opposite Burgers vectors gliding on the same slip plane and subjected to the external traction as 6.4 and −6.4 in arbitrary units along the slip direction (X), and in corresponding relaxed configurations. The edge component is determined by Disregistry.

(a)

(b)
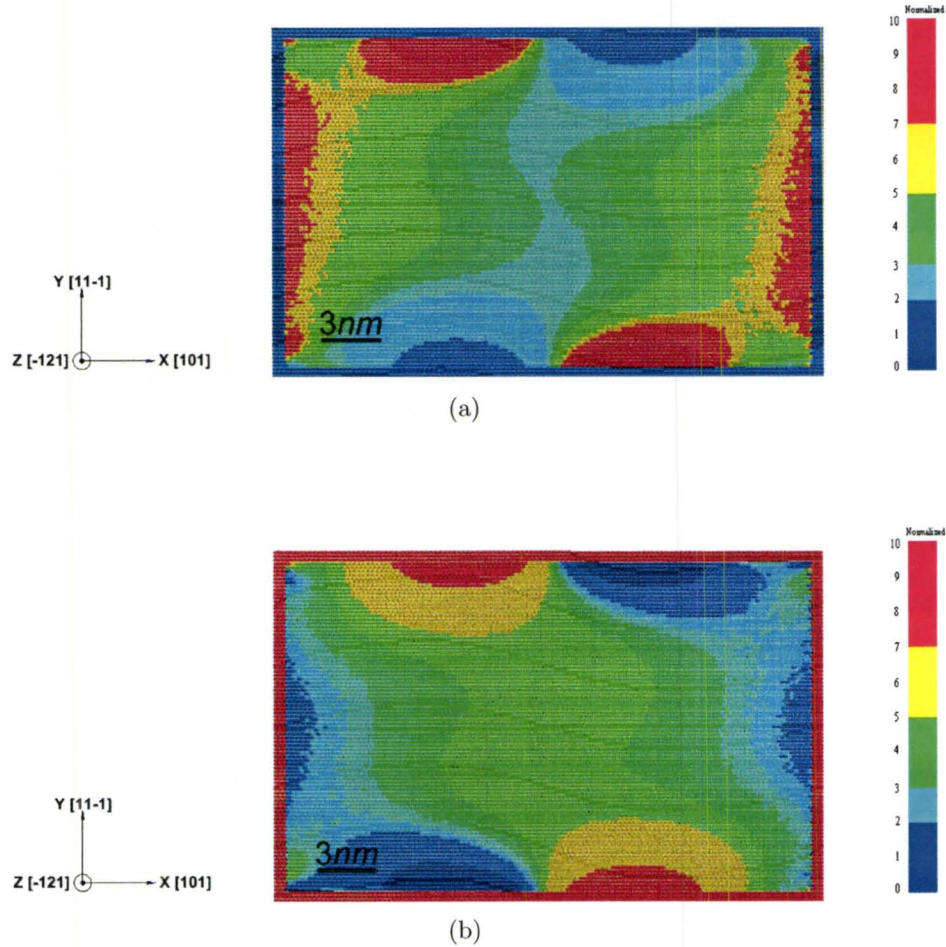
Figure 5.12: Stress component σ_{xx} in relaxed configurations from initial models containing two perfect edge dislocations with the opposite Burgers vectors gliding on the same slip plane under two boundary conditions in the slip direction (X). (a) $T_x = 6.4$ in arbitrary units and $\ddot{c}_z = 0$; (b) $T_x = -6.4$ in arbitrary units and $\ddot{c}_z = 0$.

6.15×10^{-4}, 1.24×10^{-3} and 2.50×10^{-3}. For compression cases, they are -6.02×10^{-4}, -1.19×10^{-3} and -2.33×10^{-3}. All values are higher than the results when the external traction is applied only along the X direction. This is because (i) the stress in the XY plane is slightly higher than it in the YZ plane, and (ii) the crystallographic orientation in the X and Z direction is different.

The external traction in the Z direction does not prevent the annihilation of two opposite edge dislocations as well, which is proved by the means of the analysis of the edge component of the Burgers vector shown in Figure(5.13). When the tension is applied, the periodic length in the Z direction is stretched so that atoms have a tendency to move inward to the center in the X direction. The constant periodic length in the X direction develops the positive traction along the X direction and the residual stress σ_{xx} is similar to the profile shown in Figure[5.12(a)]. Contrarily, when the periodic length in the Z direction is shortened, the periodic length in the X direction should be increased. However, the constant periodic length in the X direction develops the negative traction along the X direction, whose result is similar to Figure[5.12(b)]. The plots of the residual stress σ_{xx} of the model subjected to the external traction along the Z direction are illustrated in Figure(5.14).

At the final stage, the external traction is both applied in the slip (X) and dislocation line (Z) directions. After the relaxation, the annihilation occurs under any combination of the external traction, and the traction in the X direction plays the leading role in the development of final residual stress σ_{xx}. For example, the same model is subjected to 6.4 in arbitrary units traction in the X direction and 100.0 in arbitrary units traction in the Z direction. The strains ϵ_{xx} and ϵ_{zz} are 1.67×10^{-3} and 1.28×10^{-3}, which are 20% and 49% lower than the corresponding values in the uni-axial case. The decrease of both strains results from the mutual effects of the tension along both directions. It is obvious that the deformation of the model along

152
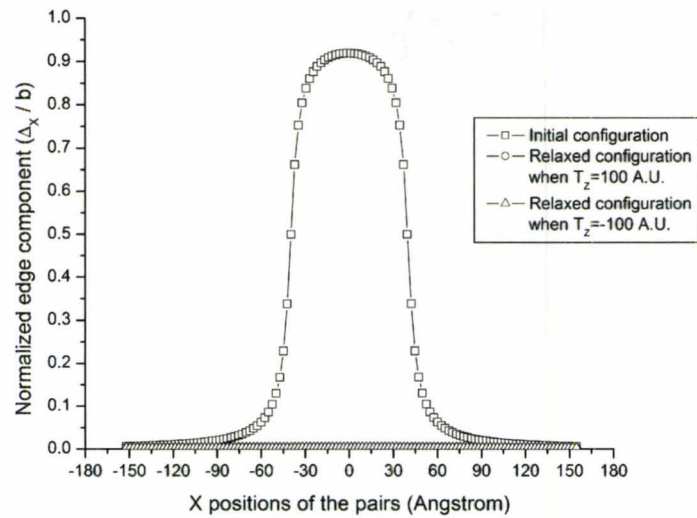
Figure 5.13: The analysis of the edge components of the Burgers vector in initial models containing two perfect edge dislocations with the opposite Burgers vectors gliding on the same slip plane and subjected to the external traction 100.0 and −100.0 in arbitrary units along the direction of dislocation line (Z), and in corresponding relaxed configurations. The edge component is determined by Disregistry.
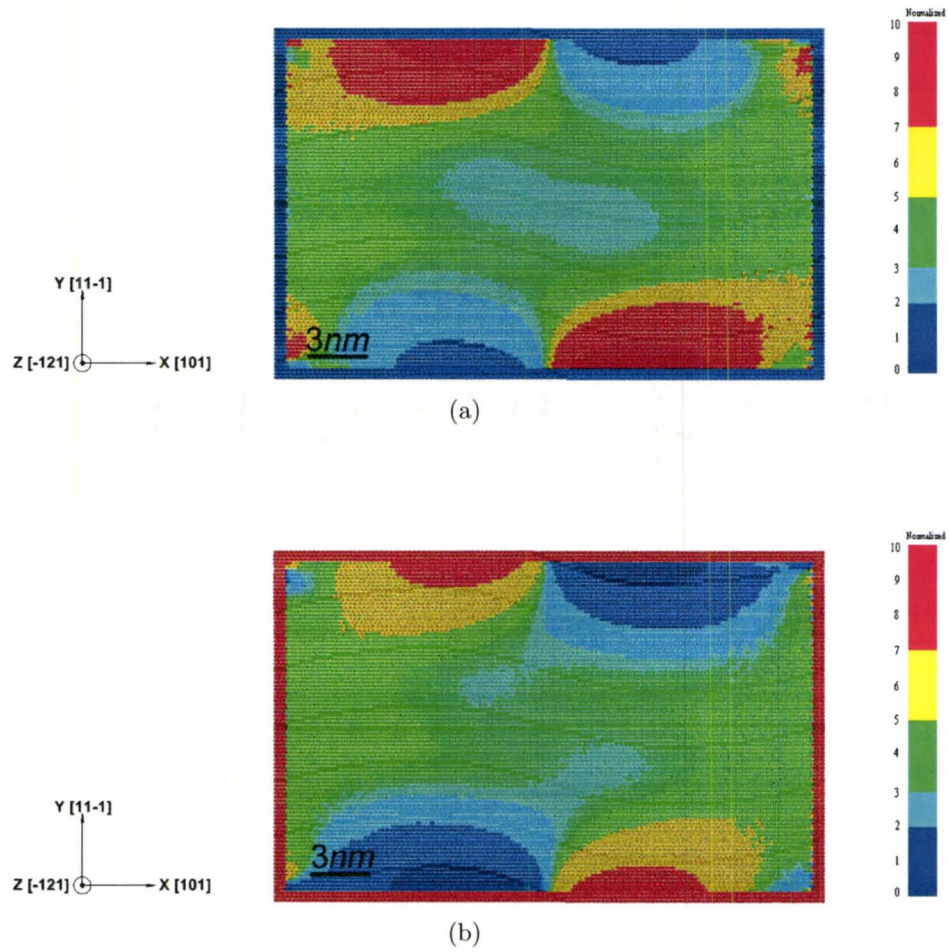
Figure 5.14: Stress component σ_{xx} in relaxed configurations from initial models containing two perfect edge dislocations with the opposite Burgers vectors gliding on the same slip plane under two boundary conditions in the direction of the dislocation line (Z). (a) $T_z = 100.0$ in arbitrary units and $\ddot{c}_x = 0$; (b) $T_z = -100.0$ in arbitrary units and $\ddot{c}_x = 0$.

the X direction is larger than it is in the Z direction when approximately the same stress is applied. Therefore, the traction applied along the slip direction is crucial in the relaxation.

In summary, the above examples of the reaction of two dislocations with the opposite Burgers vectors gliding on the same slip plane, are in agreement with the theoretical analysis based on the classical dislocation theory. This also indicates that the new DR-based energy minimization framework can be used in simulating interactions between dislocations. The uni-axial or bi-axial external traction via the new periodic symmetry method does not prevent the atomic model from relaxing to the configuration with a lower potential energy, but it alters the distribution of the residual stress. In both cases, the traction along the slip direction gives major contribution in the relaxed configuration.

5.2   Two dislocations on parallel slip planes

Two dislocations with the opposite Burgers vectors gliding on parallel slip planes attract each other to form stable configurations in the crystal structure [26]. Figure(5.15) depicts the vacancy-type dipolar configuration relaxed from two opposite dislocations on parallel planes as an example. Two perfect dislocations dissociate into four partial dislocations. Depending upon the vertical distance between their glide planes h, four partial dislocations can annihilate, form faulted dipolar structures and alternatively can form stable dipolar structures. The following summarizes the interactions between opposite dislocations gliding on parallel slip planes, which includes the pair of edge dislocations, screw dislocations and 60-degree dislocations.
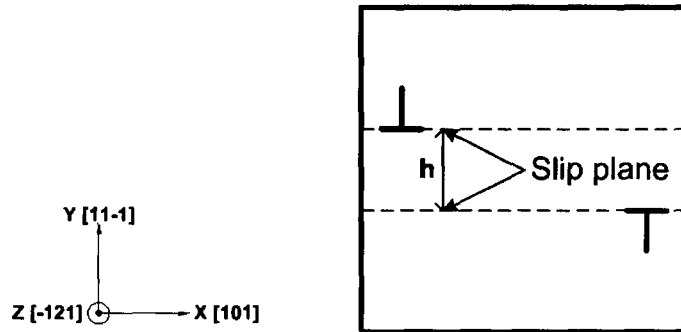
(a)
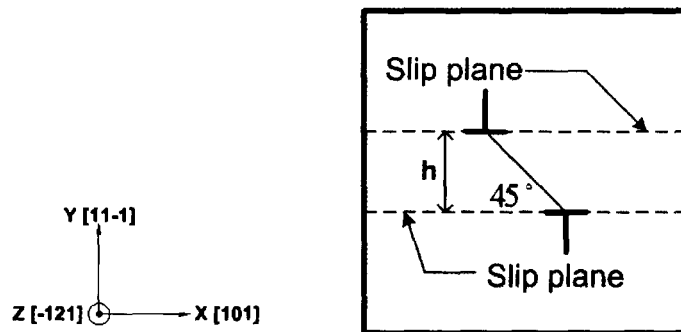
(b)

Figure 5.15: The schematic configurations of two edge dislocations with the opposite Burgers vectors gliding on parallel slip planes with the vertical distance h. (a) The initial model; (b) The relaxed model according to the theory of dislocations.

5.2.1 Pair of edge dislocations

5.2.1.1 Vacancy type edge-dislocation dipoles

The annihilation of two opposite edge dislocations could occur within the limited vertical height between two dislocations as long as the attractive force is larger than the climbing force. By experimental methods, Essmann *et al.* [15], Basinski *et al.* [4] and Niewczas *et al.* [37][38] found the critical height of the dipolar annihilation in the copper is around 1.6nm. The atomistic simulations tend to underestimate this critical value. From the early work done by Tichy *et al.* [55] to the latest research by Aslanides *et al.* [1] and Vegge *et al.* [57], the critical height for the annihilation of edge dislocation dipoles has been determined to be around 0.4nm-0.42nm with various numerical methods.

In order to compare present results with the results of other authors, the orientation of the model is changed to X[1 -1 0], Y[1 1 1] and Z[1 1 -2], whose geometry is similar to the lattice as shown in Figure[4.1(a)]. The boundary conditions used in the simulation are (i) fixing physical boundary atoms in X and Y directions and (ii) the periodic symmetry in the Z direction with keeping the periodic length unchanged. After a series of tests, under the new DR-based energy minimization framework, the critical height h for the annihilation is $0.41nm$, which agrees with the results available in the literature [1][55][57] obtained with different numerical integration and potential energy functions.

Figure(5.16) shows the positions of the dislocations in the initial and relaxed configurations, and the corresponding analysis of the edge component along the middle (1 1 1) plane between two dislocations by the Disregistry method. Both results imply that the process of the annihilation is almost finished except the center of the model, in which voids could not be filled in due to the fixed boundary layers in

Y [1 1 1]

Z [1 1 -2] ⊙ ── X [1 -1 0]

(a)

Y [1 1 1]

Z [1 1 -2] ⊙ ── X [1 -1 0]

(b)

(c)
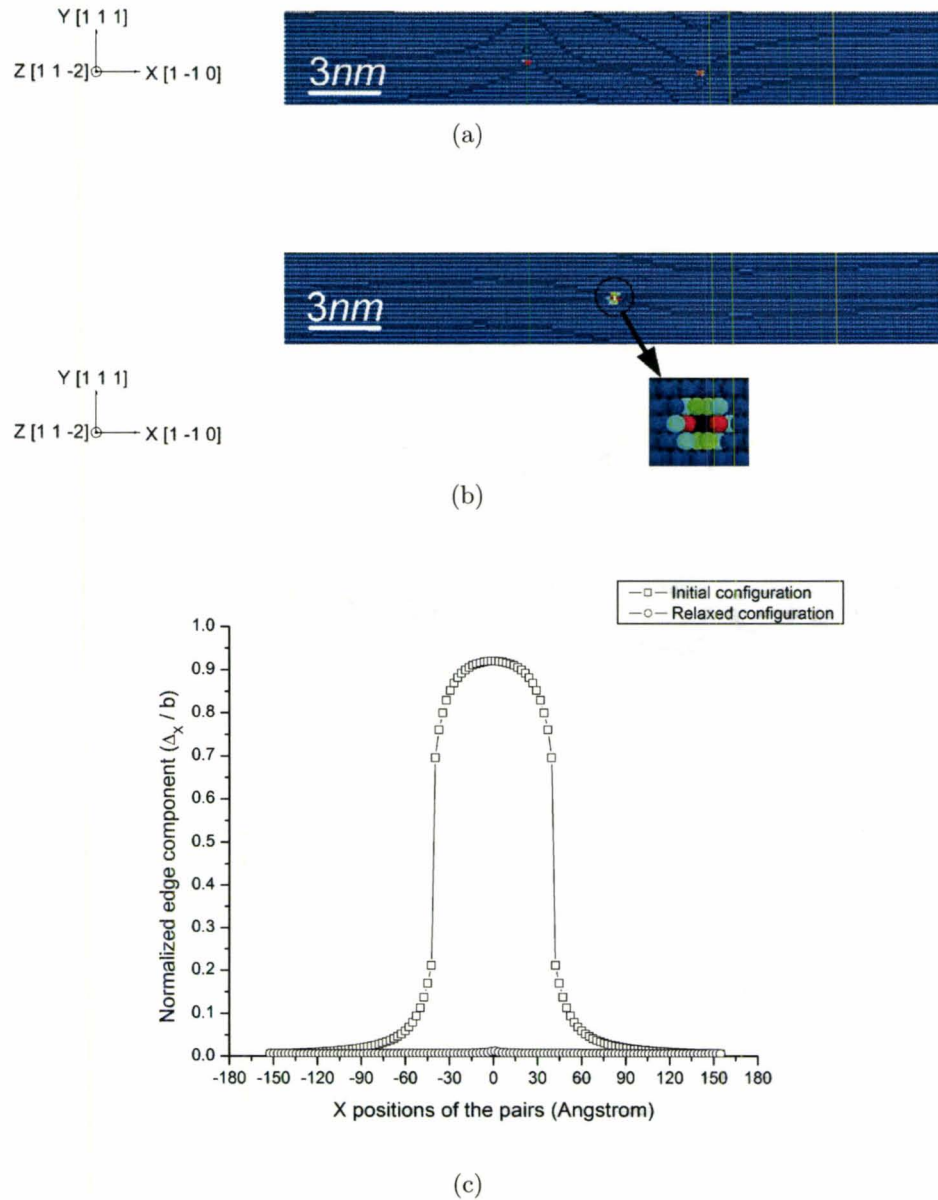
Figure 5.16: The positions of dislocations. (a) The initial configuration of two perfect edge dislocations with the opposite Burgers vectors gliding on parallel slip planes with the vertical distance of $0.41nm$; (b) The relaxed configuration of (a) (vacancy type); (c) The analysis of the edge components along the middle (1 1 1) plane between two dislocations in (a), and the edge components along the middle (1 1 1) plane between two pairs of partial dislocations in (b) by the Disregistry approach.

the X direction. Similar to the case of two opposite edge dislocations on the same slip plane, there are two major drops in the energy minimization curve as shown in Figure[5.17(a)], which means the process of the annihilation of these two perfect edge dislocations involves one pair of partial dislocations followed by another pair as shown in Figures[5.17(b)] and [5.17(c)].

When the height h is larger than $0.41nm$, the dislocations relax to form a faulted dipole depicted in Figure(5.18). These two perfect edge dislocations dissociate on their respective slip planes. Since two leading partial dislocations are with the opposite Burgers vectors, they attract each other until the 'Z' configuration is generated, in which a new stacking fault appears between two leading partial dislocations and the angle between them are acute with respect to the horizontal $\{1\ 1\ 1\}$ plane. While there is not much experimental evidence for the presence in the structure of materials of the faulted dipole with the height between $0.42nm$ to $1.6nm$, there is still the possibility of their existence and the critical height $1.6nm$ therefore could be considered as an upper limit of the annihilation of vacancy-type edge dislocation dipoles.

When the height h is at $0.42nm$, the relaxed configuration of dislocations exhibits dipolar 'Z' configuration as shown in Figure[5.19(a)]. However, the separation of partial dislocations is much smaller in this case than the value in the normal range stated in Section(4.1.1). Therefore, the relaxed configuration with the dipolar height $0.42nm$ could be regarded as a transitional structure from the annihilation to the faulted dipole. Figure(5.19) demonstrates the analysis of the edge component along the middle $(1\ 1\ 1)$ plane between two pairs of partial dislocations. There is a sudden change in the center of the curve, which means the new stacking fault is generated between two leading partial dislocations.

The space between two vertical $\{1\ 1\ 1\}$ planes along the Y direction is around

159
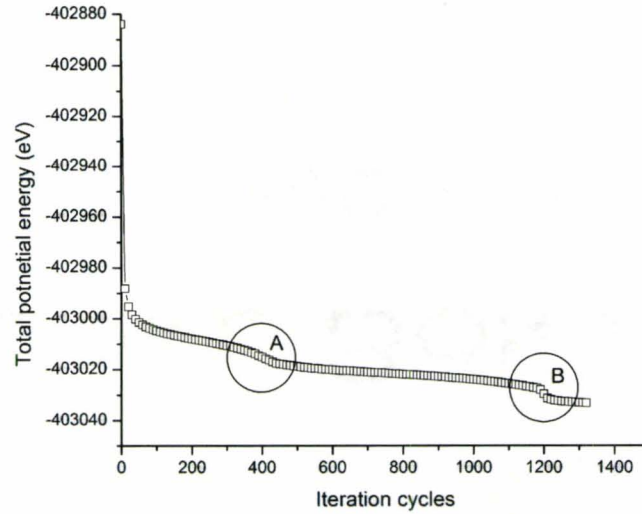
(a)
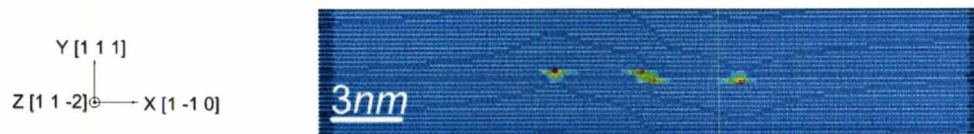
(b)

(c)

Figure 5.17: The relaxation of two perfect edge dislocations with the opposite Burgers vectors gliding on parallel slip planes with the vertical distance of $0.41nm$. (a) The total energy minimization curve; (b) The intermediate configuration of A region of (a); (c) The intermediate configuration of B region of (a).

160

(a)

(b)
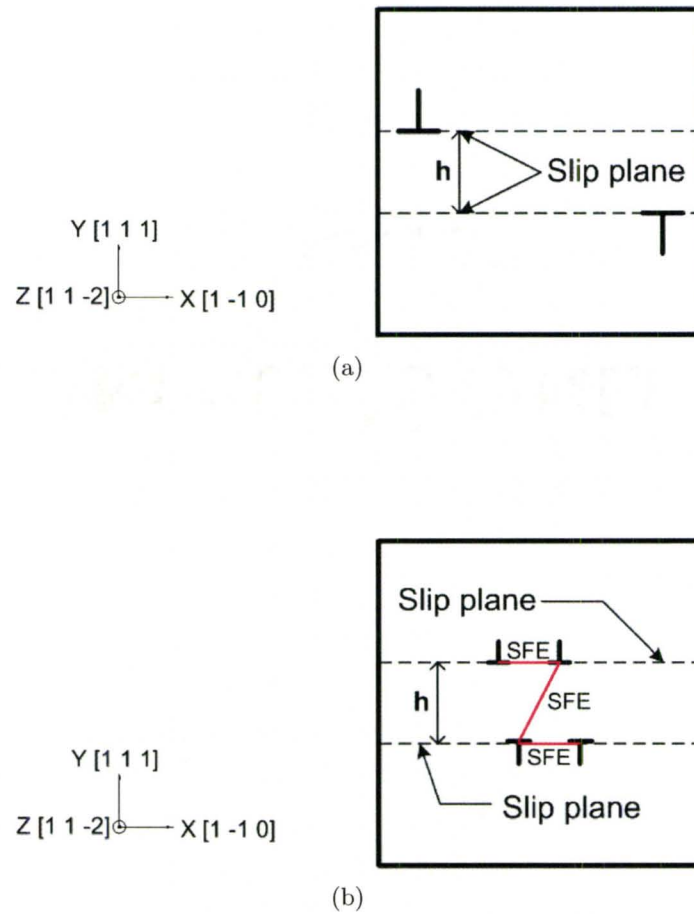
Figure 5.18: The schematic configurations of two perfect edge dislocations with the opposite Burgers vectors gliding on parallel slip planes with the vertical distance larger than $0.42nm$. (a) The initial model; (b) The relaxed model containing the dislocation dipole in the 'Z' configuration (vacancy type).

(a)
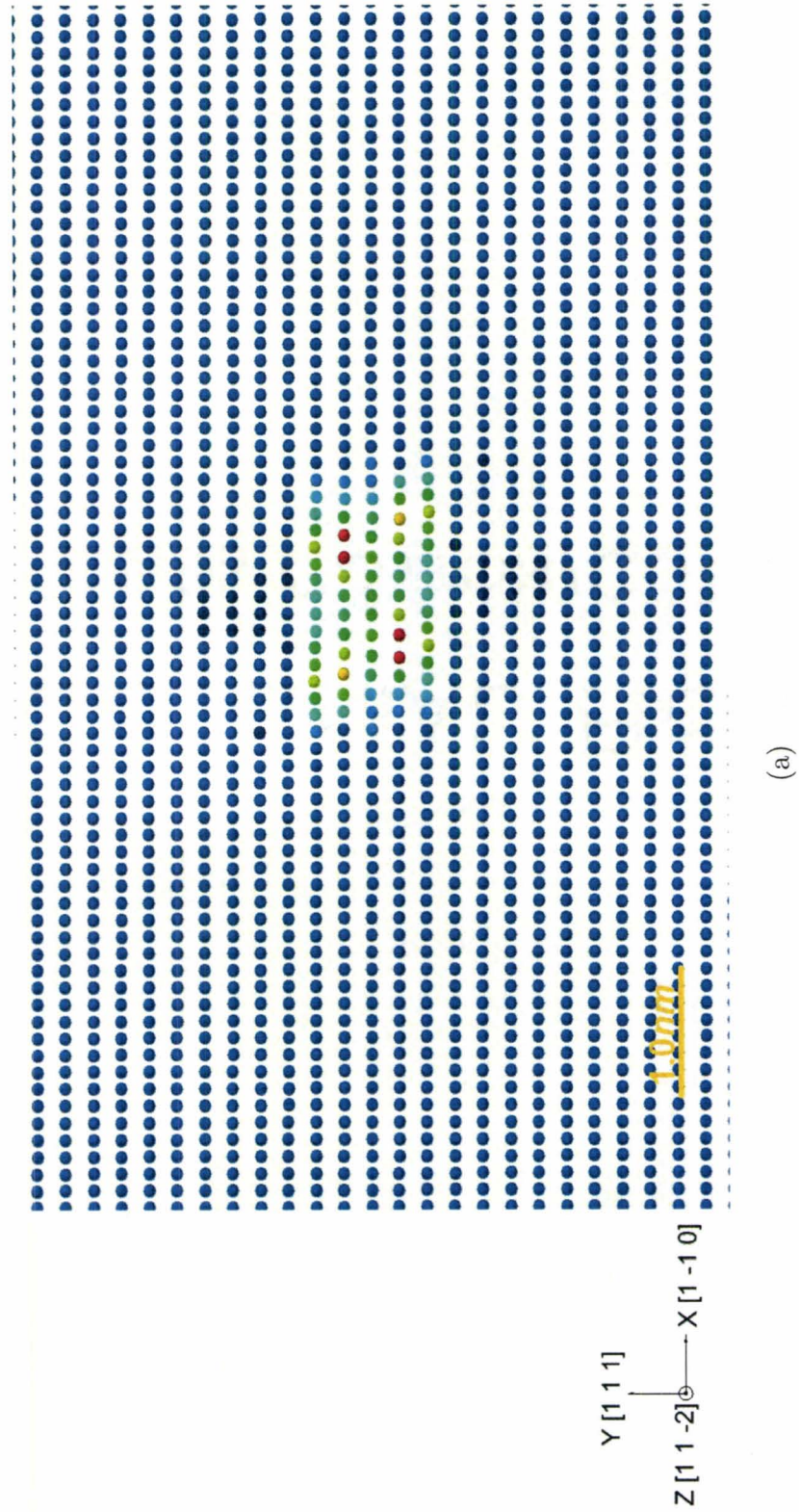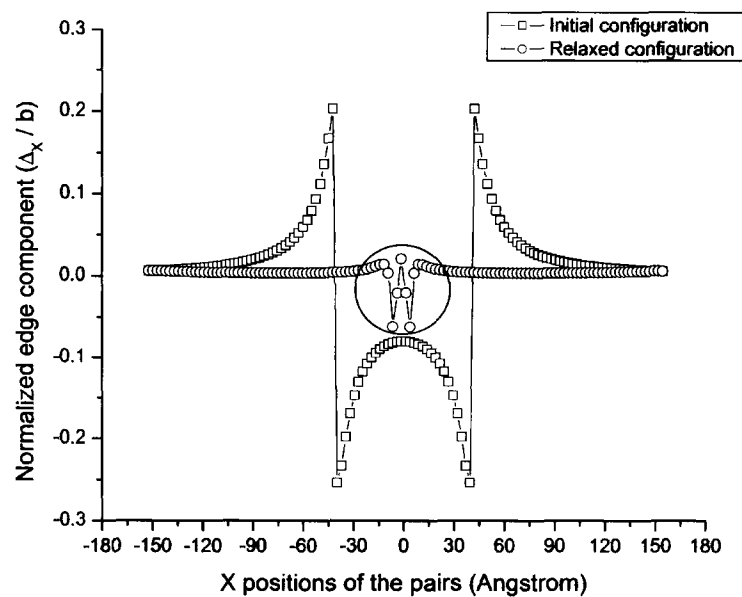
(b)

Figure 5.19: The positions of dislocations. (a) The relaxed configuration from the initial model containing two perfect edge dislocations with the opposite Burgers vectors gliding on parallel slip planes with the vertical distance of $0.42nm$ (vacancy type); (b) The analysis of the edge components along the middle (1 1 1) plane between two dislocations in the initial model, and the edge components along the middle (1 1 1) plane between two pairs of partial dislocations in the relaxed model by the Disregistry approach.

$0.208nm$. Therefore, the vertical height that could trigger the annihilation of the vacancy-type edge dislocation dipoles is only less than two interplanar $\{1\ 1\ 1\}$ spacing. In order to obtain the maximum dipolar height, under which the faulted dipole is formed, the positions of the dislocations and corresponding analysis of the edge component along the middle $(1\ 1\ 1)$ plane between two pairs of partial dislocations are investigated under various dipolar heights with the step size of $0.2nm$ starting from $0.4nm$. It is found that the approximate critical height to form 'Z' configuration for vacancy type dipoles is no larger than $2.8nm$, and the formation of the faulted dipole is only sensitive to the initial height of the dipole. The width of the stacking fault increases as the height increases due to the attraction between partial dislocations. However, the separation of each pair of partial dislocations is always smaller than the benchmark result. As an example, Figure(5.20) illustrates the intermediate process of forming the faulted dipole with the height $2.0nm$. The width of the stacking fault in both dislocations is around $3.54nm$.

When the dipolar height is larger than $2.8nm$, the stable dipole replaces the faulted dipole with 'Z' configuration. In the configuration of the stable dipole, the angle between leading partial dislocations becomes obtuse. Figure(5.21) compares the angle of the dipole with the height of $2.8nm$ and $3.0nm$, in which the values are $75°$ and $98°$, respectively. Figure(5.22) shows the analysis of the edge components along the middle $(1\ 1\ 1)$ plane between two pairs of partial dislocations in two relaxed configurations, and it is found that the curve becomes smooth when the stable dipole is formed, which implies that the new stacking fault across two leading partial dislocations disappears. Finally, Figure(5.23) compares the total potential energy minimization curve with dipolar heights of $2.6nm$, $2.8nm$ and $3.0nm$. The total potential energy in relaxed configurations with the dipolar height of $2.6nm$ and $2.8nm$ is almost the same, but values are lower than the stable dipole with the height of
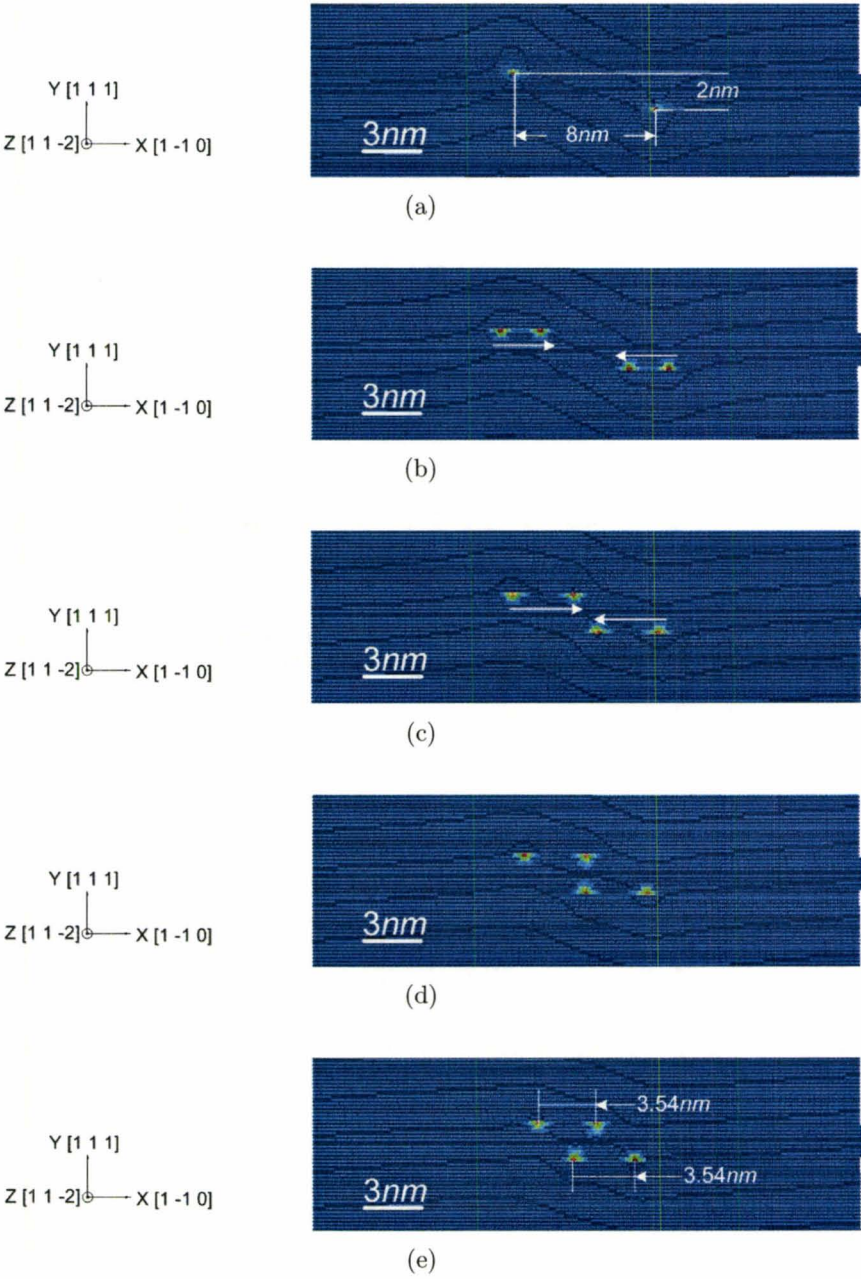
Figure 5.20: The positions of dislocations during the relaxation of two perfect edge dislocations with the opposite Burgers vectors gliding on parallel slip planes with the vertical distance of $2.0nm$ (vacancy type). (a) Cycle No: 0; (b) Cycle No: 140; (c) Cycle No: 560; (d) Cycle No: 910; (e) Cycle No: 1240.

(a)

3.0nm

98°

1.0nm

Y [1 1 1]

Z [1 1 -2]⊙———→X [1 -1 0]

(b)
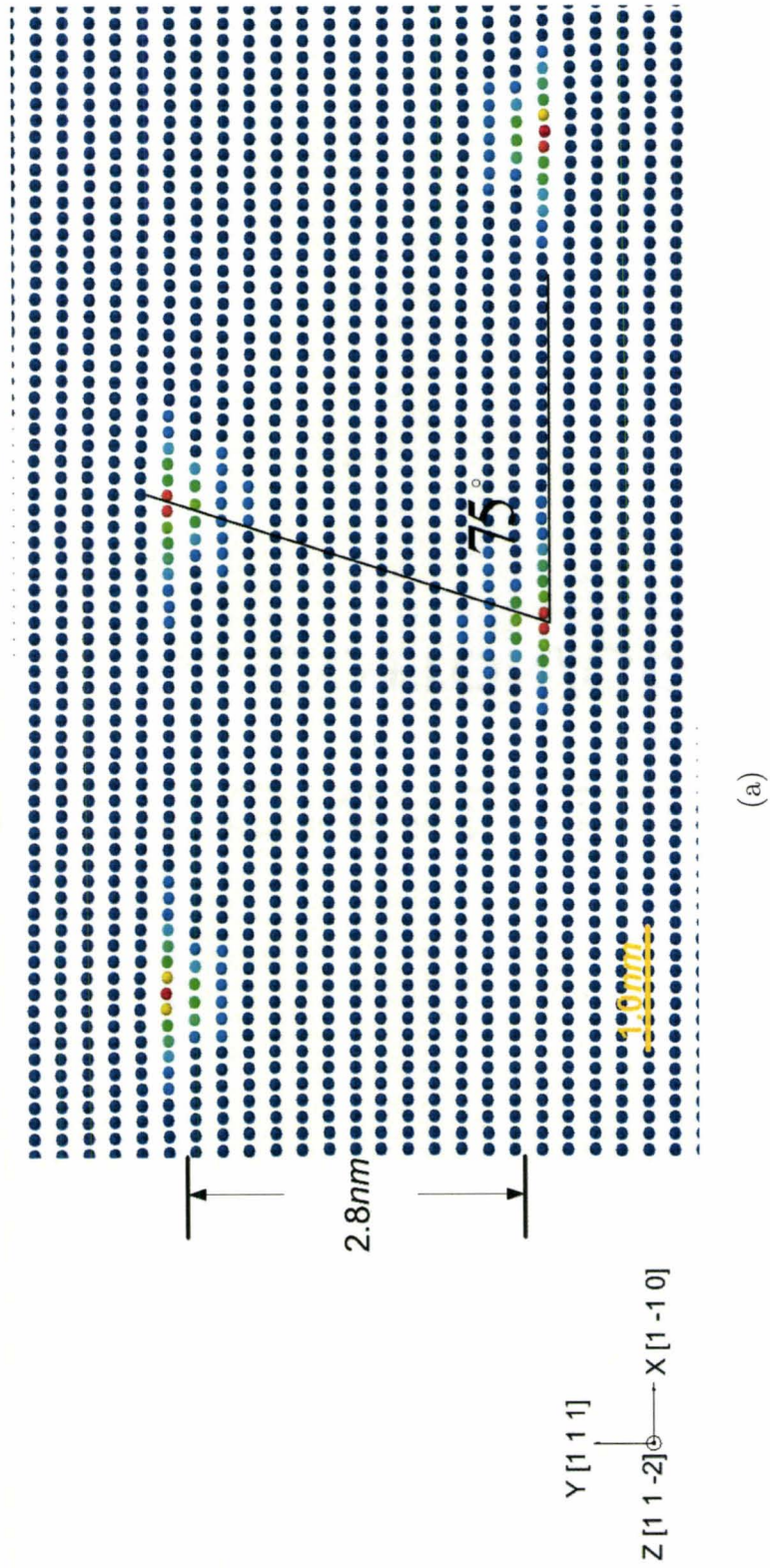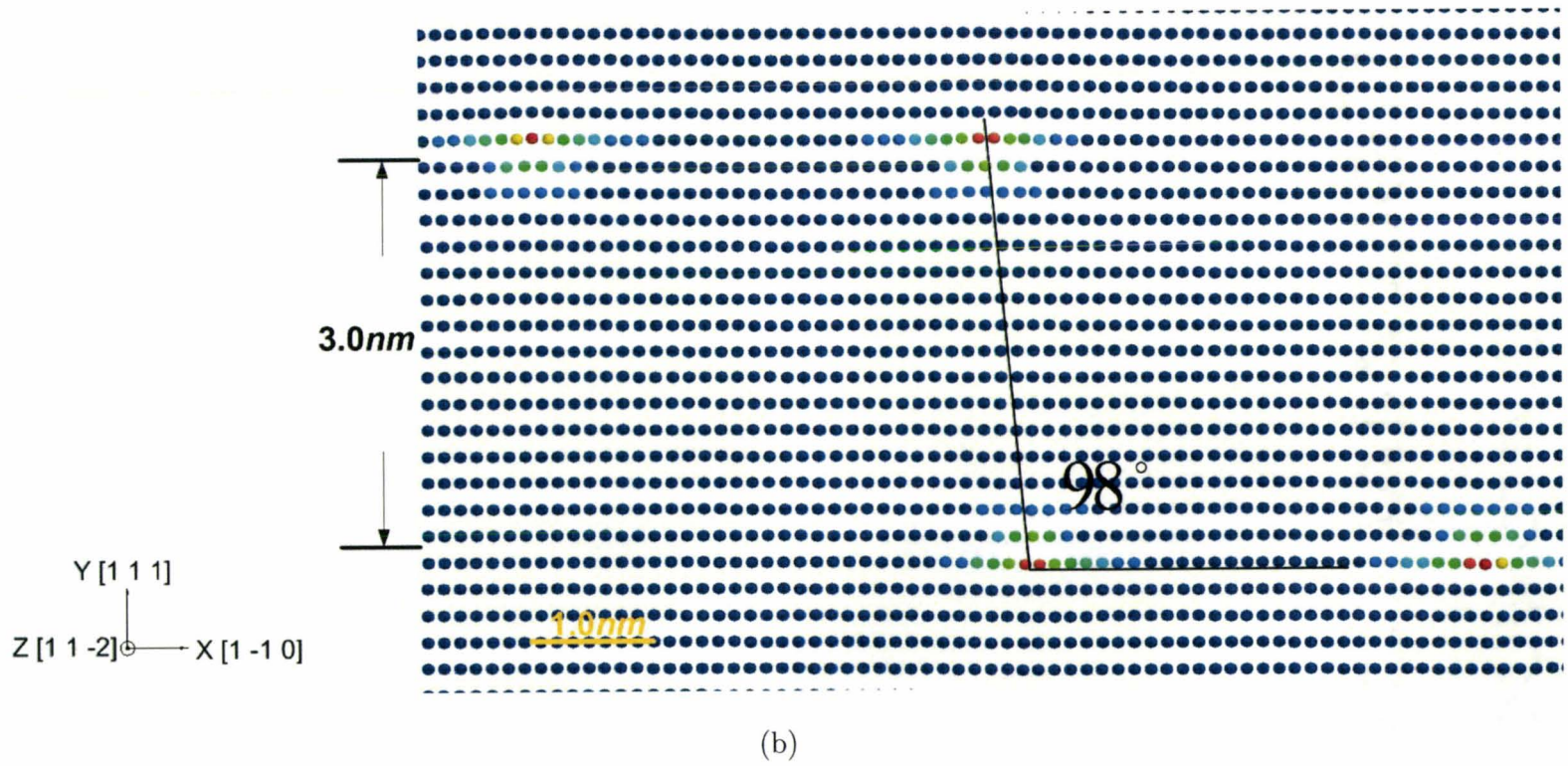
Figure 5.21: The relaxed configurations from initial models containing two perfect edge dislocations with the opposite Burgers vectors gliding on parallel slip planes (a) with the vertical distance of 2.8nm and (b) with the vertical distance of 3.0nm (vacancy type).
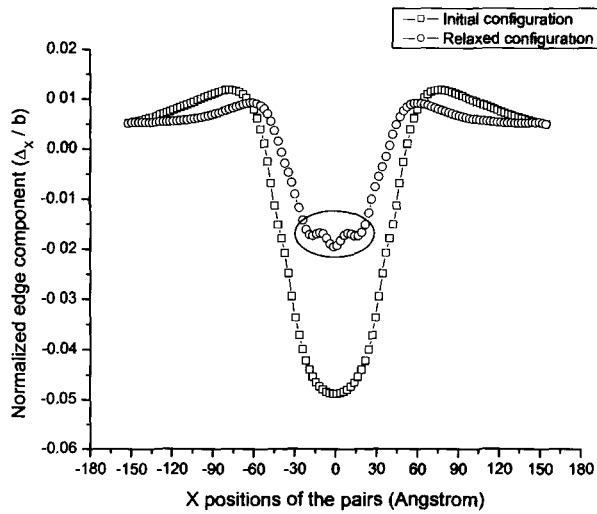
(a)
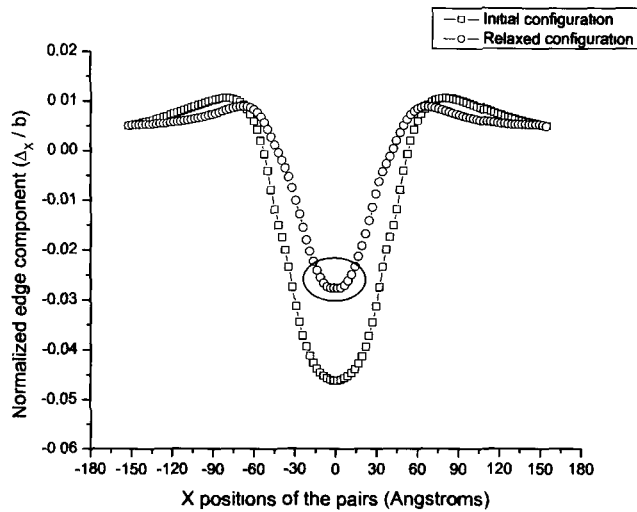
(b)

Figure 5.22: The analysis of the edge components along the middle (1 1 1) plane between two dislocations in initial models containing two perfect edge dislocations with the opposite Burgers vectors gliding on parallel slip planes (a) with the vertical distance of $2.8nm$ and (b) with the vertical distance of $3.0nm$, and the edge components along the middle (1 1 1) plane between two pairs of partial dislocations in corresponding relaxed configurations (vacancy type). The edge component is determined by the Disregistry approach.
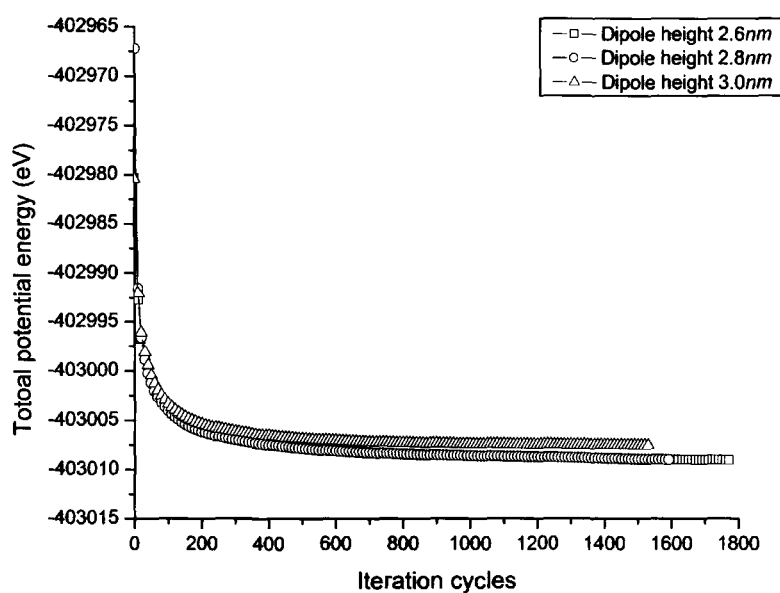
Figure 5.23: The comparison of the total potential energy in relaxed configurations as the vacancy-type dislocation dipole from initial models containing two perfect edge dislocations with the opposite Burgers vectors gliding on parallel slip planes with vertical distances of $2.6nm$, $2.8nm$ and $3.0nm$.

$3.0nm$. Therefore, the faulted dipole is a more stable configuration than the stable dipole.

5.2.1.2   Interstitial type edge-dislocation dipoles

The interstitial faulted dipole formed by two opposite edge dislocations shows different characteristics compared to the vacancy type dipole. As shown in Figure(5.24), the new stacking fault is generated between the leading partial dislocations and the angle is obtuse. Thus, such structure is called the 'S' configuration.

For the dipolar height of $0.41nm$, two edge dislocations do not annihilate but form a tiny dipole in the 'S' configuration as shown in Figure (5.25). From the numerical point of view, the possible reason could be that the overlapping region between these two dislocations in the interstitial type dipole consists of atoms rather than voids as in the vacancy type dipole. The potential energy function provides strong repulsion when atoms move closer but mild attraction between atoms in the voids, so that the annihilation of the interstitial type dipole is almost impossible under current boundary conditions.

The evolution of interstitial type dipoles seems faster than the vacancy counterpart. The critical height to form the 'S' configuration is no more than $1.2nm$. As an example, Figure(5.26) demonstrates the formation of the 'S' configuration when the dipolar height is $0.8nm$. In this case, the separation of each pair of partial dislocations is around $2.35nm$.

The stable dipole is prevalent when the dipolar height is larger than $1.2nm$. In the configuration of the stable dipole, though the angle between the leading partial dislocations is still obtuse, the new stacking fault is not formed during the relaxation. Figures(5.27) and (5.28) compare final configurations and the corresponding analysis of the edge components along the middle (1 1 1) plane between two pairs of partial

(a)

(b)
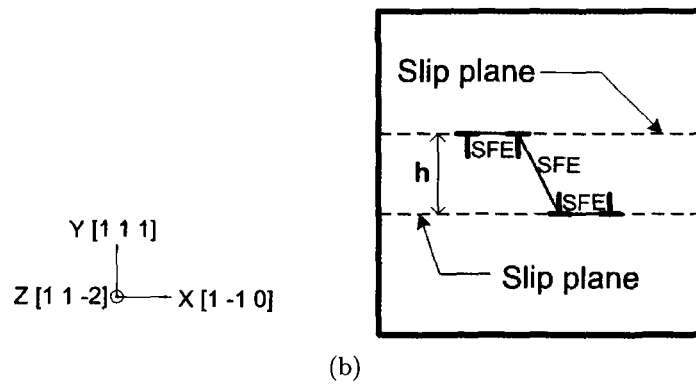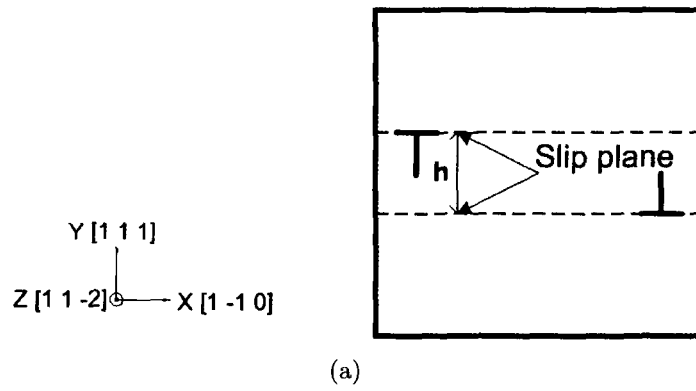
Figure 5.24: The schematic configurations of two edge dislocations with the opposite Burgers vectors gliding on parallel slip planes with the vertical distance h. (a) The initial model; (b) The relaxed model containing the dislocation dipole in the 'S' configuration (interstitial type).

(a)

(b)

(c)
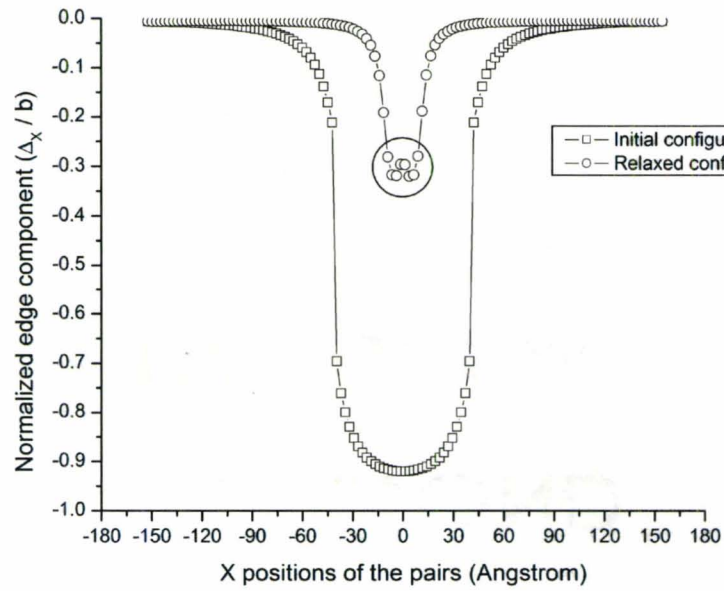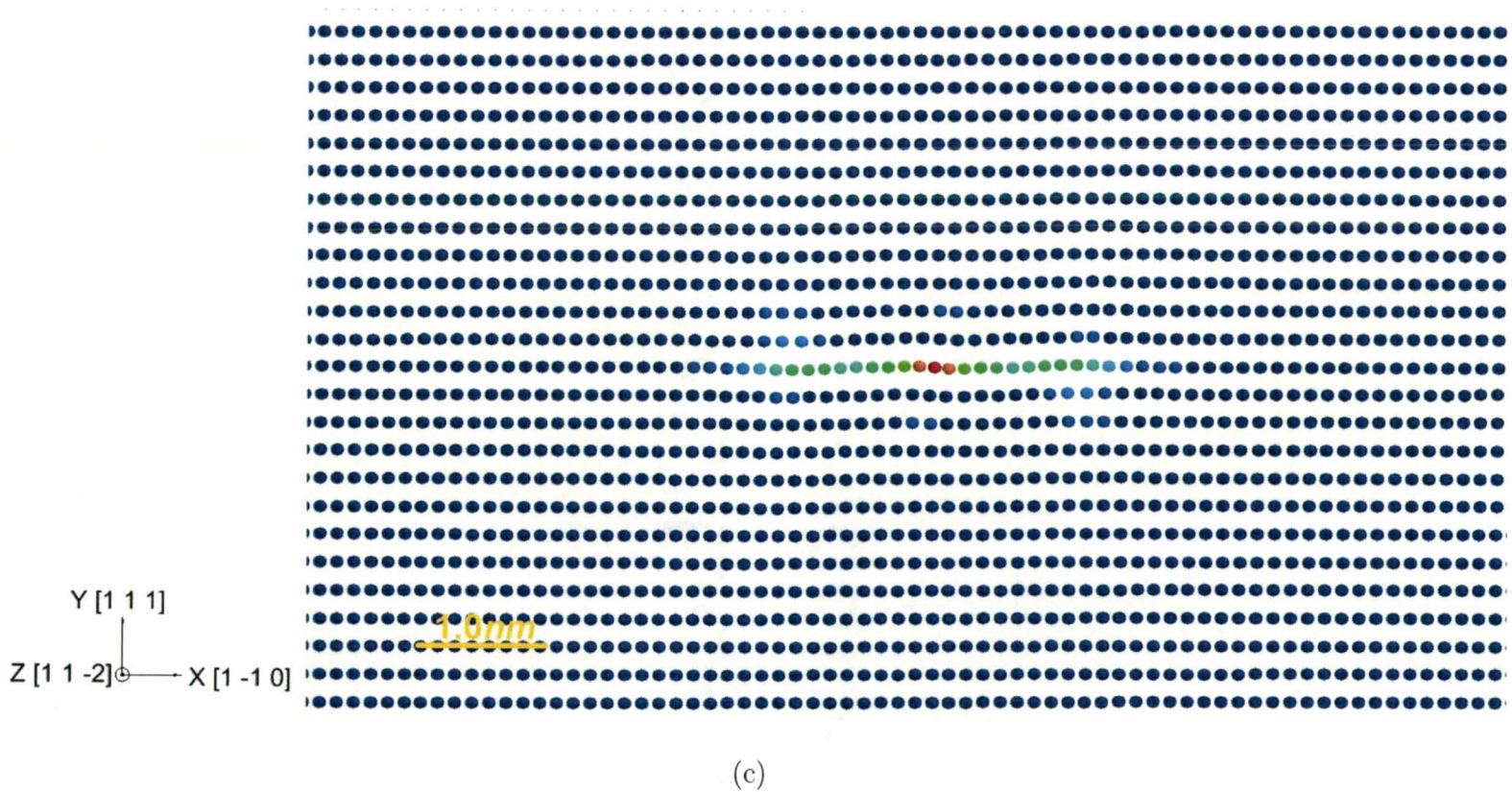
Figure 5.25: Two perfect edge dislocations with the opposite Burgers vectors gliding on parallel slip planes with the vertical distance of $0.41nm$ (a) The analysis of the edge components along the middle (1 1 1) plane between two dislocations in the initial model, and the edge components along the middle (1 1 1) plane between two pairs of partial dislocations in the relaxed model by the Disregistry approach; (b) The initial configuration; (c) The relaxed configuration (interstitial type).
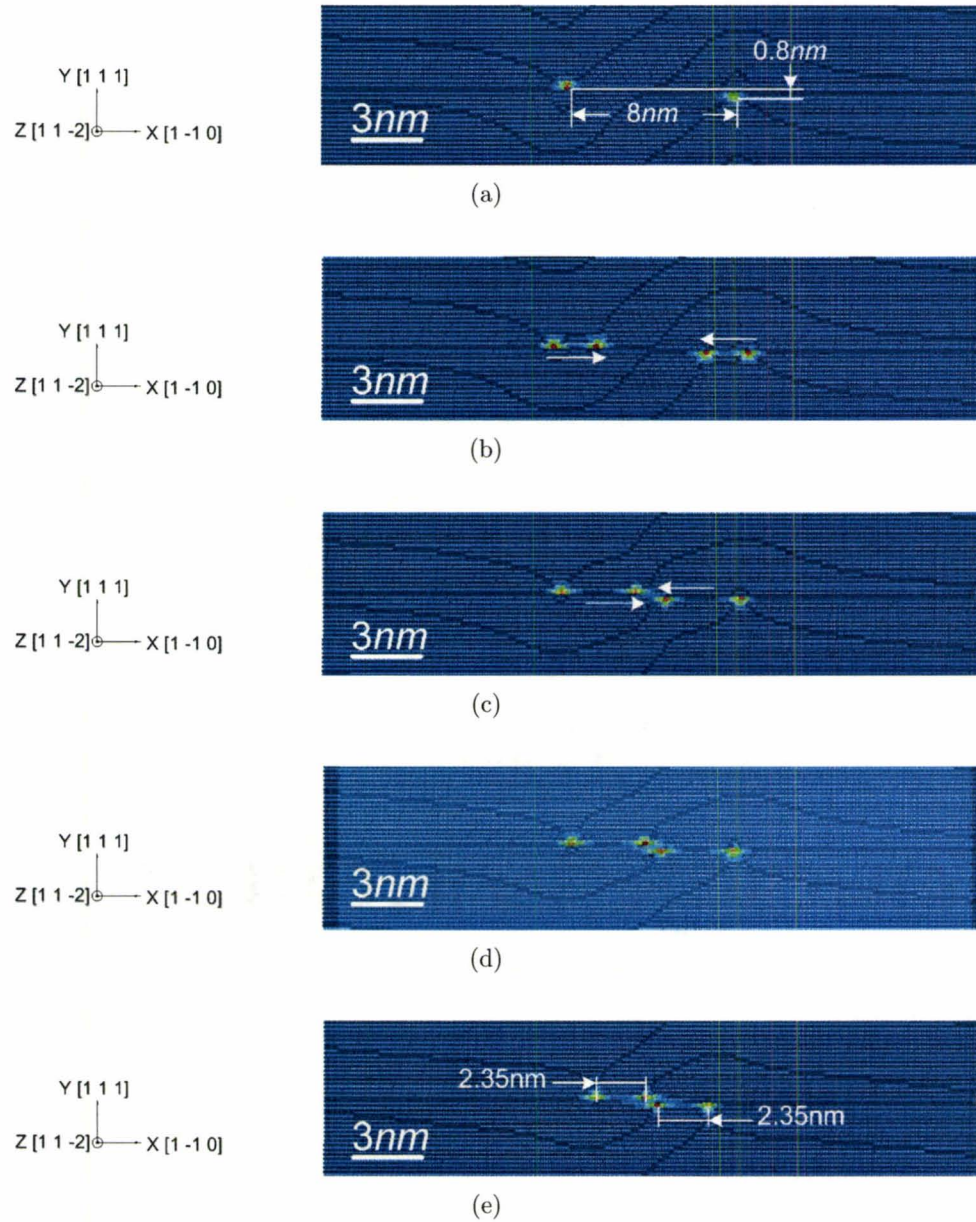
Figure 5.26: The positions of dislocations during the relaxation of two perfect edge dislocations with the opposite Burgers vectors gliding on parallel slip planes with the vertical distance of $0.8nm$ (interstitial type). (a) Cycle No: 0; (b) Cycle No: 140; (c) Cycle No: 420; (d) Cycle No: 560; (e) Cycle No: 1180.

dislocations in the faulted dipole and the stable dipole with the dipolar height of $1.2nm$ and $1.4nm$, respectively. Though two angles are almost the same, due to the absence of the third stacking fault, the total potential energy in the relaxed configuration (stable dipole) with the dipolar height of $1.4nm$ is higher than the faulted dipole case, which is shown in Figure (5.29).

Based on experimental observations, two perfect edge dislocations annihilate under the critical dipolar height of 1.6nm. From numerical simulations, the relaxed structures of interstitial type configurations change from the faulted dipole to the stable dipole when the dipolar height is below $1.6nm$. Therefore, in most occasions, the faulted dipole of the interstitial type, i.e. 'S' configuration, is difficult to be seen. This statement is supported by the Wintner *et al.* [60] experimental results, where dipoles in 'Z' configurations were observed, but 'S' configurations were not in Cu-Al alloys.

In conclusion, there are three stages for the evolution of edge dislocation dipoles with the increase of the dipolar height. They are the annihilation, the formation of the faulted dipole and the formation of the stable dipole. The critical height for the annihilation is much less than the experimental value of the copper, which could not simply be owing to the inaccuracy of potential energy functions or the limitation of numerical algorithms. There may be an unknown mechanism involved in the process, which has to be discovered and further incorporated into numerical methods. The configuration of the faulted dipole may only exist in the vacancy type because the energy of the formation of the vacancy type dipoles is lower than the interstitial type.

(a)

(b)
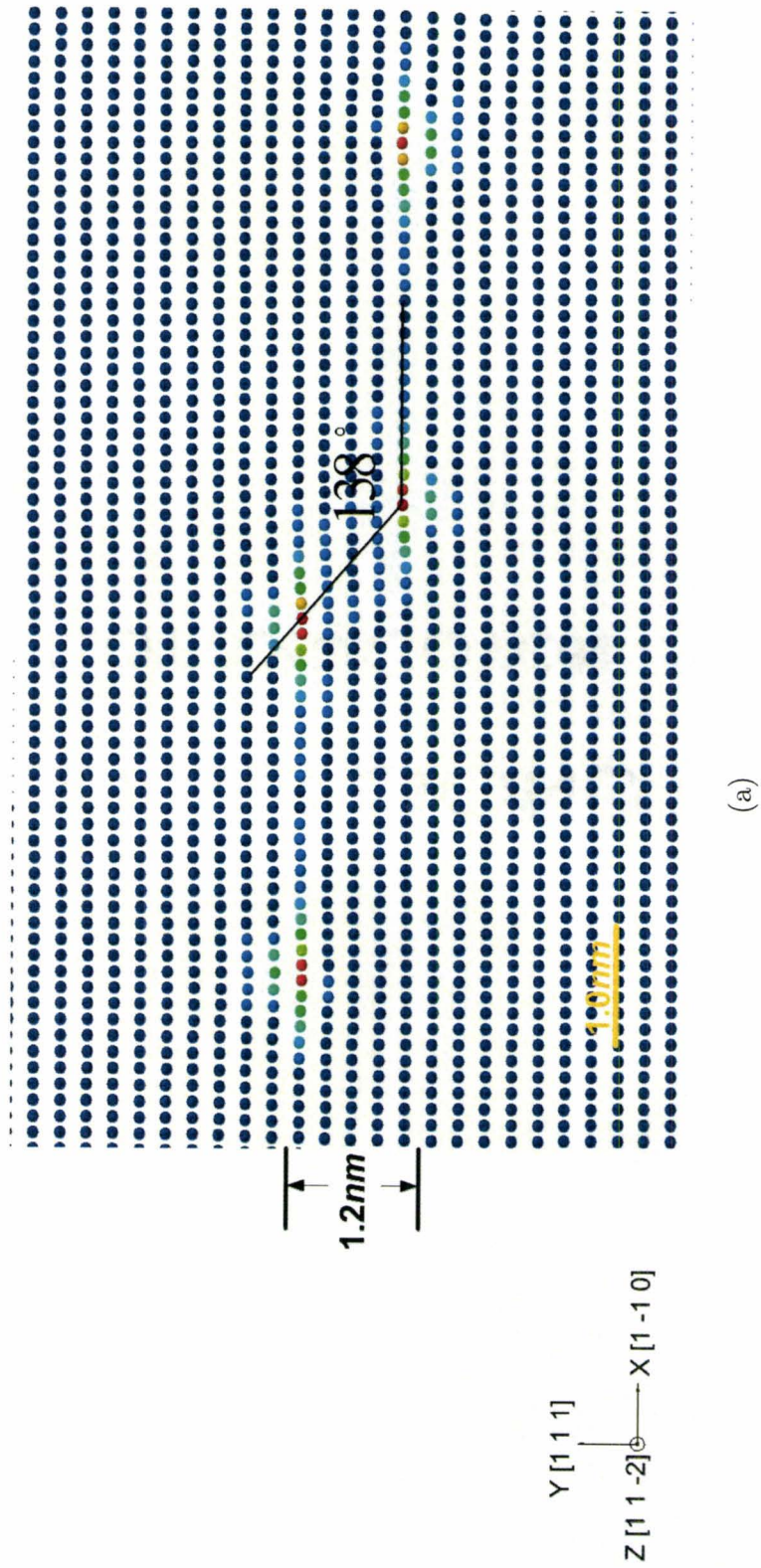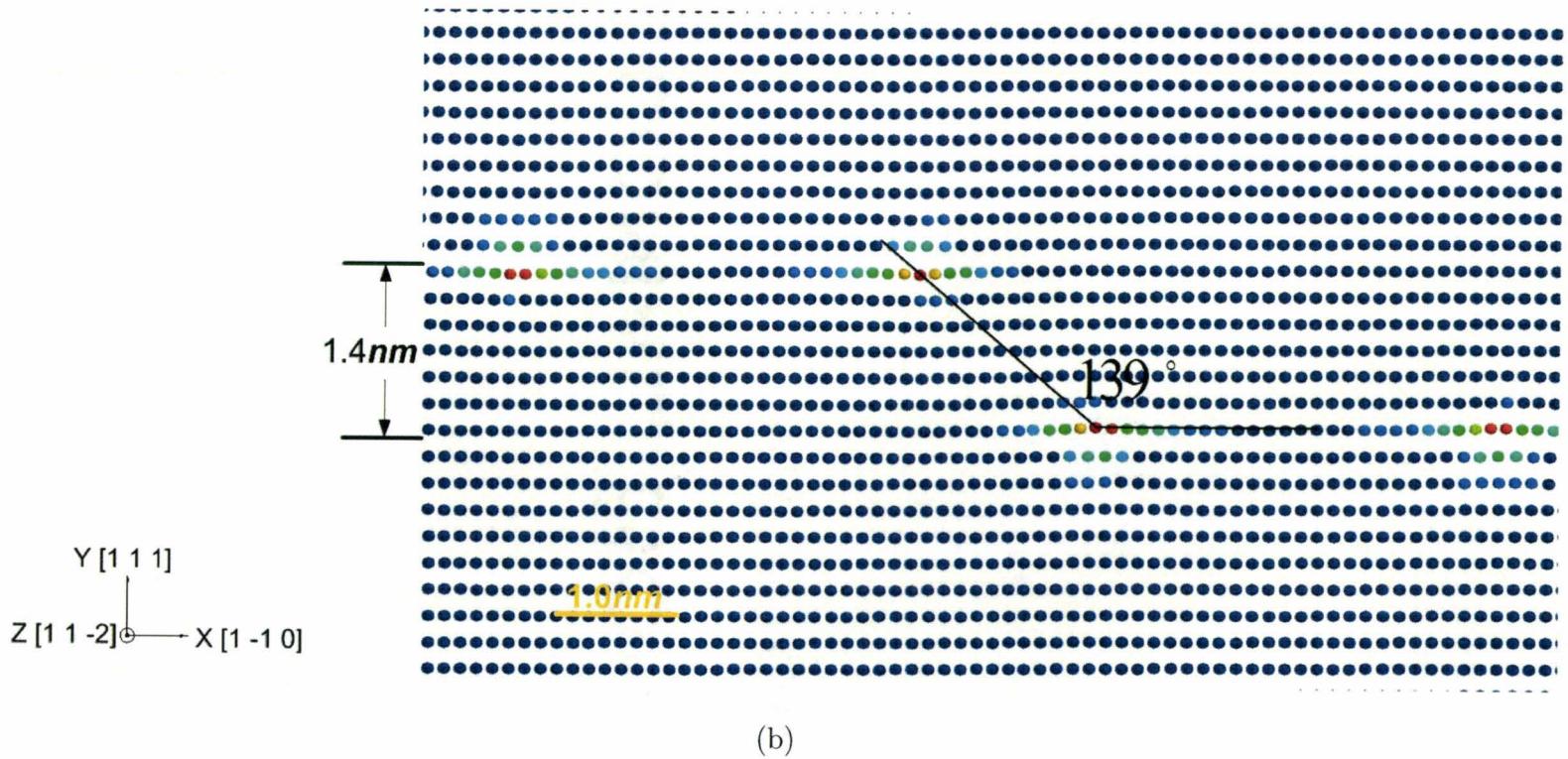
Figure 5.27: The relaxed configurations from initial models containing two perfect edge dislocations with the opposite Burgers vectors gliding on parallel slip planes (a) with the vertical distance of 1.2*nm* and (b) with the vertical distance of 1.4*nm* (interstitial type).
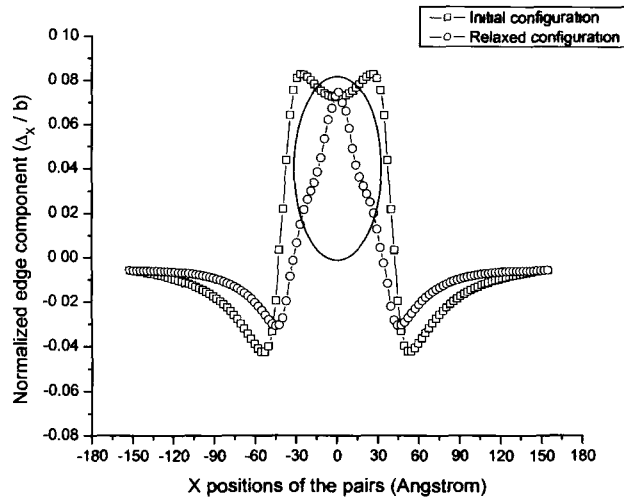
(a)
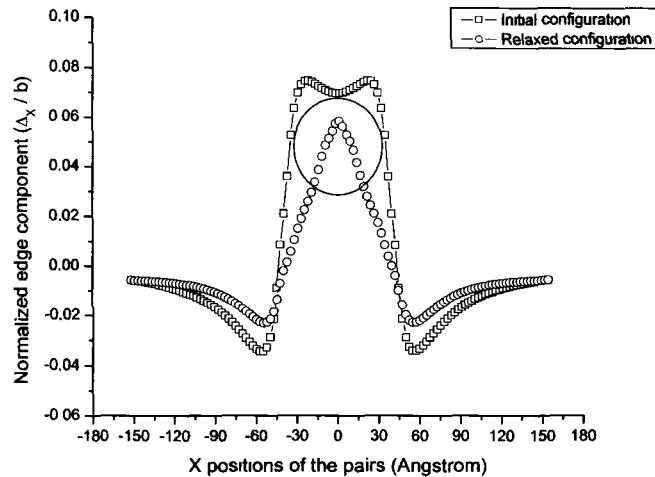
(b)

Figure 5.28: The analysis of the edge components along the middle (1 1 1) plane between two dislocations in initial models containing two perfect edge dislocations with the opposite Burgers vectors gliding on parallel slip planes (a) with the vertical distance of $1.2nm$ and (b) with the vertical distance of $1.4nm$, and the edge components along the middle (1 1 1) plane between two pairs of partial dislocations in corresponding relaxed configurations (interstitial type). The edge component is determined by the Disregistry approach.

178
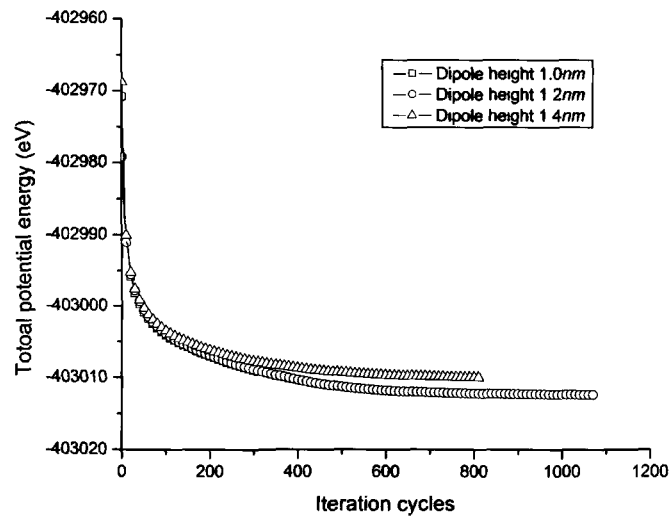
Figure 5.29: The comparison of the total potential energy in relaxed configurations as the interstitial-type dislocation dipole from initial models containing two perfect edge dislocations with the opposite Burgers vectors gliding on parallel slip planes with the vertical distances of $1.0nm$, $1.2nm$ and $1.4nm$.

5.2.2   Pair of screw dislocations

As discussed in Section(4.1.2), since the Burgers vector and the dislocation line are parallel, there is no determined slip plane for the screw dislocation. It is more difficult to manage the relaxed configuration when a pair of opposite screw dislocations is introduced into the model because both dislocations could dissociate on parallel {1 1 1} planes or parallel {1 1 -1} planes, or one on the {1 1 1} plane and the other on the {1 1 -1} plane. In order to keep both screw dislocations dissociating on the parallel horizontal {1 1 1} planes, two Shockley partial dislocations combined with edge and screw components are introduced into the model to represent the relaxed configuration of a perfect screw dislocation, which is

$$\frac{a}{2}[1 \; {-1} \; 0] = \frac{a}{6}[1 \; {-2} \; 1] + \frac{a}{6}[2 \; {-1} \; {-1}] \tag{5.3}$$

The assumption of Equation(5.3) ensures that the magnitude of the screw component in the original model and the represented model is the same, and the stacking fault is correctly built up during the simulation. For example, two partial dislocations according to Equation(5.3) are introduced into the perfect lattice to represent the relaxed configuration such as shown in Figure(4.13). After the relaxation, as shown in Figure(5.30), the screw component is almost unchanged while the edge component adjusts to make up the stacking fault between partial dislocations. Figure(5.31) compares the relaxed configurations of a perfect screw dislocation and the new model with the edge and screw components. It is found that the relaxation of the new model is in agreement with the relaxed configuration from the initial model containing a perfect screw dislocation, which implies that the stacking fault between two partial dislocations in the new model is formed correctly.

Therefore, four partial dislocations on parallel {1 1 1} slip planes are con-
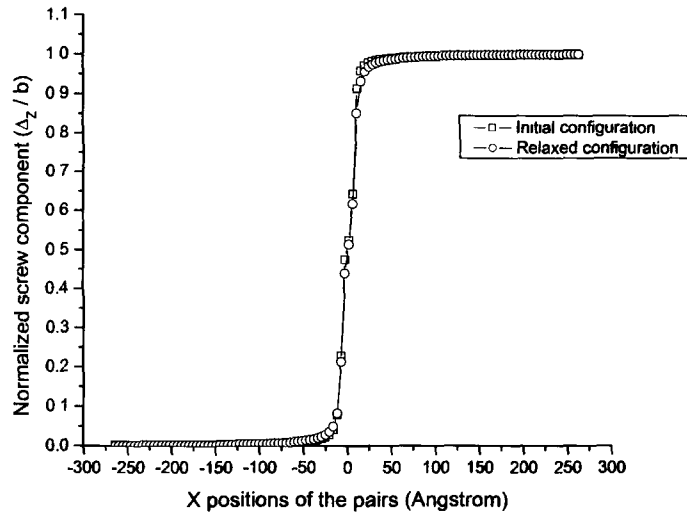
(a)
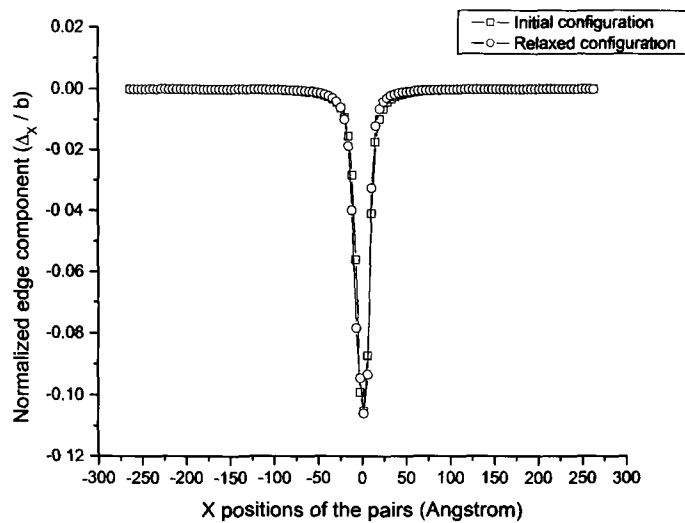
(b)

Figure 5.30: A model with two partial dislocations (initial configuration) to represent the relaxed configuration of a perfect screw dislocation (relaxed configuration). (a) The screw components of the Burgers vector; (b) The edge components of the Burgers vector. (a) and (b) are determined by Disregistry.
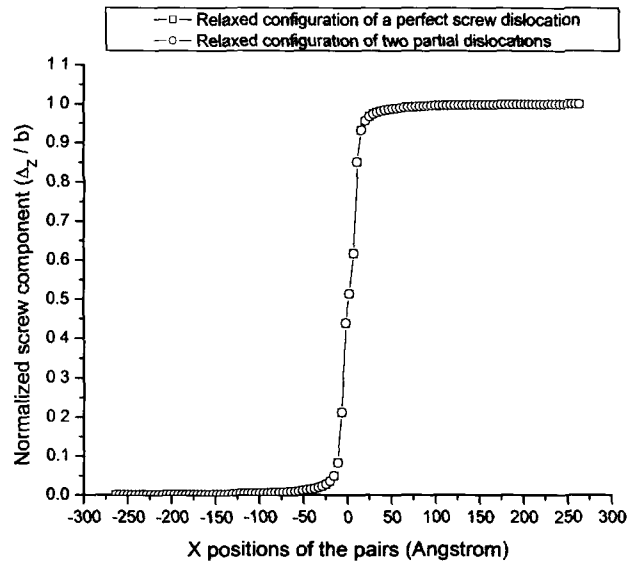
(a)
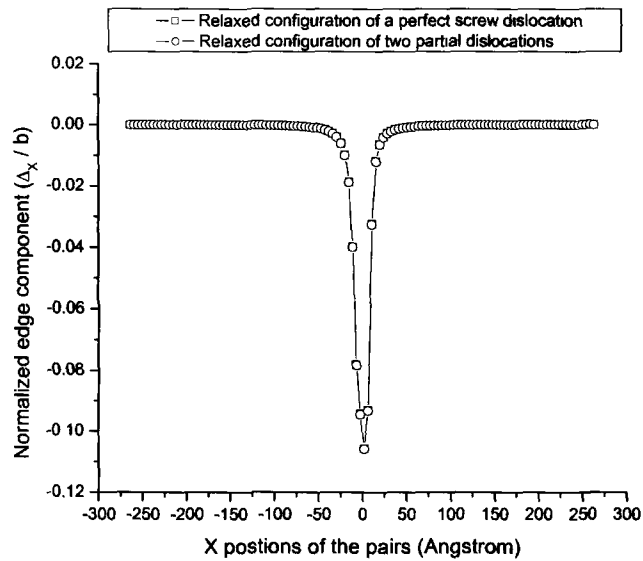
(b)

Figure 5.31: The comparison of relaxed configurations from (i) the initial model containing a perfect screw dislocation, and (ii) the initial model containing two partial dislocations to represent the relaxed configuration of a perfect screw dislocation. (a) The screw components of the Burgers vector; (b) The edge components of the Burgers vector. (a) and (b) are determined by Disregistry.

structed to represent two perfect screw dislocations forming a dipole with the height h depicted in Figure(5.32). After a series of tests with various heights of initial dipoles, it is confirmed that the critical height of the annihilation of the dipole of screw dislocations is no larger than $0.8nm$, which is in line with the conclusion drawn by Rasmussen *et al.* [47] for the spontaneous annihilation. More specifically, there are two stages in the annihilation process with the increase of the dipolar height due to the existence of the edge component during the relaxation. When the dipolar height is below $0.41nm$, both edge and screw components of the Burgers vector can completely annihilate. As an example, Figure(5.33) demonstrates the analysis of edge and screw components along the middle (1 1 1) plane in the model with the height of $0.4nm$. After the relaxation, the configuration returns to the perfect lattice. When the dipolar height is over $0.41nm$, such as $0.8nm$, the edge components in the model could not annihilate since the dipolar height is larger than the critical value. The screw components, however, completely annihilate as shown in Figure(5.34). Thus, the relaxed configuration in this case eventually results in the interaction between edge components on parallel slip planes.

When the dipolar height is $1.0nm$, the relaxed configuration shows the transitional stage from the annihilation to the faulted dipolar structure. Similar to the case of the vacancy-type edge dislocation dipole at the height of $0.42nm$, the separation of partial dislocations on respective slip planes are as narrow as $0.33nm$ so that the 'Z' configuration is smaller than the usual one as shown in Figure[5.35(c)]. From the analysis of the edge and screw components along the middle (1 1 1) plane by the Disregistry approach shown in Figure[5.35(a)] and [5.35(b)], due to the close positions of partial dislocations, the sudden change in both relaxed curves is very pronounced. This implies that the new stacking fault is generated, and the interaction between dislocations is very strong.

(a)

(b)
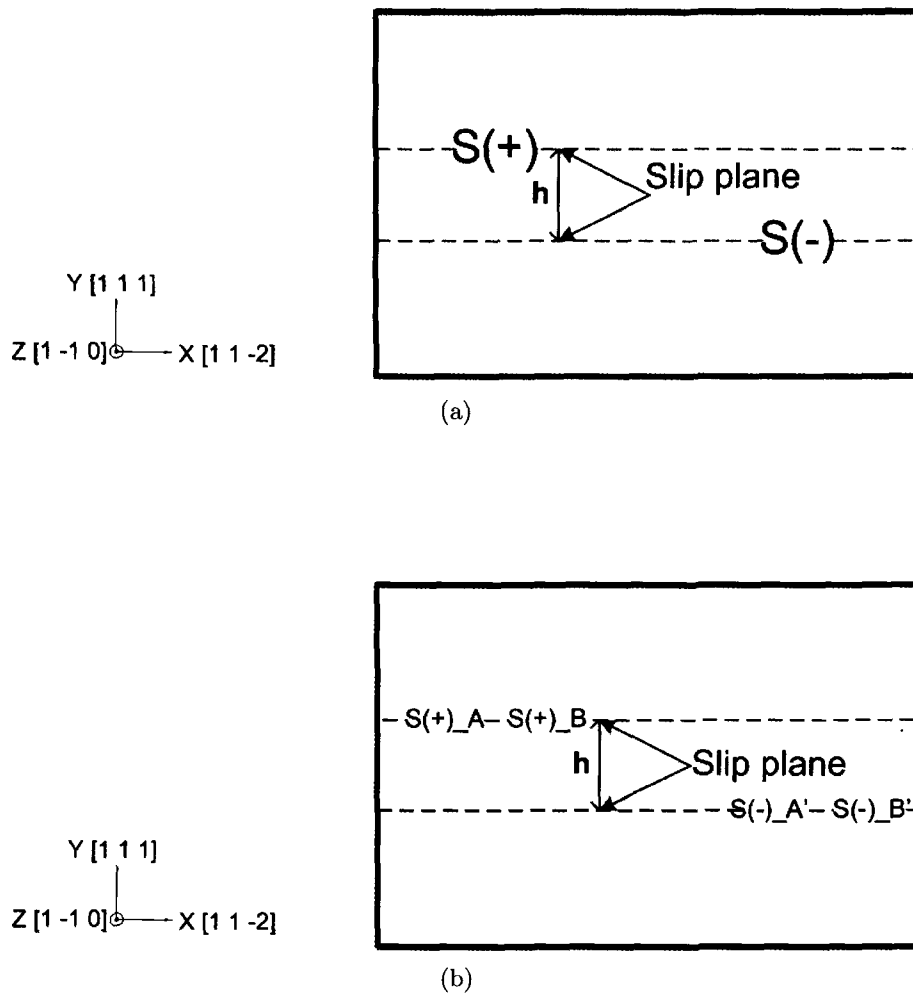
Figure 5.32: The schematic configurations of two perfect screw dislocations with the opposite Burgers vectors gliding on parallel slip planes with the vertical distance h. (a) The ideal model; (b) The substitutional model.
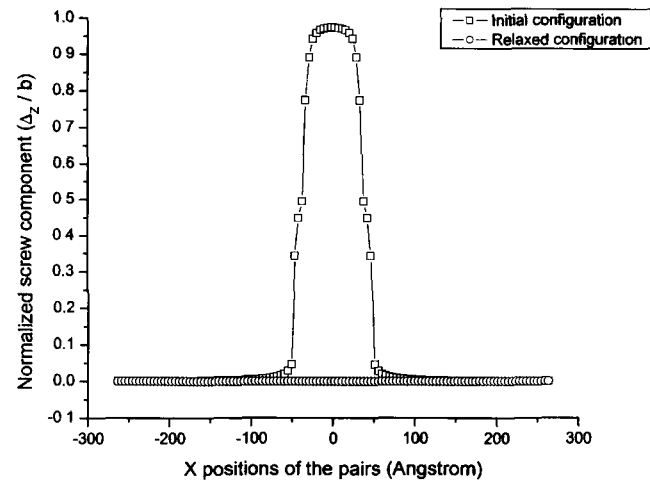
(a)
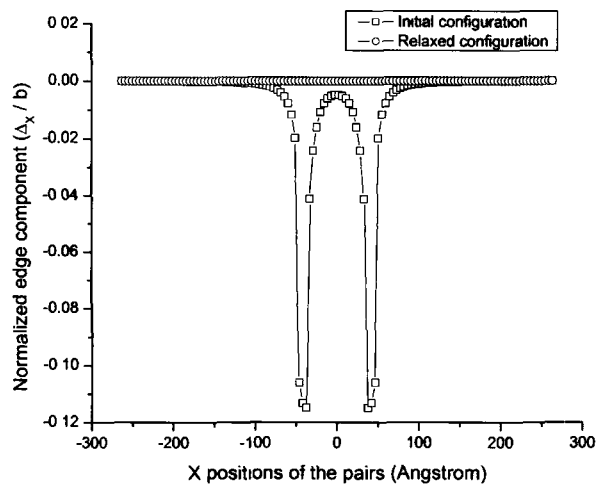
(b)

Figure 5.33: The analysis of screw and edge components along the middle (1 1 1) plane in the initial model containing two perfect screw dislocations with the opposite Burgers vectors gliding on parallel slip planes with the vertical distance of $0.4nm$, and screw and edge components along the middle (1 1 1) plane between two pairs of partial dislocations in the corresponding relaxed configuration. (a) The screw components; (b) The edge components. (a) and (b) are determined by the Disregistry approach.

185

(a)

(b)

(c)
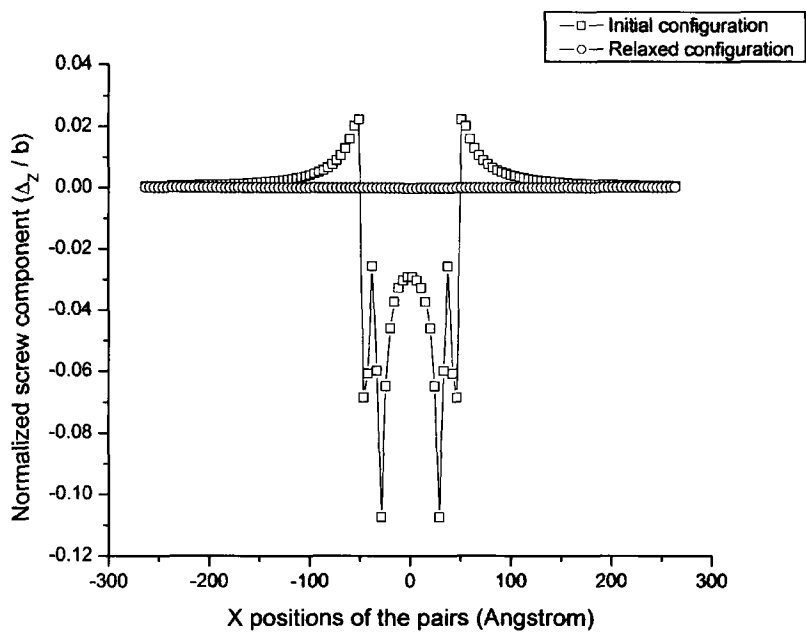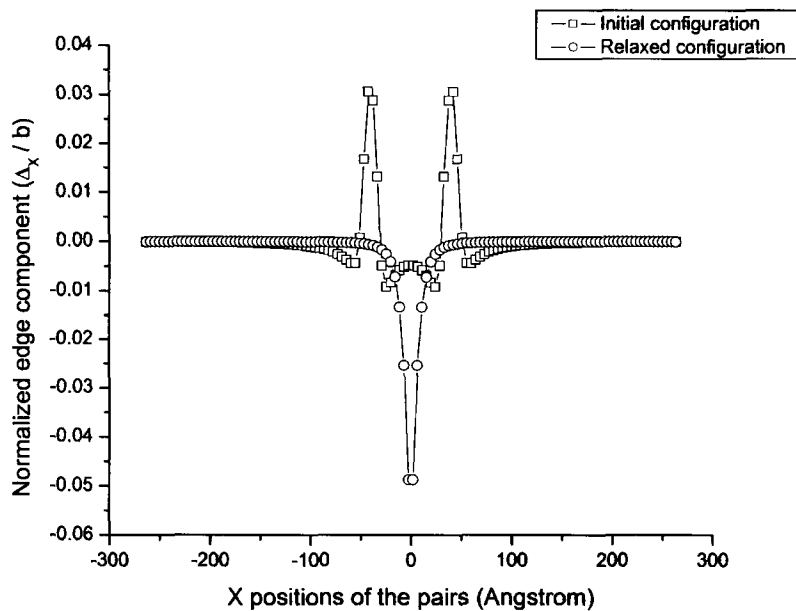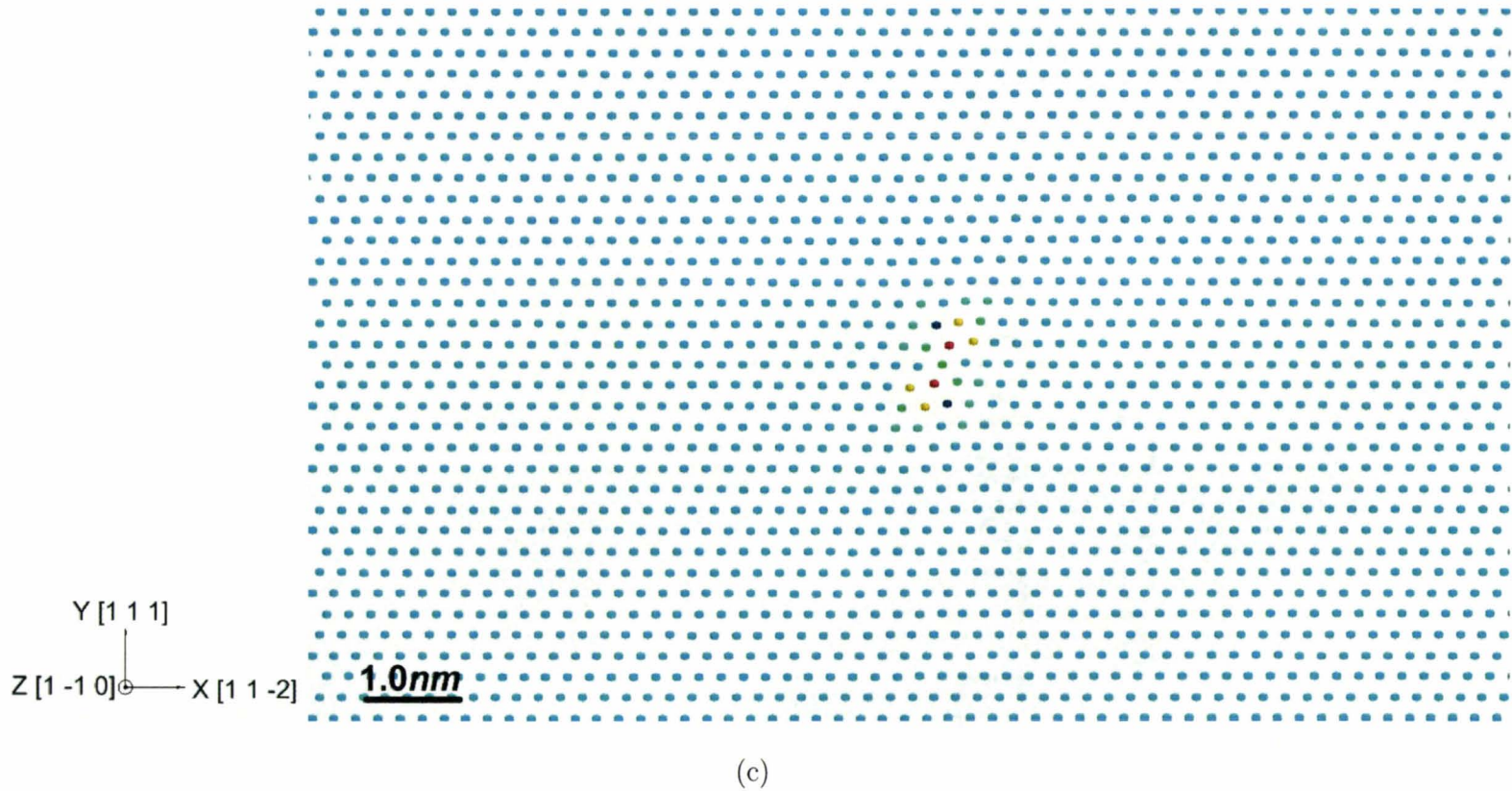
Figure 5.34: The analysis of screw and edge components along the middle (1 1 1) plane in the initial model containing two perfect screw dislocations with the opposite Burgers vectors gliding on parallel slip planes with the vertical distance of $0.8nm$, and screw and edge components along the middle (1 1 1) plane between two pairs of partial dislocations in the corresponding relaxed configuration. (a) The screw components; (b) The edge components; (c) The positions of partial dislocations in the relaxed configuration. (a) and (b) are determined by the Disregistry approach.

(a)

(b)

Y [1 1 1]

Z [1 -1 0] → X [1 1 -2]

1.0nm

(c)
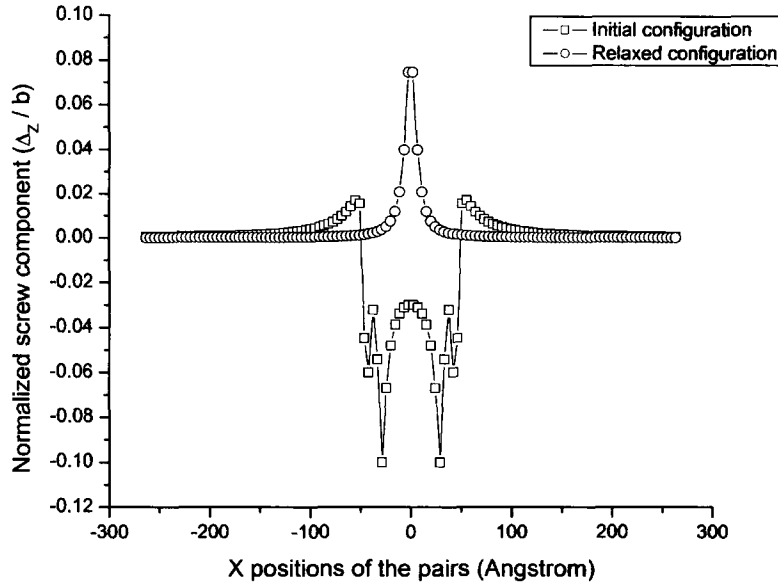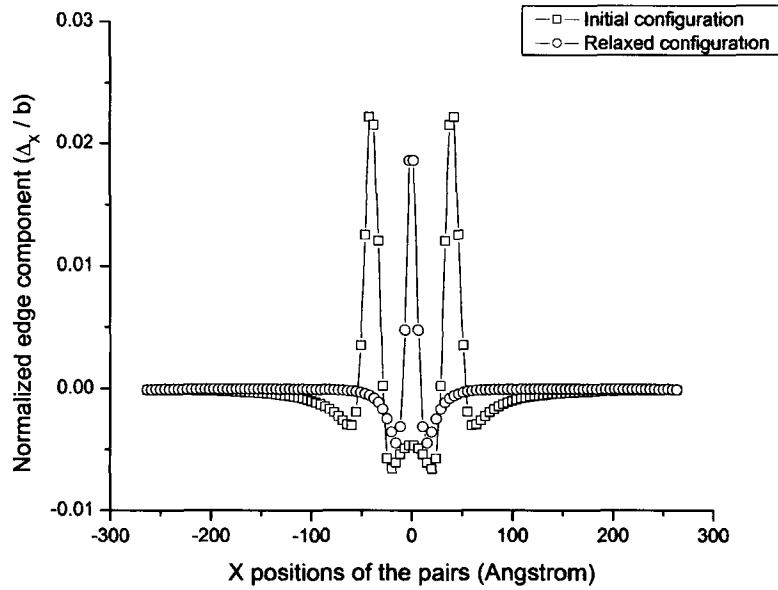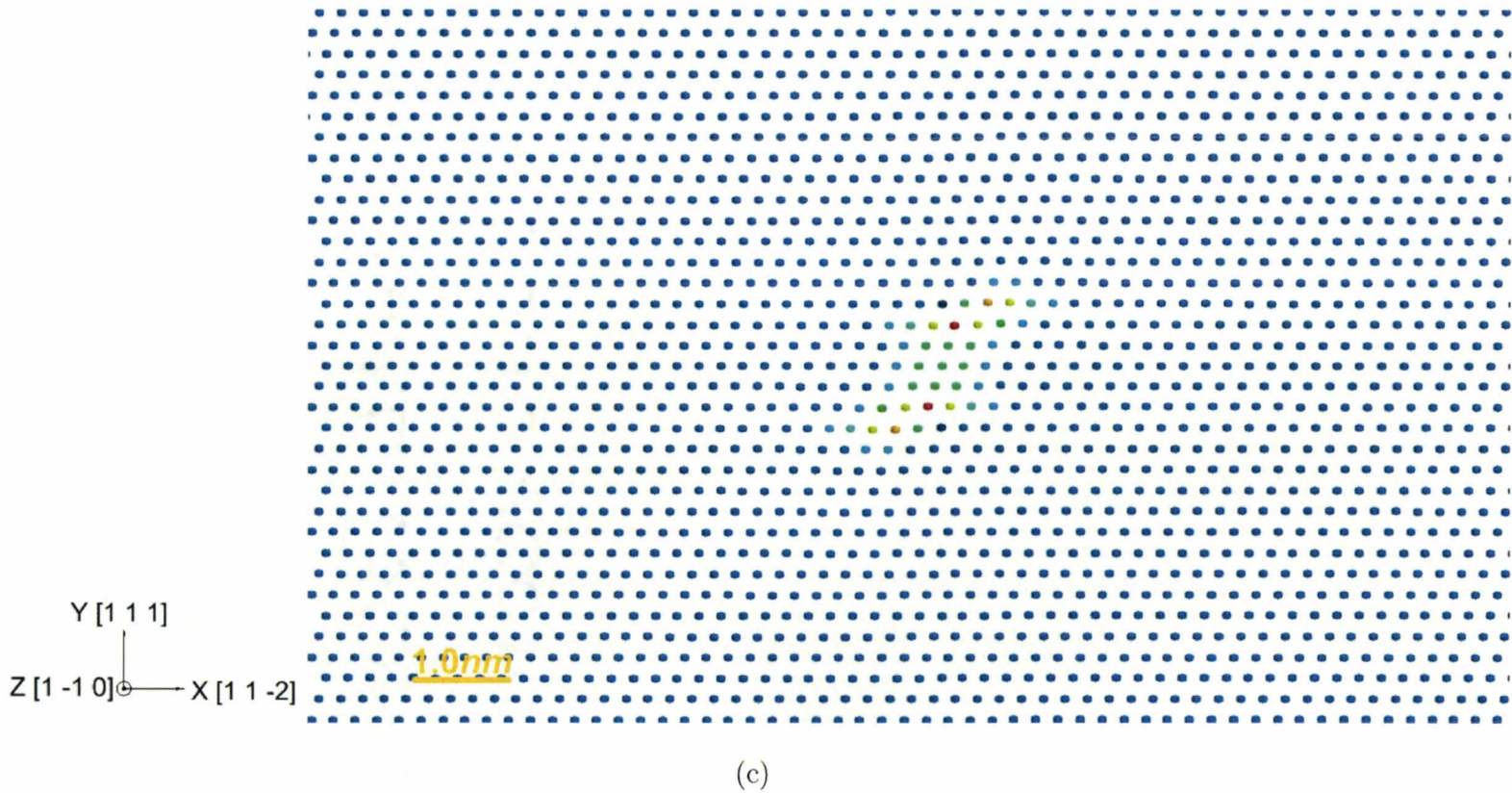
Figure 5.35: The analysis of screw and edge components along the middle (1 1 1) plane in the initial model containing two perfect screw dislocations with the opposite Burgers vectors gliding on parallel slip planes with the vertical distance of $1.0nm$, and screw and edge components along the middle (1 1 1) plane between two pairs of partial dislocations in the corresponding relaxed configuration. (a) The screw components; (b) The edge components; (c) The positions of partial dislocations in the relaxed configuration. (a) and (b) are determined by the Disregistry approach.

The faulted dipole in the 'Z' configuration is formed when the vertical height is not larger than $2.0nm$. For example, Figure(5.36) illustrates the process of the formation of the faulted dipole when the dipolar height is $1.8nm$, and the average initial horizontal distance between two screw dislocations is set to $8nm$. During the relaxation, the bond between two partial dislocations is not as tight as edge dislocation dipoles. The leading partial dislocations, such as B and A', move faster than the remaining partial dislocations A and B' but the separation between partial dislocations gradually decreases during the formation of the 'Z' dipole configuration. Finally, the splitting width between partial dislocations is around $1.5nm$, which is slightly larger than the benchmark result. From the analysis of edge and screw components along the middle (1 1 1) plane in the initial and relaxed configurations as shown in Figure(5.37), the screw component clearly implies that the new stacking fault is generated across the partial dislocations B and A' as a sudden change in the center of the curve.

Compared with relaxed configurations with the dipolar height of $2.0nm$ and $2.2nm$ as shown in Figures [5.38(c)] and [5.39(c)], the angle between partial dislocations B and A' changes from the acute value to the obtuse one, which means the relaxed structure moves from the faulted dipole to the stable dipole. Moreover, the angle between partial dislocations A and A' are in agreement with the value that is observed by Rasmussen *et al.* [47] for stable dipoles due to the anisotropic properties of the material. The separation between partial dislocations in the stable dipole doubles the benchmark result. Thus, the strength of the link between two partial dislocations in the current configuration of the screw dislocation dipole is weaker than it is in the lattice containing edge dislocation dipoles.

The curve of the screw component along the middle (1 1 1) plane in the relaxed configuration of the stable dipole becomes smooth compared to the faulted
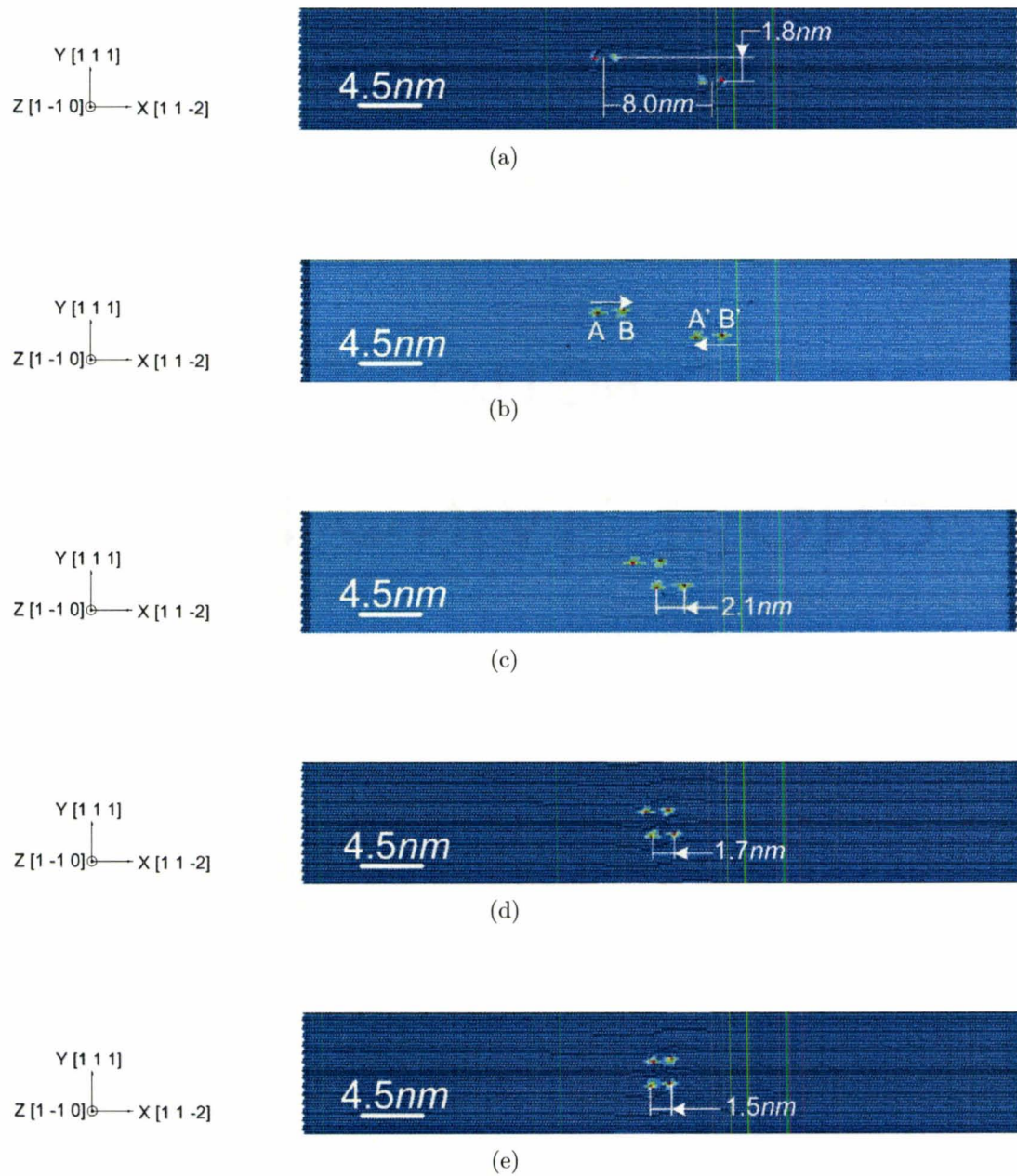
Figure 5.36: The positions of dislocations during the relaxation of two perfect screw dislocations with the opposite Burgers vectors gliding on parallel slip planes with the vertical distance of 1.8nm. (a) Cycle No: 0; (b) Cycle No: 100; (c) Cycle No: 1000; (d) Cycle No: 1100; (e) Cycle No: 2240.
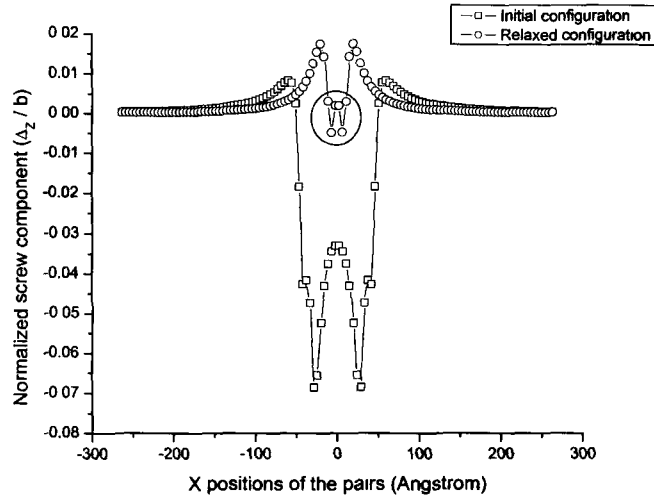
(a)
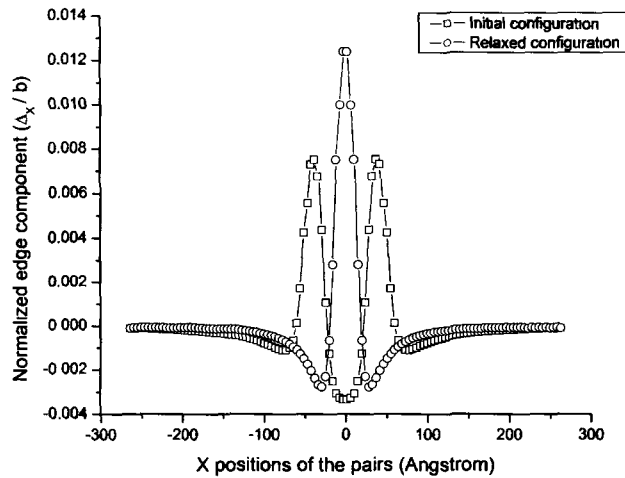
(b)

Figure 5.37: The analysis of screw and edge components along the middle (1 1 1) plane in the initial model containing two perfect screw dislocations with the opposite Burgers vectors gliding on parallel slip planes with the vertical distance of 1.8nm, and screw and edge components along the middle (1 1 1) plane between two pairs of partial dislocations in the corresponding relaxed configuration. (a) The screw components; (b) The edge components. (a) and (b) are determined by the Disregistry approach.

(a)

(b)

(c)
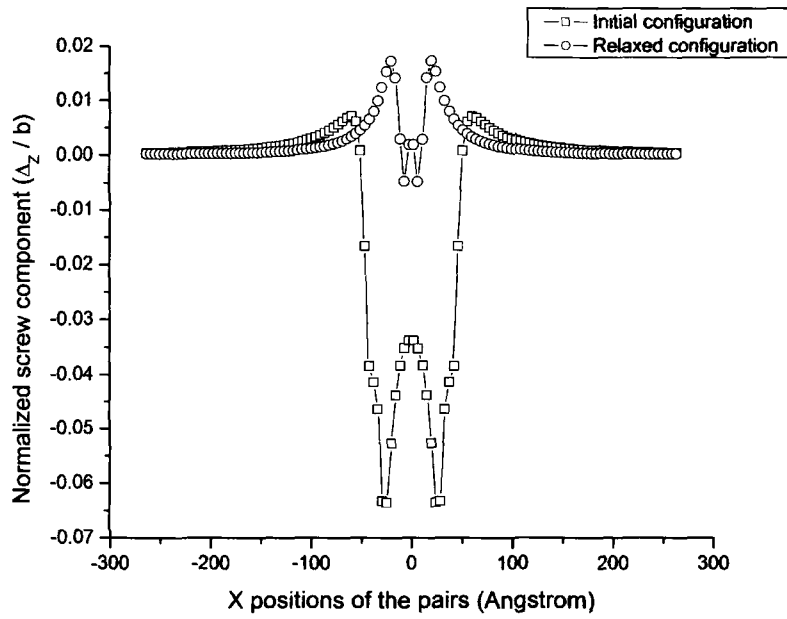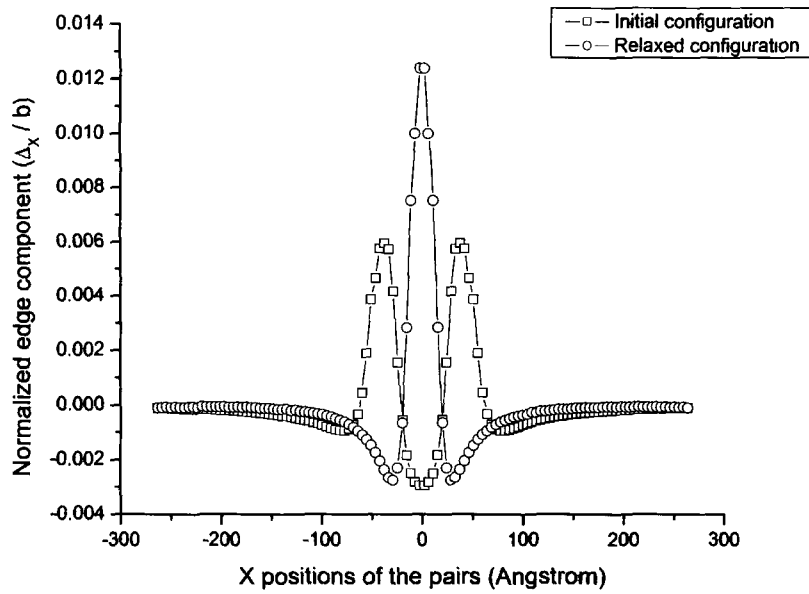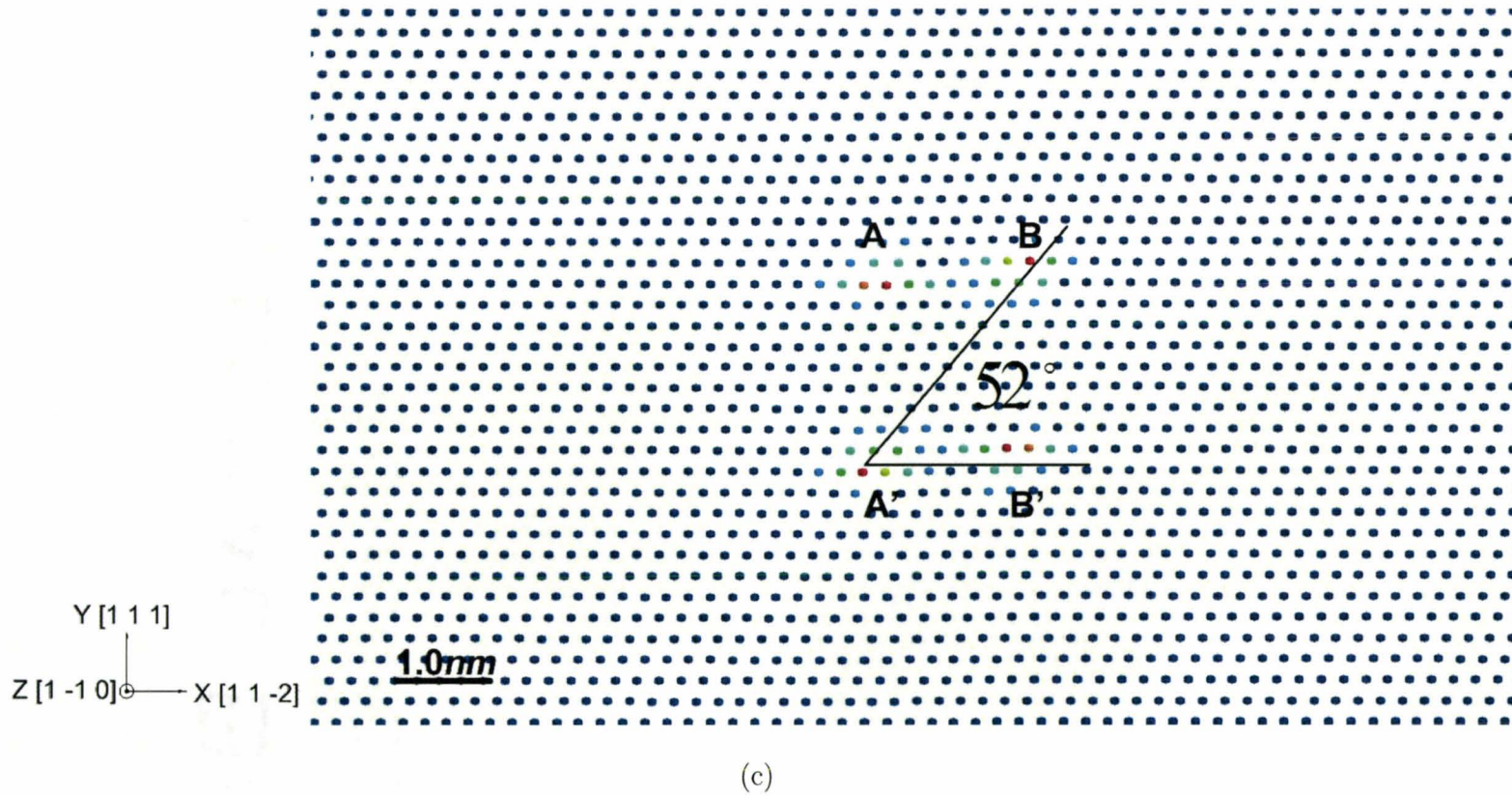
Figure 5.38: The analysis of screw and edge components along the middle (1 1 1) plane in the initial model containing two perfect screw dislocations with the opposite Burgers vectors gliding on parallel slip planes with the vertical distance of 2.0nm, and screw and edge components along the middle (1 1 1) plane between two pairs of partial dislocations in the corresponding relaxed configuration. (a) The screw components; (b) The edge components; (c) The positions of partial dislocations in the relaxed configuration. (a) and (b) are determined by the Disregistry approach.

(a)

(b)

(c)
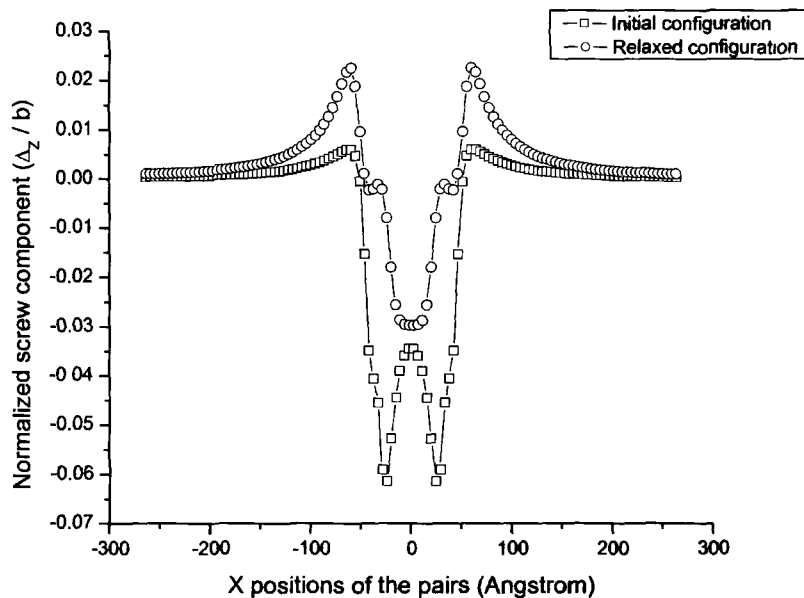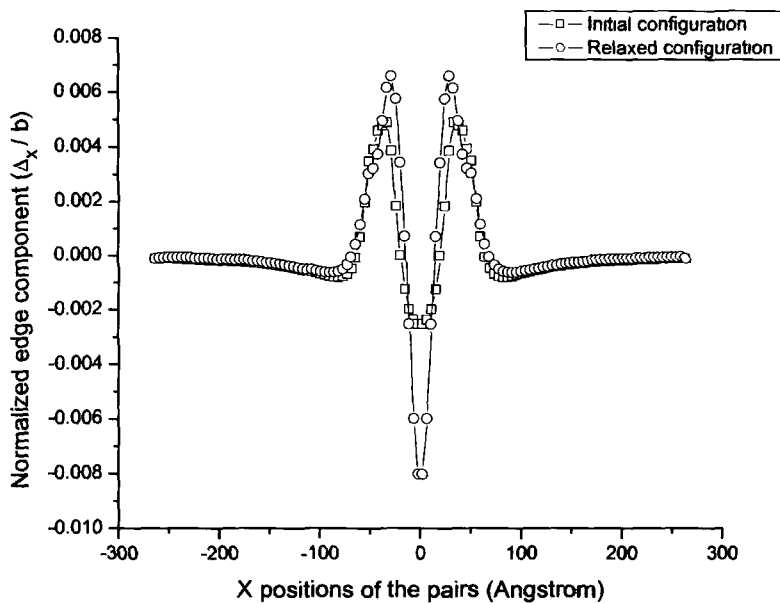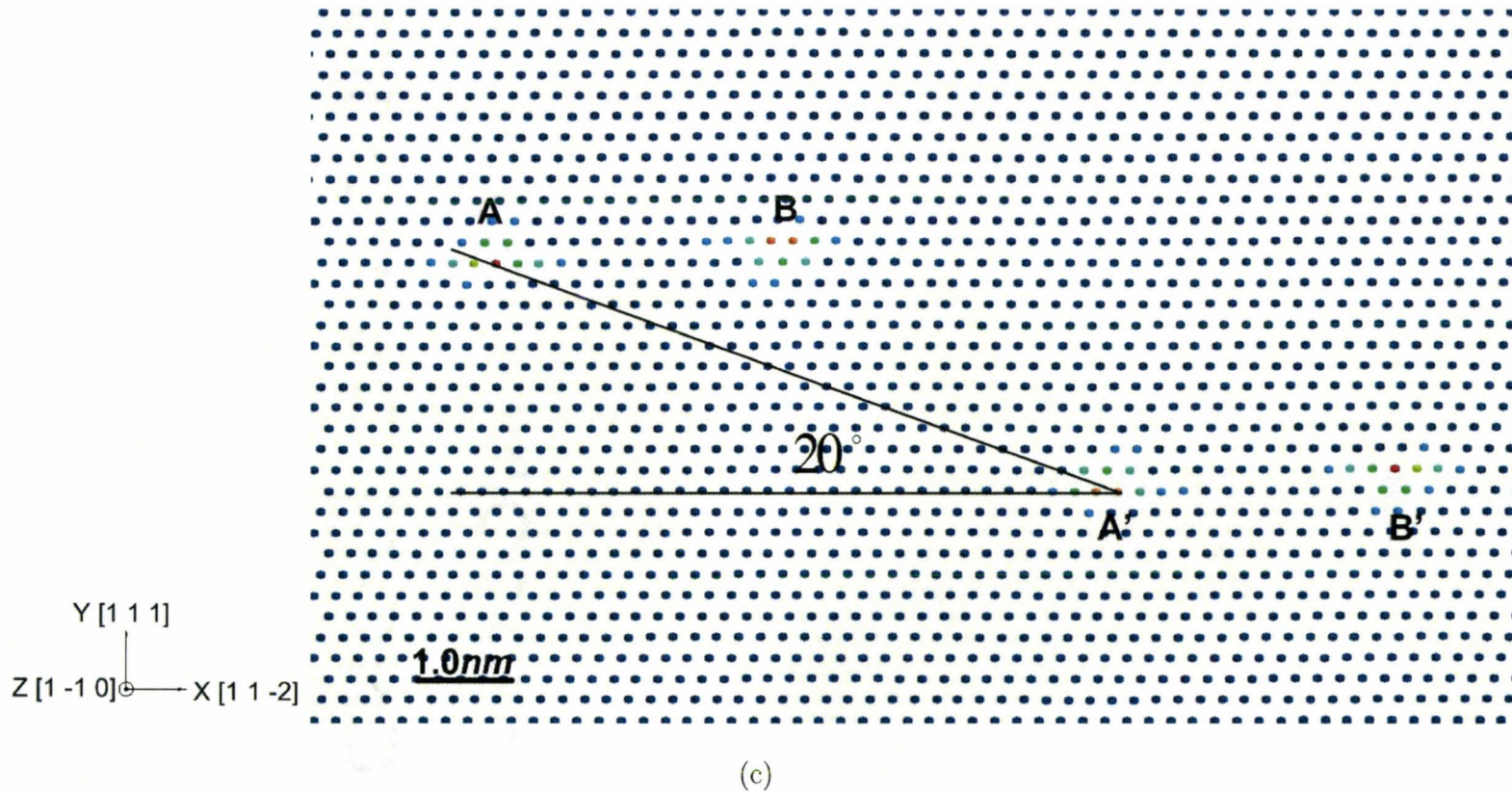
Figure 5.39: The analysis of screw and edge components along the middle (1 1 1) plane in the initial model containing two perfect screw dislocations with the opposite Burgers vectors gliding on parallel slip planes with the vertical distance of 2.2*nm*, and screw and edge components along the middle (1 1 1) plane between two pairs of partial dislocations in the corresponding relaxed configuration. (a) The screw components; (b) The edge components; (c) The positions of partial dislocations in the relaxed configuration. (a) and (b) are determined by the Disregistry approach.

dipole as shown in Figures[5.38(a)] and [5.39(a)]. With respect to the curves of edge components as shown in Figures[5.38(b)] and [5.39(b)], their trends are opposite in relaxed configurations of the faulted dipole and the stable dipole. Both evidences clearly exhibit that the interaction across the partial dislocations, such as $B - A'$, or the new stacking fault disappears starting from the dipolar height of $2.2nm$. The total potential energy in the stable dipolar structures is higher than the faulted dipole. As shown in Figure(5.40), there is no visible energy difference for the configurations with the dipolar height of $1.8nm$ and $2.0nm$. However, the energy substantially increases when the stable dipole is formed at the height of $2.2nm$. For the perfect screw dislocation dipole, the faulted dipole with lower energy again could be regarded as a more stable configuration.

If the signs of two perfect screw dislocations ($A - B$, $A' - B'$) are made opposite based on Figure(5.32), the results are virtually the same. Therefore, unlike edge dislocation dipoles, there is no obvious distinction of the 'Z' or 'S' configurations in the screw dislocation dipoles.

5.2.3   Pair of 60-degree dislocations

The model coordinates are changed to X[2 -1 -1], Y[1 1 1] and Z[0 -1 1]. The dislocation line is along the Z direction and the direction of the Burgers vector **b** is [1 -1 0]. The angle between **b** and the **Z** direction is $60°$. The 60-degree dislocation could be decomposed into edge and screw components. Thus, the corresponding edge component keeps the perfect dislocation dissociating on the horizontal {1 1 1} plane. As in previous cases of two perfect edge dislocations, two 60-degree dislocations with the opposite Burgers vectors are placed on parallel {1 1 1} slip planes with the vertical height h. The distance between two perfect dislocations is set to $8.0nm$. According
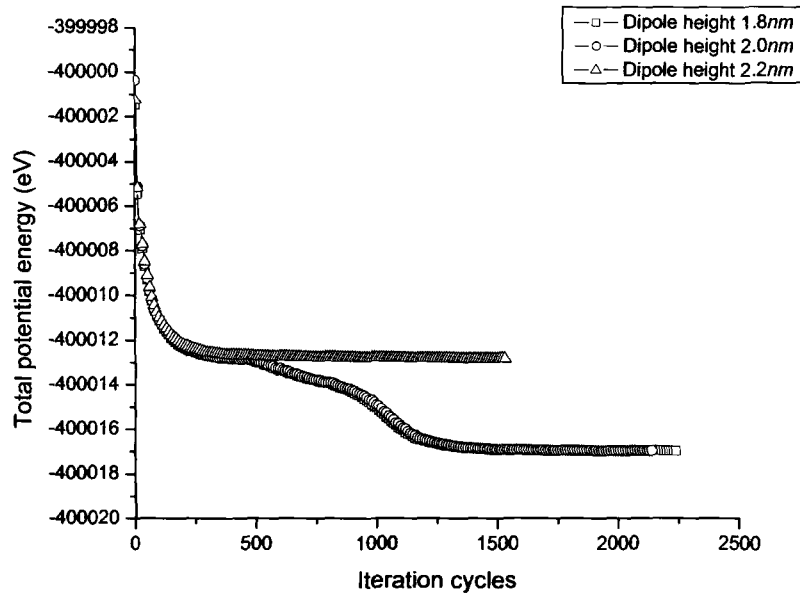
Figure 5.40: The comparison of the total potential energy in relaxed configurations from initial models of two perfect screw dislocations with the opposite Burgers vectors gliding on parallel slip planes with the vertical distances of $1.8nm$, $2.0nm$ and $2.2nm$.

to the orientation of edge components of 60-degree dislocation dipoles, the vacancy type and the interstitial type dipoles are used to distinguish two configurations.

5.2.3.1 The vacancy type

Below the dipolar height of $0.4nm$, two opposite dislocations completely annihilate as shown in Figure(5.41). When the dipolar height is in the range between $0.4nm$ and $1.0nm$ exclusive, the faulted dipole in the 'Z' configuration is formed instead of the annihilation of the screw component, which occurs in the perfect screw dislocation dipoles. For example, as shown in Figure(5.42), when the dipolar height is $0.8nm$, the curve of the edge component along the middle (1 1 1) plane between two pairs of partial dislocations in the relaxed configuration is not smooth in the center of the model. Since the separation of two partial dislocation is around $1.0nm$ in this case, the curve of the screw component along the middle (1 1 1) plane in the relaxed lattice becomes pronounced as it approaches the region of the 'Z' configuration.

The 'Z' configuration dominates in the relaxed configuration until the height is $2.0nm$. Figures(5.43) and (5.44) compare the relaxation results between configurations with the dipolar height of $2.0nm$ and $2.2nm$. When the relaxed configuration changes from the faulted dipole to the stable dipole, the angle between leading partial dislocations changes from $49°$ to $119°$. The splitting width of partial dislocations increases from $2.5nm$ to $3.9nm$, which is in line with the relaxed configurations of screw dislocation dipoles. With regard to the screw and edge components along the middle (1 1 1) plane between two pairs of partial dislocations, the sudden change in the relaxed edge curve disappears while the screw curve becomes smooth when the height h is larger than the critical value of the faulted dipole. The total potential energy of relaxed configurations with the dipolar heights of $1.8nm$, $2.0nm$, and $2.2nm$ is on the same level as shown in Figure(5.45). However, the initial potential energy
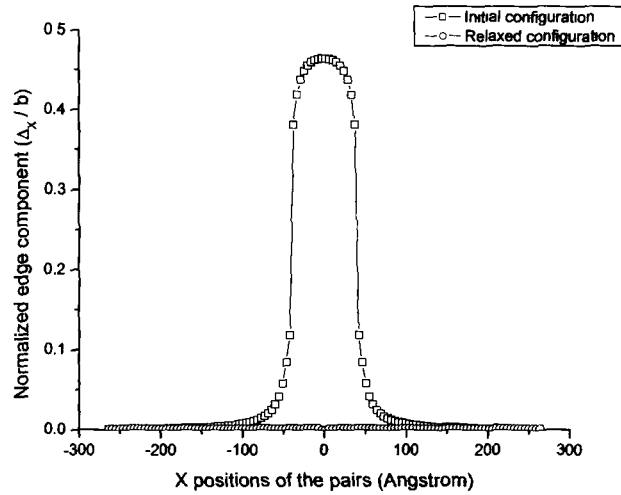
(a)
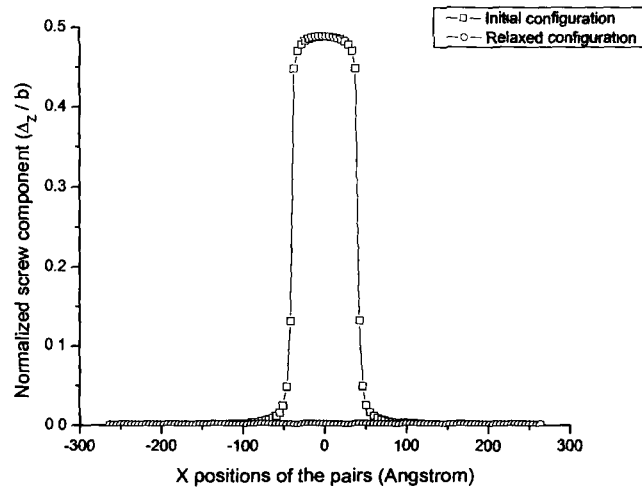
(b)

Figure 5.41: The analysis of screw and edge components along the middle (1 1 1) plane in the initial model containing two 60-degree dislocations with the opposite Burgers vectors gliding on parallel slip planes with the vertical distance of $0.4nm$, and screw and edge components along the middle (1 1 1) plane between two pairs of partial dislocations in the corresponding relaxed configuration (vacancy type). (a) The edge components; (b) The screw components. (a) and (b) are determined by the Disregistry approach.

(a)

(b)

Y [1 1 1]

Z [0 -1 1] ⊙ ——→ X [2 -1 -1]

1.0nm

(c)
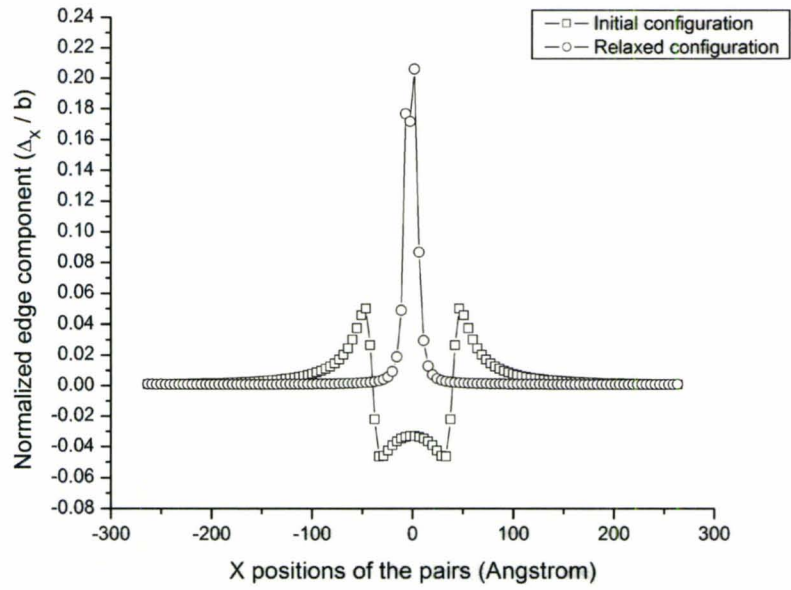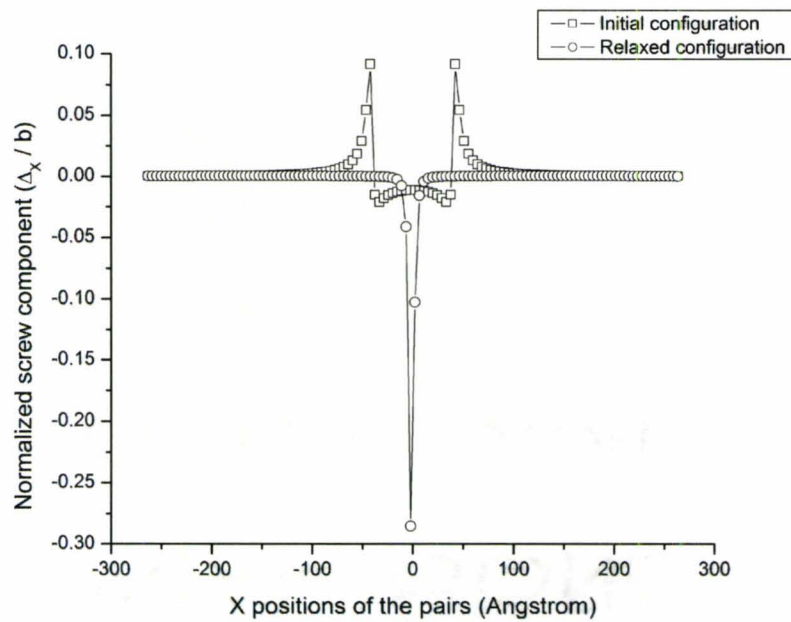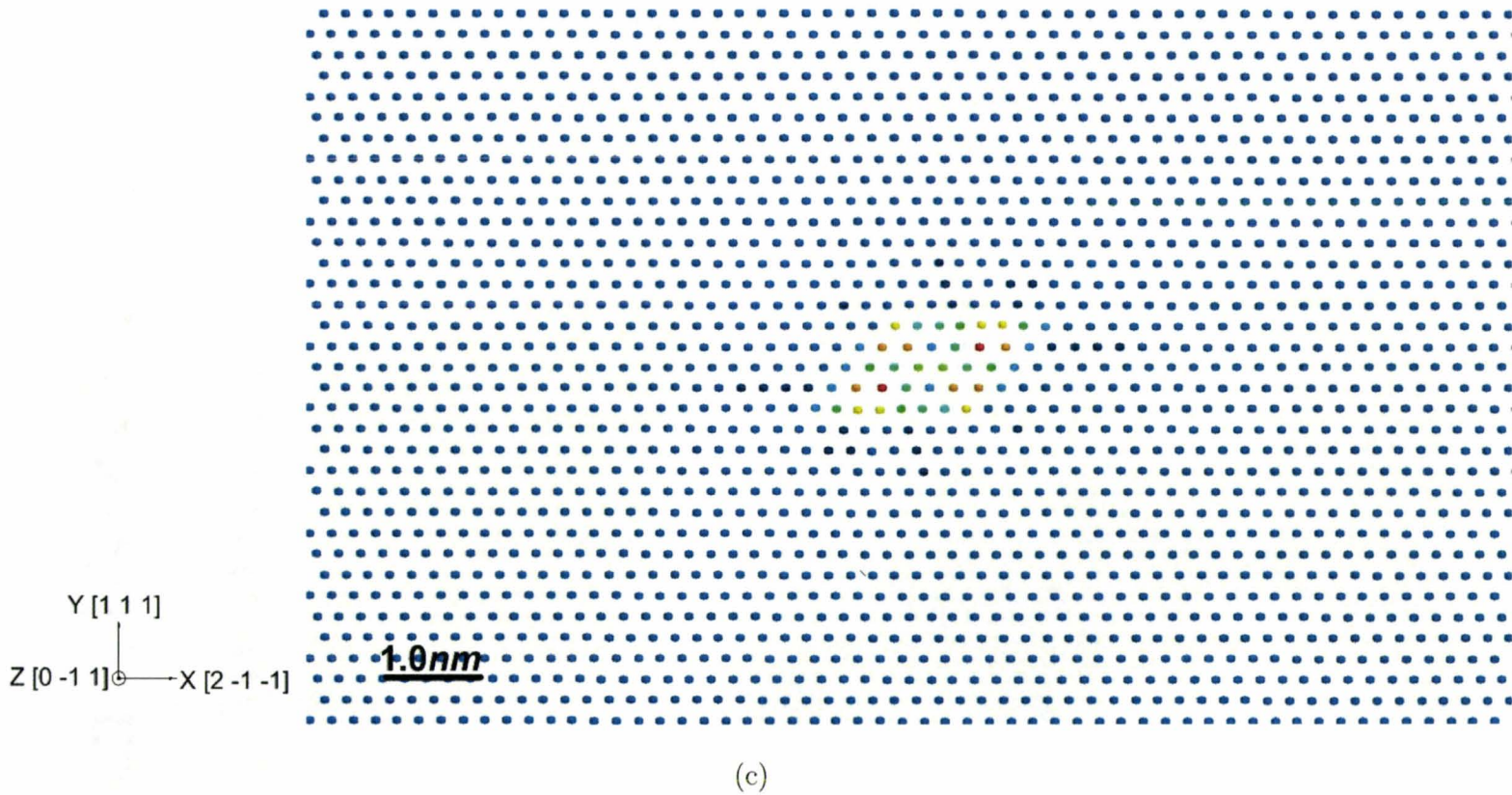
Figure 5.42: The analysis of edge and screw components along the middle (1 1 1) plane in the initial model containing two 60-degree dislocations with the opposite Burgers vectors gliding on parallel slip planes with the vertical distance of $0.8nm$, and edge and screw components along the middle (1 1 1) plane between two pairs of partial dislocations in the corresponding relaxed configuration (vacancy type). (a) The edge components; (b) The screw components; (c) The positions of partial dislocations in the relaxed configuration (vacancy type). (a) and (b) are determined by the Disregistry approach.

in the case of the dipolar height of $2.2nm$ is the lowest among these three scenarios due to the largest distance between two initial dislocations. Thus, the rate of the decrease of the potential energy in the case of the stable dipole is the smallest, so that the faulted dipole could be again regarded as the more stable configuration.

5.2.3.2   The interstitial type

The evolution of interstitial type 60-degree dislocation dipoles is similar to edge dislocation dipoles, which is faster than the vacancy counterpart. The annihilation between these two opposite mixed dislocations is not observed except the trivial case of gliding on the same slip plane. At the dipolar height of $0.4nm$, the small 'S' configuration is formed as shown in Figure(5.46), in which the splitting width between every pair of partial dislocations is $1.0nm$, and the analysis of edge and screw components along the middle (1 1 1) plane between two pairs of partial dislocations implies that the new stacking fault appears in the center of the model.

The critical height of forming the 'S' configuration under current conditions is $1.6nm$. As an example, Figure(5.47) shows the relaxed result from initial two dislocations with the vertical distance of $1.0nm$. In this case, the separation of partial dislocations is around $4.4nm$. The new stacking fault across the leading partial dislocations is formed through the obtuse angle, which can also be inferred from the potential energy distribution and the analysis of the edge component along the middle (1 1 1) plane between two pairs of partial dislocations.

Figures(5.48) and (5.49) compare the relaxed faulted dipole and the stable perfect dipole with the heights of $1.6nm$ and $1.8nm$. The transition from the faulted dipole to the stable dipole in this case is not so obvious. The angle between two leading partial dislocations is the same and the splitting width between pair of partial dislocations in two relaxed configurations is on the similar magnitude. The indicator

(a)

(b)

(c)
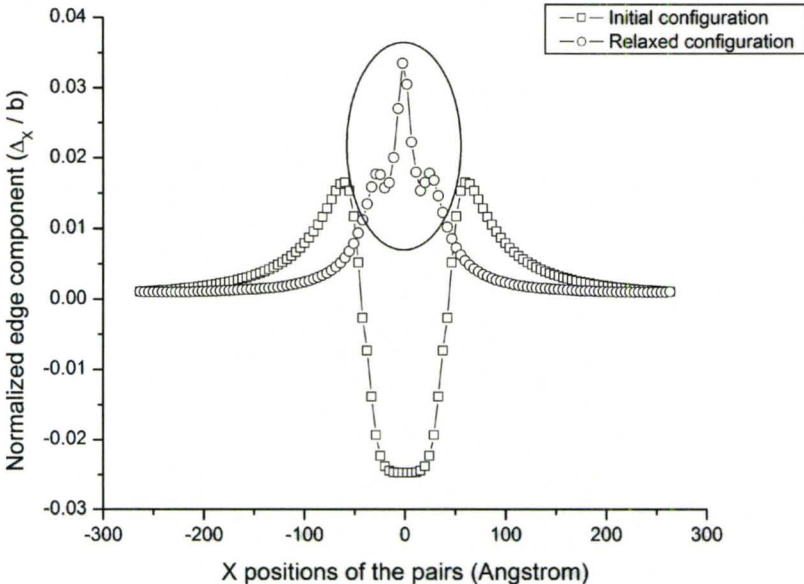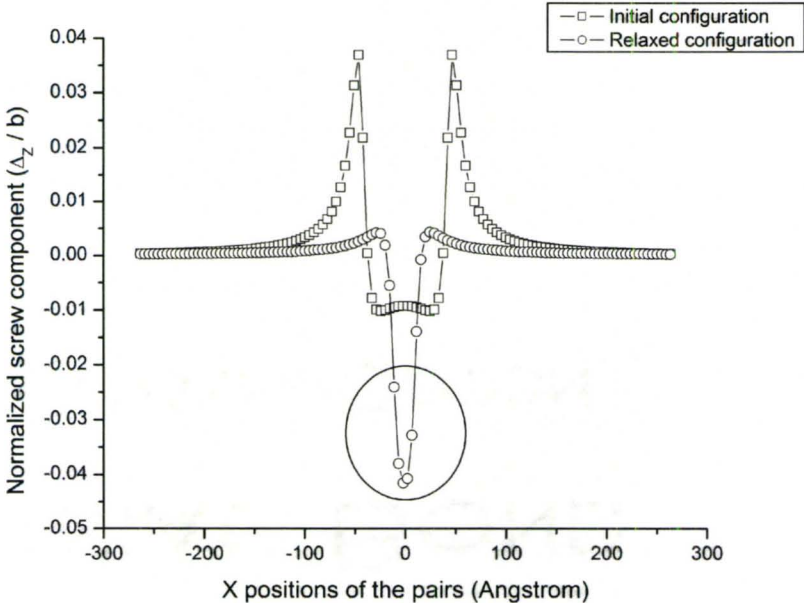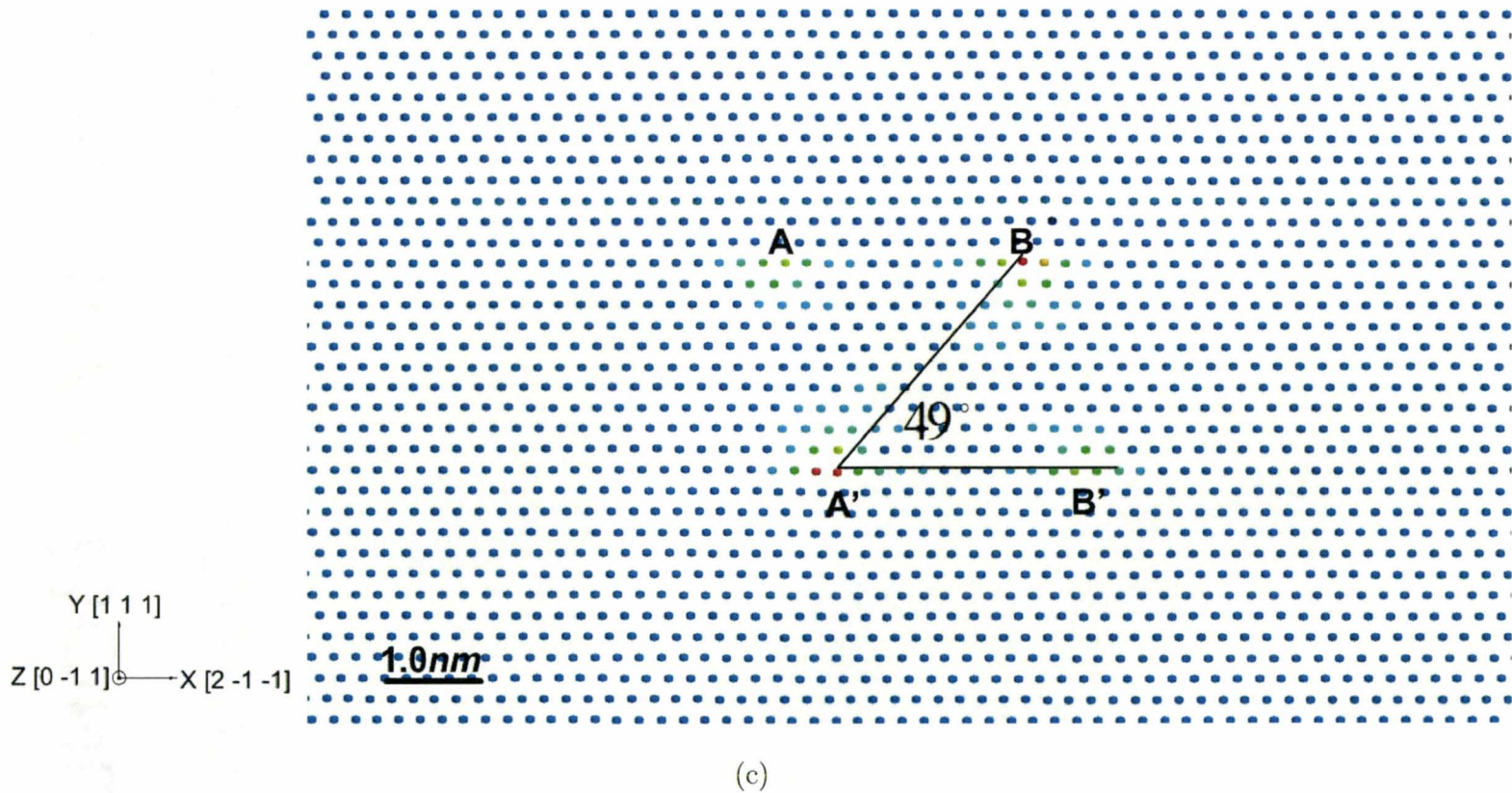
Figure 5.43: The analysis of edge and screw components along the middle (1 1 1) plane in the initial model containing two 60-degree dislocations with the opposite Burgers vectors gliding on parallel slip planes with the vertical distance of 2.0nm, and edge and screw components along the middle (1 1 1) plane between two pairs of partial dislocations in the corresponding relaxed configuration (vacancy type). (a) The edge components; (b) The screw components; (c) The positions of partial dislocations in the relaxed configuration (vacancy type). (a) and (b) are determined by the Disregistry approach.

(a)

(b)

(c)
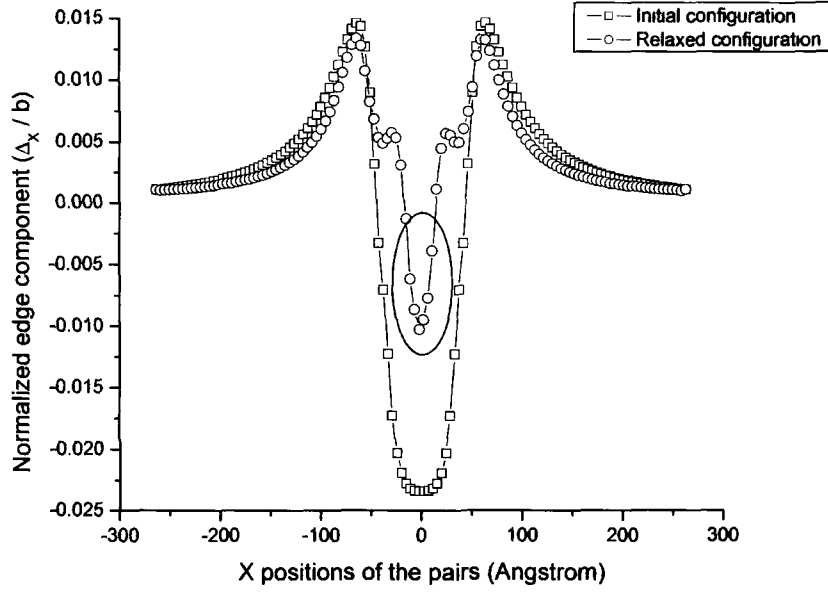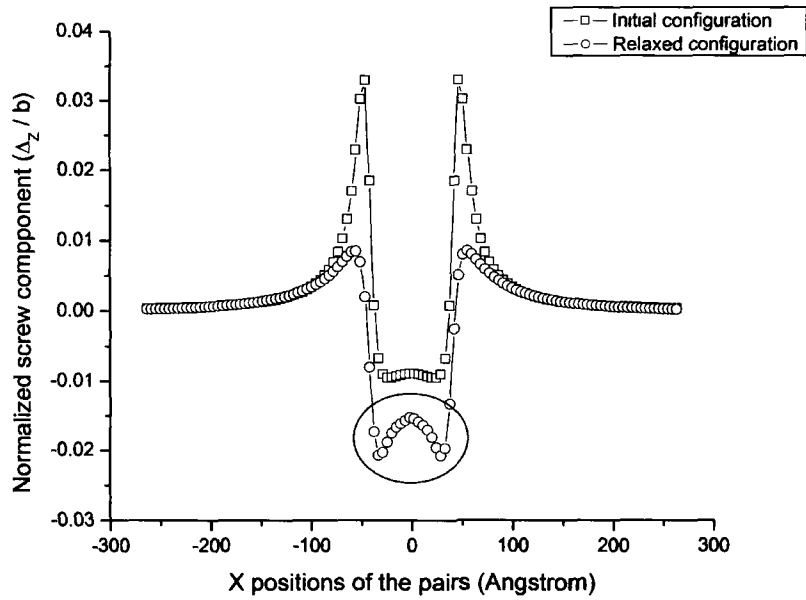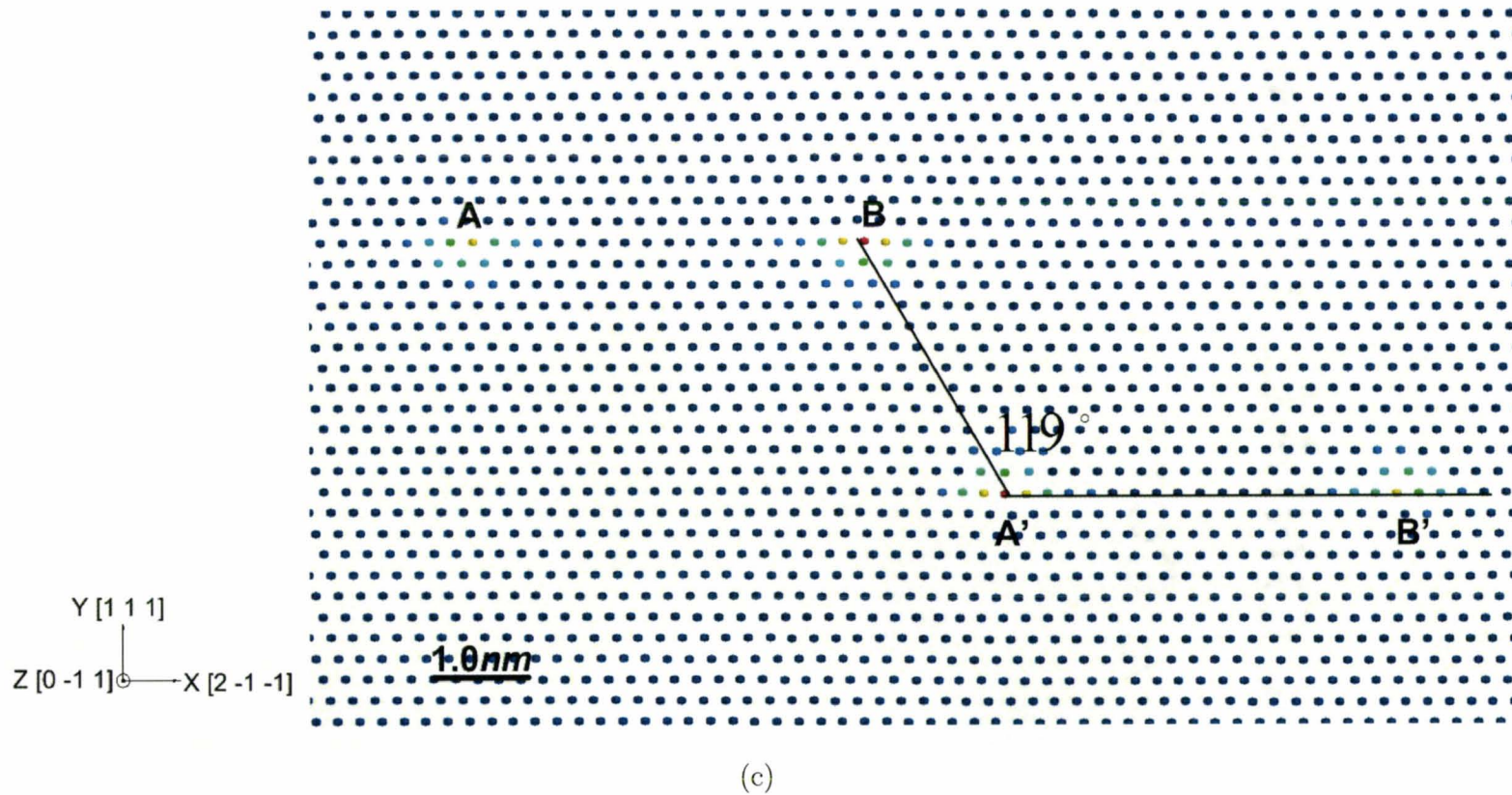
Figure 5.44: The analysis of edge and screw components along the middle (1 1 1) plane in the initial model containing two 60-degree dislocations with the opposite Burgers vectors gliding on parallel slip planes with the vertical distance of 2.2nm, and edge and screw components along the middle (1 1 1) plane between two pairs of partial dislocations in the corresponding relaxed configuration (vacancy type). (a) The edge components; (b) The screw components; (c) The positions of partial dislocations in the relaxed configuration (vacancy type). (a) and (b) are determined by the Disregistry approach.
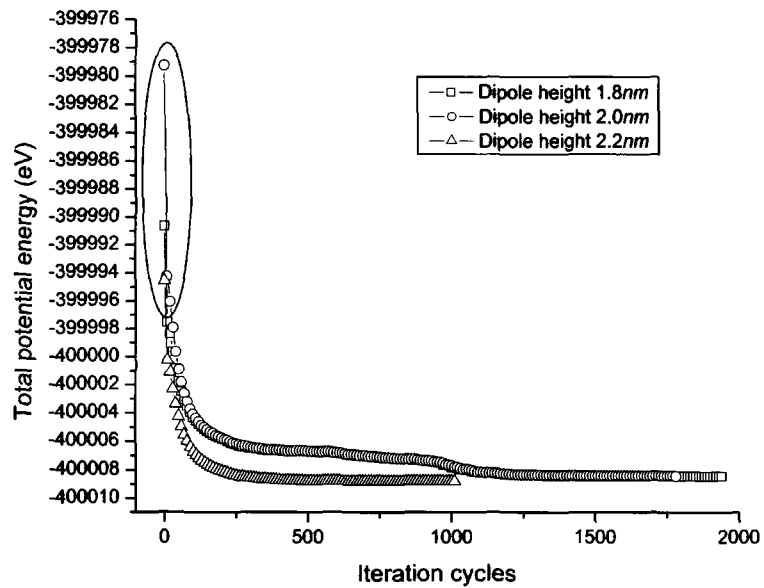
Figure 5.45: The comparison of the total potential energy in relaxed configurations from initial models containing two 60-degree dislocations with the opposite Burgers vectors gliding on parallel slip planes with the vertical distances of $1.8nm$, $2.0nm$ and $2.2nm$ (vacancy type).

(a)

(b)

Y [1 1 1]

Z [0 -1 1] → X [2 -1 -1]

1.0nm

(c)
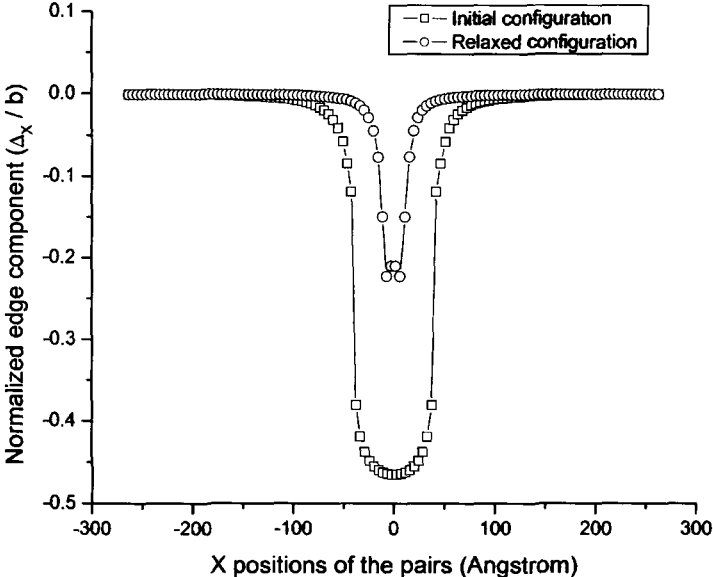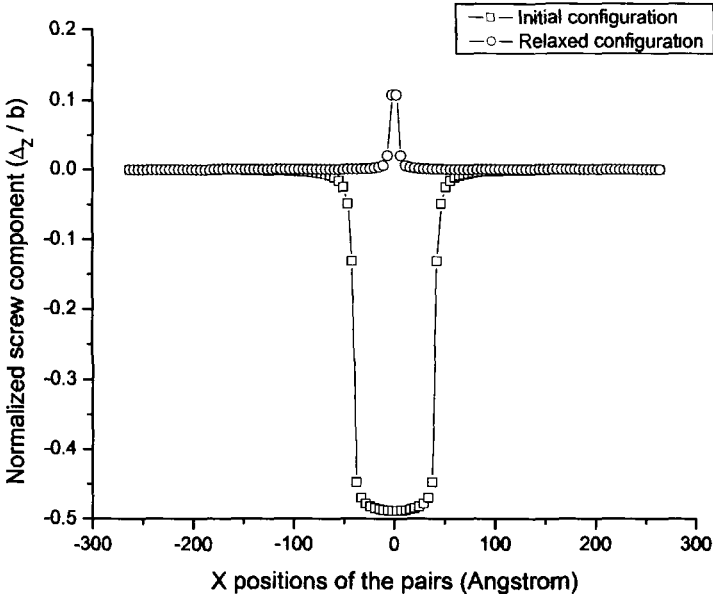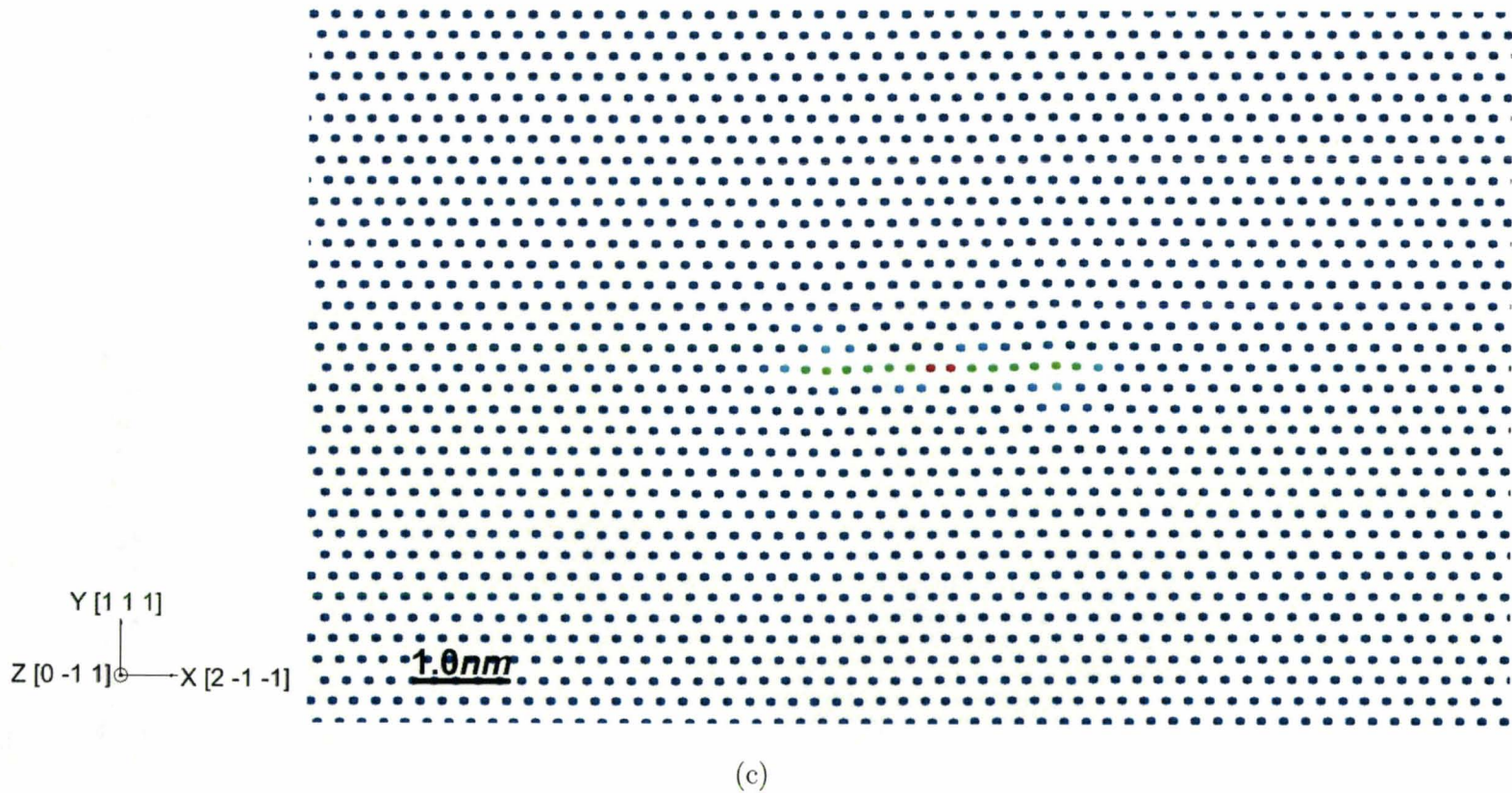
Figure 5.46: The analysis of edge and screw components along the middle (1 1 1) plane in the initial model containing two 60-degree dislocations with the opposite Burgers vectors gliding on parallel slip planes with the vertical distance of 0.4nm, and screw and edge components along the middle (1 1 1) plane between two pairs of partial dislocations in the corresponding relaxed configuration (interstitial type). (a) The edge components; (b) The screw components; (c) The positions of partial dislocations in the relaxed configuration (interstitial type). (a) and (b) are determined by the Disregistry approach.

(a)

(b)

Y [1 1 1]

Z [0 -1 1] ⊙ ——→ X [2 -1 -1]

1.0nm

(c)
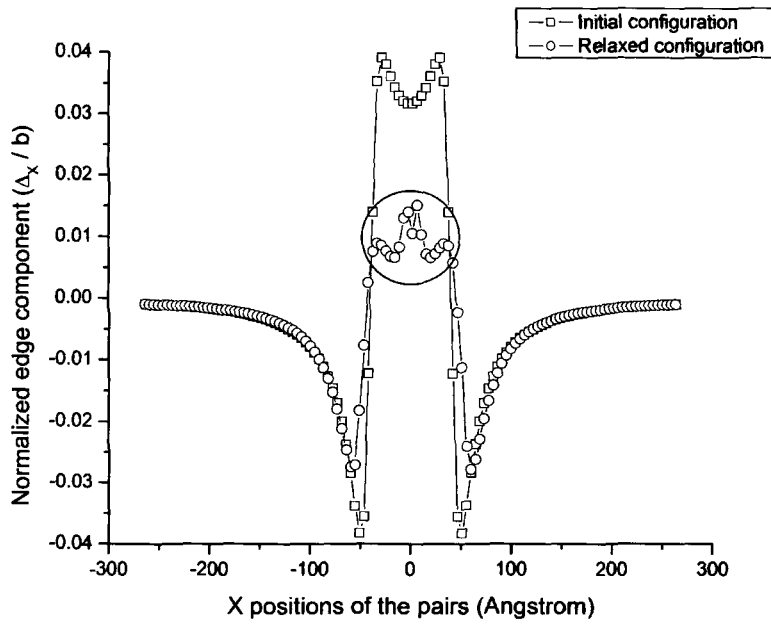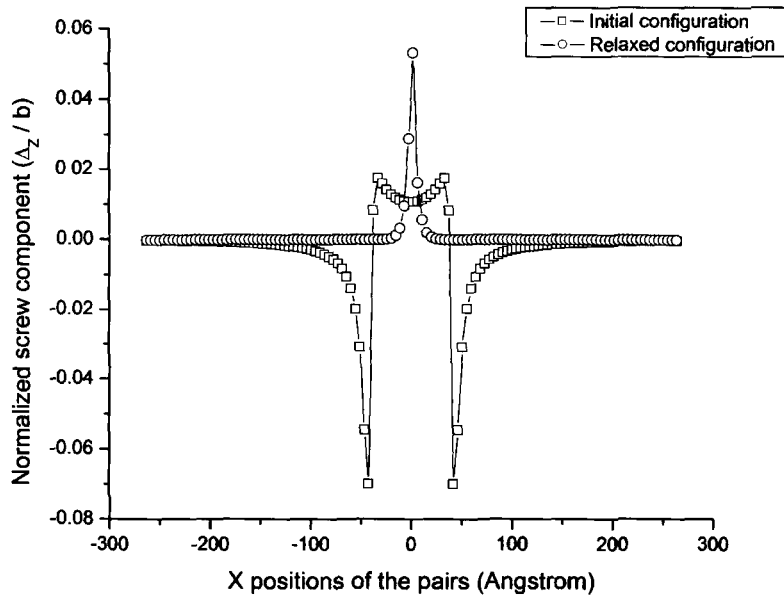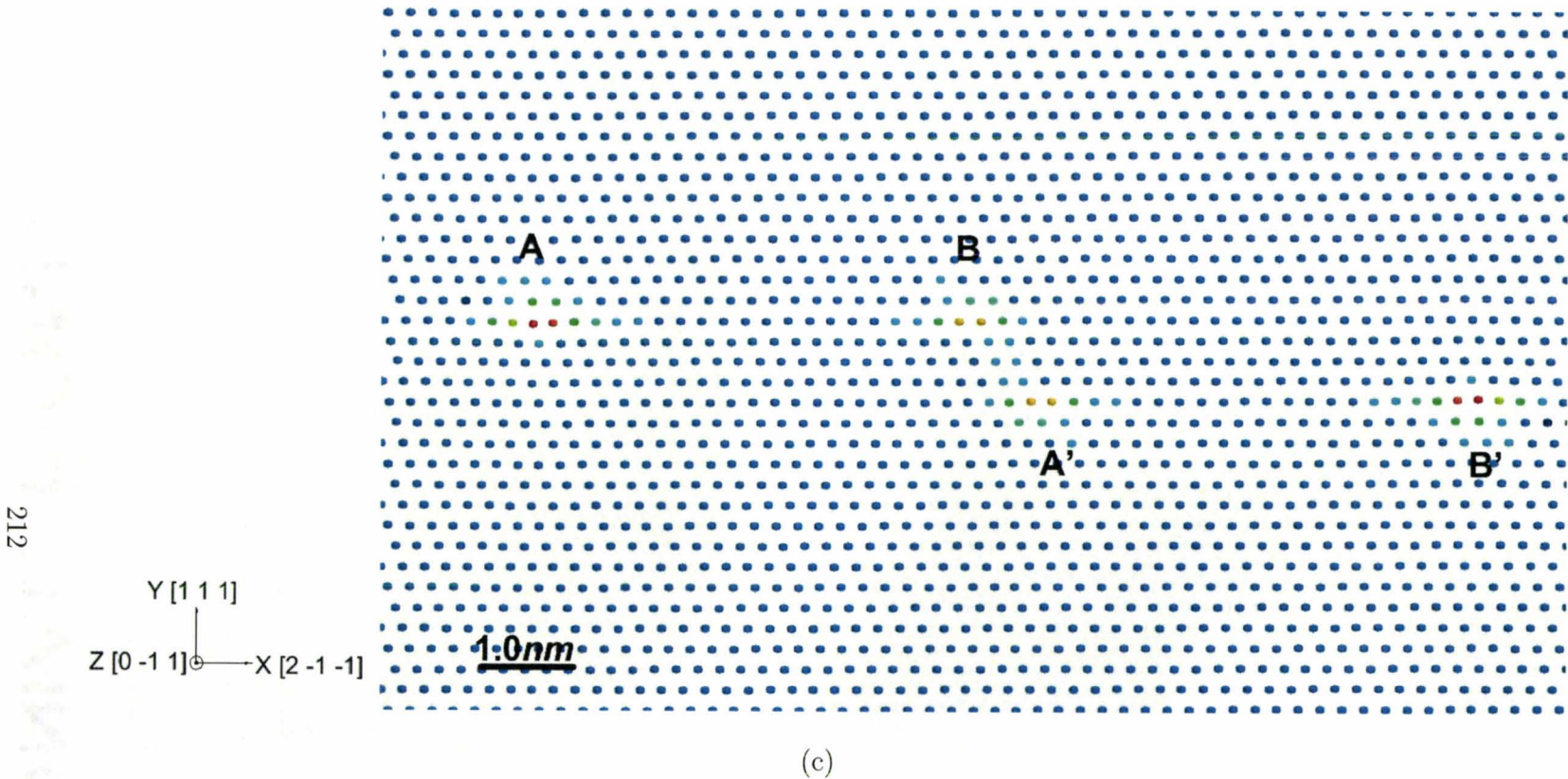
Figure 5.47: The analysis of edge and screw components along the middle (1 1 1) plane in the initial model containing two 60-degree dislocations with the opposite Burgers vectors gliding on parallel slip planes with the vertical distance of $1.0nm$, and screw and edge components along the middle (1 1 1) plane between two pairs of partial dislocations in the corresponding relaxed configuration (interstitial type). (a) The edge components; (b) The screw components; (c) The positions of partial dislocations in the relaxed configuration (interstitial type). (a) and (b) are determined by the Disregistry approach.

to distinguish the faulted dipole and the stable dipole is the edge component along the middle (1 1 1) plane between two pairs of partial dislocations in relaxed configurations. In the faulted dipole, the oscillation occurs in the center of the model but gradually dissipates in the stable dipole. Compared to the total potential energy of configurations with various dipolar heights as shown in Figure(5.50), the stable dipole with the height of $1.8nm$ has higher potential energy after the relaxation. Since the critical height forming the faulted dipole is around $1.6nm$, the interstitial type of 60-degree dislocation dipoles may still be difficult to be observed experimentally.

In summary, 60-degree dislocation dipoles combine the characteristics of perfect edge and screw dislocation dipoles. With the increase of the height h, the splitting width between partial dislocations increases gradually, and the total potential energy is lower in relaxed configurations of faulted dipoles compared to stable dipoles. The edge component in the 60-degree dislocation seems to play an important role in the formation of the relaxed structure while the screw component more affects the separation of partial dislocations.

5.3 Two screw dislocations on inclined planes

5.3.1 Models without external traction

Besides the annihilation of two perfect screw dislocations dissociating on the parallel horizontal {1 1 1} planes, there is another mechanism by which two perfect screw dislocations could annihilate each other. In this case, one perfect screw dislocation dissociates on the inclined {1 1 -1} plane and the other dissociates on the horizontal {1 1 1} plane as shown in Figure(5.51). These two pairs of partial dislocations attract each other and move closer on their respective slip planes. During this process, the

(a)

(b)

(c)
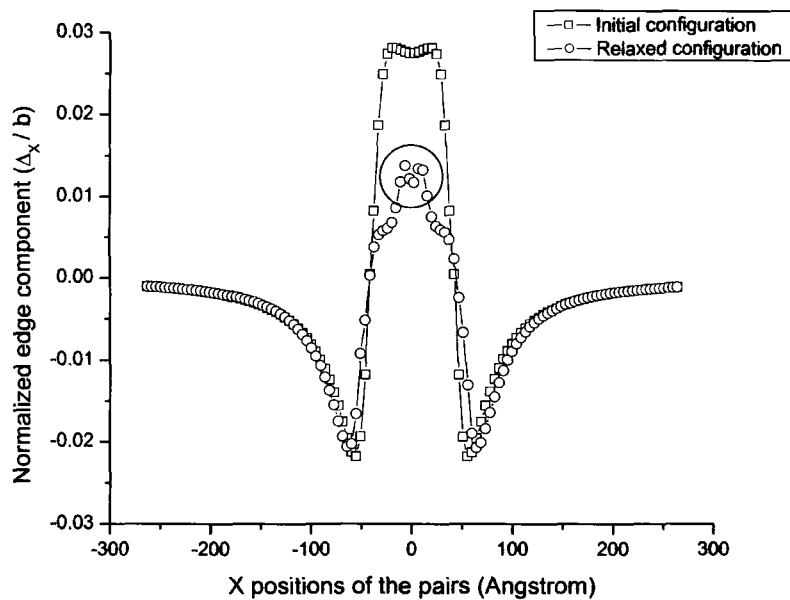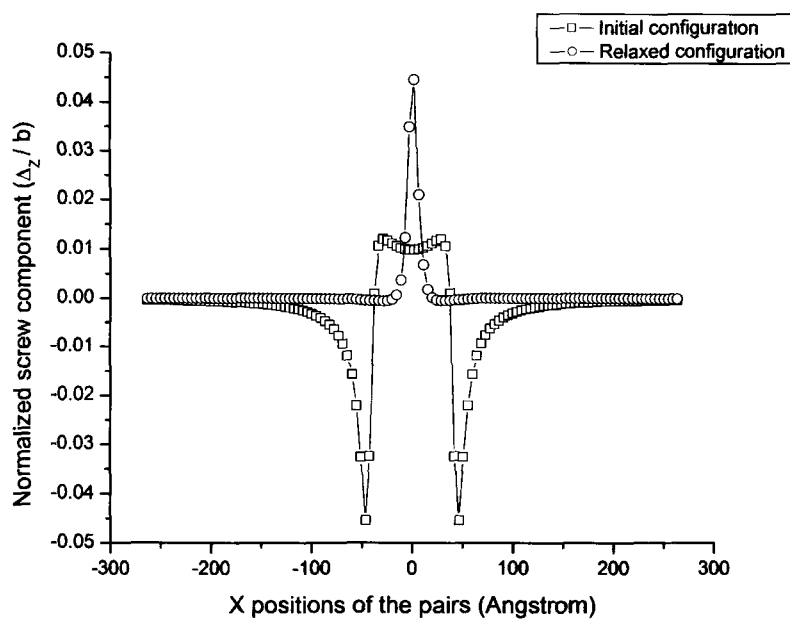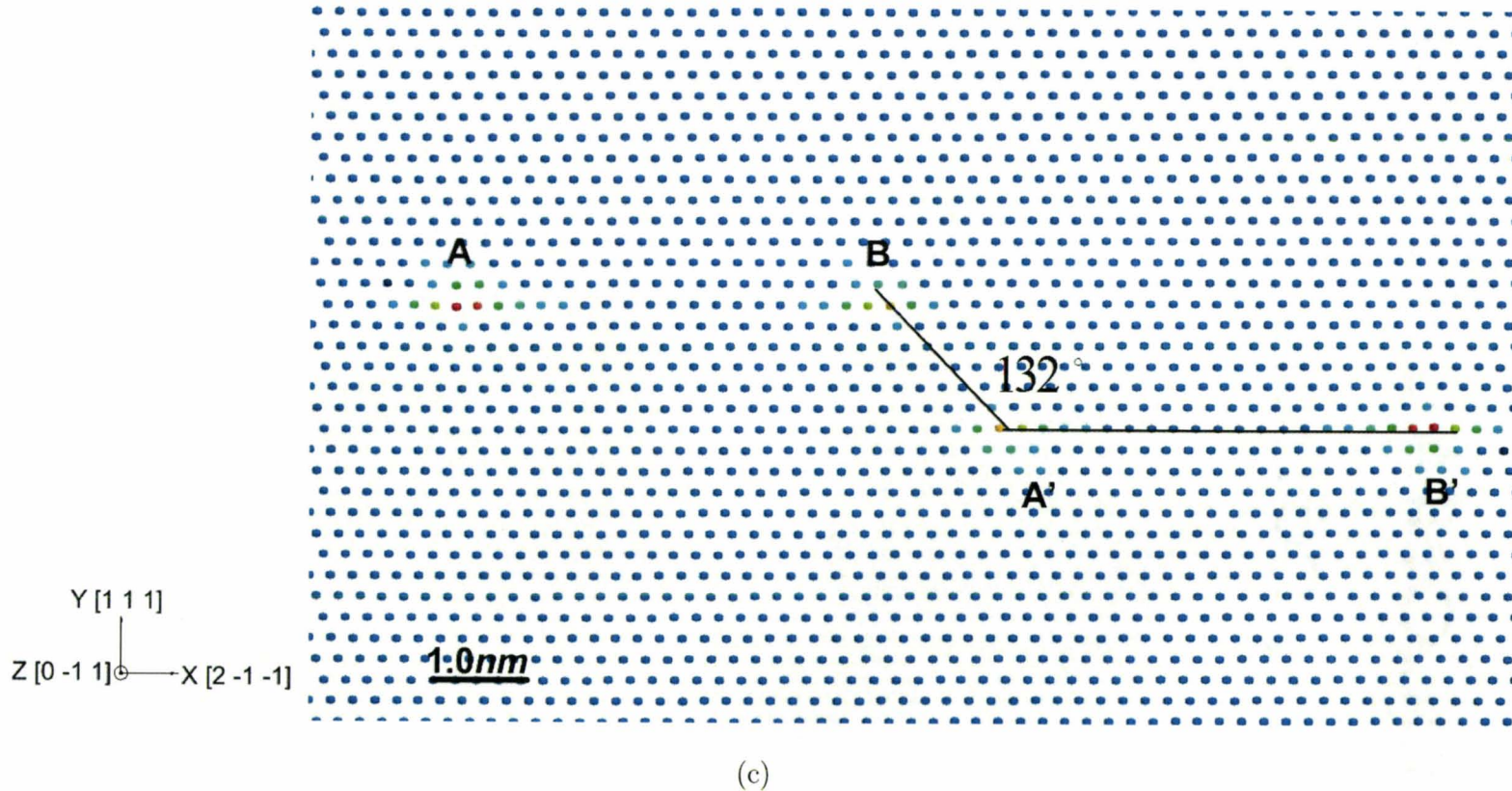
Figure 5.48: The analysis of edge and screw components along the middle (1 1 1) plane in the initial model containing two 60-degree dislocations with the opposite Burgers vectors gliding on parallel slip planes with the vertical distance of 1.6nm, and screw and edge components along the middle (1 1 1) plane between two pairs of partial dislocations in the corresponding relaxed configuration (interstitial type). (a) The edge components; (b) The screw components; (c) The positions of partial dislocations in the relaxed configuration (interstitial type). (a) and (b) are determined by the Disregistry approach.

(a)

(b)

(c)
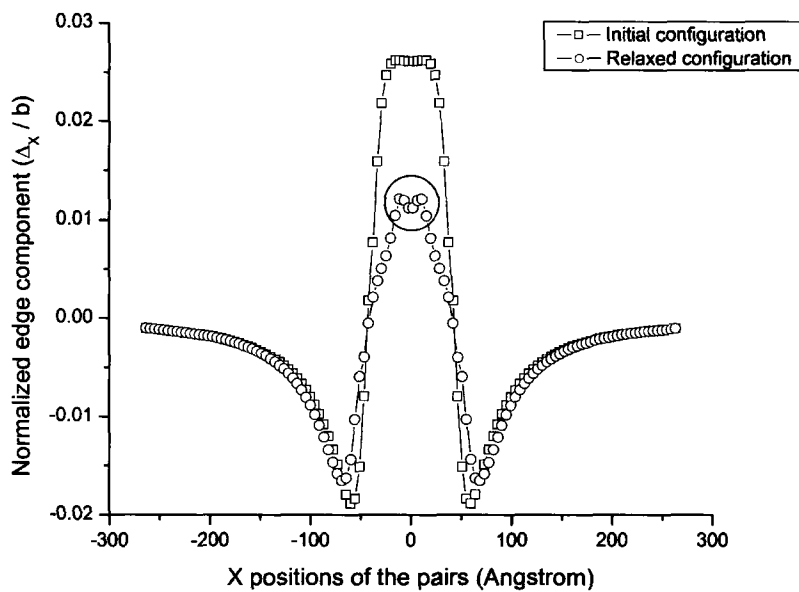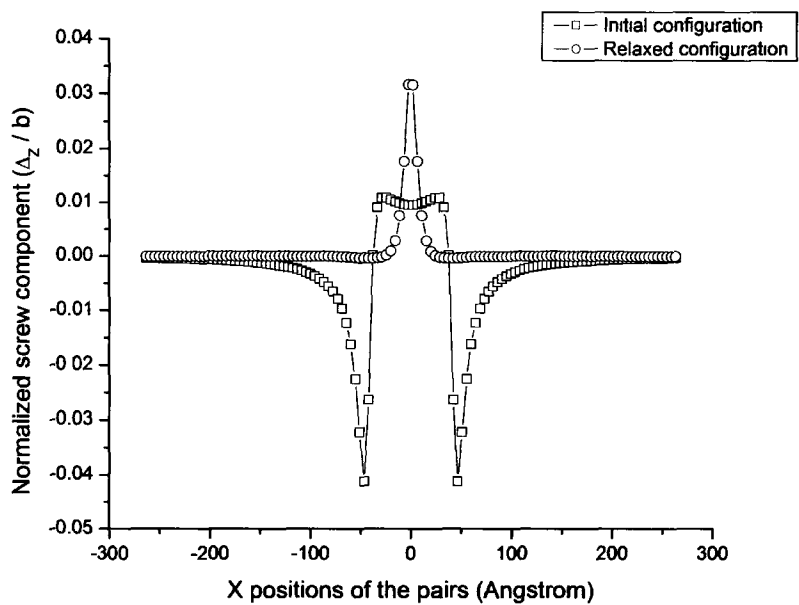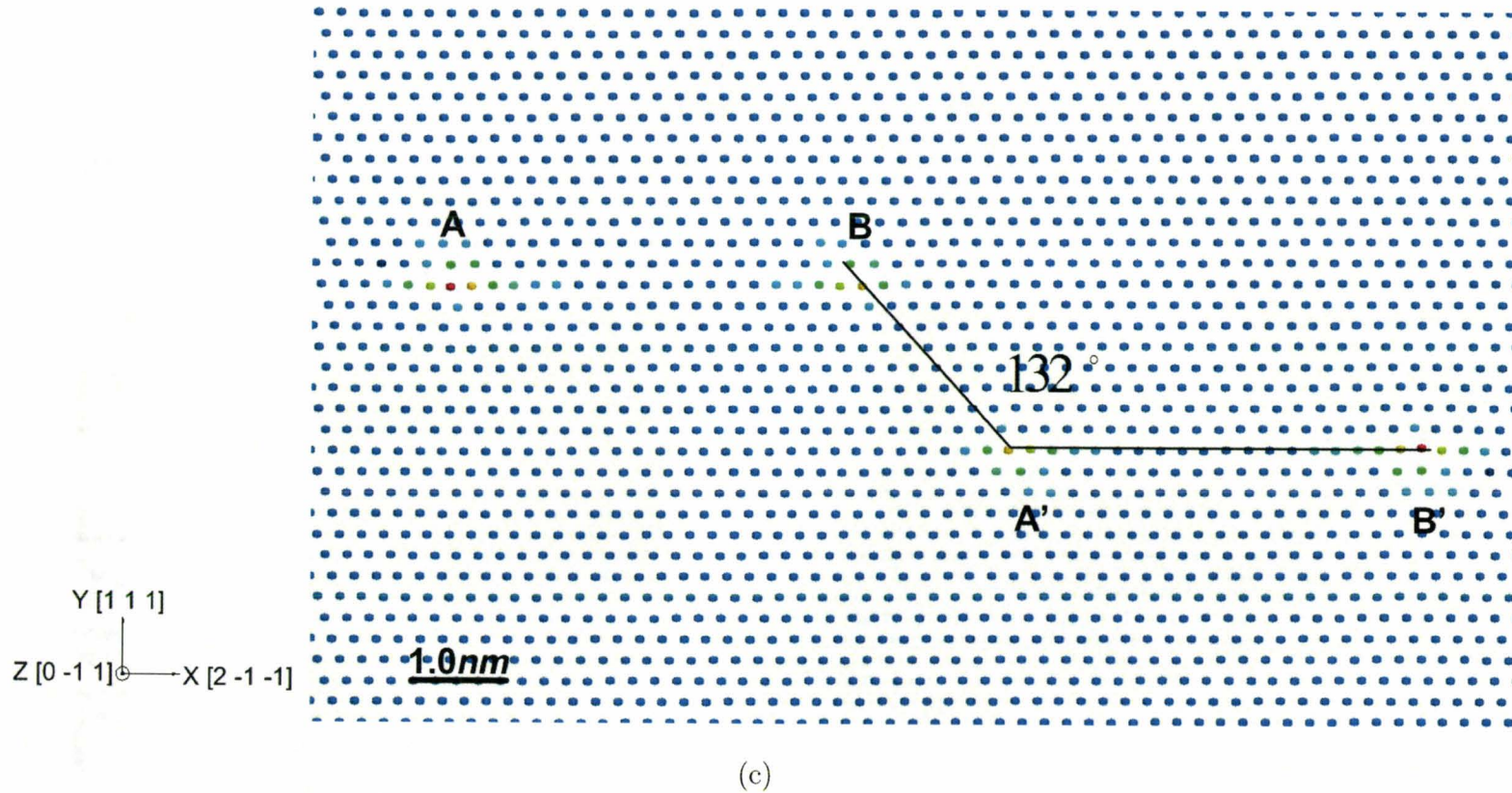
Figure 5.49: The analysis of edge and screw components along the middle (1 1 1) plane in the initial model containing two 60-degree dislocations with the opposite Burgers vectors gliding on parallel slip planes with the vertical distance of $1.8nm$, and screw and edge components along the middle (1 1 1) plane between two pairs of partial dislocations in the corresponding relaxed configuration (interstitial type). (a) The edge components; (b) The screw components; (c) The positions of partial dislocations in the relaxed configuration (interstitial type). (a) and (b) are determined by the Disregistry approach.
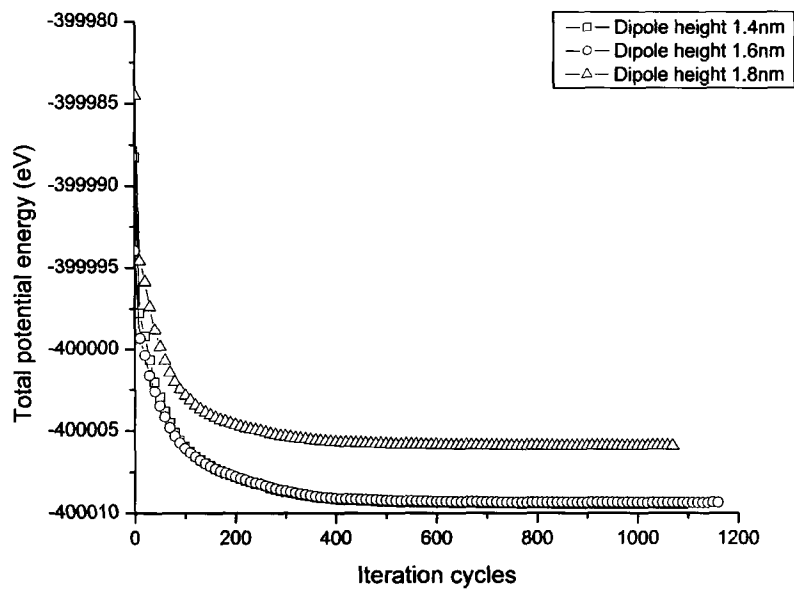
Figure 5.50: The comparison of the total potential energy in relaxed configurations from initial models containing two 60-degree dislocations with the opposite Burgers vectors gliding on parallel slip planes with the vertical distances of $1.4nm$, $1.6nm$ and $1.8nm$ (interstitial type).
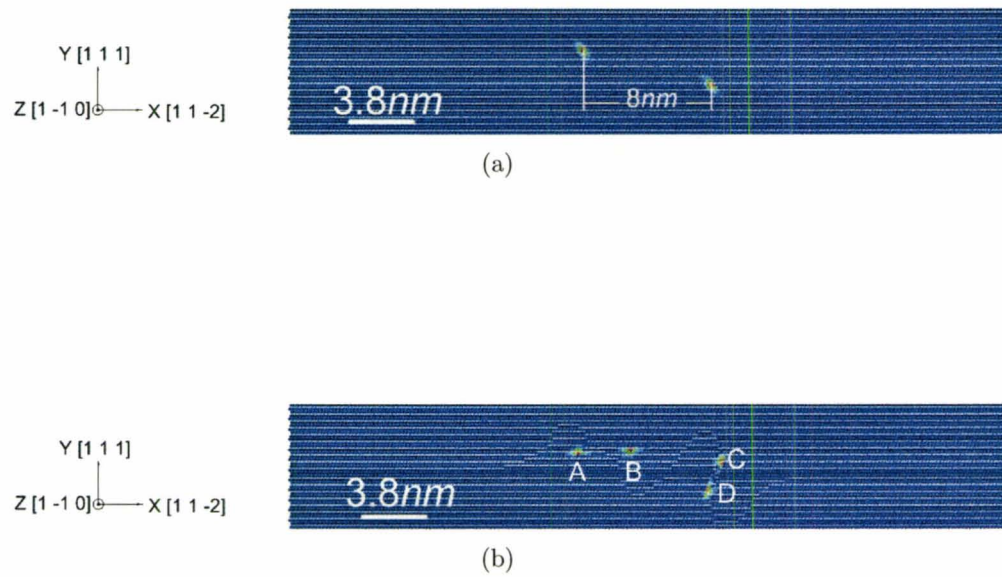
Figure 5.51: Two perfect screw dislocations dissociate on inclined slip planes. (a) The initial configuration; (b) Pair of partial dislocations A and B on the horizontal (1 1 1) plane while other pair C and D on the inclined (1 1 -1) plane.

partial dislocations on the inclined plane re-combine and re-dissociate on the horizontal plane and annihilate by the other pair of partial dislocations on the horizontal plane. Essmann et al. [15] suggested the maximum height of the screw dislocation dipole that triggers the annihilation process could be roughly $50nm$. Under current simulation framework, the critical height of the annihilation by the mechanism is $2.2nm$. Though the value is well below the experimental observation, it is almost three times larger than the critical dipolar height for the annihilation of screw dislocations on parallel slip planes, which shows that this mechanism can dramatically increase dipolar height for the spontaneous annihilation of screw dislocations.

The model for the investigation consists of 95,000 atoms. The dislocation line and Burgers vector are both along the Z[1 -1 0] direction. Two perfect screw dislocations are introduced into the model with the horizontal distance of $8.0nm$ as shown in Figure[5.52(a)]. Since the relaxation of screw dislocations depends on the atomic configuration, the positions of dislocations and applied stress, there is no general rule where to introduce these dislocations to the model so that they dissociate on inclined planes. However, by a series of tests, the positions of original perfect screw dislocations were found to ensure that they relax on inclined slip planes. The boundary conditions in the simulation are that (i) the periodic symmetry is along the Z direction with a constant periodic length and (ii) physical boundary atoms in X and Y directions are fixed.

Figure(5.52) demonstrates the process of the annihilation of two screw dislocations on inclined slip planes separated by the vertical distance of $2.2nm$. The appearance of two dislocations proceeding the annihilation is quite similar to the results of Qi et al. on Ni. [45]. Initially, the left screw dislocation dissociates into

Y [1 1 1]

Z [1 -1 0] — X [1 1 -2]

(a)

Y [1 1 1]

Z [1 -1 0] — X [1 1 -2]

(b)

Y [1 1 1]

Z [1 -1 0] — X [1 1 -2]

(c)

Y [1 1 1]

Z [1 -1 0] — X [1 1 -2]

(d)

Y [1 1 1]

Z [1 -1 0] — X [1 1 -2]

(e)

Continued on next page

Y [1 1 1]

Z [1 -1 0] — X [1 1 -2]

3.8nm

(f)

Y [1 1 1]

Z [1 -1 0] — X [1 1 -2]

3.8nm

(g)

Y [1 1 1]

Z [1 -1 0] — X [1 1 -2]

3.8nm

(h)

Y [1 1 1]

Z [1 -1 0] — X [1 1 -2]

3.8nm

(i)
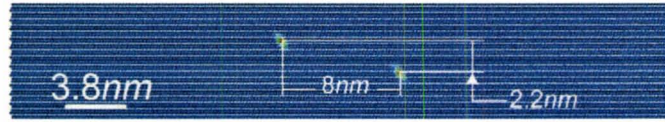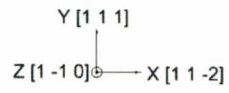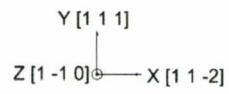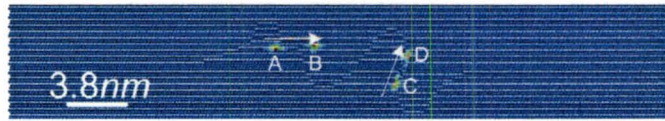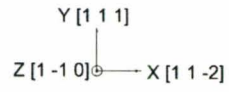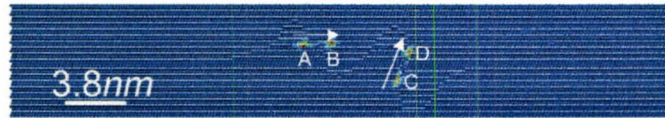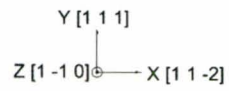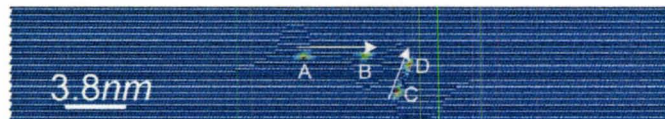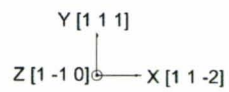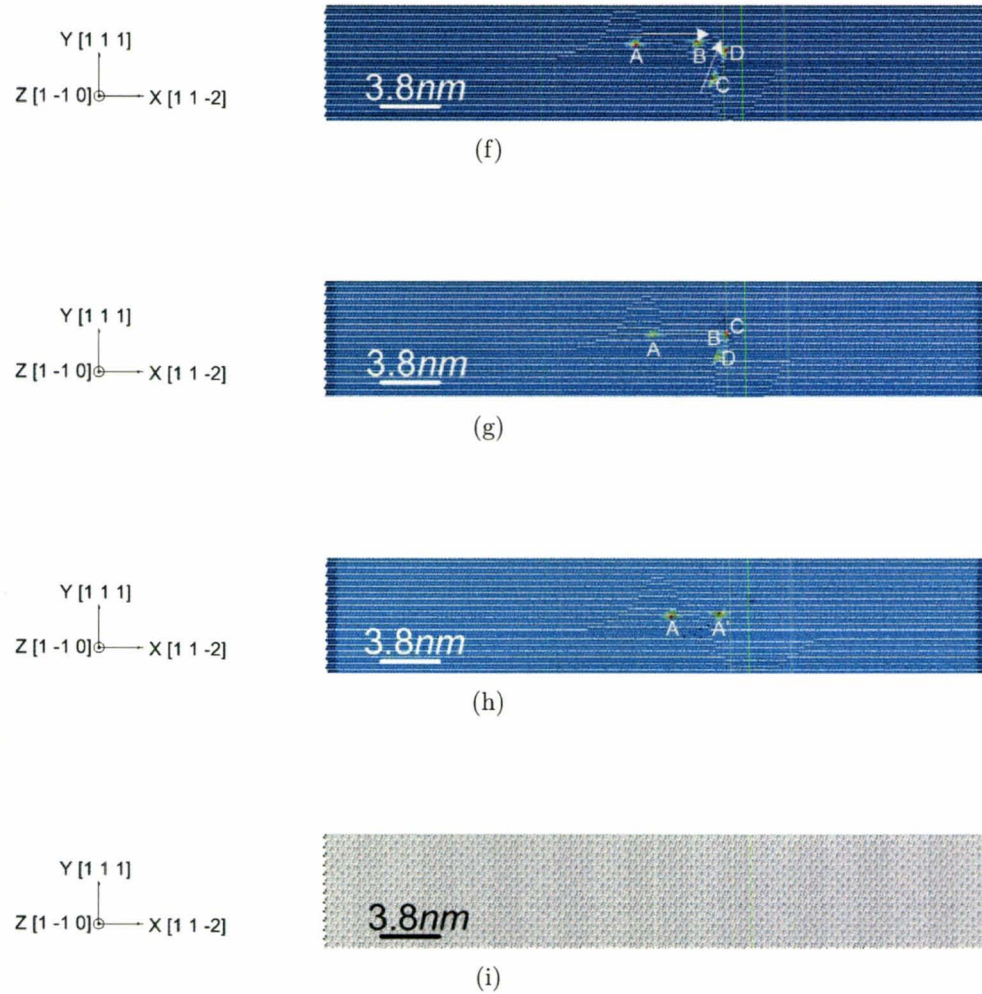
Figure 5.52: The positions of dislocations during the relaxation of two perfect screw dislocations with the opposite Burgers vectors gliding on inclined slip planes separated by the vertical distance of 2.2nm. (a) Cycle No: 0; (b) Cycle No: 150; (c) Cycle No: 300; (d) Cycle No: 1050; (e) Cycle No: 1500; (f) Cycle No: 1650; (g) Cycle No: 1800; (h) Cycle No: 1950; (i) Cycle No: 3060.

partial dislocations A and B on the (1 1 1) plane,

$$\frac{a}{2}[1 \ -1 \ 0] = \frac{a}{6}[1 \ -2 \ 1] + \frac{a}{6}[2 \ -1 \ -1] \tag{5.4}$$

And, the right screw dislocation dissociates into partial dislocations C and D on the (1 1 -1) plane,

$$\frac{a}{2}[-1 \ 1 \ 0] = \frac{a}{6}[-2 \ 1 \ -1] + \frac{a}{6}[-1 \ 2 \ 1] \tag{5.5}$$

The leading partial dislocations B and D move closer due to the attraction. Their movement is faster than their counterpart partial dislocations A and C so that there is an intermediate process of reducing the splitting width between partial dislocations on their respective slip planes as shown in Figure[5.52(d)]. When leading partial dislocations B and D meet at the line of the intersection, they cannot annihilate each other since they are not opposite dislocations as shown in Equations(5.4) and (5.5). The partial dislocation B can only annihilate the dislocation with the opposite Burgers vector. For this to happen, the partial dislocations on (1 1 -1) plane recombine and re-dissociate on (1 1 1) plane. After annihilating dislocation B, partial dislocation A' is left on the same (1 1 1) plane as dislocation A. These two dislocations A' and A annihilate subsequently and the model inherits fully a perfect lattice.

The positions of two screw dislocations in the initial model could be changed to obtain different orientations of partial dislocations on the horizontal or inclined planes. For example, as shown in Figure(5.53), partial dislocations A and B are in the right side of, or below the inclined pair C and D. The annihilation of screw dislocations occurs in all configurations when the dipolar height is not higher than the critical value $2.2nm$. Therefore, the annihilation between angled screw dislocations is insensitive to the position and angle θ between two pairs of partial dislocations.

Y [1 1 1]

Z [1 -1 0] ⊙———X [1 1 -2]

3.8nm

(a)

Y [1 1 1]

Z [1 -1 0] ⊙———X [1 1 -2]

3.8nm

(b)
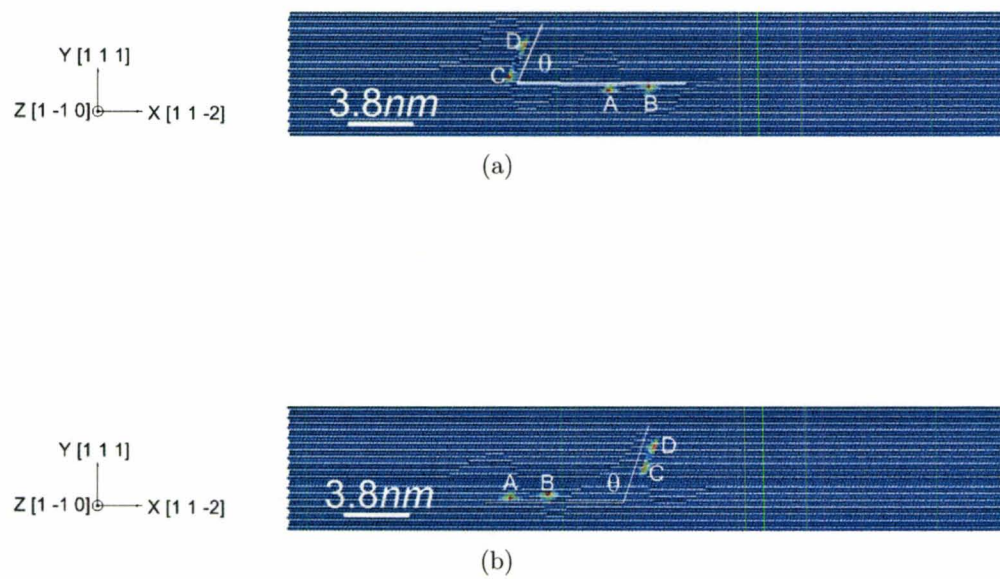
Figure 5.53: The configurations of two perfect screw dislocations dissociating on inclined slip planes. (a) The partial dislocations on the horizontal plane are at the right side of the partial dislocations on the inclined plane. (b) The partial dislocations on the horizontal plane are below the partial dislocations on the inclined plane.

Furthermore, all simulations are conducted by a low damping ratio of 0.05. A high damping ratio would not change the critical height of the annihilation in this case. Therefore, numerical parameters under current conditions do not affect the result as well.

5.3.2 Effects of the external traction

When the dipolar height is larger than $2.2nm$, two dislocations dissociate on their respective slip planes without any interaction as shown in Figure[5.54(a)] for the dislocation separation of $2.8nm$. The external traction applied to the model is found to affect the critical height of the annihilation. A large compressive force applied along the the slip direction causes the leading partial dislocations A and C to move closer and eventually triggers the annihilation by the mechanism discussed in Section(5.3.1). For example, when the compressive force along the X direction is increased to -6.0 in arbitrary unit, which is equivalent to $-432MPa$ applied to the YZ plane, two opposite screw dislocations with the dipolar height of $2.8nm$ annihilate after the relaxation. From the analysis of the screw component along the middle (1 1 1) plane in the initial and final configurations as shown in Figure[5.54(b)], It is found that the annihilation occurs with the external traction since all screw components disappear in the relaxed configuration.
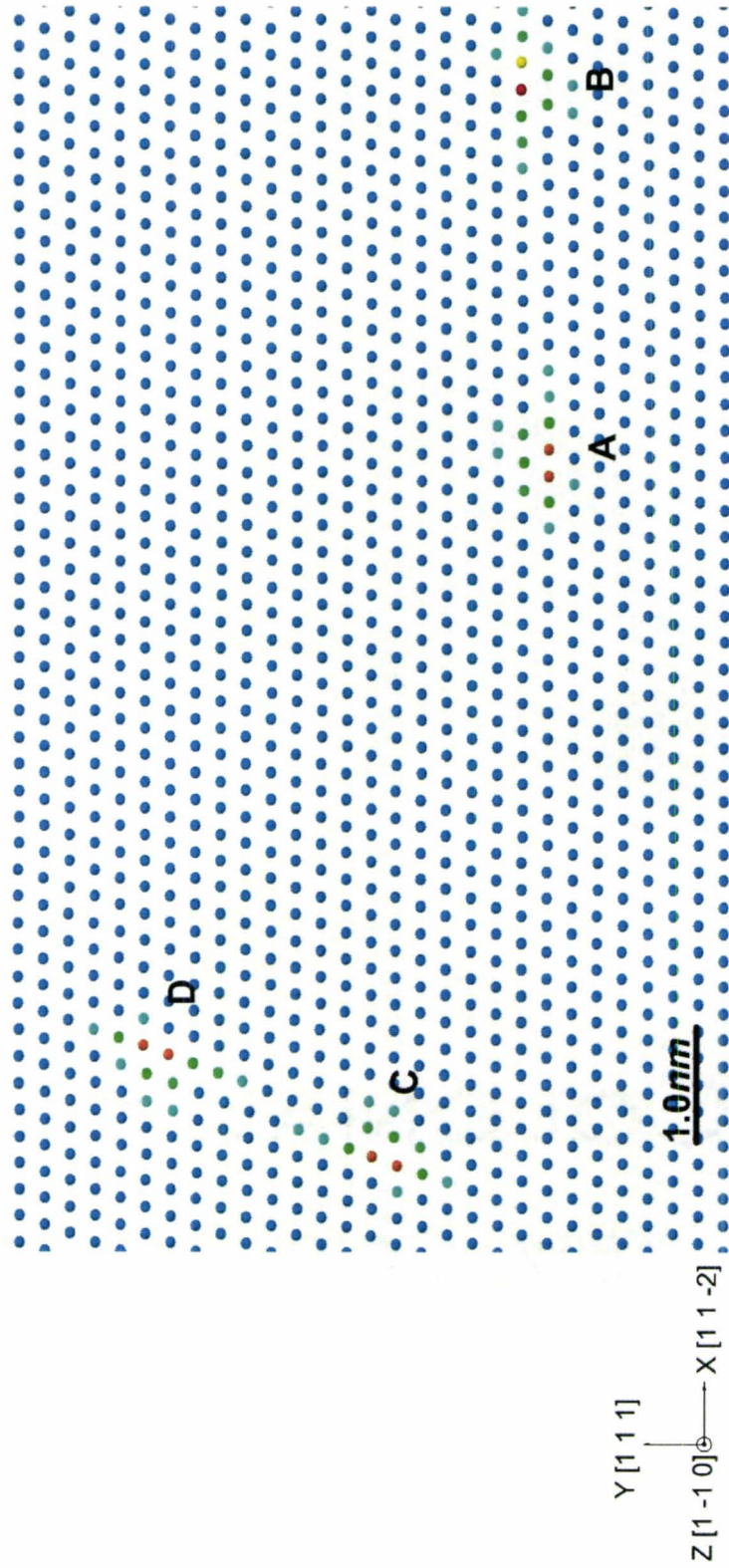
(a)
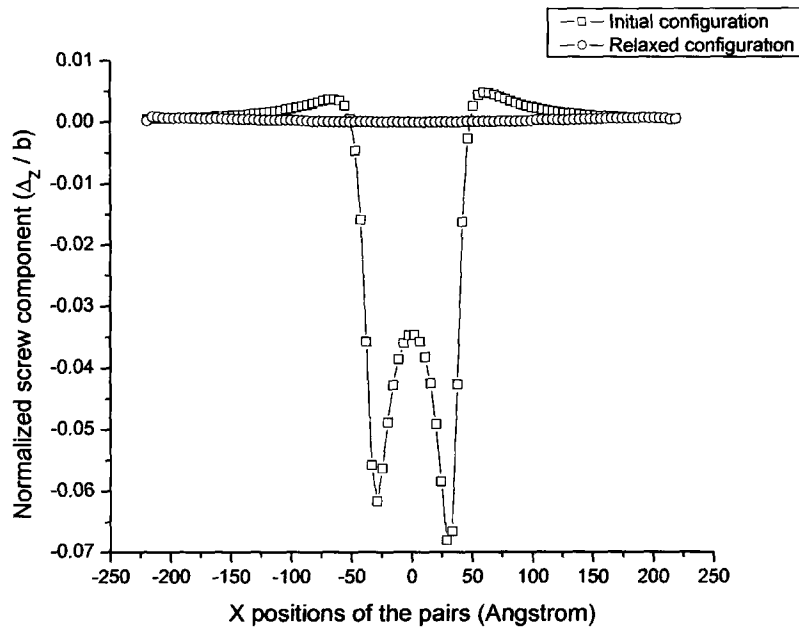
(b)

Figure 5.54: Two perfect screw dislocations with the opposite Burgers vectors gliding on inclined slip planes with the vertical distance of 2.8nm. (a) The relaxed configuration without the external traction; (b) The screw components along the middle (1 1 1) plane between two dislocations in the initial model with $-432MPa$ applied to the YZ plane, and the screw components along the middle (1 1 1) plane between two pairs of partial dislocations in the corresponding relaxed configuration. (b) is determined by the Disregistry approach.

Chapter 6

Conclusions and Recommendations

6.1 Conclusions and contributions

The present work deals with the development of a new simulation framework based on the Dynamic Relaxation (DR) technique to determine the change of the local atomic structure of a crystalline material via potential energy minimization in a computational cell with specified boundary conditions.

Dynamic Relaxation, a powerful tool for calculating steady-state results in non-linear mechanical problems, has shown its promising future for the calculation of the equilibrium of atomic positions in crystalline materials, because it achieves the equilibrium configuration with the physical trajectory in an acceptable time frame. The internal force and stiffness of individual atoms are obtained as the derivatives of the potential energy function. The revised Dynamic Relaxation algorithm is ready to be used in conjunction with Finite Element methodology for future multi-scale simulations. The damping ratio adjusts the amount of artificial damping introduced into the numerical integration so that it makes the simulation more efficient and accurate for various configurations. No divergence occurs in all cases throughout the

thesis simulated by the new approach. The convergence criterion is based on the inequality that the overall ratio of the net force compared to its maximum value during the simulation is less than the pre-determined number.

The periodic symmetry is further developed, which uses the external traction to substitute the interaction between boundary atoms and image atoms based on the equilibrium of the material model. Thus, the new periodic symmetry technique produces flexible boundary treatment in the simulation compared to the traditional method. In addition to be fully compatible to the traditional method, the new periodic symmetry technique provides a reliable measure to apply the external traction on boundary atoms of the periodic cell, which allows the deformation of the model to be carried out and ensures the stability of the model during the process. The responses of material models subjected to the external tension or compression are in agreement with experimental data, such as the elastic modulus.

The new DR-based energy minimization framework can be used to simulate the general crystalline model with structural defects, but focuses on the simulation of dislocation models of copper in the present work. The relaxation of the model with a single edge or screw dislocation without the external traction is in line with the experimental observation or theoretical predictions. Applying external traction increases the potential energy in the system so that it does not prevent the dislocation from dissociation to reduce the overall energy in the system. However, the external traction in certain directions, such as the compression along the direction of the dislocation line in the single edge dislocation model, changes the splitting width between partial dislocations.

The simulated results between two dislocations gliding on the same slip plane are in agreement with the theory of dislocations, which validates independently that the new DR-based framework works. It is shown that the present methodology can

also be used for simulating interactions between dislocations and can reveal new mechanisms on the atomic level, which can not be predicted by available theories.

The present results reveal that the increase of the vertical height of two dislocations with the opposite Burgers vectors gliding on parallel slip planes leads to the formation of faulted dipoles, or perfect stable dipoles if the dipolar height is sufficiently large. The faulted dipole develops the new stacking fault binding the partial dislocations in the state of lower potential energy compared to the stable dipole. Two opposite screw dislocations on inclined slip planes can annihilate by the mechanism of re-combination and re-dissociation, which dramatically increases the critical height of the annihilation between screw dislocations. The critical height can be even higher under the compression along the slip direction. It has been found that the critical heights for the annihilation between dislocations determined in this work are lower than the values observed experimentally. This discrepancy still requires an explanation. The trend in the evolution of dislocation dipoles, however, agrees well with experimental results, which shows that dipoles in the 'Z' configuration are widely observed in the structure, but dipoles in the 'S' configuration are not.

The main contributions of the present work rely on three aspects. First, a novel and alternative energy minimization methodology is developed to study the mechanical behavior of materials at the atomic level. The new approach could be used to validate results obtained by other numerical methods. The new technique could also help to reduce overall computational time which could be required in other methods such as MD for example. Secondly, the present approach has created the capability to provide better understanding of the mechanisms and processes of the formation of particular structures on the atomic scale, which can not be developed by other means. Finally, the numerical parameters used in present simulations, such as the size of the model, boundary conditions, damping ratios and the external traction,

230

can be adjusted for the best efficiency of the solution of a given problem.

6.2   Recommendations for the future work

The new theoretical framework developed here can be used to investigate the structure of materials at the atomic level. The framework could be further developed in the following aspects:

(a) Generally, convergence in the calculation is possible to be accelerated because the participating frequency of the overall model is lower than the highest frequency of the model. Specifically, the accelerating convergence for the cases of the screw dislocation model with the external traction and lower damping ratio could be improved to approach the equilibrium faster.

(b) Besides the external traction applied along the coordinate direction, the present methodology can accommodate other loading conditions such as the hydrostatic stress state, so that the relaxation of particular structure can be followed under these loading conditions.

(c) The new periodic symmetry method can be extended to full three dimensions.

(d) Since atoms are treated as point masses, the scheme for the integration of motion for atoms and nodes in explicit Finite Element Methods is the same. Thus, in multi-scale simulation, the key question is how to model the interface connecting the atomic and continuum regions.

(e) With the increase of the size of the model, parallel computing is an obvious solution to reduce the simulation time. OpenMP is an option due to its easy implementation and suitability for iteration problems.

On the aspect of the simulation of dislocation models, with the improvement of the lattice creator software such as considering the periodic symmetry of the model with defects, some cases are worth being investigated:

(f) The change of the splitting width of a single edge dislocation model with external traction applied along the slip direction.

(g) More detailed studies of the annihilation of two opposite screw dislocations on inclined slip planes, subjected to different loading conditions.

(h) The relaxation of two opposite edge dislocations on inclined planes, i.e. the formation of the Lomer-lock configuration.

(i) The single Frank partial dislocation or Frank partial dislocation dipoles, in which the Burgers vector of an edge dislocation is normal to $\{1\ 1\ 1\}$ planes.

(j) Three-dimensional defects such as vacancy clusters or the stacking fault tetrahedra, and the interaction between dislocations and these three-dimensional defects.

Bibliography

[1] Aslanides A. and V. Pontikis. Numerical study of the athermal annihilation of edge-dislocation dipoles. *Philosophical Magazine A*, 80(10):2337–2353, 2000.

[2] G.J. Ackland, D.J. Bacon, A.F. Calder, and T. Harry. Computer simulation of point defect properties in dilute fe-cu alloy using a many-body interatomic potential. *Philosophical Magazine A*, 75(3):713–732, 1997.

[3] G.J. Ackland, G. Tichy, V. Vitek, and M.W. Finnis. Simple n-body potentials for the noble metals and nickel. *Philosophical Magazine A*, 56(6):735–756, 1987.

[4] Z.S. Basinski, Korbel A.S., and S.J. Basinski. The temperature dependence of the saturation stress and dislocation substructure in fatigued copper single crystals. *Acta Metallurgica*, 28(2):191–207, 1980.

[5] T. Belytschko. An overview of semidiscretization and time integration procedures. *Computational Methods for Transient Analysis*, pages 1–66, 1983.

[6] J.S. Brew and D.M. Brotton. Non-linear strucutral analysis by dynamic relaxation. *International Journal of Numerical Methods in Engineering*, 3:436–483, 1971.

[7] R. Bullough and V.K. Tewary. Lattice theory of dislocations: Dislocations in solid. *Dislocations in Solid*, 2:41–62, 1979.

[8] S.C. Chapra and R.P. Canale. *Numerical methods for engineers with programming and software application.* WCB / McGraw-Hill, 3rd edition, 1998.

[9] N.E. Christensen and V. Heine. Analysis of the electronic pressure in transition and noble metals. *Physical Review B*, 32(10):6145–6156, 1985.

[10] R.D. Cook, Malkus D.S., and M.E. Plesha. *Concepts and applications of finite element analysis.* John Wiley & Sons, Ltd, 3rd edition, 1989.

[11] M.S. Daw, S.M. Foiles, and M.I. Baskes. The embedded-atom method: a review of theory and applications. *Materials Science Report*, 9:251–310, 1993.

[12] A.S. Day. An introduction to dynamic relaxation (dynamic relaxation method for structural analysis, using computer to calculate internal forces following development from initially unloaded state). *The Engineer*, 219:218–221, 1965.

[13] Ş Ercoç. Empirical many-body potential energy functions used in computer simulations of condensed matter properties. *Physics Reports*, 278:79–105, 1997.

[14] F. Ercolessi. *A molecular dynamics primer.* http://www.fisica.uniud.it/ ercolessi/md/md, 1997.

[15] U. Essmann and H. Mughrabi. Annihilation of dislocations during tensile and cyclic deformation and limits of dislocation densities. *Philosophical Magazine A*, 40(6):731–756, 1979.

[16] M.W. Finnis and J.E. Sinclair. A simple empirical n-body potential for transition metals. *Philosophical Magazine A*, 50(1):45–55, 1984.

[17] R. Fletcher and C.M. Reeves. Function minimization by conjugate gradients. *The Computer Journal*, 7:149–154, 1965.

[18] S.M. Foiles, M.I. Baskes, and M.S. Daw. Embedded-atom-method functions for the fcc metals cu, ag, au, ni, pd, pt, and their alloys. *Physical Review B*, 33(12):7983–7991, 1986.

[19] D. Frenkel and B. Smit. *Understanding molecular simulation: from algorithm to application*. Academic Press, Inc, 1996.

[20] P.C. Gehlen, J.R. Beeler, and R.I. Jaffee. *Interactomic potentials and simulation of lattice defects*. Plenum Press, 1972.

[21] J.B. Gibson, A.N. Goland, Milgram M., and Vineyard G.H. Dynamics of radiation damage. *Physical Review*, 120(4):1229–1253, 1960.

[22] J.M. Haile. *Molecular Dynamics simulation*. John Wiley & Sons, Inc, 1992.

[23] A. Hinchliffe. *Molecular Modelling for Beginners*. John Wiley & Sons Ltd, 2003.

[24] J.P. Hirth and J. Lothe. *Theory of dislocations*. 2nd edition.

[25] R.G. Hoagland. On the energetics of dislocation emission from a crack tip in nickel containing hydrogen. *Journal of Materials Research*, 9(7):1805–1819, 1994.

[26] D. Hull and J. Bacon. *Introduction to Dislocations*. 4th edition.

[27] K.W. Jacobsen, J.K. Norskov, and M.J. Puska. Interatomic interactions in the effective-medium theory. *Physical Review B*, 35(14):7423–7442, 1987.

[28] K.W. Jacobsen, Stoltze P., and J.K. Norskov. A semi-empirical effective medium theory for metals and alloys. *Surface Science*, 366:394–402, 1996.

[29] T. Kant and S. Patel. Transient/pseudo-transient finite element small/large deformation analysis of two-dimensional problems. *Computers and Structures*, 36(3):421–427, 1990.

[30] Y. Kogure and T. Kosugi. Simulation of dislocation dynamics in fcc metals. *Journal de Physique IV*, 6(C8):195–198, 1996.

[31] A.R. Leach. *Molecular Modelling, Principles and Applications*. Pearson Education Ltd, 1996.

[32] A. Machová. Stress calculation on the atomistic level. *Modelling and Simulation in Materials Science and Engineering*, 6:327–337, 2001.

[33] K. Masuda and A. Sato. Electronic theory for screw dislocation-motion in dilute bcc transition-metal alloys. *Philosophical Magazine A*, 44(4):799–814, 1981.

[34] D.R. Metzger. Periodic symmetry for explicit methods for large deformation twisting and stretching. *ASME-Pressure Vessel and Piping Division, Computer Technology and Applications*, 458:275–282, 2003.

[35] Y. Mishin, D. Farkas, M.J. Mehl, and D.A. Papaconstantopoulos. Interatomic potentials for monoatomic metals from experimental data and ab initio calculations. *Physical Review B*, 59(5):3393–3407, 1999.

[36] Daw. M.S. and M.I. Baskes. Embedded-atom method: Derivation and application to impurities, surfaces, and other defects in metals. *Physical Review B*, 20(12):6443–6453, 1984.

[37] M. Niewczas, Z.S. Basinski, S.J. Basinski, and J.D. Embury. Deformation of copper single crystals to large strains at 4.2 k - I. mechanical response and electrical resistivity. *Philosophical Magazine A*, 81(5):1121–1142, 2001.

[38] M. Niewczas, Z.S. Basinski, and J.D. Embury. Deformation of copper single crystals to large strains at 4.2 k - II. transmission electron microscopy observations of defect structure. *Philosophical Magazine A*, 81(5):1143–1159, 2001.

[39] B. Nobel. *Applied Linear Algebra*. Prentice-Hall, Inc., 1969.

[40] Y.N. Osetsky and D.J. Bacon. An atomic-level model for studying the dynamics of edge dislocations in metals. *Modelling and Simulation in Materials and Engineering*, 11:427–446, 2003.

[41] L. Pan. Meshless dynamic relaxation techniques for simulating atomic structures of materials. Master's thesis, Department of Mechanical Engineering, McMaster University.

[42] L. Pan, D.R. Metzger, and M. Niewczas. The meshless dynamic relaxation techniques for simulating atomic structures of materials. *ASME-Pressure Vessel and Piping Division, Computational Mechanics: Developments and Application*, 441:15–26, 2002.

[43] L. Pan, D.R. Metzger, and M. Niewczas. Dynamic relaxation and new periodic symmetry techniques for simulating atomistic dislocation models subjected to two-dimensional external forces. *Proceedings of the ASME Pressure Vessels and Piping Conference 2005 - Computer Technology*, 2:419–423, 2005.

[44] A. Pica and Hinton E. Transient and pseudo-transient analysis of mindlin plates. *International Journal of Numerical Methods in Engineering*, 15:189–208, 1980.

[45] Y. Qi, A. Strachan, T. Cagin, and W.A. Goddard. Large scale atomistic simulation of screw dislocation structure, annihilation and cross-slip in fcc ni. *Materials Science and Engieering A*, 309-310:156–159, 2001.

[46] S.S. Rao. *Engineering Optimization: Theory and Practice*. Wiley Interscience, 3rd edition, 1996.

[47] T. Rasmussen, T. Vegge, Leffers T., Pedersen O.B., and Jacobsen K.W. Simulation of strucutre and annihilation of screw dislocation dipoles. *Philosophical Magazine A*, 80(5):1273–1290, 2000.

[48] V. Rosato, M. Guillope, and B. Legrand. Thermodynamical and structural-properties of fcc transition-metals using a simple tight-binding model. *Philosophical Magazine A*, 59(2):321–336, 1989.

[49] R.G. Sauvé. H3dmap version 6.0 - a general three dimensional finite element computer code for linear and nonlinear analysis of structures. Technical report, 1999.

[50] R.G. Sauvé and D.R. Metzger. Advances in dynamic relaxation techniques for nonlinear finite element analysis. *Journal of Pressure Vessel Technology-Transactions of the ASME*, 117(2):170–176, 1995.

[51] R. Sayle. *Rasmol*, 1999. Software.

[52] J.R. Shewchuk. *An Introduction to the Conjugate Gradient Method Without the Agonizing Pain*. www.cs.cmu.edu/ quake-papers/painless-conjugate-gradient.pdf, 1994.

[53] I.M. Smith and D.V. Griffiths. *Programming the Finite Element Method*. John Wiley & Sons, Ltd, 3rd edition, 1997.

[54] W.M. Stobbs and C.H. Sworn. The weak beam technique as applied to the determination of the stacking-fault energy of copper. *Philosophical Magazine*, 24(192):1365–1381, 1971.

[55] G. Tichy and U. Essmann. Modelling of edge dislocation dipoles in face-centred-cubic lattices. *Philosophical Magazine B*, 60(4):503–512, 1989.

[56] P. Underwood. Dynamic relaxation. *Computation Methods for Transient Analysis*, 1:245–265, 1983.

[57] T. Vegge and K.W. Jacobsen. Atomistic simulations of dislocation processes in copper. *Journal of physics: Condensed matter*, 14:2929–2956, 2002.

[58] A.F. Voter. The embedded-atom method. *Intermetallic Compounds*, 1: Priciples:77–90, 1994.

[59] J. Weertman and J.R. Weertman. *Elementary Dislocation Theory*. The Macmillan Company, 1964.

[60] E. Wintner and H.P. Karnthaler. The geometry and formation of faulted dipoles in cu-al alloys. *Acta Metallurgica*, 26(6):941–949, 1978.